UNICAMP

Lucas Madeira

“Many-body systems: heavy rare-gases adsorbed on graphene substrates and ultracold Fermi gases”

“*Sistemas de muitos corpos: gases nobres pesados adsorvidos em substratos de grafeno e gases de Fermi ultrafrios*”

CAMPINAS
2015

UNICAMP

University of Campinas
Gleb Wataghin Physics Institute

Universidade Estadual de Campinas
Instituto de Física Gleb Wataghin

Lucas Madeira

"Many-body systems: heavy rare-gases adsorbed on graphene substrates and ultracold Fermi gases"

Supervisor:
Orientador(a): Prof. Dr. Silvio Antonio Sachetto Vitiello

"Sistemas de muitos corpos: gases nobres pesados adsorvidos em substratos de grafeno e gases de Fermi ultrafrios"

MSc Dissertation presented to the Post Graduate Program of the *Gleb Wataghin* Physics Institute of the University of Campinas to obtain a Master's degree in Physics.

This volume corresponds to the final version of the Dissertation defended by Lucas Madeira, under the supervision of Prof. Dr. Silvio Antonio Sachetto Vitiello.

Dissertação de Mestrado apresentada ao Programa de Pós-Graduação do Instituto de Física Gleb Wataghin da Universidade Estadual de Campinas para obtenção do título de Mestre em Física.

Este exemplar corresponde à versão final da Dissertação defendida por Lucas Madeira, sob orientação de Prof. Dr. Silvio Antonio Sachetto Vitiello.

Vitiello

Supervisor's signature / *Assinatura do Orientador(a)*

CAMPINAS
2015

Agência de fomento: FAPESP
Nº processo: 2012/24195-2

Ficha catalográfica
Universidade Estadual de Campinas
Biblioteca do Instituto de Física Gleb Wataghin
Valkíria Succi Vicente - CRB 8/5398

M264m
Madeira, Lucas, 1991-
Many-body systems : heavy rare-gases adsorbed on graphene substrates and ultracold Fermi gases / Lucas Madeira. – Campinas, SP : [s.n.], 2015.

Orientador: Silvio Antonio Sachetto Vitiello.
Dissertação (mestrado) – Universidade Estadual de Campinas, Instituto de Física Gleb Wataghin.

1. Adsorção. 2. Grafeno. 3. Férmions. 4. Vórtices. I. Vitiello, Silvio Antonio Sachetto,1950-. II. Universidade Estadual de Campinas. Instituto de Física Gleb Wataghin. III. Título.

Informações para Biblioteca Digital

Título em outro idioma: Sistemas de muitos corpos : gases nobres pesados adsorvidos em substratos de grafeno e gases de Fermi ultrafrios
Palavras-chave em inglês:
Adsorption
Graphene
Fermions
Vortex
Área de concentração: Física
Titulação: Mestre em Física
Banca examinadora:
Silvio Antonio Sachetto Vitiello [Orientador]
Alex Antonelli
Arnaldo Gammal
Data de defesa: 03-08-2015
Programa de Pós-Graduação: Física

IFGW
Instituto de Física Gleb Wataghin

UNICAMP

MEMBROS DA COMISSÃO JULGADORA DA DISSERTAÇÃO DE MESTRADO DE **LUCAS MADEIRA – RA 092043** APRESENTADA E APROVADA AO INSTITUTO DE FÍSICA "GLEB WATAGHIN", DA UNIVERSIDADE ESTADUAL DE CAMPINAS, EM 03 / 08 / 2015.

COMISSÃO JULGADORA:

Vitiello

Prof. Dr. Silvio Antonio Sachetto Vitiello - Orientador do Candidato
DFMC/IFGW/UNICAMP

Prof. Dr. Arnaldo Gammal – IF/USP

Alex Antonelli

Prof. Dr. Alex Antonelli – DFMC/IFGW/UNICAMP

Abstract

In this dissertation we investigated two many-body systems. For the first part we chose a classical approach to study the adsorption of heavy rare-gases, Ne, Ar, Kr, Xe and Rn, on graphene substrates. We presented evidences of commensurate adlayers, which depend strongly on the symmetry of the substrate, for two structures: Ne adlayers in the $\sqrt{7} \times \sqrt{7}$ superlattice and Kr in the $\sqrt{3} \times \sqrt{3}$ lattice. In order to study the melting of the system we introduced an order parameter, and its susceptibility. The specific heat and susceptibility as a function of the temperature were calculated for the heavy noble gases at various densities. The position and characteristic width of the specific heat and susceptibility peaks of these systems were determined. Finally, we investigated the first neighbor distance and the distance between the adlayer and the substrate, identifying contributions related to specific heat and melting peaks.

The second part of the dissertation deals with a vortex line in the unitary Fermi gas. Ultracold Fermi gases are remarkable due to the experimental possibility to tune interparticle interactions through Feshbach resonances, which allows the observation of the BCS-BEC crossover. Right in the middle of the crossover lies a strongly interacting state, the unitary Fermi gas. A vortex line corresponds to an excitation of this system with quantized units of circulation. We developed wavefunctions, inspired by the BCS wavefunction, to describe the ground state and also for a system with a vortex line. Our results for the ground state elucidate aspects of the cylindrical geometry of the problem. The density profile is flat in the center of the cylinder and vanishes smoothly at the wall. We were able to separate from the ground state of the system the wall contribution and we have determined the bulk energy as $\epsilon_0 = (0.42 \pm 0.01)E_{FG}$ per particle. We also calculated the superfluid pairing gap for this geometry, $\Delta = (0.76 \pm 0.01)E_{FG}$. For the system with a vortex line we obtained the density profile, which corresponds to a non-zero density at the core, and the excitation energy, $\epsilon_{ex} = (0.0058 \pm 0.0003)E_{FG}$ per particle. The methods employed in this dissertation, Molecular Dynamics, Variational Monte Carlo and Diffusion Monte Carlo, give us a solid basis for the investigation of related and other many-body systems in the future.

Keywords: heavy rare-gases; adsorption; graphene substrates; unitary Fermi gas; vortex line.

Resumo

Nessa dissertação nós investigamos dois sistemas de muitos corpos. Na primeira parte nós escolhemos uma abordagem clássica para estudar a adsorção de gases nobres pesados, Ne, Ar, Kr, Xe e Rn, em substratos de grafeno. Nós apresentamos evidências de camadas adsorvidas comensuradas, as quais dependem fortemente da simetria do substrato, para duas estruturas: camadas de Ne na rede $\sqrt{7} \times \sqrt{7}$ e Kr na rede $\sqrt{3} \times \sqrt{3}$. Para estudar o derretimento nós introduzimos um parâmetro de ordem e sua susceptibilidade. O calor específico e a susceptibilidade em função da temperatura foram calculados para os gases nobres pesados em diversas densidades. A posição e largura característica dos picos do calor específico e da susceptibilidade foram determinadas. Finalmente, nós investigamos a distância dos primeiros vizinhos e a distância entre a camada e o substrato, identificando contribuições relacionadas aos picos do calor específico e da susceptibilidade.

A segunda parte da dissertação trata de uma linha de vórtice no gás unitário de Fermi. Gases fermiônicos ultrafrios são notáveis devido à possibilidade experimental de variar as interações interpartículas através de ressonâncias de Feshbach, o que possibilita a observação do *crossover* BCS-BEC. No meio do *crossover* encontra-se um estado fortemente interagente, o gás unitário de Fermi. Uma linha de vórtice corresponde a uma excitação desse sistema com unidades de circulação quantizadas. Nós construímos funções de onda, inspiradas na função BCS, para descrever o estado fundamental e também o sistema com uma linha de vórtice. Nossos resultados para o estado fundamental elucidam aspectos da geometria cilíndrica do problema. O perfil de densidade é constante no centro do cilindro e vai a zero suavemente na borda. Nós separamos a contribuição devido à parede da energia do estado fundamental e determinamos a energia por partícula do *bulk*, $\epsilon_0 = (0.42 \pm 0.01)E_{FG}$. Nós também calculamos o *gap* superfluído para essa geometria, $\Delta = (0.76 \pm 0.01)E_{FG}$. Para o sistema com a linha de vórtice nós obtivemos o perfil de densidade, o qual corresponde a uma densidade não nula no centro do vórtice, e a energia de excitação por partícula, $\epsilon_{ex} = (0.0058 \pm 0.0003)E_{FG}$. Os métodos empregados nessa dissertação, Dinâmica Molecular, Monte Carlo Variacional e Monte Carlo de Difusão, nos dão uma base sólida para a investigação de sistemas relacionados, e outros sistemas, de muitos corpos no futuro.

Palavras-chave: gases nobres pesados; adsorção; substratos de grafeno; gás unitário de Fermi; linha de vórtice.

Ao meu pai e à Marina.

Acknowledgements

Aparentemente a gráfica da Unicamp tem regras bem rígidas para a formatação do manuscrito, e é aconselhável que os agradecimentos ocupem uma folha só. Quem realmente me conhece sabe que essa situação é muito confortável para mim. Ainda que eu não consiga traduzir em palavras, cada um sabe o tamanho de sua contribuição para esse trabalho. Eu agradeço cada pessoa uma vez, pela contribuição que eu acho mais importante, para evitar a reptição de certos nomes em muitos parágrafos.

Primeiramente, começo com a pessoa absolutamente essencial para todo esse trabalho. Agradeço o prof. Silvio pelas discussões e, principalmente, pela paciência. As lições que ele me ensinou não estão restritas somente à Física, mas sim representam minha formação como pesquisador. Espero um dia ter alunos, e com esses alunos ter a dedicação que o prof. Silvio teve comigo.

A escolha de dedicatória dessa dissertação, ao meu ver, é única. Com certeza a motivação para ser pesquisador veio do meu pai, o qual tem apoiado minha carreira acadêmica desde a graduação. À Marina, *la mia domenica di sole e d'azzurro*, só resta agradecer mais uma vez pelo amor e dedicação.

Agradeço ao Renato por me apoiar em seis meses muito *diferentes* (e melhorar meu gosto musical também!). E obrigado aos meus colegas de grupo pelas discussões proveitosas: Bruno, Vitor, Vinicius e Elkin.

Obrigado aos professores que participaram dos meus seminários do mestrado: Edison (EQM), Marcos Cesar (Pré-requisito), Alex (EQM, Pré-requisito e Defesa!) e Gammal (Defesa). Um agradecimento muito especial para os meus professores de disciplinas na pós, Marcus Aguiar e Amir. Também aprendi muito com os professors dos quais fui monitor: Granado, Marco Aurélio e Guzzo. Agradeço também os professores do DFMC: Brum, Marcus Bonança e Maurice; e do IMECC: Jayme e Saa. E pela prontidão e eficiência, agradeço a secretaria do DFMC, Emília e Oswaldo.

E claro que não podia deixar de agradecer as contribuições dos meus amigos! Ao Rodolfo eu agradeço por todas as vezes que eu escorreguei a cadeira para a mesa dele, interrompi o que ele estava fazendo e fiz ele pensar em algum problema; Lisan, "é o tal negócio"; Helder e Thiago pelos bons momentos da salinha; Carol por sempre saber o que dizer (ou talvez imitar?) na hora certa; e também não poderiam faltar Adriano, Elohim, Kellen, Murilo, Thais e Veronez. E meus colegas de outros departamentos: Alexandre, Ander (não é erro de digitação) e Paula, Guilherme, Hugo e Renan.

Impossível não agradecer os instrutores Küsel e Carlos (CENAPAD-SP) e Fábio (CCJDR) por me ensinarem a usar as ferramentas de HPC necessárias para essa dissertação.

I am grateful to Kevin and his family. They really helped me during my stay in the US. Working with Kevin comes very easily to me. I have not quite figured out what kind of relationship we have, certainly it is not the standard advisor-student one. Luckily, I will have more time to evaluate it. I also thank my friends Jie and Rong for the fun times and for the attempt to teach me some Chinese; and Joel for helping me with my PhD application.

I thank Stefano for teaching me the tricks of the trade when doing QMC simulations. Ringrazio Stefano e la sua famiglia per la grigliata! Infine, grazie mille per la mia bravissima professoressa di italiano, Mariana.

Os autores agradecem à Fundação de Amparo à Pesquisa do Estado de São Paulo (FAPESP) pelo apoio financeiro através dos processos #2012/24195-2 e #2013/19853-3.

"Against stupidity the gods themselves
contend in vain?"
Isaac Asimov in "*The Gods*
Themselves" inspired by Friedrich
Schiller's "*The Maid of Orleans*"

Contents

Abstract vii

Resumo ix

Dedication xi

Acknowledgements xiii

Epigraph xv

1 Introduction 1

I Heavy rare-gas atoms adsorbed on graphene 5

2 Adsorption 7

2.1 Introduction 7
2.2 Interactions 8
2.2.1 Interatomic interactions 8
2.2.2 Atom-surface interactions 11
2.2.3 Semiempirical methods 13
2.3 Monolayer physics 13
2.3.1 Commensurate structures 14
2.3.2 Topological defects 18
2.4 Heavy noble gases adlayers on graphite substrates 20
2.4.1 Neon 21
2.4.2 Argon 22
2.4.3 Krypton 25
2.4.4 Xenon 27
2.4.5 Radon 28
2.5 Heavy noble gases adlayers on graphene substrates 29

3 Methods **31**
3.1 Introduction . . . 31
3.2 Molecular Dynamics . . . 31
  3.2.1 Liouville formulation . . . 33
  3.2.2 Nosé-Hoover thermostat . . . 35
  3.2.3 Periodic boundary conditions . . . 38
  3.2.4 LAMMPS . . . 39
3.3 Potential interactions . . . 40
  3.3.1 Adatoms interactions . . . 40
  3.3.2 Adatom-substrate interaction . . . 43
  3.3.3 Substrate interactions . . . 44
3.4 Thermodynamical quantities . . . 45
  3.4.1 Specific Heat . . . 46
  3.4.2 First neighbor distance . . . 47
3.5 Simulation setup . . . 47

4 Results **51**
4.1 Introduction . . . 51
4.2 Commensurate solids . . . 51
4.3 Specific Heat . . . 54
4.4 Melting . . . 56
4.5 First neighbor distance . . . 58
4.6 Distance from the substrate . . . 61

5 Conclusions **63**

II Vortex line in the unitary Fermi gas **65**

6 Ultracold Fermi gases **67**
6.1 Introduction . . . 67
6.2 Tunable interactions . . . 69
6.3 Global phase diagram . . . 71
  6.3.1 Ground-state crossover . . . 71
  6.3.2 Finite temperature properties . . . 72
6.4 Unitary Fermi gas: quantum Monte Carlo studies . . . 72

7 Quantum Monte Carlo methods **75**
7.1 Introduction . . . 75

7.2 Monte Carlo methods 75
  7.2.1 The Metropolis algorithm 77
7.3 Variational Monte Carlo 78
7.4 Diffusion Monte Carlo 79
  7.4.1 Importance sampling 80
  7.4.2 The fixed-node approximation 82
  7.4.3 Extrapolated estimators 82
  7.4.4 QMC on parallel computers 82
7.5 Vortex line 83
  7.5.1 Introduction 83
  7.5.2 Potential 84
  7.5.3 Wavefunctions 84

8 Results **91**
8.1 Introduction 91
8.2 Density profile 91
8.3 Energy 95
  8.3.1 Ground state 95
  8.3.2 Superfluid pairing gap 96
  8.3.3 Excitation energy 98

9 Conclusions **101**

10 Final remarks **103**

Bibliography **105**

A Implementation of the Nosé-Hoover thermostat **119**
A.1 Nosé-Hoover chains 120

B Scattering theory **125**
B.1 The Lippmann-Schwinger equation 125
B.2 Transition operator 129
B.3 Partial waves method 130
  B.3.1 Unitarity and phase shifts 132
  B.3.2 Determination of phase shifts 132
B.4 Low-energy scattering and bound states 134
  B.4.1 Rectangular well or barrier 134
  B.4.2 Zero-energy scattering and bound states 135
B.5 Identical particles and scattering 137

C Superfluid Fermi gases 139
C.1 Equilibrium properties of Fermi gases . . . 139
C.2 Effects of interactions . . . 140
  C.2.1 Superfluidity . . . 141
  C.2.2 Transition temperature . . . 141
  C.2.3 Eliminating the bare interaction . . . 143
  C.2.4 Analytical results . . . 145
  C.2.5 Induced interactions . . . 146
C.3 The condensed phase . . . 148

D Classical hydrodynamics 155

E Stochastic reconfiguration method 159

List of Tables

2.1 Survey of observed commensurate lattices for spherical adsorbates on graphite substrates [1]. 21

3.1 HFD-B parameters for Ne [2], Kr [3] and Xe [4]. Not all figures displayed are significant, they are displayed only to avoid round off errors. 41
3.2 HFDID1 parameters for Ar [5]. Not all figures displayed are significant, some are displayed only to avoid round off errors. 43
3.3 Tang-Toennies parameters for Rn [6]. All values are in atomic units. 43
3.4 Lennard-Jones parameters for the interactions between noble gases and carbon atoms. 44
3.5 Tersoff parameters for C-C interactions [7, 8]. 46
3.6 Number of noble gases atoms, carbon atoms and densities employed in the simulations. 49

4.1 Position and width of the specific heat peak for various noble gases and densities. The system size for each density is found in Table 3.6. 55
4.2 Melting temperature and characteristic width for various noble gases and densities. The system size for each density is found in Table 3.6. 58

List of Figures

2.1 Bravais lattices of the graphene substrate and of the $\sqrt{3}\times\sqrt{3}$ commensurate adlayer. 15

2.2 Geometrical construction of the commensurate $\sqrt{7}\times\sqrt{7}R19.1^\circ$ lattice. . . 17

2.3 Neon phase diagram from Calisti *et al.* [9]. The $\sqrt{7}$ ordered phase at lower T is not shown, and the 2D critical and triple points, indicated as T_c and T_t respectively, occur at pressures too low to measure. Data with filled symbols: triangles, Calisti *et al.* [9]; circles, Antoniou [10]; squares, Lerner and Hanono [11]. Data with unfilled symbols: squares, Lerner *et al.* [12]; triangles, Huff and Dash [13]; inverted triangles, Demetrio de Souza *et al.* [14]. 22

2.4 Phase diagram of Ar/graphite from Shaw and Fain [15]. The upper solid line denotes the bulk vapor pressure [16]. The solid-fluid transition is denoted by asterisks and long dashes [17–19]. All other symbols denote data of Shaw and Fain. 23

2.5 Phase diagram of Kr/graphite in terms of fractional coverage and temperature [20]. C, F and IC denote commensurate, fluid and incommensurate, respectively. There is a tricritical point at the intersection of the C to F boundary and the extrapolation (dashed) of the IC to C+F. C_1 is a multicritical point. 25

2.6 Kr/graphite phase diagram as function of the chemical potential and the temperature [21]. RF stands for the reentrant fluid phase, a domain wall fluid bounded by C (commensurate) and IC (incommensurate) regimes. S and L are the 3D bulk solid and liquid phases, respectively. Solid lines denote first-order transitions and dashed lines denote continuous transitions. 26

3.1 Illustration of the PBC procedure. The central cell has three atoms (red, blue and green) and the vectors indicate their velocities. For sake of simplicity, we just replicated the central blue cell 8 times (red cells), out of the 26 in the 3D case. 39

3.2 Potential energies for the Ne-Ne, Ar-Ar, Kr-Kr, Xe-Xe and Rn-Rn interactions. 42

3.3 Potentials for the Ne-C, Ar-C, Kr-C, Xe-C and Rn-C interactions. 44
3.4 Commensurate lattice rectangular cell. The black circles represent the position of C atoms and the purple diamonds indicate the position of the heavy noble gases atoms. 48
3.5 Initial configuration of the system for $\rho = 1$. The argon atoms (purple) are arranged in the $\sqrt{3}$ commensurate structure over the carbon atoms (grey). This figure was produced with the AtomEye software [22]. 48

4.1 Radial pair distribution function for Ne atoms at $\rho = 1.71$ and $T = 10$ K. The dashed lines correspond to the ideal positions of atoms in the $\sqrt{7} \times \sqrt{7}$ superlattice. 52
4.2 Spatial distribution of Kr atoms over a cell at $\rho = 1$ and $T = 100$ K. The red circles represent the ideal positions of carbon atoms. The color code is related to the probability of finding a Kr atom at a given position in the plane parallel to the substrate. Only the regions compatible with the $\sqrt{3} \times \sqrt{3}$ lattice are occupied. 53
4.3 Spatial distribution of argon atoms over a cell at $\rho = 1$ and $T = 40$ K. The black circles represent the ideal positions of carbon atoms. The color code is related to the probability of finding an Ar atom at a given position in the plane parallel to the graphene. Although the probability of finding an Ar atom over the center of a carbon hexagon is higher than in other positions, the atoms are not arranged in the $\sqrt{3} \times \sqrt{3}$ commensurate structure. . . . 54
4.4 Ar adlayer specific heat as a function of the temperature for $\rho = 1$. The region of the peak is magnified in the inset and the line corresponds to a Lorentzian fitting. 55
4.5 Order parameter (circles) and susceptibility (squares) for Ar at $\rho = 0.38$ as a function of the temperature. The line corresponds to a Lorentzian fitting of the susceptibility peak. 57
4.6 First neighbor distance $\langle a \rangle$ as a function of the temperature for Ar adlayers at various densities. 59
4.7 First neighbor distance as a function of the temperature for Ne and Kr adlayers. 60
4.8 First neighbor distance as a function of the temperature for Xe at $\rho = 1$. The green region corresponds to the specific heat peak $T_p = 134.3$ K and its corresponding FWHM. 60
4.9 Distance from the substrate as a function of the temperature for Ar adlayers at the given densities. 61

4.10 Distance from the substrate as a function of the temperature for Kr adlayers at $\rho = 1$. The filled region corresponds to the specific heat peak $T_p = 107.4$ K and its corresponding FWHM. 62
4.11 Distance from the substrate as a function of the temperature for Xe and Rn adlayers. Note that the $y-$scale differs between the different layers. . . 62

6.1 Figures from [23] illustrating the open and closed channels in two-body scattering (a) and the scattering length a relation with the square well potential depth V_0 and the formation of a bound state with energy E_b (b). 70
6.2 Qualitative phase diagram of the BCS-BEC crossover from [23], which relates k_BT/E_F with the coupling $1/(k_Fa)$. The illustrations show schematically the evolution from large Cooper pairs (BCS) to tightly bound molecules (BEC). Unitarity, $1/(k_Fa) = 0$, corresponds to strongly interacting pairs with pair sizes $\simeq k_F^{-1}$. With increasing attraction, the pair-formation temperature T^* diverges from the transition temperature T_c. 73

8.1 Ground state density as a function of the cylindrical coordinate ρ at the given values of A, all corresponding to systems with open shells. 92
8.2 Ground state density as a function of the cylindrical coordinate ρ at the given values of A, all corresponding to systems with closed shells. 93
8.3 Density of the system with a vortex line as a function of the cylindrical coordinate ρ at the given values of A, all corresponding to systems with open shells. 93
8.4 Density of the system with a vortex line as a function of the cylindrical coordinate ρ for various values of A, all corresponding to systems with closed shells. 94
8.5 Comparison between the density profile for the ground state and the system with a vortex line, both for $A = 50$. 94
8.6 Ground state energy per particle as a function of the number of particles for open and closed shells. 95
8.7 Ground state energy per particle as a function of the cylinder radius $\mathcal{R}$. The solid line corresponds to the fitted energy per particle (Eq. (8.3)). . . . 96
8.8 Ground state energy for even and odd number of particles. The solid lines correspond to linear fits of the even and odd system energies. 98
8.9 Ground state and vortex line energy per particle. 99

B.1 Integration in the complex plane using the residues method. 127
B.2 The dashed region corresponds to the finite-range scattering potential. The point P denotes where the wavefunction $\langle \mathbf{x}|\psi^{(\pm)}\rangle$ is going to be evaluated. 128

B.3 Figures from [24] showing $u(r) \times r$ for $V = 0$ (a); $V_0 < 0$ and $\delta_0 > 0$ (b); $V_0 > 0$ and $\delta_0 < 0$ (c). 135
B.4 Figures from [24] showing $u(r) \times r$ for an attractive potential (a) and deeper attraction (b). For each case the intercept a of the zero-energy outside wavefunction with the r-axis is shown. 136

C.1 Diagrams representing two-particle (a) and two-hole (b) intermediate states in two-particle scattering. Solid lines represent the two kinds of fermions, and dashed lines correspond to the bare interactions. Time advances from left to right, thus arrows to the right stand for particles and arrows to the left are holes. 142
C.2 Diagrams representing two-particle interactions in the presence of a medium. The notation is the same of Fig. C.1. 146

Chapter 1

Introduction

Condensed matter physics is simplified by the common topologies of phase diagrams of distinct materials, and universal values of critical exponents of phase transitions. Thin films adsorbed on substrates are confined to a narrow domain near the surface of the substrate, and they are very close to a 2D phase of matter. The subject of adsorbed layers is particularly interesting because of the possibility of bidimensional phases that have no tridimensional analog, considering the same material. Furthermore, the spatial periodicity of the substrate may cause interesting effects. We look for conditions that cause near coincidence of the adsorbate and substrate length scales. The desired match is called a commensurate structure, which is an adsorbate lattice that "obeys" the symmetry of the substrate. Usually, the density distribution and other thermodynamical properties are quite different from what would be expected a simple 2D material.

The study of adsorption on solid surfaces began long time ago because of its intrinsic scientific interest and also due to its importance as a mean to better understand physical processes, at atomic level, which can be of technological interest. Adsorption of noble gases on graphite substrate has been extensively studied from the theoretical and experimental point of view. For a comprehensive review of the subject, the reader is referred to [25] and references therein. Although adsorption on graphite and other carbon structures can be considered well-known, we know very little of noble gases adsorbed on graphene.

The physics of graphene was once considered a simplified approximation to that of graphite. However, once a single graphene sheet was isolated in 2004, physicists and chemists have taken great interest in novel properties of this carbon structure. In 2010 the Royal Swedish Academy of Sciences has decided to award the Nobel Prize in Physics to Andre Geim and Konstantin Novoselov "for groundbreaking experiments regarding the two-dimensional material graphene".

> “Graphene is a form of carbon. As a material it is completely new – not only the thinnest ever but also the strongest. As a conductor of electricity it performs as well as copper. As a conductor of heat it outperforms all other known materials. It is almost completely transparent, yet so dense that not even helium, the smallest gas atom, can pass through it. Carbon, the basis of all known life on earth, has surprised us once again.” - The Nobel Foundation, press release, 5 October 2010, `http://www.nobelprize.org/nobel_prizes/physics/laureates/2010/press.html`

The first goal of this dissertation is to study heavy[1] noble gases (Ne, Ar, Kr, Xe and Rn) adsorbed on graphene substrates. We are motivated by the interesting characteristics of similar systems, noble gases adsorbed on graphite. Ne adsorbed on graphite exhibits a superlattice structure known as $\sqrt{7}\times\sqrt{7}$ [13], whereas Kr and Xe form a $\sqrt{3}\times\sqrt{3}$ commensurate lattice [1]. Although the formation of a commensurate lattice of Ar/graphite has not been reported, the specific heat of this system presents fascinating characteristics [26].

The second goal of this work is to study an intrinsically quantum system: the unitary Fermi gas. Fermions, such as electrons, protons and neutrons, are all around us: nuclei, atoms, electrons in metals and even neutron stars; and the behavior of such systems is governed by the Fermi-Dirac statistics. If a Fermi gas is cooled below the Fermi temperature, quantum statistic effects can be observed.

This ultracold Fermi gas is a dilute system in which interparticle interactions can be controlled through Feshbach resonances, which allows us to access strongly interacting regimes. Until very recently, superfluids were classified as either bosonic or fermionic. The Bose-Einstein condensate (BEC) theory was developed to describe bosonic fluids. The condensate is a macroscopic occupation of a single quantum state which occurs at a temperature of same order of magnitude as the quantum degeneracy temperature. The interparticle spacing in these systems is of the order of the thermal de Broglie wavelength. The Bardeen-Cooper-Schrieffer (BCS) theory was first conceived to describe pairing instability, arising from weak interactions, in a highly degenerate Fermi gas. The formation of the pairs and their condensation occur at a temperature which is orders of magnitude smaller than the Fermi temperature.

Later it was realized that the BCS and BEC schemes are limit cases of a continuum of interactions. The possibility of tuning parameters in order to observe the change from one paradigm to the other was conceptually interesting, but real enthusiasm came from the experimental realization of the BCS-BEC crossover [27]. In the middle of the crossover lies a strongly interacting system known as unitary Fermi gas, with remarkable properties.

---

[1] The Molecular Dynamics algorithms described in this dissertation would not depict the quantum effects observed for He, so we chose to restrict ourselves to the other noble gases.

Our goal is to investigate superfluidity in the unitary Fermi gas; particularly, we are interested in a vortex line excitation in these systems. This study is motivated by the discovery of vortex lattices in strongly interacting rotating Fermi gases [28]. The quantization of the flow manifests itself in quantized units of circulation, and there has not been evidence of vortices with more than one quanta of circulation. A large body of experimental and theoretical work has been carried out for bosonic systems, however the structure of quantized vortices in fermionic fluids still has unresolved questions.

As stated above, this dissertation is comprised of two distinct parts which complement each other, in the sense that we simulate classical systems as well as quantum systems. The first part, chapters 2 to 5, deals with physical adsorption. In chapter 2 we introduce theoretical aspects of physical adsorption, focusing on graphite and graphene substrates. In chapter 3 we present the molecular dynamics method and the potential interactions we chose to model the noble gas adsorbed on graphene systems. The results and conclusions are in chapters 4 and 5, respectively. The second part consists of chapters 6 to 9, where we develop the tools needed for the study of vortex line excitations in the unitary Fermi gas. We begin with an introduction to ultracold Fermi gases in chapter 6. The simulation methods we have employed and the wavefunctions we have constructed are presented in chapter 7. Chapter 8 contains the results for the ground state of this system as well as the vortex line excitation. Finally, we present our conclusions in chapter 9. We make our final considerations about the character of the two parts of the dissertation in chapter 10.

Part I

Heavy rare-gas atoms adsorbed on graphene

Chapter 2

Adsorption

2.1 Introduction

Consider an ideal atomic surface exposed to a vapor, held at pressure P and temperature T. In equilibrium with this vapor there will be a film on the surface, with coverage that depends on P, T and relevant interaction potentials. If P, but not necessarily T, is low, the number of atoms per unit area on the surface is small, and the atoms will be confined to a narrow domain near the surface because of the attraction of the substrate. This film is very close to a 2D phase of matter and, in the most interesting cases, with properties qualitatively distinct from the 3D phase of the same material. This subject is particularly interesting because of the vast behaviors that may occur varying P and T. Included in the possible behaviors are some phases similar to 3D phases: gases, liquids and solids; more intriguing are states totally new, with no 3D analog. Among the possibilities there are the commensurate phases, in which the adsorbed layer has its positional order imposed by the substrate symmetry.

Condensed matter physics of 3D matter is simplified, conceptually and computationally, by the common topologies of phase diagrams of distinct materials, as exemplified by universal values of the critical exponents of phase transitions. Similar *universality* is found in 2D, however there are more classes because of the numerous combinations of adsorbate and substrate. One of the many challenges of this field is to predict and model these different behaviors, which requires careful assessment of the relevant forces and, very often, imagination to conceive the possible 2D states.

This work is concerned with *physical* adsorption, sometimes called by the agglutination *physisorption*, which is the weak binding of atoms or molecules to surfaces. In contrast there is *chemisorption*, which refers to stronger binding. The distinction arises from the "chemical" forces in the latter case, while only van der Waals forces are present in the former. This is an oversimplification because there is a continuum of interactions energies and the line must be drawn somewhere.

> “In the structure of matter there can be no fundamental distinction between chemical and physical forces: it has been customary to call a force *chemical* when it is more familiar to chemists, and to call the same force *physical* when the physicist discovers an explanation of it.” - I. Langmuir, *Phenomena, Atoms, and Molecules* (Philosophical Library, NY, 1950) p.60

We adopt the arbitrary value of 0.3 eV as the upper bound for the binding energy of a single atom in the case of physical adsorption, which makes all the systems considered in this work subject to physisorption.

Several consequences of weak binding make physical adsorption interesting for theoretical and experimental study. The phenomena often reveal conceptual simplicity, making the subject ideal for fundamental research and attracting scientists from various backgrounds.

In this chapter we introduce some aspects of physical adsorption. First, we develop the theoretical background; in Sec. 2.2 we model the interactions between the constituents of an adsorption system: interatomic interactions, Sec. 2.2.1, atom-surface, Secs. 2.2.2 and 2.2.3. In Sec. 2.3 we focus on characteristics of a monolayer; we provide examples of commensurate structures, Sec. 2.3.1, and we introduce a theory which allows continuous melting in 2D systems, Sec. 2.3.2. Finally we review the advances in the study of heavy noble gases on graphite, Sec. 2.4, and graphene, Sec. 2.5.

2.2 Interactions

The properties of the adlayers are ultimately determined by the interaction between the constituents. In this section we develop the concepts that are useful to understand and model the forces acting in the system. One of the simplifying aspects of physisorption, opposed to chemisorption, is that the electronic structures of both the adsorbate and the surface are only weakly perturbed. Likewise, the interactions between the constituents of the adlayer are, to a good first approximation, determined by interactions between atoms in the gas phase.

2.2.1 Interatomic interactions

The interactions between the atoms in the adsorbed layer and between atoms and solid surfaces can be represented, to a good approximation, by the sum of interactions of pairs of atoms.

From a quantum chemistry point of view, the interaction between two atoms is unequivocally defined: for a given separation one must calculate the ground state energy. Not surprisingly enough, this is far easier stated than done.

Consider two atoms A and B, with nuclear charges Z_A and Z_B, located at $\mathbf{R}_A$ and $\mathbf{R}_B$, respectively. The Hamiltonian of the system with $N = Z_A + Z_B$ electrons can be written as

$$H = \sum_{i=1}^{N} \frac{\mathbf{p}_i^2}{2m} - \sum_{i=1}^{N} \left[\frac{e^2 Z_A}{|\mathbf{r}_i - \mathbf{R}_A|} + \frac{e^2 Z_B}{|\mathbf{r}_i - \mathbf{R}_B|} \right] + \frac{1}{2} \sum_{i \neq j} \frac{e^2}{|\mathbf{r}_i - \mathbf{r}_j|} + \frac{e^2 Z_A Z_B}{|\mathbf{R}_A - \mathbf{R}_B|}. \tag{2.1}$$

The total ground state energy of the system $E(R)$ is a function of the nuclear separation $R = |\mathbf{R}_A - \mathbf{R}_B|$

$$E(R) = \langle \Psi | H | \Psi \rangle, \tag{2.2}$$

where the total N-electron wavefunction must be antisymmetric. If at large separations the ground state energy is $E_0^A + E_0^B$, then the interatomic potential $V(R)$ is defined as

$$V(R) = E(R) - E_0^A - E_0^B. \tag{2.3}$$

Typical features of the potential are: $V(R)$ approaches zero as $R \to \infty$; it has an attractive well at interatomic separations typical of a condensed phase, few Å; strongly repulsive at small separations. The depth and position of the well depends on the atomic species and nature of bonding.

No analytical solutions of Eq. (2.1) are available and we must resort to some form of approximation. The most appropriated approach depends on the system of interest. So far in the discussion we have assumed that the electrons were shared by atoms A and B, that is, a particular subset of electrons cannot be associated with a particular nucleus, even though on average each nucleus retains a fixed number of electrons. However, at large separations, the interactions between atoms is weak and we may assume that one subset of electrons belongs to atom A and a second to atom B. This leads to a partition of the Hamiltonian

$$H = H_A + H_B + V_{AB}, \tag{2.4}$$

where

$$H_A = \sum_{i=1}^{Z_A} \frac{\mathbf{p}_i^2}{2m} - \sum_{i=1}^{Z_A} \frac{e^2 Z_A}{|\mathbf{r}_i - \mathbf{R}_A|} + \frac{1}{2} \sum_{i \neq j}^{Z_A} \frac{e^2}{|\mathbf{r}_i - \mathbf{r}_j|}, \tag{2.5}$$

similarly for H_B,

$$V_{AB} = -\sum_{i=1}^{Z_A} \frac{e^2 Z_B}{|\mathbf{r}_i - \mathbf{R}_B|} - \sum_{j=1}^{Z_B} \frac{e^2 Z_A}{|\mathbf{r}_j - \mathbf{R}_A|} + \sum_{i=1}^{Z_A} \sum_{j=1}^{Z_B} \frac{e^2}{|\mathbf{r}_i - \mathbf{r}_j|} + \frac{e^2 Z_A Z_B}{|\mathbf{R}_A - \mathbf{R}_B|}. \tag{2.6}$$

If V_{AB} is neglected then the product states $|\Psi_m^A \Psi_n^B\rangle = |\Psi_m^A\rangle \otimes |\Psi_n^B\rangle$ are eigenstates of H. The ground state is $|\Psi_0^A \Psi_0^B\rangle$ with the energy value of infinite separation, $E_0^A + E_0^B$. The product state makes a distinction between electrons of the two atoms, violating the antisymmetry requirement for the total wavefunction. However, exchange terms have negligible effects on the ground state energy when R is large.

At large interatomic separations the Coulomb term V_{AB} can be treated as a perturbation of the isolated atomic Hamiltonians. V_{AB} induces correlations between electronic motions of the two atoms, resulting in an attractive force that arises from the change in the total correlation energy of the system. This interaction between atoms with no permanent electrostatic moment was first hypothesized by van der Waals and it is referred as *van der Waals* force. The leading term in the interaction at large R arises from the fluctuations of the dipole moments

$$V_{vdW}(R) = -\frac{C_6}{R^6}, \tag{2.7}$$

with

$$C_6 = \frac{3\hbar}{\pi} \int_0^\infty du \; \alpha_a(iu) \; \alpha_b(iu), \tag{2.8}$$

where $\alpha_a(\omega)$ and $\alpha_b(\omega)$ are the dynamic dipole polarizabilities of the atoms, continued to imaginary frequencies $\omega = iu$. Higher R^{-n} terms are obtained including the interaction of higher multipole moments, but it still fails at small R, due to the negligence of the antisymmetric parity of the wavefunction.

We resort to a semiempirical construction [1]. The idea is to write the total interaction $V(R)$ as a sum of the repulsive $V_{rep}(R)$ and attractive $V_{att}(R)$ parts

$$V(R) = V_{rep}(R) + V_{att}(R). \tag{2.9}$$

We must keep in mind that only $V(R)$ has a definite physical meaning. At large separations only $V_{att}(R)$ survives, and it has the form of Eq. (2.7) [1]. At small separations, a self-consistent-field approximation such as Hartree-Fock (HF) is useful. The electronic wavefunction is approximated as a Slater determinant of molecular orbitals, optimized to minimize the electronic energy. We rewrite Eq. (2.9) as

$$\begin{aligned} V(R) &= V_{HF}(R) + V_{corr}(R), \\ V_{HF}(R) &= E_{HF} - E_{HF}^A - E_{HF}^B, \\ V_{corr}(R) &= E_{corr} - E_{corr}^A - E_{corr}^B, \end{aligned} \tag{2.10}$$

where V_{HF} is the change in energy at the HF level and V_{corr} is the change in the correlation energy. This definition conforms to the usual definition of correlation energy as the correction to the total energy obtained in the HF approximation. The partitioning in Eq. (2.10) has the advantage that the HF energy $V_{HF}(R)$ can be evaluated numerically, with reasonable accuracy, for many atomic combinations. For a pair of closed shell atoms, such as the noble gases, $V_{HF}(R)$ is expected to be purely repulsive. The repulsive interaction can be approximated, over a limited range, as

---

[1] For now we will assume that only dipolar interactions are relevant. Higher multipole contributions can be included in a similar fashion.

$$V_{HF}(R) = V_0 e^{-\alpha R}. \tag{2.11}$$

The change in the total correlation energy $V_{corr}(R)$ is assumed to be [29]

$$\begin{aligned} V_{corr}(R) &= -f_N(\alpha R)\frac{C_6}{R^6}, \\ f_N(x) &= 1 - e^{-x}\sum_{n=0}^{N}\frac{x^n}{n!}. \end{aligned} \tag{2.12}$$

The damping factor f_N vanishes as x^{N+1} as $x \to 0$; tends to 1 for large x; and it eliminates the small R divergence for $N \geqslant 5$. When several terms are retained in the multipole series, it is usual to separate f_N for each inverse power law, and set the value of N equal to that power. The value of α is the range parameter in the exponential repulsion, although it is commonly treated as an adjustable parameter. This prescription, Eqs. (2.11) and (2.12), turns out to be a good representation of the interactions of noble gases pairs [30].

2.2.2 Atom-surface interactions

Conceptually, the problem of an atom interacting with a surface is similar to the atom-atom problem. However, it is more complex due to the number of interacting components. Let us consider the interaction of one adatom at $\mathbf{R}$ with N_a substrate atoms at $\mathbf{R}_i$ ($i = 1, \ldots, N_a$). Analogously to the Born-Oppenheimer approximation, we could calculate the electronic energy states of the total system, and obtain the ground state energy $E(\{\mathbf{R}_i\})$ as a function of the atomic positions. The minimization of this function with respect to the $\{\mathbf{R}_i\}$ offers the possibility of deriving the surface structure. In practice, the atom-surface interaction is much weaker than interactions within the substrate, so the latter minimization is not performed.

The total energy of the combined system is given by

$$E(\mathbf{R}) = \langle\Psi|H(\mathbf{R})|\Psi\rangle, \tag{2.13}$$

where $\mathbf{R}$ is the position of the adsorbate and Ψ is the total electronic wavefunction. The interaction energy is defined as

$$V(\mathbf{R}) = E(\mathbf{R}) - E_0^a - E_0^s, \tag{2.14}$$

where E_0^a and E_0^s are the adsorbate and the substrate ground-state energies, respectively. At large separations $V(\mathbf{R})$ is a correlation energy, the analogue of the van der Waals interaction for a pair of atoms. The correlation energy changes when the adatom and substrate wave functions overlap significantly, ultimately leading to a short-range repulsion.

However, if we consider large enough separations, we can extend the van der Waals interaction between two closed-shell atoms to the atom-surface problem. We begin with a heuristic discussion of the interaction, which at large separations, takes the form

$$V_{vdW}(Z) \simeq -\frac{C_3}{Z^3}, \tag{2.15}$$

with C_3 given by

$$C_3 = \frac{\hbar}{4\pi}\int_0^\infty d\omega \frac{[\epsilon(i\omega)-1]}{[\epsilon(i\omega)+1]}\alpha(i\omega), \tag{2.16}$$

where α is the electric dipole polarizability of the adatom and ϵ is the long wavelength dielectric function of the substrate; both continued to imaginary frequencies.

In order to obtain Eq. (2.15) we consider Lennard-Jones' elementary model [1]. Consider a neutral spherically symmetric atom at a distance Z from a metal surface. Because of the motion of the electrons in the atom [2], the atom has instantaneous multipole moments with which the metallic electrons interact. If we assume a perfect conductor, its electrons respond instantaneously to the fields generated by the atomic charges and screen them. The leading term at large Z is determined by dipole interactions and we use the method of images to evaluate it. A dipole moment $\mathbf{p} = p_x\hat{x} + p_y\hat{y} + p_z\hat{z}$ has an image $\mathbf{p}' = -p_x\hat{x} - p_y\hat{y} + p_z\hat{z}$ at $-Z$, and the potential energy between the two is

$$V_p(Z) = \frac{1}{2}\left[\frac{\mathbf{p}\cdot\mathbf{p}' - 3p_z p_z'}{(2Z)^3}\right]. \tag{2.17}$$

First order perturbation theory leads to

$$V_p(Z) = -\frac{\langle p_z^2\rangle}{4Z^3} = -\frac{\langle \mathbf{p}^2\rangle}{12Z^3}, \tag{2.18}$$

where the brackets denote an average taken in the atomic ground state. Equations Eq. (2.16) and Eq. (2.18) are consistent since perfect screening corresponds to $\epsilon \to \infty$ and

$$\hbar\int_0^\infty d\omega\alpha(i\omega) = \pi\langle p_z^2\rangle. \tag{2.19}$$

Thus we have shown that an attractive interaction arises from the correlation between substrate charges and fluctuations of the adatom density, even when the time-dependent dipole moment has zero average value. Surely the idealization of perfect screening is extreme, but it is possible to show that, when all contributions to the screening response are included, we obtain Eq. (2.16).

---

[2] Because of the zero-point energy this statement holds even at $T = 0$ K.

2.2.3 Semiempirical methods

Most adsorbates are complex enough that first principles calculations do not provide realistic adatom-substrate interactions. We resort to semiempirical methods to construct the interactions [1].

The starting point is to consider the sum of pairwise interactions between the adsorbate with adatoms α and the substrate with components β at sites j_β

$$V(\{\mathbf{R}_\alpha\}) = \sum_{\alpha, j_\beta} \phi_{\alpha,\beta}(\mathbf{R}_\alpha - \mathbf{R}_{j_\beta}). \tag{2.20}$$

First we must choose a functional form for $\phi_{\alpha,\beta}(\mathbf{r})$, taking into account our knowledge of the substrate. Even if we know the exact interaction of an isolated α-β pair, the function entering Eq. (2.20) would be different because the β atoms are in a dense substrate environment, and the α atoms also suffer modifications. Luckly, for physical adsorption, the substrate is only weakly perturbed so that we may find an effective function for $\phi_{\alpha,\beta}(\mathbf{r})$.

The most extensive use of (2.20) is with the Lennard-Jones (12,6) potential

$$\phi(r) = 4\epsilon\left[\left(\frac{\sigma}{r}\right)^{12} - \left(\frac{\sigma}{r}\right)^{6}\right]. \tag{2.21}$$

The $1/r^6$ term is the London-van der Waals dispersion energy, while $1/r^{12}$ is included to model the strong short range repulsion.

We analyze the holding potential obtained from using Eq. (2.21) in Eq. (2.20). Usually, the Lennard-Jones (LJ) parameters for a pair of like atoms X-X, σ_{XX} and ϵ_{XX}, are known and we wish to obtain the LJ parameters for a mixed pair X-Y, σ_{XY} and ϵ_{XY}. A set of combining rules was devised to determine the parameters of the mixed pair X-Y in terms of like pairs X-X and Y-Y, which is

$$\begin{aligned}\sigma_{XY} &= \frac{(\sigma_{XX} + \sigma_{YY})}{2} \\ \epsilon_{XY} &= \sqrt{\epsilon_{XX}\ \epsilon_{YY}}\end{aligned} \tag{2.22}$$

2.3 Monolayer physics

Adsorption experiments are not always carried in thermodynamical equilibrium between the film and vapor. The main advantage of conducting experiments in equilibrium is that the state's properties are independent of the path taken to achieve it. Other advantage is the certainty that the chemical potential of the film equals that of the vapor.

It is physically plausible, and it can be proven [1], that a low density film coexists with a low pressure vapor [3]. In this regime, the linear relationship between coverage and pressure is called Henry's law

$$P = k_H(T)\frac{N}{A} \qquad (N/A \ll 1), \tag{2.23}$$

where $k_H(T)$ depends on the adsorption potential and the coverage, or density, is a 2D quantity, the number of adsorbed atoms N per unit area of surface A.

At higher pressures, many film structures are possible. The physical adsorption usually involves the formation of one or more well-defined layers with increasing P. Our concern in this work is the properties of the first layer. Often there is little ambiguity in experiments and simulations regarding this concept. However we should bear in mind that, at finite T, there is always an incomplete first layer at the same time that second layer sites are increasing in occupancy. This is one example of the several ambiguities in the definition of monolayer *completion*.

In the next section, Sec. 2.3.1, we present two commensurate lattices of the graphene and graphite substrates. In Sec. 2.3.2 we show how topological defects may result in a continuous melting of a bidimensional solid.

2.3.1 Commensurate structures

Physically adsorbed monolayer solids have lattice constants on the scale of few angstroms, and they may be compressed by increasing the pressure of the coexisting 3D gas. A small number of lattice classes is sufficient to describe most monolayer solids. The primitive vectors and basis vectors provide a convenient set of coordinates to express the periodicity of the lattice. Furthermore, the spatial periodicity of the potential arising from the substrate is conveniently described with such vectors.

First, we must introduce the 2D Bravais lattices that is basic to the description of the adlayer and substrate surface. For 2D disks there is one close-packed lattice, the triangular (or hexagonal), Fig. (2.1a). The primitive lattice vectors $\mathbf{a}_1$ and $\mathbf{a}_2$ of this lattice can be chosen to be

$$\begin{aligned} \mathbf{a}_1 &= a\left(\frac{\sqrt{3}}{2}\hat{x} + \frac{1}{2}\hat{y}\right), \\ \mathbf{a}_2 &= a\left(\frac{\sqrt{3}}{2}\hat{x} - \frac{1}{2}\hat{y}\right), \end{aligned} \tag{2.24}$$

---

[3] The converse is not necessarily true, at sufficient low temperatures the film is at a high density phase coexisting with a low pressure vapor.

both of length a and at an angle of 60°. It may be intuitive that inert gases tend to solidify in a triangular lattice, maximizing the packing. In fact, it is the most encountered lattice in monolayer solids.

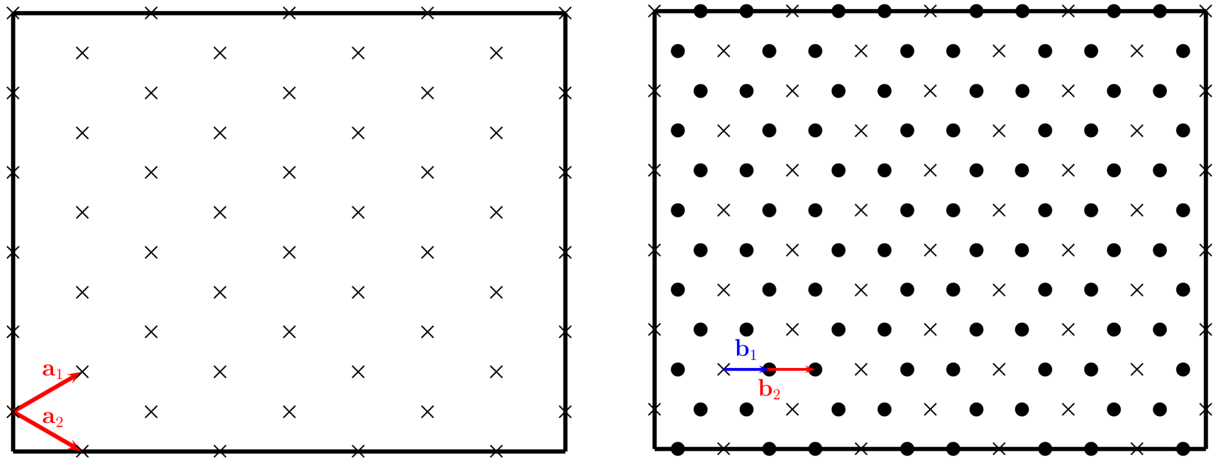

(a) Illustration of the triangular lattice sites (×) spawned by the vectors $\mathbf{a}_1$ and $\mathbf{a}_2$.

(b) The graphene honeycomb lattice (●) is generated by adding a two atom basis, $\mathbf{b}_1$ and $\mathbf{b}_2$, to the triangular lattice.

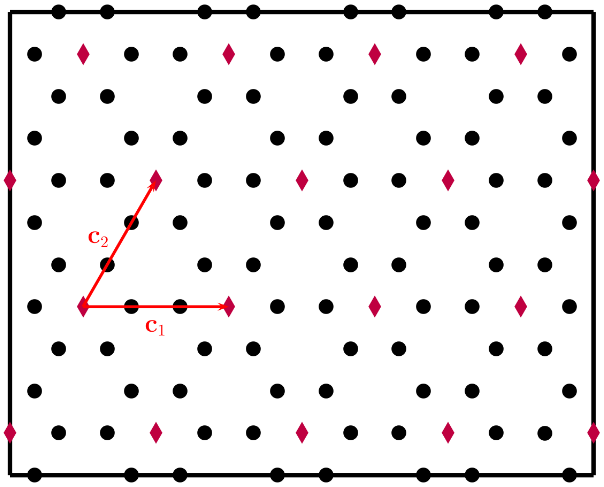

(c) Triangular lattice (♦) of the commensurate $\sqrt{3} \times \sqrt{3}$ structure. Notice the 30° rotation of the vectors with respect to Fig. (2.1a).

Figure 2.1: Bravais lattices of the graphene substrate and of the $\sqrt{3} \times \sqrt{3}$ commensurate adlayer.

Points $\mathbf{R}_{m,n}$ of the Bravais lattice are linear combinations of the primitive lattice vectors

$$\mathbf{R}_{m,n} = m\mathbf{a}_1 + n\mathbf{a}_2. \tag{2.25}$$

A more general lattice is achieved with a Bravais lattice with a basis. For example, a graphene sheet is a triangular lattice with a basis of two carbon atoms, Fig. (2.1b), at

$$\begin{aligned}\mathbf{b}_1 &= \frac{(\mathbf{a}_1+\mathbf{a}_2)}{3} = b\ \hat{x},\\ \mathbf{b}_2 &= 2\mathbf{b}_1 = 2b\ \hat{x},\end{aligned} \tag{2.26}$$

where we took $a = b\sqrt{3}$, with the bond length of two carbon atoms $b = 1.42$ Å. Generally, the sites of a Bravais lattice with a basis are generate by

$$\mathbf{R}_{m,n,j} = \mathbf{R}_{m,n} + \mathbf{b}_j. \tag{2.27}$$

A shift in the origin of the adlayer may be accomplished by addition of a constant vector on the right-hand side of Eq. (2.27).

The commensurate structure $\sqrt{3}\times\sqrt{3}R30^\circ$

The commensurate structure $\sqrt{3}\times\sqrt{3}R30^\circ$ [4] is a triangular lattice with a lattice constant of $3b$, and its axes are rotated (R) by 30° relative to the underlying triangular lattice, Fig. (2.1c). The primitive vectors $\mathbf{c}_1$ and $\mathbf{c}_2$ are obtained from Eq. (2.24) by performing a 30° rotation

$$\begin{aligned}\mathbf{c}_1 &= 3b\hat{x},\\ \mathbf{c}_2 &= \frac{3b}{2}\hat{x} + \frac{3b\sqrt{3}}{2}\hat{y},\end{aligned} \tag{2.28}$$

and with the identification $a = 3b$. Deviations of this commensurate structure, or incommensurability, are measured by the misfit, m_3, defined as

$$m_3 = \frac{\bar{a} - 3b}{3b}, \tag{2.29}$$

where $\bar{a}$ is the average nearest neighbor distance in the monolayer.

The commensurate structure $\sqrt{7}\times\sqrt{7}R19.1^\circ$

The $\sqrt{7}\times\sqrt{7}R19.1^\circ$ [5], Fig. (2.2c), is a superlattice structure with four atoms in the basis. The primitive vectors, Fig. (2.2a), are

$$\begin{aligned}\mathbf{d}_1 &= \mathbf{a}_1 + 2\mathbf{a}_2,\\ \mathbf{d}_2 &= 3\mathbf{a}_2 - 2\mathbf{a}_1.\end{aligned} \tag{2.30}$$

---

[4] It is common in the literature, and in this work, to reference this structure by shorter names: $\sqrt{3}\times\sqrt{3}$, $\sqrt{3}R30^\circ$, or simply $\sqrt{3}$ commensurate lattice.

[5] Analogously to Footnote (4), several terms are available for this commensurate lattice: $\sqrt{7}\times\sqrt{7}$, $\sqrt{7}R19.1^\circ$ and $\sqrt{7}$.

Notice that $|\mathbf{d}_1| = |\mathbf{d}_2| = a\sqrt{7}$, and the angle between the vectors $\mathbf{d}_1$ and $\mathbf{a}_1$ is 19.1°, hence the designation $\sqrt{7}\times\sqrt{7}R19.1^\circ$. The 4-atom basis vectors, Fig. (2.2b), are

$$\begin{aligned}
\mathbf{f}_1 &= \mathbf{0}, \\
\mathbf{f}_2 &= \frac{\mathbf{d}_1}{2}, \\
\mathbf{f}_3 &= \frac{\mathbf{d}_2}{2}, \\
\mathbf{f}_4 &= \frac{\mathbf{d}_1+\mathbf{d}_2}{2}. \qquad (2.31)
\end{aligned}$$

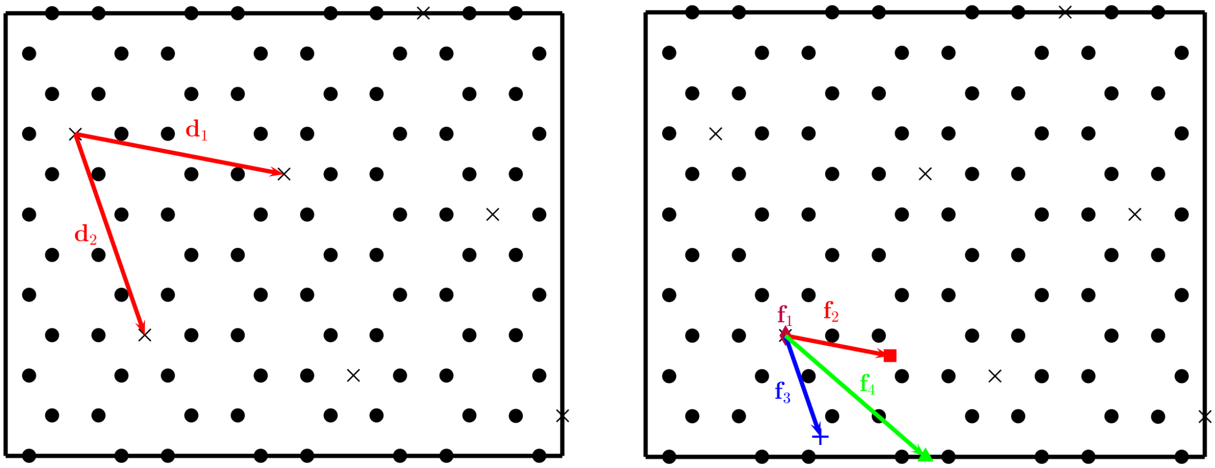

(a) Triangular lattice sites (×) spawned by the vectors $\mathbf{d}_1$ and $\mathbf{d}_2$.

(b) Four sites generated by the basis vectors $\mathbf{f}_1$ (♦), $\mathbf{f}_2$ (■), $\mathbf{f}_3$ (+) and $\mathbf{f}_4$ (▲).

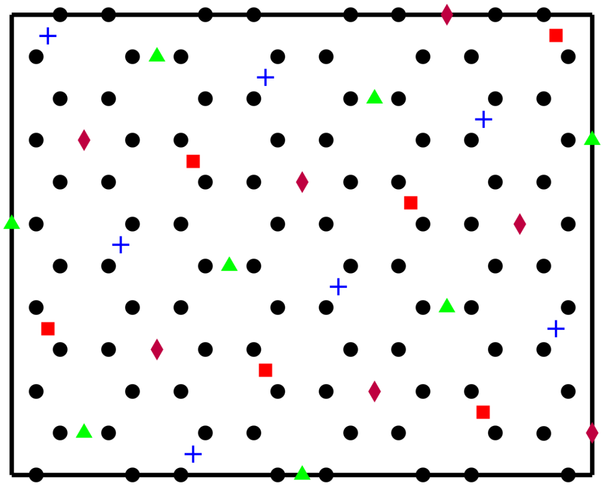

(c) Commensurate $\sqrt{7}\times\sqrt{7}R19.1^\circ$ lattice.

Figure 2.2: Geometrical construction of the commensurate $\sqrt{7}\times\sqrt{7}R19.1^\circ$ lattice.

2.3.2 Topological defects

So far we have adopted an approach based on discrete atomic positions. Over a wide range of conditions, the substrate potential constrains the monolayer to an effectively quasi-two-dimensional system. This creates situations where the long-range order is characteristic of continuous low-dimensional systems, with strong fluctuation effects which lead to singular thermodynamical behavior.

An edge dislocation is a point defect in a monolayer solid which has a role analogous to vortex singularities in a superfluid film. The energy of an isolated edge dislocation depends logarithmically on the area of the monolayer; the corresponding entropy of number of sites, which is also logarithmically on the area, leads to a threshold temperature at which edge dislocations can be thermally excited. It is characteristic of 2D systems that such topological defects may have quite large thermal populations, which contribute in a dominant way to the thermodynamics of the adlayer. A theory for melting of a 2D isotropic elastic solid was introduced by Kosterlitz, Thouless, Halperin, Nelson and Young (KTHNY) [31–35].

We use continuum elasticity theory to describe the monolayer solid and to provide an estimate of the temperatures to thermally activate dislocations. The deformation tensor u_{ij}, in Cartesian coordinates, of a continuous distortion of positions r_i to r_i' $(i = 1, 2, 3)$ is accomplished by introducing a displacement vector $\mathbf{u}$

$$r_i' = r_i + u_i(\mathbf{r}), \tag{2.32}$$

which is related to the deformation tensor

$$u_{ij} = \frac{du_i}{dr_j}. \tag{2.33}$$

Although linear elasticity theory is based on ‘smooth’ strains, it also admits point defects, solutions for which the closed line integral about the site of the dislocation does not vanish

$$\oint d\mathbf{u} = \mathbf{b}_0, \tag{2.34}$$

where $\mathbf{b}_0$ is the Burgers vector of the dislocation. We will use the lowest energy dislocation in the following discussion, which implies that $|\mathbf{b}_0| = a_0$, the lattice constant of the underlying lattice.

Deforming a 2D solid that is initially in a triangular lattice of total area A and spreading pressure Π requires an energy

$$\Delta E = \int_A d^2r \left[-\Pi \sum_i \eta_{ii} + \frac{1}{2}\lambda \left(\sum_i \eta_{ii} \right)^2 + \mu \sum_{ij} \eta_{ij}^2 \right], \tag{2.35}$$

where λ and μ are the Lamé constants of an isotropic elastic medium and the Lagrange strain tensor η_{ij} is related to the deformation tensor u_{ij} by

$$\eta_{ij} = \frac{1}{2}\left[u_{ij} + u_{ji} + \sum_k u_{ki}u_{kj}\right]. \tag{2.36}$$

Inversion and 6-fold-rotation symmetries of the triangular lattice were employed to produce Eq. (2.35). Nelson and Halperin [34] present an expression for the asymptotic behavior of an isolated dislocation obeying Eqs. (2.34) and (2.35). The energy increment at $\Pi = 0$ is

$$\Delta E_1 = \frac{a_0^2}{4\pi}\left[\frac{\mu(\lambda+\mu)}{(\lambda+2\mu)}\right]\ln\left(\frac{A}{A_0}\right). \tag{2.37}$$

The area A_0 is set by the small-distance behavior of the dislocation, which lies outside of the elastic approximation. The most important information in this result is the logarithmic dependence on the area A. Since the entropy of the dislocation is $S \simeq k_B \ln(A/A_0)$, the free energy will be lowered by spontaneous creation of dislocations above a temperature T_m given by

$$\frac{a_0^2}{4\pi k_B T_m} = \frac{1}{\mu} + \frac{1}{\mu+\lambda}. \tag{2.38}$$

Kosterlitz and Thouless [31] argue that below T_m there are bound pairs of dislocations with Burgers vectors of same magnitude and opposite directions, so that the logarithmic dependence on the total area is canceled and the energy of a pair depends logarithmically on its separation. The separation increases with increasing temperature and diverges at T_m. A more accurate description includes the effects of other thermally excited dislocation pairs on the energy of this pair, which requires a renormalization $\mu \to \mu_R$ and $\lambda \to \lambda_R$. Qualitatively, the relation between thermally excited dislocations to melting is that they are a mechanism for the solid to release shear stress; contrary to the solid, the fluid is not able to withstand a static shear. Thus, if there are unbound dislocations they must be in a medium that has melted.

For an incommensurate monolayer on a periodic substrate there is an additional term to the energy increment of Eq. (2.35),

$$\Delta E' = \Delta E - \frac{h}{2}\int d^2r \cos(6\theta), \tag{2.39}$$

where h is a substrate-dependent elastic constant [36].

The long-range orientational order in the triangular 2D solid is described by the correlation function

$$c_6(\mathbf{R}) = \langle \exp\left[i6\{\theta(\mathbf{R}) - \theta(0)\}\right]\rangle, \tag{2.40}$$

where $\theta(\mathbf{R})$ is the orientation of the bond between two neighboring atoms relative to a fixed axis; $\theta(\mathbf{R})$ is related to $\mathbf{u}(\mathbf{r})$ by

$$\theta(\mathbf{r}) = \frac{1}{2}\left(\frac{du_y}{dx} - \frac{du_x}{dy}\right). \tag{2.41}$$

The KTHNY theory characterizes the low temperature solid by long-range bond-orientational order in c_6, considering the triangular lattice on a smooth surface; and defects, such as dislocations, are defined by local short-range order. The melting scenario is characterized by the evolution of the correlations with increasing temperature. An isolated dislocation has an energy that increases logarithmically with the total area of the solid, thus it has a low thermodynamic probability at low temperatures. However, the strain field can be localized enough that pairs are thermally excited. Increasing the temperature increases the the relative separation of the pair, and at T_m the dislocations unbind and move *freely* relative to each other. As this system does not support shear stress we characterize it as a liquid. The orientational long-range order may remain for a temperature interval after the shear stress modulus has vanished, this is called a *hexatic* phase. For a second temperature T_i, higher than T_m, $c_6(\mathbf{R})$ has an exponential decay for large R. Both transitions at T_m and T_i are continuous, with no signatures in the specific heat. Interest in observing evidences of this theory in experiments arises from the contrasting discontinuous first-order melting with a latent heat that occurs for 3D solids of the same adsorbate.

2.4 Heavy noble gases adlayers on graphite substrates

In this section we survey several characteristics of physically adsorbed heavy noble gases layers on graphite substrates, which present a very diverse set of phenomena. The graphite substrate can be considered "well known" [1]: the basal plane surface exhibits a honeycomb net of carbon atoms spaced by 1.42 Å and its triangular Bravais cell of area 5.24 Å^2 contains a basis of two carbon atoms.

The spatially periodic potential arising from the substrate lattice may cause the density to be quite different from what would be expected of the bulk bidimensional noble gas. We are interested in conditions that enhance effects of the near coincidence of the adsorbate and the substrate length scales. Thus we scan the heavy noble gases looking for systems close enough to the desired match, and the remaining difference can be manipulated with thermomechanical stress. Solid phases present a diverse set of structures in the monolayer regime and their lattices vary with temperature and lateral stress. As an overview we present in Table 2.1 a survey of the commensurate structures, introduced in Sec. 2.3.1, observed for noble gases on graphite, which are discussed in the following sections. We also present several phase diagrams; while it is a cliché to repeat that we are “standing on the shoulders of giants”, each figure represents contributions of many authors and experiments.

Table 2.1: Survey of observed commensurate lattices for spherical adsorbates on graphite substrates [1].

Adsorbate	Structure
Ne	$\sqrt{7}$
Ar	None
Kr	$\sqrt{3}$
Xe	$\sqrt{3}$

2.4.1 Neon

Quantum effects are much smaller for neon than for helium, but are still significant. This is evident even in the 3D solid where the nearest neighbor distance L_{nn} in the ground state is 3.155 Å, whereas the minimum in the pair potential R_m occurs at ≈ 3.09 Å [1]. For a classical monoatomic solid L_{nn} is smaller than R_m, because it is compressed due to energy terms from farther neighbors.

Neutron diffraction experiments [37] found the lattice constant of monolayer solid Ne/graphite to be (3.25 ± 0.02) Å at 1.5 K. This length coincides with a higher order superlattice on graphite, the $\sqrt{7} \times \sqrt{7}R$ 19.1° lattice containing 4 neon atoms in the basis [13]. Further evidence which supports the existence of the superlattice in this system is low temperature specific heat data [13] showing an energy gap of 3.5 K. A model for Ne/graphite was constructed with 4-atoms unit cell [38] and calculations based on this model obtained a gap compatible with the experimental data [39].

Low energy electron diffraction (LEED) experiments [9,40] have shown an orientational angle between the incommensurate adlayer and the substrate for $14.5\ K \leqslant T \leqslant 17.5\ K$. The angle is $12° - 13°$ relative to the primitive vector $\vec{a_1}$, for lattice constants of $3.09 - 3.23$ Å. The smallest lattice constant is $\approx 2\%$ smaller than L_{nn} for the 3D solid, which makes the compressed monolayer a relative poor template for epitaxial growth of bulk neon.

A phase diagram from Calisti *et al.* [9] is shown in Fig. 2.3. The $\sqrt{7}$ superlattice is not indicated in the figure, it has been observed only for temperatures less than 5 K. The phase diagram indicates a gas-liquid critical point at $T_c = 15.8$ K and a gas-liquid-solid triple point at $T_t = 13.6$ K [41].

Modeling studies of the Ne/graphite include: the monolayer equation of state [42], layering transitions [43] and lattice dynamics of the monolayer solid [44].

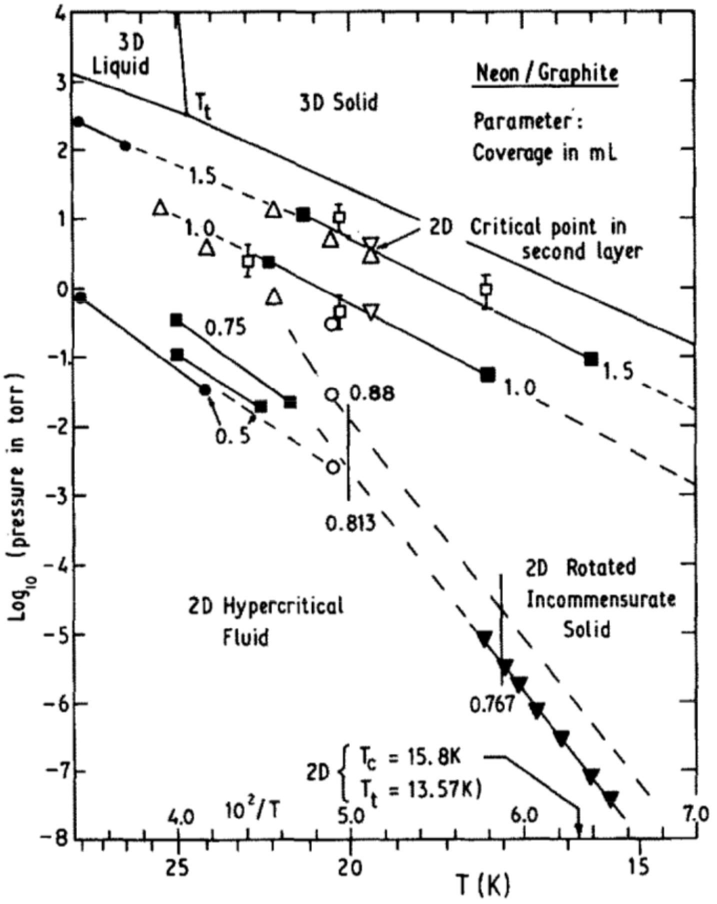

Figure 2.3: Neon phase diagram from Calisti *et al.* [9]. The $\sqrt{7}$ ordered phase at lower T is not shown, and the 2D critical and triple points, indicated as T_c and T_t respectively, occur at pressures too low to measure. Data with filled symbols: triangles, Calisti *et al.* [9]; circles, Antoniou [10]; squares, Lerner and Hanono [11]. Data with unfilled symbols: squares, Lerner *et al.* [12]; triangles, Huff and Dash [13]; inverted triangles, Demetrio de Souza *et al.* [14].

2.4.2 Argon

The argon atom is massive enough that quantum effects are small. The monolayer solid Ar/graphite was one of the first adsorption systems to have a wide range of structural data, mainly because the isotope ^{36}Ar has a large neutron scattering cross section. The $P-T$ phase diagram for Ar/graphite [15] is shown in Fig. 2.4. It presents gas, liquid and incommensurate solid phases (only a triangular lattice is observed). There is a triple point at $T_t = 49.7$ K according to D'Amico *et al.* [45] or at 47 K according to Migone *et al.* [46]; and a critical point $T_c = 59$ K [47] or 55 K [46]. The nearest neighbor spacing in the ground state of the 3D solid is 3.756 Å [1]. The monolayer solid is a triangular lattice with nearest neighbor spacing of 3.86 Å near $T = 0$ K [48]; and 3.97 Å at $T = 49.7$ K [45]. The first few layers of Ar/graphite provide a relative good template for further layer growth [49].

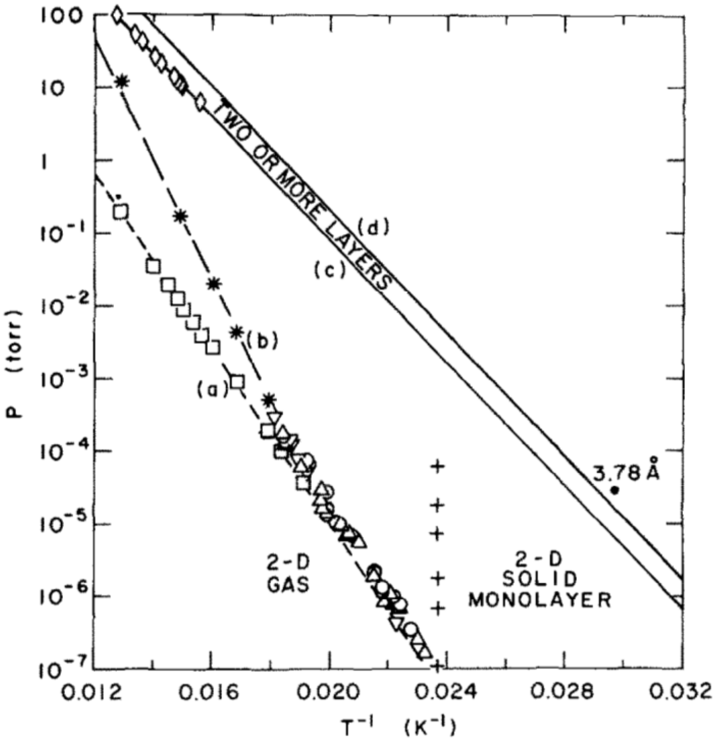

Figure 2.4: Phase diagram of Ar/graphite from Shaw and Fain [15]. The upper solid line denotes the bulk vapor pressure [16]. The solid-fluid transition is denoted by asterisks and long dashes [17–19]. All other symbols denote data of Shaw and Fain.

Experiments show that the behavior of argon films on graphite substrates (Ar/Graphite) is complex due to the quasi-bidimensional characteristics of the system. The first measurements of the system were performed by Chung [50] and they showed only one specific heat peak centered in ≈ 50 K with a Full Width at Half Maximum (FWHM) of the order of 20 K. Some words concerning the FWHM are in order. If we consider a Lorentzian function

$$f(T) = \frac{1}{\pi\gamma\left[1 + \left(\frac{T-T_0}{\gamma}\right)^2\right]}, \tag{2.42}$$

where T_0 is the mean, it is easy to show that the FWHM is 2γ. Other functions, for example Gaussians, also present well defined FWHM. These measurements were performed with superficial densities $n \leq 0,84\ n_0$, where n_0 corresponds to a complete monolayer. For $n = 0,97\ n_0$ the peak was centered in 78.5 K. The author concluded that the results were consistent with a continuous phase transition (melting).

Experiments with better resolution performed by Migone *et al.* [46] showed an additional feature not observed by Chung. For superficial densities $n \leq 0.83\ n_0$ a peak centered in 49.5 K with FWHM of 6.0 K was observed, in accordance to the previous experiments, but also a sharp peak with FWHM of 0.3 K was observed at 47.5 K. Thus the authors identified the sharp peak as evidence of a "weakly first order transition", and the broad peak was related to a gradual loss of sixfold symmetry. In a more recent study [51], Ma *et al.* reproduced the experiments of Migone for $n = 0.32\ n_0$ with the same results. However, with the addition of a small fraction of CH_4 or Xe to the argon mixture, only the broad peak remained.

Scattering experiments [45, 48, 52–54] contributed with much information about the Ar/Graphite system. The LEED results showed that the hexagonal lattice of the Ar adlayer is not aligned with the $\sqrt{3} \times \sqrt{3}$ symmetry axes of the substrate, in fact it is rotated [54]. In the x-ray experiments of D'Amico *et al.* [45], for $n = 0.65\ n_0$, the rotation angle varied from 2,87°, at 44.29 K, to 2°, at 50.03 K. The measured melting temperature was $T_m = 49.67K$, thus they concluded that the rotated state persists in the fluid. However, the scattering experiments concluded that melting is continuous and none could identify the character of the narrow or the broad peak.

Interest in the order of bidimensional melting arises from the possibility of continuous melting, unlike 3D systems which exhibit first order transitions. A theory for melting of *strictly* bidimensional films was introduced by Kosterlitz, Thouless, Halperin, Nelson and Young (KTHNY) [31–35], where a continuous transition is possible. According to the theory, Sec. 2.3.2, melting is preceded by a hexatic fluid with short range spatial ordering and quasi-long-range bond orientation. At higher temperatures, the system would undergo a second transition into an isotropic fluid. It is noteworthy that the KTHNY theory predicts an undetectable singularity in the specific heat at the first melting temperature, followed by a large anomaly at higher temperatures. First order melting, similar to 3D systems, is another possibility predicted by this theory. Many of the 2D systems which have been examined exhibited first order melting transitions. Two possible exceptions are Xe/Graphite and Ar/Graphite. It is settled that melting submonolayer Xe/Graphite is of first order [55, 56], but at higher densities there is no agreement on the order of melting [52, 57].

Uncertainty in the order of melting in Ar/Graphite is raised in Refs. [46], [51] and [53]. Many computer simulations were designed to probe the characteristics of the phase transition of Ar/graphite. One study [58] observed continuous melting over an interval of 7 K; and it also determined that the probability of finding an Ar atom over the center of a substrate hexagon is higher than in other sites, despite the incommensurate lattice of Ar. The broad peak of the specific heat was successfully observed in a more recent calculation [59], and the extension of these simulations [60] showed the narrow peak at

43.8 K in addition to the broad peak at 49.5 K, in accordance with Refs. [46] and [51]. However, the interpretation was quite different: the sharp peak was associated with a rotational transition of the adlayer, from an angle off the substrate symmetry axis to zero; and the broad peak was interpreted as a signature of continuous melting. Another study by the same authors [26] investigated the disappearance of the sharp peak for densities $n \gtrsim 0.84\ n_0$ and was able to relate it to the rotational transition.

2.4.3 Krypton

Although the characteristic length increase from Ar to Kr is only $\approx 6\%$, this leads to a system which has a monolayer phase diagram dominated by effects of substrate corrugation [20, 61]. The ground state of the 3D solid has a nearest neighbor spacing of 3.993 Å [1] and the monolayer condensates at low temperature to the $\sqrt{3} \times \sqrt{3}R30°$ lattice, which means 6.5% dilation is required.

We present two phase diagrams for Kr/graphite: Fig. 2.5 [20] which gives an overview of the monolayer phase diagram; and Fig. 2.6 [21] with significant differences in the region of commensurate solid to fluid transitions. It is noteworthy that these diagrams do not present a gas-liquid critical point. Some authors claim that the substrate corrugation has such a large effect on the monolayer that the distinction between gas and liquid is lost [61, 62].

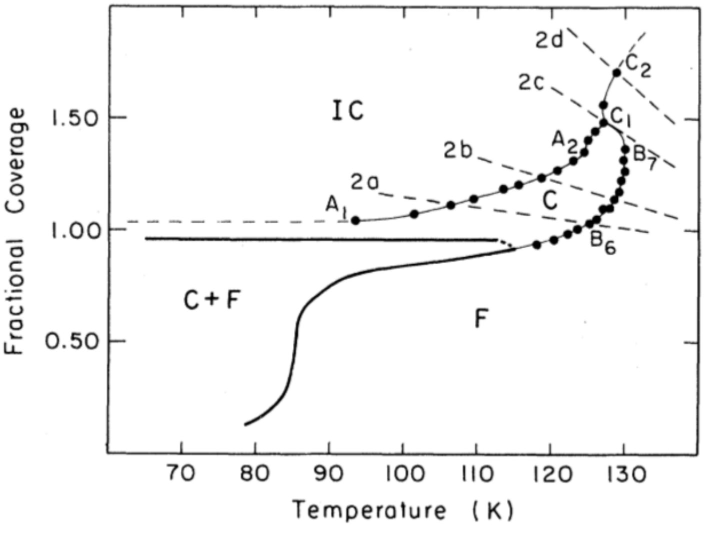

Figure 2.5: Phase diagram of Kr/graphite in terms of fractional coverage and temperature [20]. C, F and IC denote commensurate, fluid and incommensurate, respectively. There is a tricritical point at the intersection of the C to F boundary and the extrapolation (dashed) of the IC to C+F. C_1 is a multicritical point.

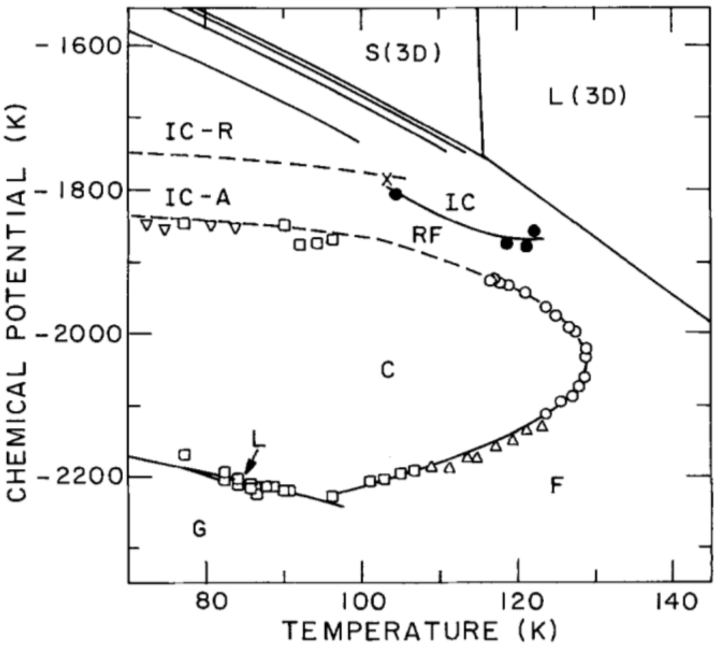

Figure 2.6: Kr/graphite phase diagram as function of the chemical potential and the temperature [21]. RF stands for the reentrant fluid phase, a domain wall fluid bounded by C (commensurate) and IC (incommensurate) regimes. S and L are the 3D bulk solid and liquid phases, respectively. Solid lines denote first-order transitions and dashed lines denote continuous transitions.

At low temperatures the fluid coexisting with the solid has a very low (gas-like) density, and for $T > 90$ K it has the characteristic density of the coexistence at a melting curve. The density difference between the fluid and the commensurate solid appears to vanish at a tricritical point at a temperature above 100 K [63]. This is quite remarkable when we recall that the melting transition in 3D is of first order, with no indication that the density difference between liquid and solid should vanish [6]. The phase diagram of Fig. 2.5 has a tricritical point at ≈ 115 K on the fluid-commensurate solid phase boundary; and at higher temperatures the density is no longer discontinuous upon solidification. The fluid to commensurate solid transition becomes continuous at (117 ± 2) K [64].

The higher density region in Fig. 2.6 is denoted as fluid, but it is in fact a subtly disordered phase. Before it was recognized, the results for the transition from commensurate to incommensurate solid appeared to be a continuous transition to a hexagonal incommensurate lattice. Analysis [65] had indicated that the alternatives for this transition were a continuous transition to a striped lattice or a discontinuous transition to a hexagonal lattice, both not observed experimentally. The fluid phase between the two regions of solid in Fig. 2.6 is termed domain wall fluid to escape this contradiction. The well separated walls in the uniaxial incommensurate lattice are subject to large meanderings [66], but with a low level of thermal excitations, which cause the subtle disorder.

---

[6] The melting curve in the P-T diagram presents vertical tangent for some materials which, according to the Clausius–Clapeyron relation, would imply a vanishing specific volume difference. Here the monolayers appear to have a *range* of temperature where the density difference of coexisting liquid and solid vanishes.

The incommensurate solid can be compressed by increasing the 3D gas pressure (at constant temperature) or by decreasing the temperature (constant gas pressure). These processes terminate with bilayer formation; at 47 K the nearest neighbor distance is (4.02±0.02) Å, which coincides with the spacing of bulk Kr at this temperature [1].

The low temperature specific heat data shows a gap of $\approx$ 10 K [67], which corresponds to a corrugation amplitude large enough to stabilize the commensurate solid as the ground state [68].

Modeling of the Kr/graphite monolayer includes: simulations of the coexistence of 2D gas and commensurate solid [69, 70]; analysis of the domain wall network in the incommensurate solid at $T = 0$ K [71] and finite temperature [72, 73]; adjustments of the interaction model to include substrate-mediated interactions in order to improve the agreement with experimental data [74].

2.4.4 Xenon

The ground state of the 3D xenon solid, with $L_{nn} = 4.336$ Å [1], has a length scale 8% larger than krypton. Thus the $\sqrt{3} \times \sqrt{3}$ commensurate lattice corresponds to $\approx$ 2% compression. The condensation of the Xe/graphite monolayer is a hexagonal incommensurate lattice down to the lowest observed temperatures, with $L_{nn} = 4.32$ Å at 25 K [75]. The $\sqrt{3}$ lattice is reached by compression at sufficient low temperatures [76–78]. There does not seem to be a striped uniaxially incommensurate solid phase between the triangular incommensurate and commensurate solids [79].

Features expected from a 2D system occur for most of the monolayer regime, only with small perturbations arising from the substrate corrugation. The density temperature phase diagram has the appearance of a classical triple point system with $T_t = 99$ K and $T_c = 117$ K. Unexpected behavior is shown when following the melting curve to temperatures above 120 K.

The nearest neighbor spacing in the triangular lattice increases from 4.32 Å at 25 K to 4.34 Å at 60 K, 4.54 Å at 80 K, and 4.59 Å at 97 K, just below the triple point [75–78]. The lattice constant of the solid varies little (4.55-4.59 Å) along the melting curve up to 150 K [80–82]. In comparison, the values for the 3D solid are $L_{nn} = 4.42$ Å at 100 K and 4.49 Å at 160 K.

The melting transition is found to be of first order [55, 76]. The density difference between the solid and fluid along the melting line decreases with temperature increase. A discontinuity is observed up to ≈ 150 K [56, 83, 84], but some experiments report a continuous transition for temperatures above 125 K [81, 85]. Some evidence points out to a two-stage melting process in the temperature range 110-120 K [86].

The incommensurate solid has a dependence between L_{nn} and orientational alignment of the adlayer. There is a small rotation angle at low temperatures, which decreases to zero near the melting transition. The Xe solid melts from the aligned $R30°$ phase [87, 88].

There is a domain of temperature and pressure where the commensurate solid is stable, for example, below 70 K just before bilayer condensation. The observations differ whether the transition from the hexagonal commensurate lattice to the commensurate solid is of first order [78] or continuous [88].

Modeling of the Xe/graphite system includes commensurate solid lattice dynamics [89] and computer simulations of the solid at relatively high temperatures [58, 90–94]. Abraham and coworkers found in their simulations of the melting that there is an appreciable density of second layer atoms, and the exchange of atoms between layers plays an important role in the system. Suh *et al.* used a different potential model which stabilized the commensurate monolayer and identified a transition to a rotated lattice.

2.4.5 Radon

Radon is set apart from the other noble gases because of its radioactivity. The ^{222}Rn isotope is of great importance since it is a decay product of ^{238}U. Because of the relatively long lifetime (5.5 days) of ^{222}Rn, it emanates to a considerable amount from the soil into the atmosphere. Atmospheric particles containing Rn decay products are of high relevance to humans since they may be deposited in the respiratory tract, raising concerns about radiation hazards. Thus the great interest in Rn filters, which require knowledge of adsorption behavior on solid surfaces.

Little is known about adsorption of Rn on solid surfaces. Hobson *et al.* [95] conducted calculations of adsorption isotherms of Rn on a heterogeneous surface, but they were unable to compare the results to experimental data due to lack of experiments. Eichler *et al.* [96] investigated adsorption on ice surfaces, mainly the molar adsorption enthalpy. Pershina *et al.* [97] used fully relativistic *ab initio* Dirac-Coulomb CCSD(T) calculations of atomic properties to investigate the interaction of Rn with various surfaces, including graphite. The Van der Waals coefficient C_3 and the adsorption enthalpy for Rn/graphite were calculated.

2.5 Heavy noble gases adlayers on graphene substrates

The physics of graphene was once considered a simplified approximation to that of graphite. This is not unreasonable because in graphite the individual layers are weakly interacting and the electrons are confined to the plane of the carbon nuclei. The ability to produce graphene in the laboratory turned attention to experiments and theories concerning adsorption in this substrate. There is particular interest in this problem because physical adsorption on graphite has been extensively investigated in the past 60 years. Although the great interest in noble gases adsorbates on graphene, very little can be found in the literature about experiments, simulations and theories concerning these systems.

Bruch *et al.* [98] conducted a theoretical study of the phase behavior of gases physically adsorbed on graphene. The authors addressed 3 problems: the condensation of quasi-2D films bound on both sides of a single graphene sheet, and it is shown that the critical temperature of this transition is only 5% higher than that of a single film adsorbed on graphite; the ground-state of a quantum He monolayer; and the wetting transition. None of the problems had been explored experimentally.

Ab Initio studies of Xe adsorption on graphene where conducted by Li *et al.* [99]. The results showed that Xe preferentially occupies the hollow site on the graphene surface. The equilibrium distance of Xe at the hollow site is calculated as 3.56 Å, which is in agreement with the experimental value of (3.59±0.05) Å. The corresponding binding energy at the hollow site is calculated as -142.9 meV, whereas the binding energies at the bridge and on-top sites are calculated as -130.8 and -127.4 meV, respectively.

There have been several molecular dynamics simulations of noble gases adsorption on structures somewhat similar to graphene, for example: Ne adsorbed on nanocones [100]; Ar [101], Kr [102] and Xe [103] on nanotubes; Ne and Xe adsorbed on nanotube bundles [104].

Chapter 3

Methods

3.1 Introduction

In this chapter we present the methods used to model, simulate and analyze the results of noble gases atoms adsorbed on graphene systems. Sec. 3.2 is an introduction to molecular dynamics simulations in which we introduce the basic aspects of this powerful method. We chose to use the Liouville formulation of classical mechanics to obtain an integration algorithm for the canonical *ensemble*. The potential interactions we used to model our system are presented in Sec. 3.3, and they were carefully chosen to model, as accurately as possible, the interactions of each atomic species. In Sec. 3.4 we show how to obtain certain thermodynamical properties during molecular dynamics simulations. Finally, we present some technical aspects of the simulations in Sec. 3.5.

3.2 Molecular Dynamics

Molecular Dynamics (MD) is a technique for computing the properties of a classical many-body system. We wish to solve Newton's equations of motion numerically for the N particles until the system reaches a steady state. After equilibration, we perform the actual estimates. The calculation of an observable in MD simulations requires us to be able to write it as a function of the positions and momenta of the particles in the system.

First, we assign arbitrary initial positions and velocities to all particles in the system. The particle positions should be compatible with the structure that we aim to simulate, and choosing carefully the velocities may reduce considerably the equilibration time. The next step is the most time-consuming in MD simulations: the calculation of the force acting on each particle. If we model the potential energy as pairwise additive interactions, we must evaluate $N(N-1)/2$ interactions. The force on particle i due to j, $\mathbf{F}_{ij}$, follows from

$$\mathbf{F}_{ij} = -\nabla V(r_{ij}), \tag{3.1}$$

where $V(r)$ is the pairwise potential energy and r_{ij} is the distance between particles i and j. After computing all the forces, we can integrate Newton's equations of motion. First, we present the Verlet algorithm, which is one of the simplest and, usually, the best algorithm. In the next section, Sec. 3.2.1, we present a more formal derivation for it. Consider the Taylor expansion of the coordinate of a particle around time t,

$$r(t+\Delta t) = r(t) + v(t)\Delta t + \frac{f(t)}{2m}(\Delta t)^2 + \frac{(\Delta t)^3}{3!}\dddot{r} + \mathcal{O}((\Delta t)^4). \tag{3.2}$$

Similarly,

$$r(t-\Delta t) = r(t) - v(t)\Delta t + \frac{f(t)}{2m}(\Delta t)^2 - \frac{(\Delta t)^3}{3!}\dddot{r} + \mathcal{O}((\Delta t)^4). \tag{3.3}$$

Summing Eq. (3.2) and (3.3) we obtain

$$r(t+\Delta t) + r(t-\Delta t) = 2r(t) + \frac{f(t)}{m}(\Delta t)^2 + \mathcal{O}((\Delta t)^4, \tag{3.4}$$

or

$$r(t+\Delta t) \approx 2r(t) - r(t-\Delta t) = +\frac{f(t)}{m}(\Delta t)^2. \tag{3.5}$$

Thus the estimate of the new position contains an error of order $(\Delta t)^4$, where Δt is the step in the MD simulation. Note that we did not use the velocity to compute the new position, but it is possible to cast the Verlet algorithm in a form that uses positions and velocities computed at equal times. This velocity Verlet algorithm is

$$\begin{aligned} r(t+\Delta t) &= r(t) + v(t)\Delta t + \frac{f(t)}{2m}(\Delta t)^2, \\ v(t+\Delta t) &= v(t) + \frac{(f(t+\Delta t) + f(t))}{2m}\Delta t. \end{aligned} \tag{3.6}$$

In this scheme, we can compute the updated velocities only after we have computed the new positions and, from these, the new forces.

In the next section, Sec. 3.2.1, we use the Liouville formulation of classical mechanics to formally obtain Eq. (3.6). In Sec 3.2.2, we introduce the Nosé-Hoover thermostat in order to extend MD simulations to the NVT *ensemble* [1], which is the *ensemble* employed in all our simulations of heavy rare-gases adsorbed on graphene. The periodic boundary conditions are presented in Sec. 3.2.3. Finally, we conclude with the MD program which was employed in this work, Sec. 3.2.4.

---

[1] In Appendix A we use the Liouville formalism to obtain a numerical algorithm for the canonical *ensemble*

3.2.1 Liouville formulation

So far we have considered algorithms for integrating Newton's equations purely mathematical. We now use the Liouville formulation of classical mechanics to derive an algorithm. Recently, Tuckerman *et al.* [105] have shown how to derive time-reversible, area preserving MD algorithms using the Liouville formulation of classical mechanics. Let f be an arbitrary function that depends on all coordinates $\mathbf{r}^N$ and momenta $\mathbf{p}^N$ of the N-body classical system. The function $f(\mathbf{p}^N(t), \mathbf{r}^N(t))$ depends implicitly on the time t. The time derivative of f is

$$\dot{f} = \dot{\mathbf{r}}\frac{\partial f}{\partial \mathbf{r}} + \dot{\mathbf{p}}\frac{\partial f}{\partial \mathbf{p}} \equiv iLf, \tag{3.7}$$

where we have used the shorthand notation $\mathbf{r}$ for $\mathbf{r}^N$ and $\mathbf{p}$ for $\mathbf{p}^N$. The last term in Eq. (3.7) defines the Liouville operator

$$iL = \dot{\mathbf{r}}\frac{\partial}{\partial \mathbf{r}} + \dot{\mathbf{p}}\frac{\partial}{\partial \mathbf{p}}. \tag{3.8}$$

Integrating Eq. (3.7) yields

$$f(\mathbf{p}^N(t), \mathbf{r}^N(t)) = \exp(iLt) f(\mathbf{p}^N(0), \mathbf{r}^N(0)). \tag{3.9}$$

Suppose that the Liouville operator contained only the first term on the right-hand side of Eq. (3.7). We denote this part of iL by iL_r

$$iL_r = \dot{\mathbf{r}}(0)\frac{\partial}{\partial \mathbf{r}}. \tag{3.10}$$

Inserting Eq. (3.10) in (3.9) and expanding the exponential using a Taylor series, we have

$$\begin{aligned} f(\mathbf{p}^N(t), \mathbf{r}^N(t)) &= \exp\left(\dot{\mathbf{r}}(0)t\frac{\partial}{\partial \mathbf{r}}\right) f(\mathbf{p}^N(0), \mathbf{r}^N(0)) \\ &= \sum_{n=0}^{\infty} \frac{(\dot{\mathbf{r}}(0)t)^n}{n!}\frac{\partial^n}{\partial \mathbf{r}^n} f(\mathbf{p}^N(0), \mathbf{r}^N(0)) \\ &= f\left[\mathbf{p}^N(0), (\mathbf{r} + \dot{\mathbf{r}}(0)t)^N\right]. \end{aligned} \tag{3.11}$$

Thus, the effect of $\exp(iL_r t)$ is a shift in the coordinates. Similarly, $\exp(iL_p t)$ given by

$$iL_p = \dot{\mathbf{p}}(0)\frac{\partial}{\partial \mathbf{p}}, \tag{3.12}$$

is a shift of momenta. The total Liouville operator is given by $iL = iL_r + iL_p$, however iL_r and iL_p are non-commuting operators. We may use the Trotter identity to evaluate the exponential of a sum of two non-commuting operators A and B

$$\exp(A + B) = \lim_{P\to\infty} \left(e^{A/(2P)} e^{B/P} e^{A/(2P)}\right)^P. \tag{3.13}$$

For finite P this expression is approximated by

$$\exp\left(A+B\right) = \left(e^{A/(2P)} e^{B/P} e^{A/(2P)}\right)^P \; e^{\mathcal{O}(1/P^2)}. \tag{3.14}$$

Now let us apply this expression to the solution of the Liouville equation, Eq. (3.9). We identify

$$\begin{aligned} \frac{A}{P} &\equiv \frac{iL_p t}{P} \equiv \Delta t \dot{\mathbf{p}}(0) \frac{\partial}{\partial \mathbf{p}}, \\ \frac{B}{P} &\equiv \frac{iL_r t}{P} \equiv \Delta t \dot{\mathbf{r}}(0) \frac{\partial}{\partial \mathbf{r}}, \end{aligned} \tag{3.15}$$

where $\Delta t \equiv t/P$. We replace the formal solution of the Liouville equation by a discretized version. In this scheme, one time step corresponds to applying once the operator

$$e^{iL_p \Delta t/2} e^{iL_r \Delta t} e^{iL_p \Delta t/2}. \tag{3.16}$$

Let us see what is the effect of this operator on the coordinates and momenta of the particles. Applying the operator, Eq. (3.16), to $f(\mathbf{p}^N(0), \mathbf{r}^N(0))$ yields

$$\begin{aligned} e^{iL_p \Delta t/2} e^{iL_r \Delta t} e^{iL_p \Delta t/2} f(\mathbf{p}^N(0), \mathbf{r}^N(0)) &= \\ &= e^{iL_p \Delta t/2} e^{iL_r \Delta t} f\left\{ \left[\mathbf{p}(0) + \frac{\Delta t}{2}\dot{\mathbf{p}}(0)\right]^N, \mathbf{r}^N(0) \right\} \\ &= e^{iL_p \Delta t/2} f\left\{ \left[\mathbf{p}(0) + \frac{\Delta t}{2}\dot{\mathbf{p}}(0)\right]^N, \left[\mathbf{r}(0) + \Delta t \dot{\mathbf{r}}(\Delta t/2)\right]^N \right\} \\ &= f\left\{ \left[\mathbf{p}(0) + \frac{\Delta t}{2}\dot{\mathbf{p}}(0) + \frac{\Delta t}{2}\dot{\mathbf{p}}(\Delta t)\right]^N, \left[\mathbf{r}(0) + \Delta t \dot{\mathbf{r}}(\Delta t/2)\right]^N \right\}. \end{aligned} \tag{3.17}$$

It is important to note that the shift in $\mathbf{r}$ is a function of $\mathbf{p}$ only, because $\dot{\mathbf{r}} = \mathbf{p}/m$; and the shift in $\mathbf{p}$ is a function of $\mathbf{r}$ only, because $\dot{\mathbf{p}} = \mathbf{F}(\mathbf{r}^N)$. The Jacobian of the transformation $(\mathbf{p}^N(0), \mathbf{r}^N(0)) \to (\mathbf{p}^N(\Delta t), \mathbf{r}^N(\Delta t))$ is the product of the three transformations, but, as each Jacobian is one, the overall transformation has an unitary Jacobian. Hence, the algorithm is area preserving in the phase space.

The overall effect of these transformations in the positions and momenta are

$$\begin{aligned} \mathbf{p}(0) &\to \mathbf{p}(0) + \frac{\Delta t}{2}(\mathbf{F}(0) + \mathbf{F}(\Delta t)), \\ \mathbf{r}(0) &\to \mathbf{r}(0) + \Delta t \dot{\mathbf{r}}(\Delta t/2) = \\ &= \mathbf{r}(0) + \Delta t \dot{\mathbf{r}}(0) + \frac{(\Delta t)^2}{2m}\mathbf{F}(0). \end{aligned} \tag{3.18}$$

These are precisely the equations of the Verlet algorithm (Eq. (3.6))! Thus we conclude that the Verlet algorithm is area preserving. Its reversibility follows from the fact that past and future coordinates are symmetric in the algorithm.

3.2.2 Nosé-Hoover thermostat

So far we have restricted ourselves to the NVE (microcanonical) *ensemble*, however it is useful to extend MD simulations to the NVT (canonical) *ensemble*, which is the *ensemble* employed in our adsorption simulations. We discuss the Nosé thermostat, however it is more common to utilize Nosé's scheme with the formulation of Hoover. The approach we present [106] is a clever use of an extended Lagrangian, which is a Lagrangian containing additional artificial coordinates and velocities.

The Lagrangian of a classical N-body system is given by

$$\mathcal{L} = \sum_{i=1}^{N} \frac{m_i \dot{\mathbf{r}}_i^2}{2} - \mathcal{U}(\mathbf{r}^N), \tag{3.19}$$

where m_i is the mass of the i-th atom, $\mathbf{r}_i$ is the position of the i-th particle and $\mathcal{U}(\mathbf{r}^N)$ is the potential energy which depends on the N-particle configuration $\mathbf{r}^N$. In order to construct isothermal MD, Nosé introduced an additional coordinate s in Eq. (3.19)

$$\mathcal{L}_{\text{Nosé}} = \sum_{i=1}^{N} \frac{m_i s^2 \dot{\mathbf{r}_i}^2}{2} - \mathcal{U}(\mathbf{r}^N) + \frac{Q\dot{s}^2}{2} - \frac{L}{\beta} \ln s, \tag{3.20}$$

where L is a parameter that will be fixed later and Q is an effective mass associated with s. The momenta conjugate to $\mathbf{r}_i$ and s are

$$\begin{aligned} \mathbf{p}_i &\equiv \frac{\partial \mathcal{L}}{\partial \dot{\mathbf{r}}_i} = m_i s^2 \dot{\mathbf{r}}_i, \\ p_s &\equiv \frac{\partial \mathcal{L}}{\partial \dot{s}} = Q\dot{s}. \end{aligned} \tag{3.21}$$

Thus, the Hamiltonian of the extended system is

$$\mathcal{H}_{\text{Nosé}} = \sum_{i=1}^{N} \frac{\mathbf{p}_i^2}{2m_i s^2} + \mathcal{U}(\mathbf{r}^N) + \frac{p_s^2}{2Q} + \frac{L}{\beta} \ln s. \tag{3.22}$$

We consider a system containing N atoms, which makes the extended system spawn a microcanonical *ensemble* with $6N + 2$ degrees of freedom ($\mathbf{r}_i$, $\mathbf{p}_i$, s and p_s). The partition function of this *ensemble* is

$$\begin{aligned} Q_{\text{Nosé}} &= \frac{1}{N!} \int dp_s ds d\mathbf{p}^N d\mathbf{r}^N \delta\left[E - \mathcal{H}_{\text{Nosé}}\right] \\ &= \frac{1}{N!} \int dp_s ds d\mathbf{p}'^N d\mathbf{r}^N s^{3N} \delta\left[\sum_{i=1}^{N} \frac{\mathbf{p}_i'^2}{2m_i} + \mathcal{U}(\mathbf{r}^N) + \frac{p_s^2}{2Q} + \frac{L}{\beta} \ln s - E\right], \end{aligned} \tag{3.23}$$

with $\mathbf{p}' = \mathbf{p}/s$. One useful property of a delta function of a function $h(s)$ with a single root s_0 is

$$\delta\left[h(s)\right] = \frac{\delta(s - s_0)}{|h'(s_0)|}. \tag{3.24}$$

If we define

$$\mathcal{H}(\mathbf{p}',\mathbf{r}) = \sum_{i=1}^{N} \frac{\mathbf{p}_i'^2}{2m_i} + \mathcal{U}(\mathbf{r}^N), \tag{3.25}$$

and take

$$h(s) = \mathcal{H}(\mathbf{p}',\mathbf{r}) + \frac{p_s^2}{2Q} + \frac{L}{\beta}\ln s - E, \tag{3.26}$$

then

$$s_0 = \exp\left[-\frac{\beta}{L}\left(\mathcal{H}(\mathbf{p}',\mathbf{r}) + \frac{p_s^2}{2Q} - E\right)\right] \text{ and } \ h'(s_0) = \frac{L}{\beta s_0}. \tag{3.27}$$

Rewriting Eq. (3.23), using Eq. (3.24), we have

$$\begin{aligned} Q_{\text{Nosé}} &= \frac{1}{N!}\int dp_s ds d\mathbf{p}'^N d\mathbf{r}^N \frac{\beta s^{3N}}{L} \exp\left[-\frac{\beta}{L}\left(\mathcal{H}(\mathbf{p}',\mathbf{r}) + \frac{p_s^2}{2Q} - E\right)\right] \times \\ & \delta\left[s - \exp\left[-\frac{\beta}{L}\left(\mathcal{H}(\mathbf{p}',\mathbf{r}) + \frac{p_s^2}{2Q} - E\right)\right]\right]. \end{aligned} \tag{3.28}$$

Integrating in s we have

$$\begin{aligned} Q_{\text{Nosé}} &= \underbrace{\frac{1}{N!}\frac{\beta}{L}\exp\left[\beta E\left(\frac{3N+1}{L}\right)\right]\int dp_s \exp\left[-\beta\left(\frac{3N+1}{L}\right)\frac{p_s^2}{2Q}\right]}_{C} \\ &\times \int d\mathbf{p}'^N d\mathbf{r}^N \exp\left[-\beta\left(\frac{3N+1}{L}\right)\mathcal{H}(\mathbf{p}',\mathbf{r})\right] \\ &= C\frac{1}{N!}\int d\mathbf{p}'^N d\mathbf{r}^N \exp\left[-\beta\left(\frac{3N+1}{L}\right)\mathcal{H}(\mathbf{p}',\mathbf{r})\right]. \end{aligned} \tag{3.29}$$

We wish to relate this *ensemble* partition function with the NVT partition function

$$Q_{NVT} = \frac{1}{N!}\int d\mathbf{p}'^N d\mathbf{r}^N \exp\left[-\beta\mathcal{H}(\mathbf{p}',\mathbf{r})\right]. \tag{3.30}$$

In this Nosé *ensemble*, the time-average $\overline{\mathcal{A}}$ of a quantity $\mathcal{A}$ that depends on $\mathbf{p}'$ and $\mathbf{r}$ is given by

$$\overline{\mathcal{A}} = \lim_{\tau\to\infty}\frac{1}{\tau}\int_0^\tau dt\ \mathcal{A}(\mathbf{p}(t)/s(t),\mathbf{r}(t)) \equiv \langle\mathcal{A}(\mathbf{p}/s,\mathbf{r})\rangle_{\text{Nosé}}. \tag{3.31}$$

If we take $L = 3N+1$, this expression reduces to the canonical average

$$\begin{aligned} \langle\mathcal{A}(\mathbf{p}/s,\mathbf{r})\rangle_{\text{Nosé}} &\equiv \frac{\int d\mathbf{p}'^N d\mathbf{r}^N \mathcal{A}(\mathbf{p}',\mathbf{r})\exp\left[-\beta\mathcal{H}(\mathbf{p}',\mathbf{r})(3N+1)/L\right]}{\int d\mathbf{p}'^N d\mathbf{r}^N \exp\left[-\beta\mathcal{H}(\mathbf{p}',\mathbf{r})(3N+1)/L\right]} \\ &= \frac{(1/N!)\int d\mathbf{p}'^N d\mathbf{r}^N \mathcal{A}(\mathbf{p}',\mathbf{r})\exp\left[-\beta\mathcal{H}(\mathbf{p}',\mathbf{r})\right]}{Q_{NVT}} \\ &= \langle\mathcal{A}(\mathbf{p}',\mathbf{r})\rangle_{NVT}. \end{aligned} \tag{3.32}$$

Let us look carefully into the role of the variable s. The phase space is spawned by $\mathbf{r}$ and the scaled momenta $\mathbf{p}' = \mathbf{p}/s$. As the scaled momentum is most directly related to observable quantities, we refer to $\mathbf{p}'$ as the real momentum and $\mathbf{p}$ is a virtual momentum. We make similar distinctions between the other variables; real variables are indicated by a prime and unprimed variables are the virtual counterparts. We summarize the relations in the following set of equations

$$\begin{aligned} r' &= r \\ p' &= p/s \\ s' &= s \\ \Delta t' &= \Delta t/s. \end{aligned} \tag{3.33}$$

From Eq. (3.33) we note that s can be interpreted as a scaling factor of the time step, implying that the real time step fluctuates during a simulation. However, we are interested to sample the system at equal intervals in the real time. We define

$$\lim_{\tau'\to\infty} \frac{1}{\tau'} \int_0^{\tau'} dt' \mathcal{A}[\mathbf{p}(t')/s(t'), \mathbf{r}(t')] \tag{3.34}$$

as a different average than Eq. (3.31). Real τ' and virtual τ measuring times are related through

$$\tau' = \int_0^{\tau} dt\ 1/s(t). \tag{3.35}$$

Thus

$$\begin{aligned} \lim_{\tau'\to\infty} \frac{1}{\tau'} \int_0^{\tau'} dt'\ \mathcal{A}[\mathbf{p}(t')/s(t'), \mathbf{r}(t')] &= \lim_{\tau'\to\infty} \frac{\tau}{\tau'} \frac{1}{\tau} \int_0^{\tau} dt\ \mathcal{A}[\mathbf{p}(t)/s(t), \mathbf{r}(t)]/s(t) \\ &= \frac{\lim_{\tau\to\infty} \frac{1}{\tau} \int_0^{\tau} dt\ \mathcal{A}[\mathbf{p}(t)/s(t), \mathbf{r}(t)]/s(t)}{\lim_{\tau\to\infty} \frac{1}{\tau} \int_0^{\tau} dt\ 1/s(t)} \\ &= \frac{\langle \mathcal{A}(\mathbf{p}/s, \mathbf{r})/s \rangle}{\langle 1/s \rangle}. \end{aligned} \tag{3.36}$$

Using $Q_{\text{Nosé}}$, Eq. (3.29), to calculate the averages yields

$$\begin{aligned} \frac{\langle \mathcal{A}(\mathbf{p}/s, \mathbf{r})/s \rangle}{\langle 1/s \rangle} &\equiv \frac{\left\{ \frac{\int d\mathbf{p}'^N d\mathbf{r}^N \mathcal{A}(\mathbf{p}',\mathbf{r}) \exp\left[-\beta\mathcal{H}(\mathbf{p}',\mathbf{r})(3N)/L\right]}{\int d\mathbf{p}'^N d\mathbf{r}^N \exp\left[-\beta\mathcal{H}(\mathbf{p}',\mathbf{r})3(N+1)/L\right]} \right\}}{\left\{ \frac{\int d\mathbf{p}'^N d\mathbf{r}^N \mathcal{A}(\mathbf{p}',\mathbf{r}) \exp\left[-\beta\mathcal{H}(\mathbf{p}',\mathbf{r})(3N)/L\right]}{\int d\mathbf{p}'^N d\mathbf{r}^N \exp\left[-\beta\mathcal{H}(\mathbf{p}',\mathbf{r})3(N+1)/L\right]} \right\}} \\ &= \frac{\int d\mathbf{p}'^N d\mathbf{r}^N \mathcal{A}(\mathbf{p}/s, \mathbf{r}) \exp\left[-\beta\mathcal{H}(\mathbf{p}', \mathbf{r})(3N)/L\right]}{\int d\mathbf{p}'^N d\mathbf{r}^N \exp\left[-\beta\mathcal{H}(\mathbf{p}', \mathbf{r})(3N)/L\right]} \\ &= \langle \mathcal{A}(\mathbf{p}/s, \mathbf{r}) \rangle_{NVT}, \end{aligned} \tag{3.37}$$

noting that we assumed $L = 3N$ in the last step. Therefore, if we want to sample our system on equal time steps in real time we have to use a different value for L than the previously found $3N + 1$.

From the Hamiltonian, Eq. (3.22), we can derive the equations of motion for the virtual variables

$$\begin{aligned}
\frac{d\mathbf{r}_i}{dt} &= \frac{\partial \mathcal{H}_{\text{Nosé}}}{\partial \mathbf{p}_i} = \frac{\mathbf{p}_i}{m_i s^2}, \\
\frac{d\mathbf{p}_i}{dt} &= -\frac{\partial \mathcal{H}_{\text{Nosé}}}{\partial \mathbf{r}_i} = -\frac{\partial \mathcal{U}(\mathbf{r}^N)}{\partial \mathbf{r}_i}, \\
\frac{ds}{dt} &= \frac{\partial \mathcal{H}_{\text{Nosé}}}{\partial p_s} = \frac{p_s}{Q}, \\
\frac{dp_s}{dt} &= -\frac{\partial \mathcal{H}_{\text{Nosé}}}{\partial s} = \frac{1}{s}\left(\sum_i \frac{p_i^2}{m_i s^2} - \frac{L}{\beta}\right).
\end{aligned} \tag{3.38}$$

We can rewrite these equations in terms of real variables

$$\begin{aligned}
\frac{d\mathbf{r}'_i}{dt'} &= s\frac{d\mathbf{r}_i}{dt} = \frac{\mathbf{p}'_i}{m_i}, \\
\frac{d\mathbf{p}'_i}{dt'} &= s\frac{d}{dt}\left(\frac{\mathbf{p}_i}{s}\right) = \frac{d\mathbf{p}_i}{dt} - \frac{\mathbf{p}_i}{s}\frac{ds}{dt} = -\frac{\partial \mathcal{U}(\mathbf{r}'^N)}{\partial \mathbf{r}'_i} - \frac{s' p'_s}{Q}\mathbf{p}'_i, \\
\frac{1}{s}\frac{ds'}{dt'} &= \frac{s}{s}\frac{ds}{dt} = \frac{s' p'_s}{Q}, \\
\frac{d}{dt'}\left(\frac{s' p'_s}{Q}\right) &= \frac{s}{Q}\frac{dp_s}{dt} = \frac{1}{Q}\left(\sum_i \frac{p'^2_i}{m_i} - \frac{L}{\beta}\right).
\end{aligned} \tag{3.39}$$

The quantity conserved for these equations of motion is

$$H'_{\text{Nosé}} = \sum_{i=1}^{N} \frac{\mathbf{p}'^2_i}{2m_i} + \mathcal{U}(\mathbf{r}'^N) + \frac{s' p'^2_s}{2Q} + \frac{L}{\beta}\ln s'. \tag{3.40}$$

This expression for $H'_{\text{Nosé}}$ is not a Hamiltonian! It is a conserved quantity, but the equations of motion cannot be derived from it. For the full algorithm and implementation of the Nosé-Hoover thermostat, the reader is referred to Appendix A.

3.2.3 Periodic boundary conditions

Let us consider a simulation of 1000 particles arranged in a $10 \times 10 \times 10$ cube. No less than 488 particles appear on the faces! Atoms on the surface will experience quite different forces from those in the bulk. The problem might be mitigated by implementing periodic boundary conditions (PBC) [107]. The cubic box is replicated throughout space to form an infinite lattice, Fig. (3.1). During the simulation, as an atom moves in the original box, its image in each of the neighboring boxes moves the exact same way. If a particle leaves the central box, one of its images will enter through the opposite face, thus the number density in the system is conserved.

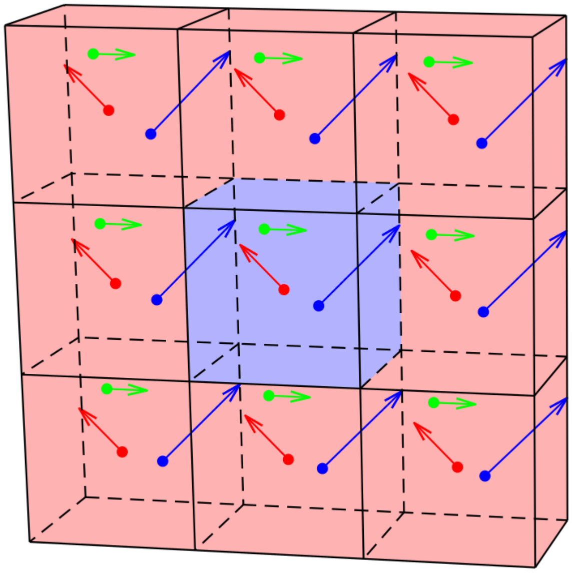

Figure 3.1: Illustration of the PBC procedure. The central cell has three atoms (red, blue and green) and the vectors indicate their velocities. For sake of simplicity, we just replicated the central blue cell 8 times (red cells), out of the 26 in the 3D case.

3.2.4 LAMMPS

For the MD simulations we employed the LAMMPS [108] code.

> "LAMMPS is a classical molecular dynamics code, and an acronym for Large-scale Atomic/Molecular Massively Parallel Simulator. LAMMPS has potentials for solid-state materials (metals, semiconductors) and soft matter (biomolecules, polymers) and coarse-grained or mesoscopic systems. It can be used to model atoms or, more generically, as a parallel particle simulator at the atomic, meso, or continuum scale. LAMMPS runs on single processors or in parallel using message-passing techniques and a spatial-decomposition of the simulation domain. The code is designed to be easy to modify or extend with new functionality." - LAMMPS web site, `http://lammps.sandia.gov`, accessed on 16/03/2015.

3.3 Potential interactions

We adopted pair potentials to describe the interactions between noble gases atoms, and the semiempirical approach of Sec. 2.2.3 to model atom-surface interactions, Eq. (2.20). The considered potential energy of the system is given by

$$U = \sum_{i<j}^{N_X} U_{X-X}(r_{ij}) + \sum_{i}^{N_X}\sum_{j}^{N_C} U_{X-C}(r_{ij}) + \sum_{i,j,k}^{N_C} U_{ijk}, \tag{3.41}$$

where X is one of the heavy noble gases (Ne, Ar, Kr, Xe or Rn); N_X and N_C are the number of X atoms and carbon atoms, respectively; $r_{ij} = |\vec{r_i} - \vec{r_j}|$, $\vec{r_i}$ is the position of the i-th atom; and we devote ourselves to explain the U_{X-X}, U_{X-C} and U_{ijk} in the following sections.

3.3.1 Adatoms interactions

The first term on the right-hand side of Eq. (3.41) presents a pairwise interaction U_{X-X} between the adatoms. In Sec. 2.2.1 we wrote the potential energy as a sum of a Hartree-Fock term and a correlation part, Eq. (2.10). We adopted pair interactions that are similar to those of Eqs. (2.11) and (2.12), but represent a more accurate description of the potential energies.

HFD-B potential

For Ne-Ne [2], Kr-Kr [3] and Xe-Xe [4] we employed an interatomic potential called HFD-B. The designation arises from the acronym of Hartree-Fock Dispersion, and 'B' refers to a second attempt for a functional form of the Hartree-Fock term. This potential is derived by refining the procedure of Sec. 2.2.1 and by empirical values of the constants involved. The form of HFD-B is

$$U^{(\text{HFD-B})}(x) = \epsilon \left[U^{(\text{HFD-B})}_{SCF}(x) + U^{(\text{HFD-B})}_{Cor}(x) \right], \tag{3.42}$$

where $U^{(\text{HFD-B})}_{SCF}$ is the self-consistent field (SCF) Hartree-Fock interaction energy for rare gas dimers, $U^{(\text{HFD-B})}_{Cor}$ is the correlation energy and $x = r/r_m$. Hereafter we adopt the convention that starred constants are dimensionless. The SCF term is often represented by

$$U^{(\text{HFD-B})}_{SCF}(x) = A^* \exp(-\alpha^* x + \beta^* x^2), \tag{3.43}$$

where the parameters A^*, α^* and β^* are obtained by fitting *ab initio* SCF results. In the single-damped HFD model, $U^{(\text{HFD-B})}_{Cor}$ takes the form

$$U^{(\text{HFD-B})}_{Cor}(x) = -F(x) \sum_{j=0}^{2} \frac{C^*_{2j+6}}{x^{2j+6}}, \tag{3.44}$$

with

$$F(x) = \begin{cases} \exp\left[-\left(\frac{D^*}{x-1}\right)^2\right] & \text{if} \quad x < D^*, \\ 1 & \text{if} \quad x \geqslant D^*. \end{cases} \tag{3.45}$$

The parameters are presented in Table 3.1 and we plot the potential energy as a function of the separation in Fig. 3.2.

Table 3.1: HFD-B parameters for Ne [2], Kr [3] and Xe [4]. Not all figures displayed are significant, they are displayed only to avoid round off errors.

	Ne	Kr	Xe
A^*	$8.957\ 179\ 5\times10^{5}$	$1.101\ 468\ 11\times10^{5}$	$0.210\ 582\ 98\times10^{5}$
α^*	13.864 346 71	9.394 904 95	5.416 370 17
c_6^*	1.213 175 45	1.088 225 26	1.028 717 48
c_8^*	0.532 227 49	0.539 115 67	0.576 558 12
c_{10}^*	0.245 707 03	0.421 741 19	0.431 846 85
β^*	-0.129 938 22	-2.326 076 47	-4.948 619 34
D^*	1.36	1.28	1.45
ϵ/k_B (K)	42.25	201.2	282.29
r_m (Å)	3.091	4.008	4.362 7

HFDID1 potential

For Ar-Ar interactions we employed a modified version of HFD-B called HFDID1 (Hartree-Fock Dispersion Individually Damped) [5],

$$U^{(\text{HFDID1})}(R) = \epsilon U_{SCF}^{(\text{HFDID1})}(R) + U_{Cor}^{(\text{HFDID1})}(R). \tag{3.46}$$

The SCF term has the same functional form of Eq. (3.43),

$$U_{SCF}^{(\text{HFDID1})}(R) = A^* \exp(-\alpha^* R + \beta^* R^2), \tag{3.47}$$

where R is in atomic units hereafter. However, the correlation energy includes more terms in the inverse power law and it is "doubly corrected"

$$U_{Cor}^{(\text{HFDID1})}(R) = -f(\rho^* R) \sum_{j=0}^{4} \left[\frac{C_{2j+6}}{R^{2j+6}} g_n(\rho^* R)\right], \tag{3.48}$$

with

$$g_n(R) = \left[1 - \exp\left(-\frac{2.1R}{n} - \frac{0.109R^2}{\sqrt{n}}\right)\right]^n, \tag{3.49}$$

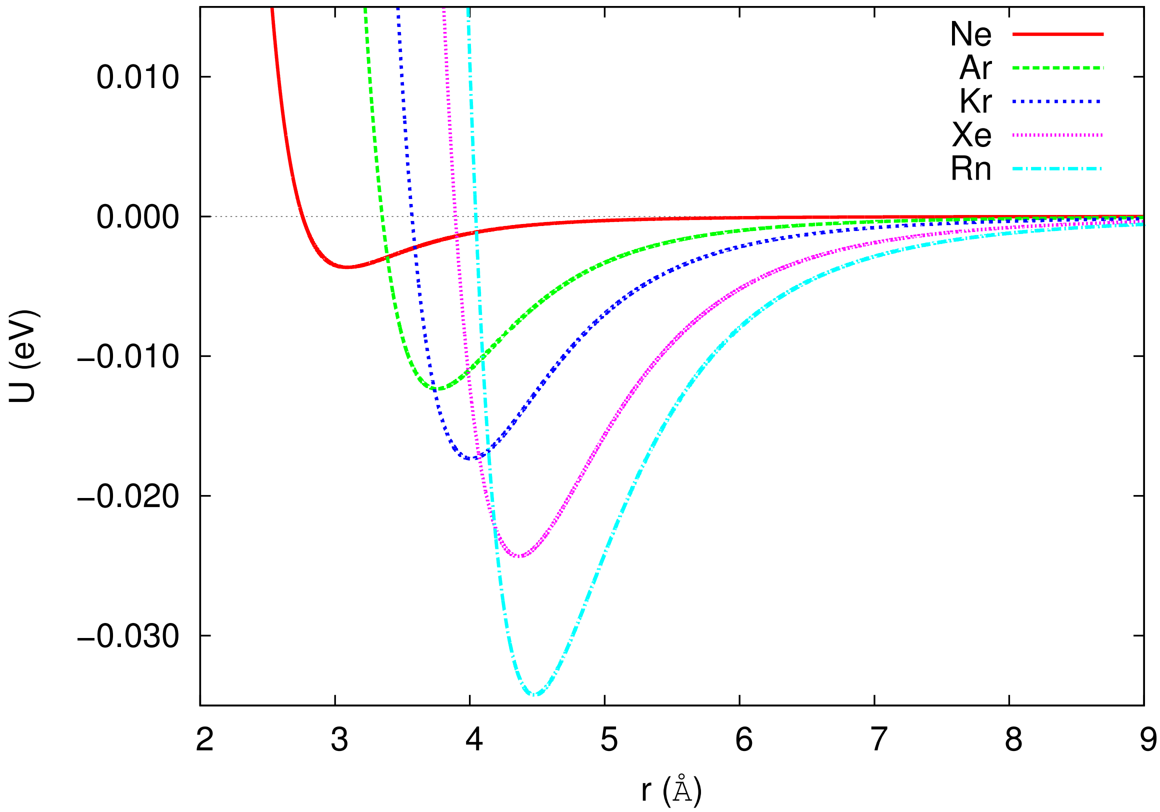

Figure 3.2: Potential energies for the Ne-Ne, Ar-Ar, Kr-Kr, Xe-Xe and Rn-Rn interactions.

and

$$f(R) = 1 - R^{1.68}\exp(-0.78R). \tag{3.50}$$

Table 3.2 summarizes the employed parameters and we plot the Ar-Ar potential energy in Fig. 3.2.

Tang-Toennies potential

The Rn-Rn interactions were based on the Tang-Toennies model: a short range Born-Mayer potential plus a long-range attractive potential [6]

$$U^{(\mathrm{TT})}(R) = Ae^{-bR} - \sum_{n=3}^{5} f_{2n}(bR)\frac{C_{2n}}{R^{2n}}, \tag{3.51}$$

where

$$f_{2n}(x) = 1 - e^{-x}\sum_{k=0}^{2n}\frac{x^k}{k!}. \tag{3.52}$$

Table 3.2: HFDID1 parameters for Ar [5]. Not all figures displayed are significant, some are displayed only to avoid round off errors.

	Ar
A^*	$8.739\ 339\ 27 \times 10^4$
α^*	9.032 283 28
C_6 (a.u.)	63.50
C_8 (a.u.)	1 510.00
C_{10} (a.u.)	$4.800\ 000\ 00 \times 10^4$
C_{12} (a.u.)	$2.069\ 581\ 26 \times 10^6$
C_{14} (a.u.)	$1.166\ 706\ 33 \times 10^8$
β^*	-2.371 328 23
ρ^*	1.107 000 00
ϵ/k_B (K)	143.235

Table 3.3 contains the parameters for this potential and Fig. 3.2 presents the potential energy of a Rn pair as a function of the distance.

Table 3.3: Tang-Toennies parameters for Rn [6]. All values are in atomic units.

	Rn
C_6	420.6
C_8	19 260
C_{10}	1 067 000
A	5 565
b	1.824

3.3.2 Adatom-substrate interaction

The second term on the right-hand side of Eq. (3.41) contains U_{X-C}, which is a pairwise interaction between adsorbate and substrate atoms. We employed the Lennard-Jones potential to model these interactions, Eq. (2.21). The chosen carbon-carbon LJ parameters are $\sigma_{CC} = 3.35$ Å and $\epsilon_{CC} = 0.0024$ eV [109], thus we may use the combining rules, Eq. (2.22), to determine the LJ parameters of the mixed X-C interactions. Table 3.4 summarizes σ_{XX} and ϵ_{XX} from the literature, as well as the obtained X-C parameters. The corresponding LJ potential energies are plotted in Fig. 3.3.

Table 3.4: Lennard-Jones parameters for the interactions between noble gases and carbon atoms.

	σ_{XX} (Å)	ϵ_{XX} (eV)	σ_{XC} (Å)	ϵ_{XC} (eV)
Ne [2]	2.759	0.0036	3.055	0.003
Ar [5]	3.400	0.0103	3.375	0.005
Kr [3]	3.571	0.0173	3.460	0.006
Xe [4]	3.892	0.0243	3.621	0.008
Rn [6]	3.988	0.0343	3.669	0.009

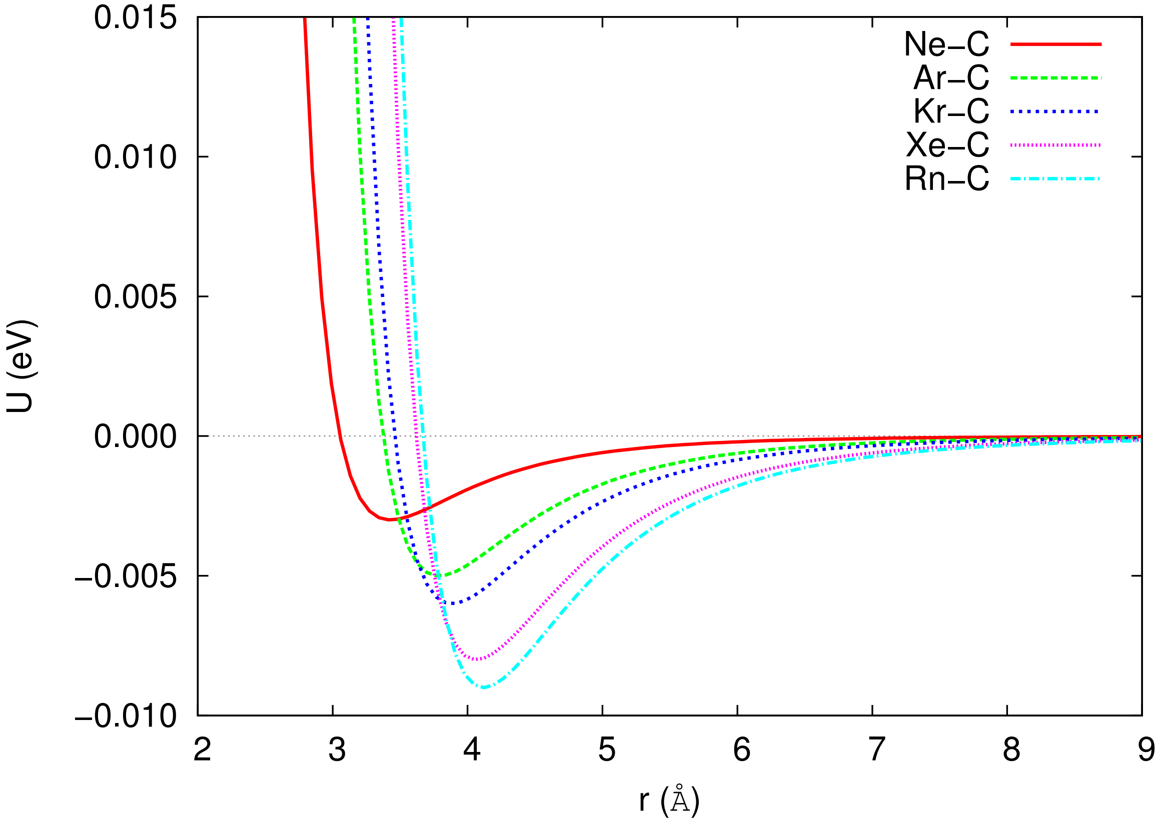

Figure 3.3: Potentials for the Ne-C, Ar-C, Kr-C, Xe-C and Rn-C interactions.

3.3.3 Substrate interactions

The last term on the right-hand side of Eq. (3.41) models interactions between the constituents of the substrate. U_{ijk} is related to the Tersoff potential [7, 8, 110] which takes into account three-body interactions between carbon atoms. Tersoff studied the trade-off between energy per bond and coordination number in order to construct this potential for carbon and silicon. The interatomic potential includes an environment-dependent bond order explicitly, and it is taken to be

$$\begin{aligned} E &= \sum_i E_i = \frac{1}{2}\sum_{i\neq j} V_{ij}, \\ V_{ij} &= f_C(r_{ij})\left[f_R(r_{ij}) + b_{ij} f_A(r_{ij}))\right]. \end{aligned} \tag{3.53}$$

Here E is the total energy of the system, conveniently decomposed into a site energy E_i and a bond energy V_{ij}. The summations are over all atoms i and j of the system. The function f_R is a repulsive pair potential, which takes into account overlapping atomic wavefunctions

$$f_R(r) = A\exp(-\lambda_1 r); \tag{3.54}$$

f_A is an attractive pair potential associated with bonding

$$f_A(r) = -B\exp(-\lambda_2 r); \tag{3.55}$$

and the f_C term is a smooth cutoff function

$$f_C(r) = \begin{cases} 1 & \text{if} \quad r < R - D, \\ \frac{1}{2} - \frac{1}{2}\sin\left(\frac{\pi(r-R)}{2D}\right) & \text{if} \quad R - D < r < R + D, \\ 0 & \text{if} \quad r > R + D. \end{cases} \tag{3.56}$$

The function b_{ij} was the novel feature introduced by Tersoff; it represents a measure of the bond order and determining a satisfactory form for it is the most difficult part of this approach. The following set of equations defines b_{ij}

$$\begin{aligned} b_{ij} &= (1 + \beta^n \zeta_{ij}^n)^{-\frac{1}{2n}}, \\ \zeta_{ij} &= \sum_{k\neq i,j} f_C(r_{ik}) g(\theta_{ijk}) \exp\left[\lambda_3^m (r_{ij} - r_{ik})^m\right], \\ g(\theta) &= \gamma_{ijk}\left(1 + \frac{c^2}{d^2} - \frac{c^2}{[d^2 + (\cos\theta - \cos\theta_0)^2]}\right), \end{aligned} \tag{3.57}$$

where θ_{ijk} is the bond angle between bonds ij and ik. We present the parameters for C-C interactions in Table 3.5.

3.4 Thermodynamical quantities

In the following sections we give some insight of how to extract thermodynamical quantities such as specific heat, Sec. 3.4.1, and the pair distribution function, Sec. 3.4.2, from MD simulations in the canonical *ensemble.*

Table 3.5: Tersoff parameters for C-C interactions [7,8].

	Tersoff
m	3.0
γ	1.0
λ_3 (Å^{-1})	0.0
c	38 049
d	4.3484
$\cos\theta_0$	-0.57058
n	0.72751
β	1.5724×10^{-7}
λ_2 (Å^{-1})	2.2119
B (eV)	346.7
R (Å)	1.95
D (Å)	0.15
λ_1 (Å^{-1})	3.4879
A (eV)	1 393.6

3.4.1 Specific Heat

The partition function Z of the NVT *ensemble* is defined [111] as

$$Z = \sum_j \exp\{-\beta E_j\}, \tag{3.58}$$

where $\beta = 1/(k_B T)$ and E_j is the energy of a particular microstate j. The energy fluctuates in the NVT *ensemble*, thus we can calculate the mean energy value using

$$\langle E_j \rangle = \frac{\sum\limits_j E_j \exp\{-\beta E_j\}}{\sum\limits_j \exp\{-\beta E_j\}} = -\frac{\partial}{\partial\beta} \ln Z, \tag{3.59}$$

where we have used the definition of a mean value in the canonical *ensemble*. We also can compute the fluctuation of the mean value

$$\begin{aligned}\langle \delta E^2 \rangle = \langle (E_j - \langle E_j \rangle)^2 \rangle &= \langle E_j^2 \rangle - \langle E_j \rangle^2 = \\ &= \frac{1}{Z}\sum_j E_j^2 \exp\{-\beta E_j\} - \left[\frac{1}{Z}\sum_j E_j \exp\{-\beta E_j\}\right]^2 .\end{aligned} \tag{3.60}$$

Rewriting Eq. (3.60) as a function of Z yields

$$\langle \delta E^2 \rangle = \frac{\partial}{\partial\beta}\left[\frac{1}{Z}\frac{\partial Z}{\partial\beta}\right] = -\frac{\partial}{\partial\beta}\langle E_j \rangle. \tag{3.61}$$

Finally, we identify the expected value of the energy as the internal energy U of the thermodynamical system

$$\langle \delta E^2 \rangle = -\frac{\partial U}{\partial \beta} = k_B T^2 \frac{\partial U}{\partial T}. \tag{3.62}$$

Hence, the specific heat is given by

$$c_v = \frac{1}{N}\frac{\partial U}{\partial T} = \frac{\langle \delta E^2 \rangle}{N k_B T^2}, \tag{3.63}$$

which is a common method for evaluating the specific heat in MD simulations [112].

3.4.2 First neighbor distance

The distance to the first neighbor is related to the lattice parameter for temperatures below melting, and it gives insight about the structure of the liquid for temperatures above melting. The structure of simple solids and fluids is characterized by a set of distribution functions for the atomic positions, and one of the simplest is the pair distribution function $g(r)$ [107]. This function gives the probability of finding a pair of atoms a distance r apart, relative to a random distribution at the same density. One useful form of $g(r)$ for computer simulations is

$$g(r) = \rho^{-2} \langle \sum_i \sum_{j \neq i} \boldsymbol{\delta}(\mathbf{r}_i) \delta(\mathbf{r}_j - \mathbf{r}) \rangle = \frac{V}{N^2} \langle \sum_i \sum_{j \neq i} \delta(\mathbf{r} - \mathbf{r}_{ij}) \rangle, \tag{3.64}$$

where $\langle \cdot \rangle$ denotes an *ensemble* average, ρ is the density and V is the volume. In practice, the delta function is replaced by a function which is non-zero in a small range of separations and a histogram is accumulated of all pair separations falling within each such range. Analyzing the first peak of this function we may determine the first neighbor distance in the adlayer.

3.5 Simulation setup

Properties of the noble gases adsorbed on graphene systems were determined using MD in the canonical (NVT) *ensemble*. Thermal averages of physical quantities were formed from as many as 10^7 time steps of 1 fs.

The initial positions of the atoms must be chosen carefully. In Sec. 2.3.1 we presented two commensurate structures: $\sqrt{3} \times \sqrt{3}R30°$ and $\sqrt{7} \times \sqrt{7}R19.1°$. The two dimensional unit cell of the $\sqrt{3}$ commensurate lattice corresponds to 12 carbon atoms and 2 heavy noble gases atoms, as shown in Figure 3.4. The lengths of the cell are $L_x = 3\sqrt{3}\, b$ and $L_y = 3\, b$, where $b = 1.42$ Å is the bond length of two carbon atoms in graphene. The repetition of this unit cell in the xy plane spawns our system, Fig. 3.5. The surface density ρ will be given hereafter in units of ρ_0=0.0636 atoms/Å^2, the density of the $\sqrt{3}\times\sqrt{3}$ commensurate lattice. The initial z coordinate of the noble gases atoms is set based on the minimum of the X-C pair potential. Initial positions using the $\sqrt{7}\times\sqrt{7}$ superlattice can be achieved with a cell of 224 Ne atoms and 784 C atoms, obeying the lattice presented in Sec. 2.3.1 (see Fig. 2.2 for instance). The corresponding superficial density is $\rho = 1.71$.

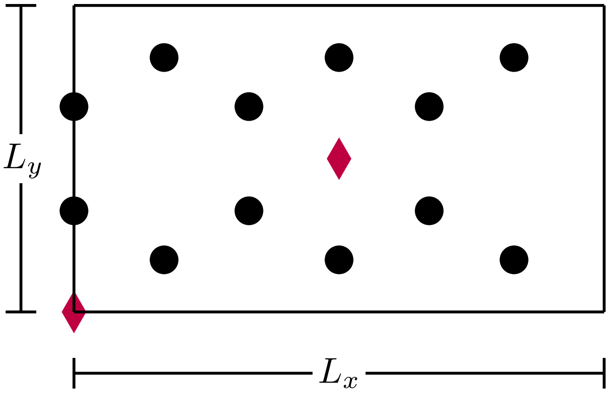

Figure 3.4: Commensurate lattice rectangular cell. The black circles represent the position of C atoms and the purple diamonds indicate the position of the heavy noble gases atoms.

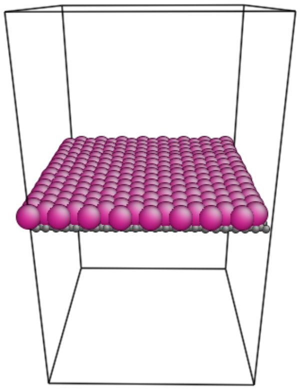

Figure 3.5: Initial configuration of the system for $\rho = 1$. The argon atoms (purple) are arranged in the $\sqrt{3}$ commensurate structure over the carbon atoms (grey). This figure was produced with the AtomEye software [22].

Densities other than the densities of the two commensurate structures were initialized with triangular lattices with suitable lattice parameters. Tab. 3.6 summarizes the number of noble gases atoms, carbon atoms and corresponding densities employed in the simulations. We used PBC in the xy plane of the substrate and we fixed the z coordinates only of the carbon atoms. No PBC were employed in the z direction, normal to the substrate, in order to allow evaporation of noble gases atoms. Because the adlayer may be incommensurate with the substrate symmetry, we must choose certain surface densities which will guarantee PBC to both the substrate and the adlayer. The initial velocities were chosen from a Gaussian distribution compatible with the desired temperature.

Table 3.6: Number of noble gases atoms, carbon atoms and densities employed in the simulations.

ρ	N_X	N_C
0.38	210	3360
0.73	232	1920
1.00	224	1344
1.08	216	1200
1.71	224	784

Chapter 4

Results

4.1 Introduction

In this chapter we present our results for heavy noble gases adsorbed on graphene substrates. Our main focus is on Ar/graphene systems, due to interesting behavior of the relate system Ar/graphite. Thus we studied properties for four Ar surface densities: the $\sqrt{3} \times \sqrt{3}$ commensurate density ($\rho = 1$), one slightly above ($\rho = 1.08$) and two below ($\rho = 0.73$ and 0.38). Ne/graphite exhibits a superlattice $\sqrt{7} \times \sqrt{7}$ thus, in addition to $\rho = 1$, we also considered the $\sqrt{7} \times \sqrt{7}$ density ($\rho = 1.71$) for neon adlayers. For Xe, Kr and Rn we restricted ourselves to calculations at $\rho = 1$.

First we show evidences of commensurate structures of Ne and Kr, section 4.2. In section 4.3 we present the main motivation for this work, the specific heat calculations. In section 4.4 we analyze the melting transition. We study the behavior of the first neighbor distance and the distance between the layer and the substrate in the context of melting and specific heat peaks in Sections 4.5 and 4.6, respectively.

4.2 Commensurate solids

The radial pair distribution function $g(r)$, Sec. 3.4.2, presents peaks at distances corresponding to the positions of the neighbors of a atom. These positions are easily calculated for the ideal commensurate structures. Fig. 4.1 shows $g(r)$ for Ne atoms, at $\rho = 1.71$ and $T = 10$ K, and we also plot dashed lines corresponding to the ideal positions of the $\sqrt{7} \times \sqrt{7}$ structure. The coincidence between the peaks and the superlattice positions occurs for low temperatures, which is evidence of the $\sqrt{7} \times \sqrt{7}$ commensurate adlayer. However, as the temperature increases towards the melting temperature, the peaks broaden and the adlayer is no longer in the commensurate structure.

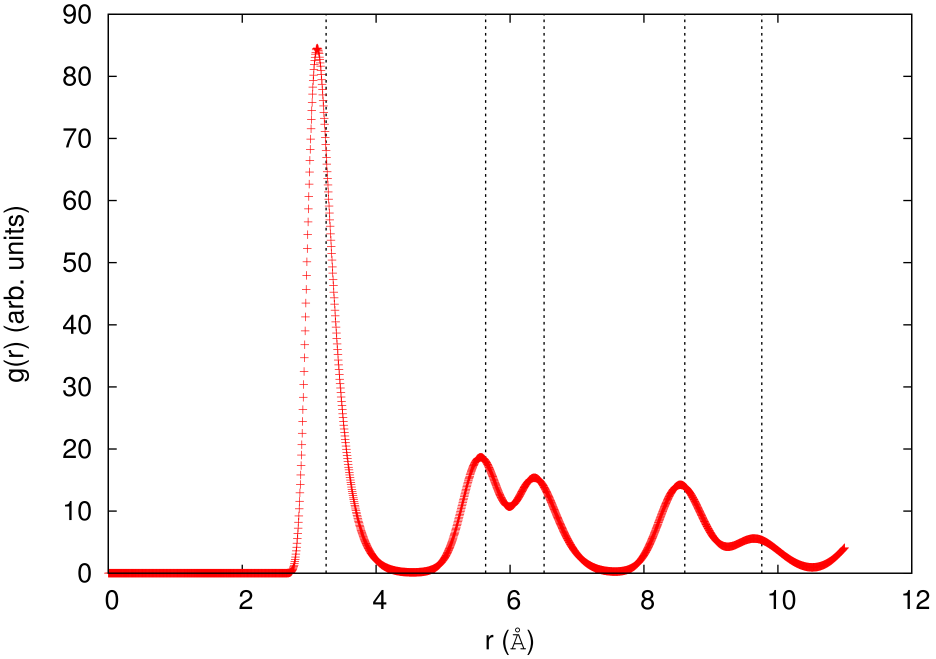

Figure 4.1: Radial pair distribution function for Ne atoms at $\rho = 1.71$ and $T = 10$ K. The dashed lines correspond to the ideal positions of atoms in the $\sqrt{7} \times \sqrt{7}$ superlattice.

Another method to analyze the spatial distribution of rare-gas atoms over the graphene sheet is to determine the probability of finding an atom in a given position. Thus, we accumulated a two-dimensional histogram in a grid of the xy plane and then formed an average of the results over a unit cell. In Fig. 4.2 we present the result for krypton atoms at $\rho = 1$ and $T = 100$ K. If we compare this figure with Fig. 3.4 we see that the Kr atoms are located exactly in the positions corresponding to the $\sqrt{3} \times \sqrt{3}$ commensurate lattice. Further evidence to support this claim comes from the coincidence of the peaks of $g(r)$ and the expected positions of the commensurate structure. This behavior is observed for temperatures below melting; for higher temperatures the probability of finding a Kr atom over the center of a substrate hexagon is higher, although it can be found in other positions.

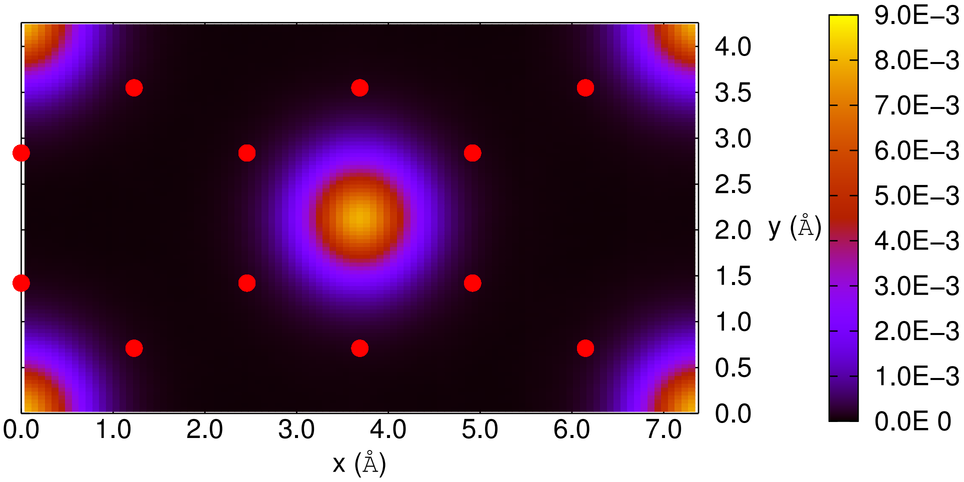

Figure 4.2: Spatial distribution of Kr atoms over a cell at $\rho = 1$ and $T = 100$ K. The red circles represent the ideal positions of carbon atoms. The color code is related to the probability of finding a Kr atom at a given position in the plane parallel to the substrate. Only the regions compatible with the $\sqrt{3} \times \sqrt{3}$ lattice are occupied.

We found no evidence of commensurate structures for Ar, Xe and Rn adlayers. Fig. 4.3 illustrates the spatial distribution of argon adatoms in the unit cell at $\rho = 1$ and $T =$ 40 K. Although the minimum energy state of the system is not an adlayer commensurated with the substrate symmetry, the probability of finding one adatom over the center of a substrate hexagon is larger than in other positions. Also, the lowest probability is right on top of carbon atoms. This behavior is qualitatively the same for Xe and Rn. For higher temperatures we observed similar distributions, but with slightly less intense peaks at the center of the substrate hexagons.

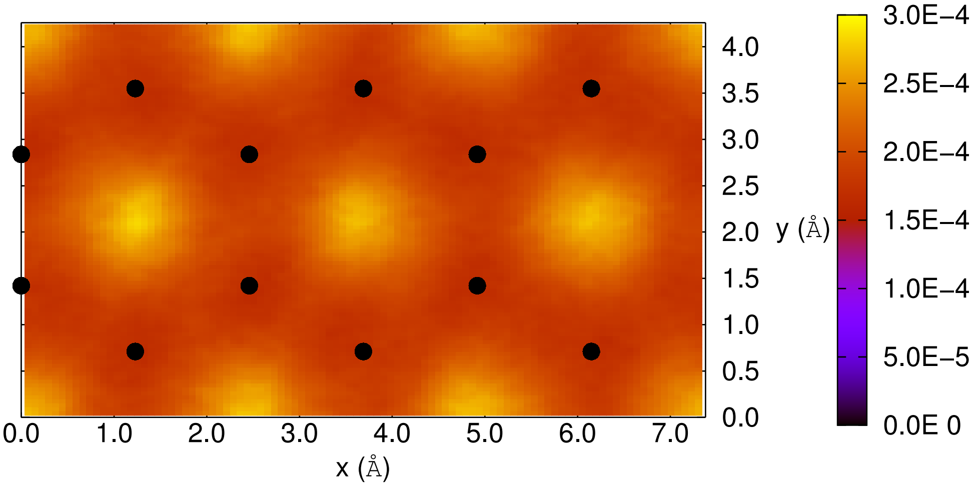

Figure 4.3: Spatial distribution of argon atoms over a cell at $\rho = 1$ and $T = 40$ K. The black circles represent the ideal positions of carbon atoms. The color code is related to the probability of finding an Ar atom at a given position in the plane parallel to the graphene. Although the probability of finding an Ar atom over the center of a carbon hexagon is higher than in other positions, the atoms are not arranged in the $\sqrt{3} \times \sqrt{3}$ commensurate structure.

4.3 Specific Heat

The specific heat c_v is a quantity of thermodynamical interest which can be experimentally measured. It is computed using the fluctuation of the internal energy of noble gases atoms δE^2

$$c_v = \frac{\langle \delta E^2 \rangle_{NVT}}{N_{Ar} k_B T^2}, \tag{4.1}$$

where the brackets indicate an average in the canonical ensemble.

In Fig. 4.4 we show the calculated specific heat for Ar at $\rho = 1$. The behavior of the specific heat for other noble gases and densities is qualitatively the same. The region of the peak is magnified in the inset and the errorbars are shown only in the region of interest.

In order to associate a temperature to the specific heat peak and a characteristic width we fitted the specific heat as a function of the temperature using a Lorentzian function

$$c_v(T) = \frac{a_s}{\pi \gamma_s \left[1 + \left(\frac{T - T_s}{\gamma_s} \right)^2 \right]} + b_s, \tag{4.2}$$

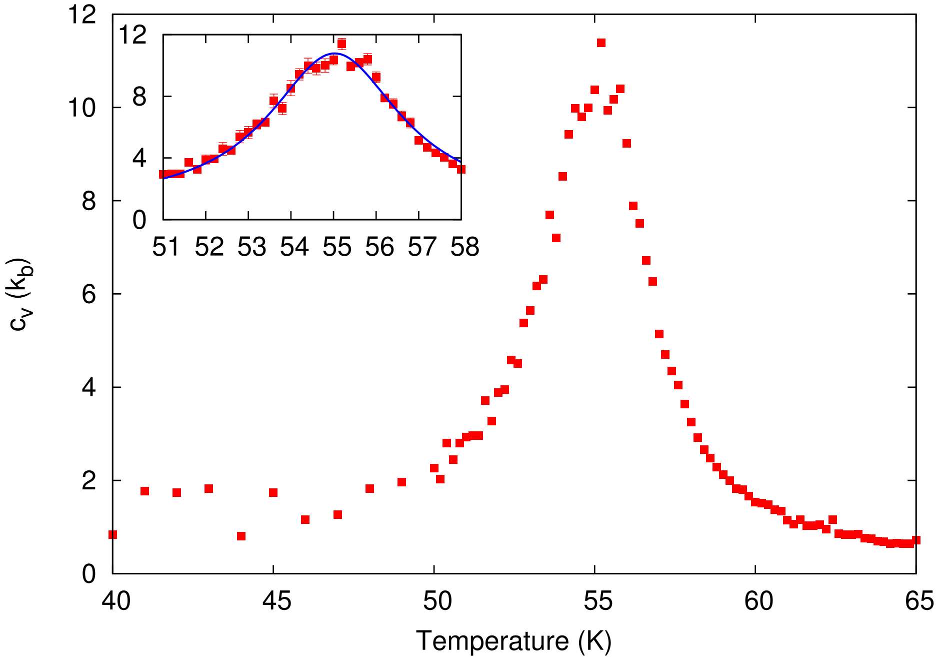

Figure 4.4: Ar adlayer specific heat as a function of the temperature for $\rho = 1$. The region of the peak is magnified in the inset and the line corresponds to a Lorentzian fitting.

where T_s is the location of the peak, $2\gamma_s$ corresponds to the FWHM of the peak, a_s is related to the area of the curve and b_s is a $y-$shift. For example, the inset of Fig. 4.4 contains the fitted curve. We carried out the procedure to other rare-gases and densities; the results are summarized in Table 4.1.

Table 4.1: Position and width of the specific heat peak for various noble gases and densities. The system size for each density is found in Table 3.6.

	ρ	T_s (K)	FWHM (K)
Ne	1.00	15.7 ± 0.1	1.9 ± 0.2
	1.71	35.6 ± 0.2	8.3 ± 0.8
Ar	0.38	54.4 ± 0.2	12.7 ± 1.3
	0.73	54.4 ± 0.1	4.0 ± 0.3
	1.00	55.0 ± 0.1	3.8 ± 0.2
	1.08	53.6 ± 0.1	3.7 ± 0.2
Kr	1.00	107.4 ± 0.2	6.5 ± 1.2
Xe	1.00	134.3 ± 0.5	7.9 ± 1.3
Rn	1.00	180.4 ± 5.6	59.4 ±11.3

Comparing the different noble gases at the same density ($\rho = 1$) we note that, as the atomic number increases, the position of the peak corresponds to higher temperatures. Additionally, we observe an enlargement of the characteristic width of the peak. These properties are consistent with bulk properties of the same noble gases in the absence of the graphene substrate.

Interesting properties arise when we compare Ar adlayers at different densities. The position of the peak increases with higher densities between $0.38 \leqslant \rho \leqslant 1$, but for $\rho = 1.08$ it is considerably lower than for the commensurate density. One possible explanation for this deviation is that although the Ar adlayer is not commensurate, substrate forces tend to expand the adlayer towards the $\sqrt{3} \times \sqrt{3}$ structure. Clearly this is possible only for $\rho \leqslant 1$, and increasing the density actually contributes to lowering the temperature of the peak in the specific heat. The FWHM of the peaks is very similar, except for $\rho = 0.38$ due to size effects: for low densities the coverage of the graphene sheet is not complete, and the proportion of atoms in the border of the adlayer to bulk atoms is substantial, thus deviations are expected.

4.4 Melting

In order to investigate the melting of the adlayer, which is intimately related to loss of sixfold symmetry, we introduce the order parameter

$$\Psi_6 = \frac{1}{N_B} \left\langle \left| \sum_{j,k}^{N} \exp\left(6i\Phi_{jk}\right) \right| \right\rangle , \tag{4.3}$$

where Φ_{jk} is the angle between the projections in the xy plane of rare-gas atoms j and k with respect to a fixed axis in this plane and N_B is the number of bonds used in the calculation. The sum on j extends over all noble gas atoms, and the sum in k considers only the nearest neighbors of j. The brackets indicate a thermal average. If the adlayer possesses six-fold symmetry, as a triangular lattice does, $\Psi_6 = 1$. If the fluid is isotropic, then Ψ_6 is zero. The loss of sixfold symmetry can be characterized by a peak in the susceptibility χ_6 of Ψ_6 given by

$$\chi_6 = \frac{\langle \Psi_6^2 \rangle - \langle \Psi_6 \rangle^2}{T} . \tag{4.4}$$

Fig. 4.5 shows the order parameter and susceptibility for Ar at $\rho = 0.38$, for other rare-gases and densities the behavior is qualitatively the same. The order parameter is near unity for low temperatures and drops when the melting occurs, while the susceptibility peaks near the transition.

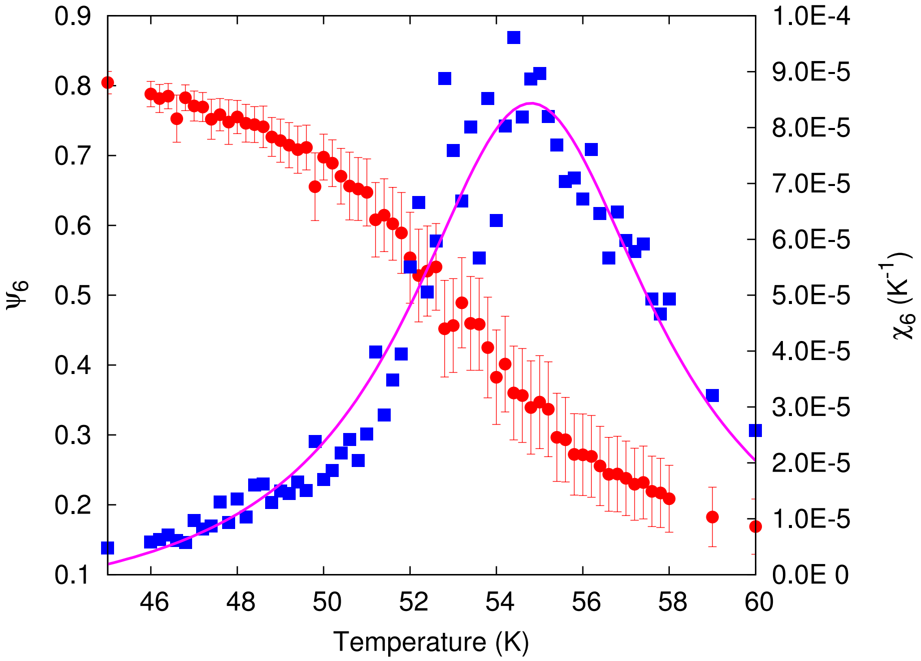

Figure 4.5: Order parameter (circles) and susceptibility (squares) for Ar at $\rho = 0.38$ as a function of the temperature. The line corresponds to a Lorentzian fitting of the susceptibility peak.

We also assumed a Lorentzian form for the susceptibility peak as a function of the temperature,

$$\chi_6(T) = \frac{a_m}{\pi\gamma_m\left[1 + \left(\frac{T-T_m}{\gamma_m}\right)^2\right]} + b_m, \tag{4.5}$$

where T_m is taken to be the melting temperature, $2\gamma_m$ corresponds to the FWHM of the peak, a_m is related to the area of the curve and b_m is a $y-$shift. We present our results in Table 4.2.

If we compare different systems at the same density, $\rho = 1$, the melting temperature increases as we consider increasing atomic number. Furthermore, the increase of the melting temperature is accompanied by an enlargement of the FWHM. The only exception is the characteristic width of the Kr melting. As we recall, we have evidences of the $\sqrt{3} \times \sqrt{3}$ only for Kr, which may explain this smaller FWHM. Comparing Ar adlayers at different densities we see that the melting temperature increases with higher densities, although for $\rho = 1.08$ it is within the errorbars.

In general, the melting temperatures and FWHM obtained from the susceptibility peaks do not coincide with the specific heat peaks, which suggests that melting is not the only phenomena contributing to the specific heat. In the next sections, Sec. 4.5 and 4.6,

Table 4.2: Melting temperature and characteristic width for various noble gases and densities. The system size for each density is found in Table 3.6.

	ρ	T_m (K)	FWHM (K)
Ne	1.00	16.2 ± 0.1	1.5 ± 0.2
	1.71	25.9 ± 0.2	9.9 ± 1.6
Ar	0.38	54.8 ± 0.1	7.0 ± 0.5
	0.73	55.7 ± 0.1	2.9 ± 0.3
	1.00	56.9 ± 0.1	7.6 ± 1.8
	1.08	56.5 ± 0.4	4.9 ± 1.3
Kr	1.00	107.9 ± 0.1	4.2 ± 0.6
Xe	1.00	181.3 ± 0.7	19.4 ± 4.4
Rn	1.00	250.0 ± 0.8	34.8 ± 6.8

we investigate how the specific heat peaks and melting are related to other properties of the adlayers.

4.5 First neighbor distance

The average first neighbor distance $\langle a \rangle$ can be obtained from the position of the first peak of the pair distribution function $g(r)$. The behavior of $\langle a \rangle$ as a function of the temperature can be quite different for the various densities and rare-gases studied. We begin analyzing the first neighbor distance for Ar adlayers, Fig. 4.6. For low temperatures, $T \approx 40$ K, and temperatures above melting, $T \gtrsim 58$ K, increasing density corresponds to lower first neighbor distances, as expected. However, for temperatures near the melting transition and the specific heat, $\langle a \rangle$ does not necessarily follow this expectation. For high temperatures the distance tends towards a constant value, which can be explained if we think in terms of the Helmholtz free energy F (since we are working with the canonical *ensemble*),

$$F = E - TS, \tag{4.6}$$

where S is the entropy. For low temperatures, the free energy is dominated by the internal energy E, and the layer expands. The term TS is significant at higher temperatures, and disorder of the layer is energetically favored instead of expansion. This situation of nearly constant $\langle a \rangle$ would persist until second layer promotion would be thermally activated.

Fig. 4.7 shows the first neighbor distance as function of the temperature for Ne and Kr adlayers. For Ne at $\rho = 1$ the first neighbor distance increases with the temperature and tends toward a constant for high temperatures, qualitatively the same as Ar. More interesting behavior arises with the commensurate structures, Ne at $\rho = 1.71$ and Kr

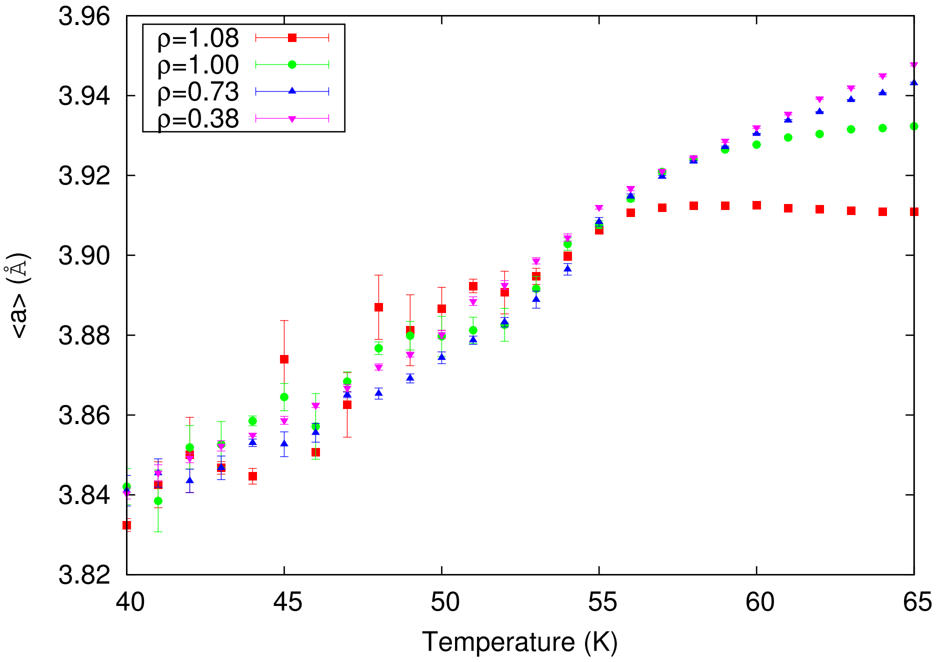

Figure 4.6: First neighbor distance $\langle a \rangle$ as a function of the temperature for Ar adlayers at various densities.

at $\rho = 1$, which present minimums and decreasing lattice parameters with increasing temperatures. In Fig. 4.7a we plot $\langle a \rangle$ alongside with the temperature range of the melting peak (T_m and the corresponding FWHM) for Ne at $\rho = 1.71$; and in Fig. 4.7b we repeat the procedure with Kr at $\rho = 1$. The melting temperature corresponds approximately to the minimum of the first neighbor distance, and the characteristic width encompasses the change between negative and positive slopes. One possible explanation is that, with increasing temperature, the adatoms have sufficient energy to overcome the substrate potential expansion and get closer. This is possible for temperatures below melting, for temperatures above T_m the liquid expands as it would be expected.

Finally, a third behavior is observed in the first adsorbed layer of Xe and Rn. Fig. 4.8 shows the first neighbor distance for Xe at $\rho = 1$; the same quantity for Rn presents similar features. The abrupt change near 134 K coincides with the specific heat peak, as we can see in the filled region corresponding to the temperature range of the specific heat peak.

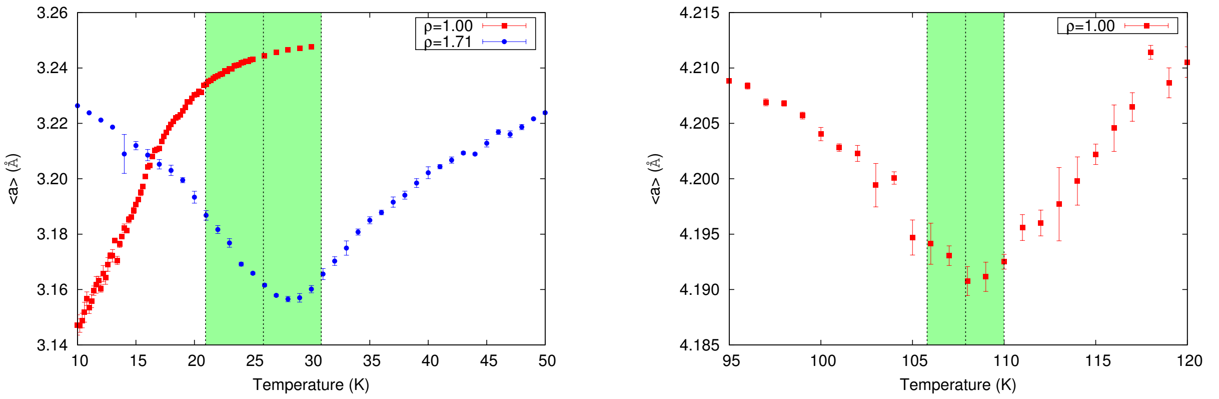

(a) First neighbor distance for Ne adlayers at $\rho = 1$ and 1.71. The green region corresponds to the melting temperature $T_m = 25.9$ K and FWHM of the melting peak of $\rho = 1.71$.

(b) First neighbor distance for Kr adlayers at $\rho = 1$. The green region corresponds to the melting temperature $T_m = 107.9$ K and FWHM of the melting peak.

Figure 4.7: First neighbor distance as a function of the temperature for Ne and Kr adlayers.

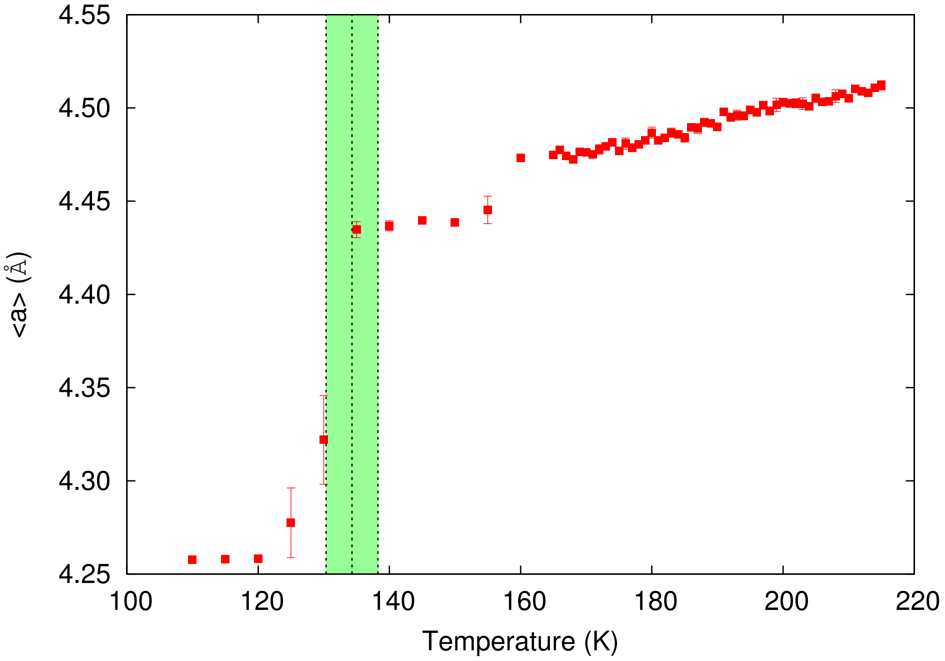

Figure 4.8: First neighbor distance as a function of the temperature for Xe at $\rho = 1$. The green region corresponds to the specific heat peak $T_p = 134.3$ K and its corresponding FWHM.

4.6 Distance from the substrate

In this section we are interested in the dimension perpendicular to the substrate plane, the distance between the adlayer and the graphene sheet. We accumulated the z coordinates of the adatoms during the simulations and obtained the mean value $\langle z \rangle$ which corresponds to the average distance to the substrate. Fig. 4.9 shows this quantity for Ar adlayers at $\rho = 0.38$, 0.73, 1 and 1.08. The expected behavior of increasing the distance from the substrate with increasing density is observed at low and high temperatures, however near the melting and specific heat peaks deviations occur. For example, $\rho = 1$ presents the highest value of $\langle z \rangle$ during the temperature range if compared with the other densities. For Ar adlayers we have no evidence of second layer formation for the range of densities and temperatures employed.

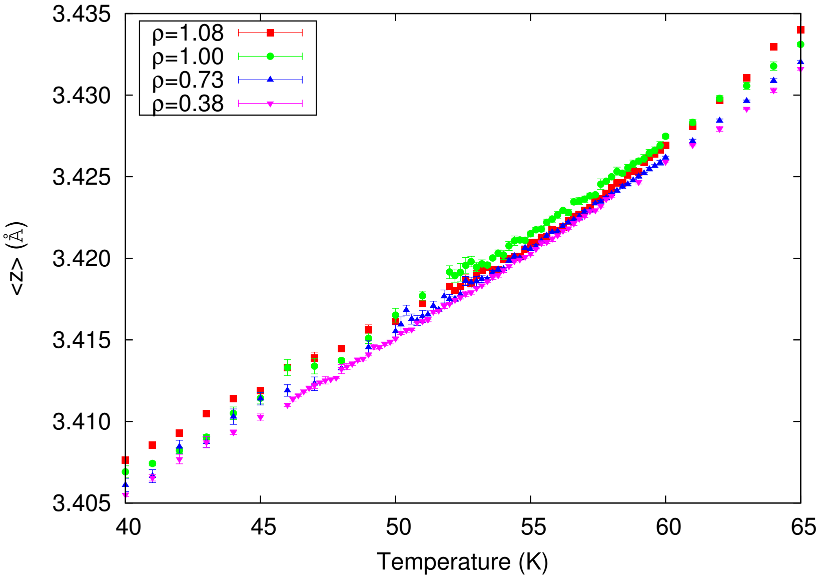

Figure 4.9: Distance from the substrate as a function of the temperature for Ar adlayers at the given densities.

Ne adlayers present similar characteristics of the Ar adlayers, with the difference that $\rho = 1$ is always closer to the substrate than $\rho = 1.71$, for the considered temperature range. On the other hand, Kr adlayers present fascinating behavior. Fig 4.10 shows that the distance from substrate has an inflection point, which coincides with the specific heat peak temperature.

Finally, we analyze the two systems that formed a second adsorbed layer, Xe and Rn adlayers, Fig 4.11. For Xe adlayers, the sharp increase in the distance of the second adsorbed layer coincides with the specific heat peak, Fig. 4.11a. Interestingly, there is no sharp change in the first adlayer. The distance of the second adsorbed layer of Rn,

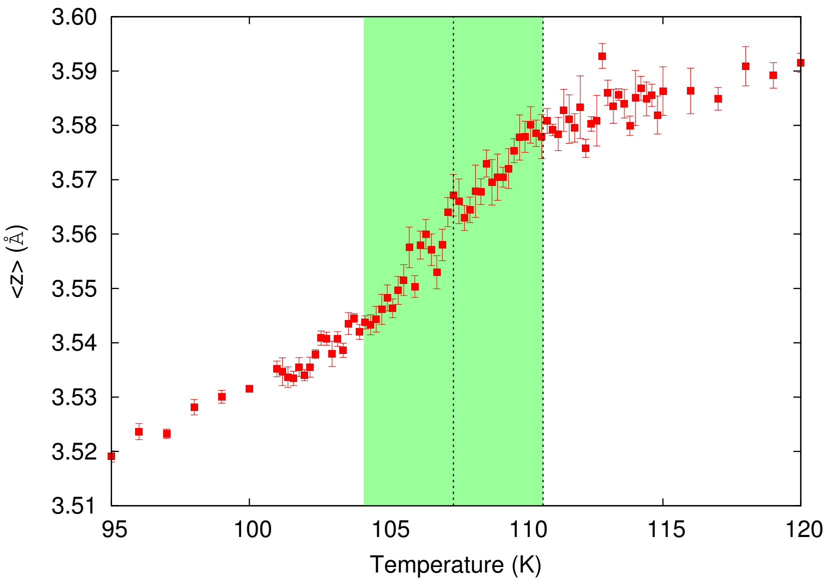

Figure 4.10: Distance from the substrate as a function of the temperature for Kr adlayers at $\rho = 1$. The filled region corresponds to the specific heat peak $T_p = 107.4$ K and its corresponding FWHM.

Fig. 4.11b, decreases with increasing temperature, while the first layer remains at an approximately constant $\langle z \rangle$.

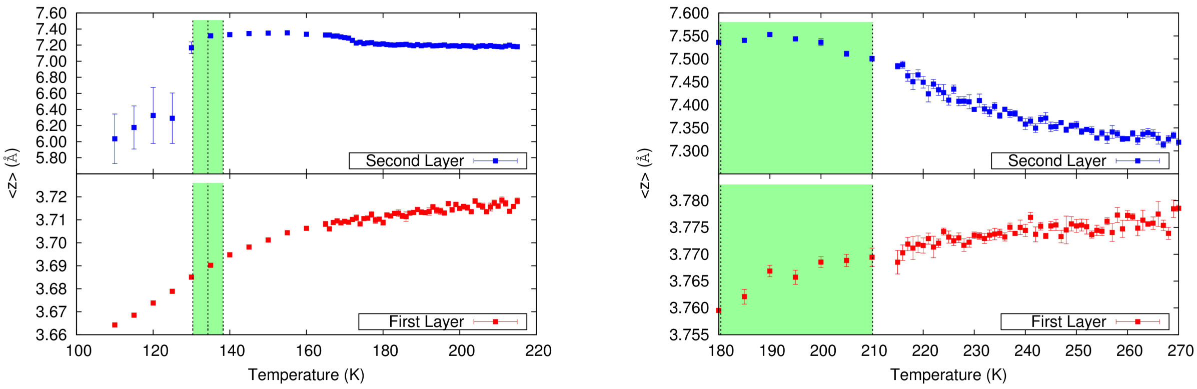

(a) Distance from the substrate as a function of the temperature for Xe adlayers at $\rho = 1$. The green region corresponds to the specific heat peak $T_p = 134.3$ K and its corresponding FWHM.

(b) Distance from the substrate as a function of the temperature for Rn adlayers at $\rho = 1$. The green region corresponds to the specific heat peak $T_p = 180.4$ K and its corresponding FWHM.

Figure 4.11: Distance from the substrate as a function of the temperature for Xe and Rn adlayers. Note that the $y-$scale differs between the different layers.

Chapter 5

Conclusions

We consider that one of the main contributions of our work on adsorption of noble gases on graphene is evidences of commensurate adlayers, which depend strongly on the symmetry of the exposed surface. Since graphite and graphene present the same surface, we looked for the two well-known commensurate structures previously observed on graphite: $\sqrt{3}\times\sqrt{3}$ and $\sqrt{7}\times\sqrt{7}$ [1]. Interestingly, we observed the two structures for low temperatures; the Ne adlayer forms a $\sqrt{7}\times\sqrt{7}$ lattice and Kr adatoms are found in the $\sqrt{3}\times\sqrt{3}$ structure. Although graphite and graphene share many aspects, this is remarkable because graphene is a much less attractive substrate than graphite, and we could not know if these structures would be found *a priori*.

The specific heat is a quantity of thermodynamical interest that can be measured in experiments with relatively simple apparatus. Its peaks contain information on the system and it can be used to determine the order of the melting transition. For graphite substrates, all heavy noble gases present continuous melting, with the possible exception of Ar due to a narrow peak in the specific heat (at the shoulder of a broad peak). We determined the position and width of the peaks for the heavy rare-gases at various densities, and we only found evidences of continuous melting, due to the broad FWHM observed.

The melting, in the sense of loss of sixfold symmetry, was also investigated. We introduced an order parameter and determined the melting temperature using the susceptibility associated with the order parameter. The melting temperature, alongside with the FWHM, indicates a temperature range in which we have solid-liquid coexistence.

In order to better understand the specific heat peaks and the melting transition we have to consider the influence of the substrate on the adlayer. The pair interaction noble-gas-noble-gas is stronger than noble-gas-carbon, enough to prevent the formation of the commensurate lattice in most cases. However, the probability of finding one noble gas atom over the center of a carbon hexagon is higher than in other positions, as shown in Sec. 4.2. This might explain the deviations found for Ar at $\rho = 1.08$. Apparently increasing the density slightly above the commensurate density allows, energetically, more frequent occupation of sites other than the center of the hexagons, which facilitates the melting transition.

We also studied two other properties of the adlayers: the first neighbor distance and the distance between the adlayer and the substrate. It is possible to relate the behavior of these quantities directly to the specific heat peaks or the melting transition. It is noteworthy that the commensurate adlayers have a signature behavior for the first neighbor spacing near the melting transition.

It was our intention to complement a large body of knowledge of the literature about relate systems, namely noble gases adsorbed on graphite substrates, see [1] and references therein. Unfortunately, to the best of our knowledge, experimental data is not available for the noble-gas/graphene system. We hope that this study motivates experiments to enlarge our understanding of this system and to improve the simulations.

Part II

Vortex line in the unitary Fermi gas

Chapter 6

Ultracold Fermi gases

6.1 Introduction

Fermions, such as electrons, protons and neutrons, compose all the usual matter around us. The Fermi-Dirac statistics governs the behavior of a wide range of systems: electrons in metals, nuclei, atoms and even neutron stars. Several Fermi systems are dense and strongly interacting. On the other hand, ultracold atomic gases are dilute systems in which the interparticle interactions can be tuned via Feshbach resonances, leading to strongly interacting systems.

The statistics of a neutral atom is determined by its number of neutrons, which must be odd for a fermionic atom. Alkali atoms have odd atomic number Z and their fermionic isotopes have even mass number A. These isotopes are less abundant than their odd-A counterparts, since they have an unpaired neutron and an unpaired proton, which increases the energy due to the odd-even effect [113]. In Sec. 8.3.2 we will comment on how superfluid pairing in nuclear matter is related to pairing in cold atoms.

In early experiments designed to cool Fermi gases, ^{40}K [114, 115] and ^{6}Li [116, 117] were cooled to approximately one quarter of their Fermi temperature. More recently, lower temperatures were achieved and degenerate gases of ^{173}Yb have been prepared at temperatures of the order of μK [118].

In the classical limit, low densities and/or high temperatures, fermions and bosons behave alike. The quantum degeneracy is governed by the phase-space density $\bar{\omega}$, which is defined as the number of particles contained within a volume equal to the cube of the thermal de Broglie wave length λ_T

$$\bar{\omega} = n\lambda_T^3 = n\left(\frac{2\pi\hbar^2}{mk_BT}\right)^{3/2}, \tag{6.1}$$

where n is the number density. In the classical limit $\bar{\omega} \ll 1$, and for $\bar{\omega}$ of the order of the unit, gases become degenerate. Bosons condense in the lowest energy state, while fermions tend to a filled Fermi sea. The Fermi temperature T_F controls the degeneracy.

Experimental difficulties arise from the evaporative cooling of degenerate fermionic gases. The efficiency of evaporative cooling depends strongly on the scattering cross section, which vanishes at low energies due to the antisymmetry requirement of the wavefunction, Eq. (B.81). Thus, evaporative cooling with a single fermionic state is not feasible. Two internal states of fermions, for instance the hyperfine states $|9/2, 9/2\rangle$ and $|9/2, 7/2\rangle$ of ^{40}K [114], or a boson-fermion mixture, ^{7}Li and ^{6}Li [116], overcome this experimental challenge.

Interparticle interactions in ultracold atomic gases can be tuned via Feshbach resonances, thus realizing the BCS-BEC crossover, a problem of significant interest [119]. The investigation of Bardeen-Cooper-Schrieffer (BCS) to Bose-Einstein condensate (BEC) crossover arises in an attempt to better understand superfluidity and superconductivity beyond the standard paradigms [23]. Recent developments led to realizations of the BCS-BEC crossover of ultracold Fermi gases in the laboratory. The most interesting results are related to a very strongly interacting state of matter, the unitary Fermi gas, which is right at the heart of the crossover. Until recently, all superconductors and superfluids fell into one of two classes, bosonic and fermionic. This led to two different paradigms, BEC and BCS, for understanding the properties of quantum fluids.

In the BEC scheme, first developed for noninteracting bosons and later generalized to include repulsive interactions, it is possible to describe bosonic fluids, such as ^{4}He, and ultracold Bose gases, ^{87}Rb for instance. The condensate is a macroscopic occupation of a single quantum state that occurs below a transition temperature T_c, which is of the same order of magnitude as the quantum degeneracy temperature, at which the interparticle spacing is of the order of the thermal de Broglie wavelength. Although the ultracold Bose gases studied in laboratory are composite particles, with even number of fermionic constituents, the internal structure is quite irrelevant for low-energy properties of the superfluid and normal states.

The BCS paradigm, first conceived for metallic superconductors, describes a pairing instability arising from a weak attractive interaction in a highly degenerate system of fermions. Both the formation of pairs and their condensation occur at the same temperature T_c, which is orders of magnitude smaller than E_F/k_B, which sets the degeneracy temperature. The BCS theory is very successful in describing conventional superconductors and it has been generalized to describe various systems, such as superfluidity in ^{3}He and pairing in nuclei.

Early theoretical work on the crossover was conceptually interesting, but real enthusiasm came from its experimental realization [27]. Now there is recognition that the BCS and BEC theories are not as distinct as they were once thought to be, instead they are two extrema of a continuum. Right in the middle of this crossover lies a strongly interacting state, the unitary Fermi gas, with remarkable properties.

In the next section, Sec. 6.2, we show how Feshbach resonances may be used to tune interactions between components of the gas, from the BCS regime up to the BEC scheme. Sec. 6.3 focuses on obtaining a phase diagram for the ground state crossover. Finally, Sec. 6.4 presents some quantum Monte Carlo results for the unitary Fermi gas. Aspects of scattering theory related to development of this chapter are in Appendix B; and we review some aspects of superfluidity in Appendix C.

6.2 Tunable interactions

The fermionic species used in the BCS-BEC usually are ^{6}Li or ^{40}K. Typical experimental parameters are: total number of atoms $N \sim 10^5$ - 10^7, interparticle distance k_F^{-1} approximate one micron, $E_F/k_B \sim 100$ nanoKelvin, and temperatures of $\sim 0.1 E_F/k_B$. The two species of fermions are two different hyperfine states, but are often called $|\uparrow\rangle$ and $|\downarrow\rangle$, in accordance with the standard BCS theory.

The most important difference between ultracold Fermi gases and all previously studied superfluids is that the interaction between spin $|\uparrow\rangle$ and spin $|\downarrow\rangle$ can be tuned in the laboratory. The average separation between atoms, k_F^{-1}, is much larger than the range of the interatomic potential r_0. For a dilute gas with $k_F r_0 \ll 1$, the interaction is described by a single parameter, the s-wave scattering length a. All thermodynamic properties of the gas can be written in a universal scaling form. For example, the free-energy F takes the form

$$F = N E_F \mathcal{F}(k_B T/E_F, 1/(k_F a)), \tag{6.2}$$

where $\mathcal{F}$ is a scaling function. This result is universal in the sense that it is independent of microscopic details, as long as $k_F r_0 \to 0$.

Consider the two-body scattering in vacuum at $T = 0$. A Feshbach resonance is a dramatic increase in the collision cross-section of two atoms, due to a bound state in the closed channel crossing the scattering continuum of the open channel, Fig. 6.1 (a). Let us consider the specific example of ^{6}Li, of electronic spin $S = 1/2$ and nuclear spin $I = 1$. The electric spin is fully polarized, usually the magnetic field $B \geqslant 500\ G$, and aligned in the same direction for each of the three lowest hyperfine states [1]. Hence, two colliding ^{6}Li atoms are in a continuum spin-triplet state in the open channel. The closed channel has a singlet-bound state that can resonantly mix with the open channel as a result of the hyperfine interaction that couples the electron spin to the nuclear spin.

---

[1] Here we explicit discuss the electronic spin states of the Fermi atoms. At all other places, spin up and spin down are short-hand notations for the two hyperfine states of the two-species Fermi gas.

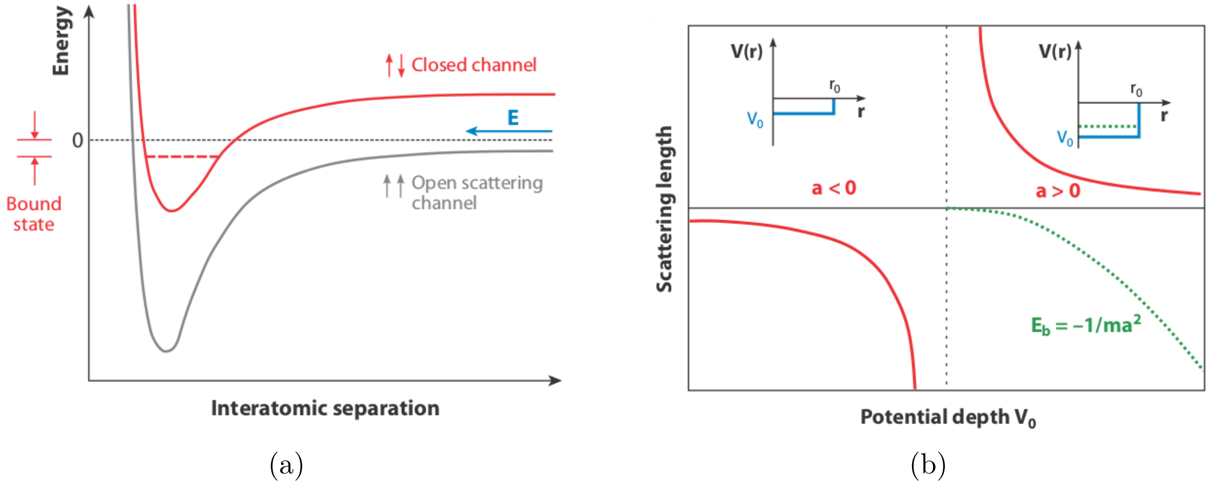

(a) (b)

Figure 6.1: Figures from [23] illustrating the open and closed channels in two-body scattering (a) and the scattering length a relation with the square well potential depth V_0 and the formation of a bound state with energy E_b (b).

The difference in the magnetic moments in the closed and open channels allows experimentalists to use an external magnetic field B to tune a Feshbach resonance. The resulting interatomic interaction in the open channel can be described by a B-dependent scattering length which, near the resonance, is

$$a(B) = a_{BG}\left[1 - \frac{\Delta B}{B - B_0}\right], \tag{6.3}$$

where a_{BG} is the background value, in the absence of the coupling to the closed channel, B_0 is the location of the resonance and $|\Delta B|$ is the width. Experimental results are often plotted as a function of $-1/(k_F a)$, rather than $1/(k_F a)$, because usually $a_{BG}\Delta B > 0$ which means that for increasing B the inverse scattering length goes from positive to negative.

We do not need to understand the intricacies of the two-channel model of a Feshbach resonance. A simple model of a single-channel short range two-body scattering can give an intuitive feel of the problem. The reason for the validity of this model is that most experiments are in the broad resonance limit, where the effective range of the Feshbach resonance is much smaller that k_F^{-1}. This implies that the fraction of closed-channel particles is extremely small, which is observed in experiments [120].

Let us consider the problem of two fermions with spin $|\uparrow\rangle$ and spin $|\downarrow\rangle$ interacting with a two-body potential with range r_0. The low-energy properties as a function of the momentum k, such that $kr_0 \ll 1$, are described by the s-wave scattering amplitude

$$f(k) = \frac{1}{k\cot[\delta_0(k)] - ik} \approx -\frac{1}{1/a + ik}. \tag{6.4}$$

The scattering length a completely determines $\delta_0(k \to 0) = -\tan^{-1}(ka)$, the s-wave scattering phase shift with low-energy. The effective interaction is independent of the shape of the potential, thus we choose the simplest one: a square well of depth V_0 and range r_0, studied in detail in Sec. B.4.2. Figure 6.1 (b) shows $a < 0$ for weak attraction, grows in magnitude with increasing V_0, and diverges to $-\infty$ at the formation of a bound state in vacuum ($V_0 = \hbar^2\pi^2/(mr_0^2)$, where the reduced mass is $m/2$). Once the bound state has been formed, the scattering length changes to $a > 0$ and decreases from $+\infty$ with increasing V_0. For positive a, the scattering length a is the size of the bound state, with energy $-\hbar^2/(ma^2)$.

The threshold for bound-state formation, where $|a| \to \infty$, is called unitary point. The phase shift is $\delta_0(k = 0) = \pi/2$, and the scattering amplitude takes the maximum value $f \approx -1/(ik)$. The unitary regime is the most strongly interacting regime in the BCS-BEC crossover.

The s-wave wavefunction for the relative motion of two particles in vacuum, with vanishing energy at infinity, is [23]

$$\psi(r) \propto \frac{1}{r} - \frac{1}{a}, \quad \text{for } r \geqslant r_0. \tag{6.5}$$

Hence, the N-particle wavefunction in the many-body problem must have the same short-distance behavior when two particles of unlike spins come together.

6.3 Global phase diagram

We now address the many-body problem of a finite density of spin up and spin down fermions with a two-body interaction specified by the scattering length a, so that the dimensionless coupling constant is $1/(k_F a)$. The BCS limit, $1/(k_F a) \to -\infty$, corresponds to a weak attraction which leads to a collective Cooper instability in the presence of a Fermi surface. On the other extreme, $1/(k_F a) \to +\infty$, the BEC regime leads to tightly bound diatomic molecules.

6.3.1 Ground-state crossover

The BCS wavefunction provides a reasonable variational description of the pairing correlations for arbitrary attraction. The zero-temperature crossover mean-field theory (MFT) is in essence the same as the standard BCS theory, however the chemical potential μ is self-consistently renormalized in the gap equation. The chemical potential decreases with increasing attraction, from E_F in the BCS limit to a negative value in the BEC extreme, approaching half of the pair-binding energy $-\hbar^2/(2ma^2)$.

In the MFT scheme, the crossover is smooth: in the BCS limit the Cooper pairs of size $\xi_{\text{pair}} \sim k_F^{-1} \exp[\pi/(2k_F|a|)] \gg k_F^{-1}$; and in the BEC limit exhibits tightly bound dimers $\xi_{\text{pair}} \ll k_F^{-1}$. There is no singularity in the many-body state at unitarity, the threshold for a two-body state in vacuum, because the collective Cooper pairs have already formed.

We emphasize that, although the attraction increases from BCS to BEC, both limits are weakly interacting. This is straightforward to notice in the BCS limit; for the BEC regime, once the dimers are formed, all that remains is a weak residual repulsion between dimers which vanishes in the "deep" BEC limit.

At the heart of the crossover, $1/(k_F a) = 0$ with $|a| \gg k_F^{-1}$. The pair size is of the order of interparticle spacing $\xi_{\text{pair}} \simeq k_F^{-1}$.

6.3.2 Finite temperature properties

In order to determine the $T > 0$ phase diagram, we need to calculate T_c as a function of $1/(k_F a)$. MFT [121] yields the BCS result, see Eq. (C.39),

$$T_c = \left(\frac{8\gamma}{\pi e^2}\right) E_F \exp\left[-\frac{\pi}{2k_F a}\right], \tag{6.6}$$

when $1/(k_F a) \to -\infty$. With increasing interaction, the T_c estimate becomes qualitatively incorrect. In [121], it is argued that the MFT estimate is in fact a pairing temperature T^*, below which a significant fraction of fermions are bound in pairs and this has nothing to do with condensation, except in the BCS limit. The dissociation energy for dimers with binding energy $E_b = -\hbar^2/(ma^2)$ in the strong-coupling limit is $T^* \sim |E_b|/\ln(|E_b|/E_F)$ [121].

An exponential interpolation of T_c between the BCS result and the non-interacting BEC is carried out in [122], which is

$$T_c = \frac{\pi}{m}\left(\frac{n}{2\zeta(3/2)}\right)^{2/3} \simeq 0.22 E_F, \tag{6.7}$$

where ζ is the Riemann zeta function, the mass of the dimers is $2m$ and the density is $n/2$. Figure 6.2 is an illustration of the BCS-BEC phase diagram.

6.4 Unitary Fermi gas: quantum Monte Carlo studies

The 3D unitary Fermi gas is a strongly interacting system of fermions with short-range interactions in the continuum. When $|a| = \infty$, the low-energy s-wave scattering phase shift is $\delta_0 = \pi/2$, and the scattering amplitude $f(k) = i/k$ has no scale. The ground state

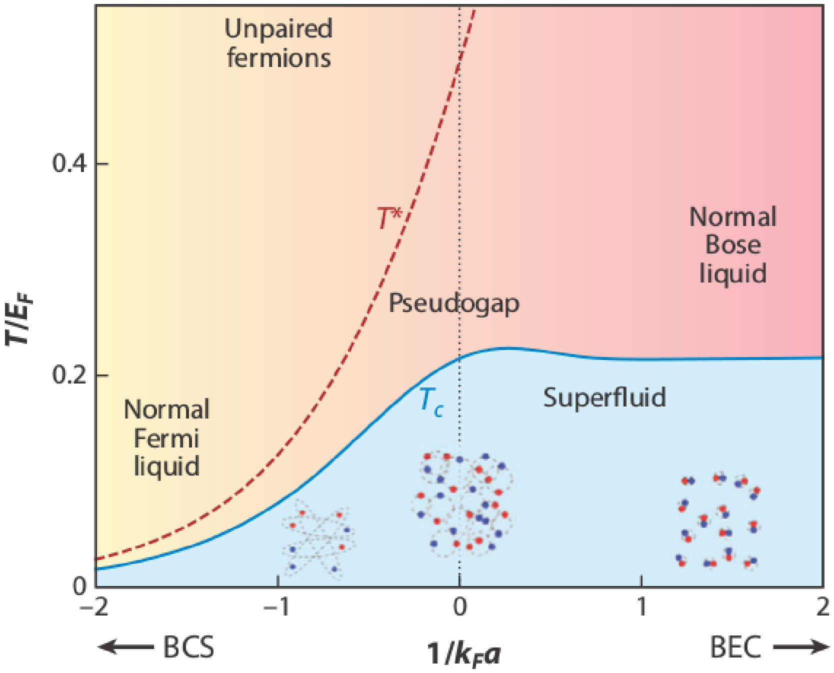

Figure 6.2: Qualitative phase diagram of the BCS-BEC crossover from [23], which relates $k_B T/E_F$ with the coupling $1/(k_F a)$. The illustrations show schematically the evolution from large Cooper pairs (BCS) to tightly bound molecules (BEC). Unitarity, $1/(k_F a) = 0$, corresponds to strongly interacting pairs with pair sizes $\simeq k_F^{-1}$. With increasing attraction, the pair-formation temperature T^* diverges from the transition temperature T_c.

energy per particle E_0 is proportional to that of the noninteracting Fermi gas E_{FG}, Eq. C.10,

$$E_0 = \xi E_{FG} = \xi \frac{3}{10} \frac{k_F^2}{M}, \tag{6.8}$$

where the constant ξ is known as the Bertsch parameter. In the limit $ak_F \to -\infty$, theoretical estimates of $\xi = 0.326$ and 0.568 were reported [123, 124].

The main theoretical challenge is to determine properties of the unitary Fermi gas (ground-state energy, T_c and scaling functions) in the absence of a small parameter. Numerical simulations using various quantum Monte Carlo (QMC) methods have been quite successful at calculating some of these properties.

The earliest QMC works focused on the ground-state properties across the crossover using diffusion QMC at $T = 0$. The energy of the gas at unitarity was found to be $\simeq 0.42$ to 0.44 times that of the noninteracting gas [125, 126], while a more recent study gives a bound of 0.383(1) [127].

Other QMC studies [128] found a Bogoliubov quasiparticle dispersion of the from

$$E(\mathbf{k}) = \left[\left(\frac{\hbar^2 k^2}{2m^*} - \tilde{\mu} \right)^2 + \Delta^2 \right]^{1/2}, \tag{6.9}$$

at $T = 0$, where the gap is $\Delta/E_F \simeq 0.5$ at unitarity [129, 130].

Chapter 7

Quantum Monte Carlo methods

7.1 Introduction

In this chapter we introduce the methods used for the study of dilute fermionic systems. Particularly, we are interested in the study of vortex excitations in the unitary Fermi gas.

Quantum Monte Carlo (QMC), which is a way of sampling multidimensional integrals, is presented in Sec. 7.2. The Variational Monte Carlo (VMC) method is introduced in Sec. 7.3. It relies on a trial wavefunction which should include as much information as we know about the system. In Sec. 7.4, we introduce the Diffusion Monte Carlo method (DMC). The DMC calculations for the ground state energy yield the best results that are compatible with the nodal structure introduced by a guide function. In a DMC calculation, quantities that do not commute with the Hamiltonian can be determined by using both VMC and DMC results. In Sec. 7.5 we present the problem have studied: a single vortex line in the unitary Fermi gas.

7.2 Monte Carlo methods

The core of a Monte Carlo simulation is the evaluation of multidimensional integrals by sampling the integrand statistically and averaging the sampled values [131]. Suppose we define a $3N$-dimensional vector

$$\mathbf{R} = (\mathbf{r}_1, \mathbf{r}_2, \ldots, \mathbf{r}_N), \tag{7.1}$$

where $\mathbf{r}_i$ is the position of the i-th particle. Commonly, a particular $\mathbf{R}$ is called *configuration* or *walker*. If the probability density of finding the particles in the configuration $\mathbf{R}$

is given by

$$\begin{aligned} &\mathcal{P}(\mathbf{R}) \geqslant 0, \\ &\int d\mathbf{R}\mathcal{P}(\mathbf{R}) = 1. \end{aligned} \tag{7.2}$$

then let $\{\mathbf{R}_m : m = 1, M\}$ be a set of uncorrelated configurations distributed accordingly to $\mathcal{P}(\mathbf{R})$. We define a random variable $\mathbf{Z}_f$ by

$$\mathbf{Z}_f = \frac{[f(\mathbf{R}_1) + f(\mathbf{R}_2) + \cdots + f(\mathbf{R}_M)]}{M}. \tag{7.3}$$

The function $f(\mathbf{R})$ is any *reasonable* function with mean μ_f and variance σ_f^2 given by

$$\begin{aligned} \mu_f &= \int d\mathbf{R} f(\mathbf{R})\mathcal{P}(\mathbf{R}), \\ \sigma_f^2 &= \int d\mathbf{R}[f(\mathbf{R}) - \mu_f]^2\mathcal{P}(\mathbf{R}). \end{aligned} \tag{7.4}$$

For large enough M, $\mathbf{Z}_f$ is normally distributed with mean μ_f and standard deviation $\sigma_f/\sqrt{M}$. Thus, regardless of $\mathcal{P}(\mathbf{R})$, the mean value of a function of $\mathbf{R}$ will be a good estimator of the mean of that function with respect to $\mathcal{P}(\mathbf{R})$. Moreover, the standard deviation will decrease as $1/\sqrt{M}$, regardless of the dimension of the integral.

Suppose we want to evaluate an integral such as

$$I = \int d\mathbf{R} g(\mathbf{R}). \tag{7.5}$$

We begin by introducing an "importance function" $\mathcal{P}(\mathbf{R})$ and cast the integral in the form

$$I = \int d\mathbf{R} f(\mathbf{R})\mathcal{P}(\mathbf{R}), \tag{7.6}$$

where $f(\mathbf{R}) \equiv g(\mathbf{R})/\mathcal{P}(\mathbf{R})$. The importance function is chosen such that it obeys Eq. (7.2), hence it is a probability density. The value of I may be obtained by drawing an infinite number of vectors from $\mathcal{P}(\mathbf{R})$,

$$I = \lim_{M\to\infty} \left\{ \frac{1}{M} \sum_{m=1}^{M} f(\mathbf{R}_m) \right\}. \tag{7.7}$$

A Monte Carlo estimate of I is obtained by a large, but finite, number of samples drawn from $\mathcal{P}(\mathbf{R})$,

$$I \approx \frac{1}{M} \sum_{m=1}^{M} f(\mathbf{R}_m). \tag{7.8}$$

The variance σ_f^2/M is

$$\frac{\sigma_f^2}{M} \approx \frac{1}{M(M-1)} \sum_{m=1}^{M} \left[f(\mathbf{R}_m) - \frac{1}{M} \sum_{n=1}^{M} f(\mathbf{R}_n) \right]^2, \tag{7.9}$$

leading to error bars of $\pm\sigma_f/\sqrt{M}$ on the computed value of I. A wise choice of $\mathcal{P}(\mathbf{R})$ can significantly reduce the variance for a fixed number of samples.

7.2.1 The Metropolis algorithm

The method described in the previous section relies on evaluating multidimensional integrals by sampling probability distributions in high-dimensional spaces. Generally, normalizations of these distributions are unknown. The Metropolis rejection algorithm [132] allows us to sample complex distributions without knowledge of its normalization.

The Metropolis algorithm generates a sequence of sampling points $\mathbf{R}_m$, and it can be summarized as the following:

`(1) Start the walker at a random position` $\mathbf{R}$.

`(2) Make a trial move to a new position` $\mathbf{R}$’ `chosen from a probability density function` $T(\mathbf{R}' \leftarrow \mathbf{R})$.

`(3) Accept the trial move to` $\mathbf{R}$’ `with probability`

$$A(\mathbf{R}' \leftarrow \mathbf{R}) = \min\left(1, \frac{T(\mathbf{R} \leftarrow \mathbf{R}')\mathcal{P}(\mathbf{R}')}{T(\mathbf{R}' \leftarrow \mathbf{R})\mathcal{P}(\mathbf{R})}\right), \tag{7.10}$$

`If the trial move is accepted,` $\mathbf{R}$’ `becomes the next walker, otherwise` $\mathbf{R}$ `is the next walker.`

`(4) Return to step (2) and repeat.`

To understand how this algorithm works, let us consider an enormous number of walkers executing random walks according to the algorithm. After an equilibration period, we assume an equilibrium state in which the average number of walkers in the element $d\mathbf{R}$ is $n(\mathbf{R})d\mathbf{R}$. We also assume that the average number of walkers moving from $d\mathbf{R} \rightarrow d\mathbf{R}'$ in one time step is the same as $d\mathbf{R}' \rightarrow d\mathbf{R}$.

The probability that a walker at $\mathbf{R}$ is taken to $d\mathbf{R}'$ in one move is $d\mathbf{R}'A(\mathbf{R}' \leftarrow \mathbf{R})T(\mathbf{R}' \leftarrow \mathbf{R})$, the average number of walkers moving from $d\mathbf{R} \rightarrow d\mathbf{R}'$ in a single move is

$$d\mathbf{R}'A(\mathbf{R}' \leftarrow \mathbf{R})T(\mathbf{R}' \leftarrow \mathbf{R}) \times n(\mathbf{R})d\mathbf{R}. \tag{7.11}$$

This must be balanced with the number moving from $d\mathbf{R}' \rightarrow d\mathbf{R}$,

$$d\mathbf{R}'A(\mathbf{R}' \leftarrow \mathbf{R})T(\mathbf{R}' \leftarrow \mathbf{R})n(\mathbf{R})d\mathbf{R} = d\mathbf{R}A(\mathbf{R} \leftarrow \mathbf{R}')T(\mathbf{R} \leftarrow \mathbf{R}')n(\mathbf{R}')d\mathbf{R}'. \tag{7.12}$$

Hence, $n(\mathbf{R})$ satisfies

$$\frac{n(\mathbf{R})}{n(\mathbf{R}')} = \frac{A(\mathbf{R} \leftarrow \mathbf{R}')T(\mathbf{R} \leftarrow \mathbf{R}')}{A(\mathbf{R}' \leftarrow \mathbf{R})T(\mathbf{R}' \leftarrow \mathbf{R})}. \tag{7.13}$$

Since the ratio of acceptance probabilities are

$$\frac{A(\mathbf{R} \leftarrow \mathbf{R}')}{A(\mathbf{R}' \leftarrow \mathbf{R})} = \frac{T(\mathbf{R}' \leftarrow \mathbf{R})\mathcal{P}(\mathbf{R})}{T(\mathbf{R} \leftarrow \mathbf{R}')\mathcal{P}(\mathbf{R}')}, \tag{7.14}$$

then

$$\frac{n(\mathbf{R})}{n(\mathbf{R}')} = \frac{\mathcal{P}(\mathbf{R})}{\mathcal{P}(\mathbf{R}')}. \tag{7.15}$$

Therefore, the equilibrium walker density $n(\mathbf{R})$ is proportional to $\mathcal{P}(\mathbf{R})$, and the probability of finding any given walker in $d\mathbf{R}$ is $\mathcal{P}(\mathbf{R})d\mathbf{R}$, as required.

7.3 Variational Monte Carlo

The Variational Monte Carlo (VMC) method is based on the variational principle, and the Monte Carlo method is applied in the evaluation of the resulting multidimensional integrals [131]. It relies on a trial wave function Ψ_T which should mimic as many as possible properties of the true ground state function Ψ_0.

The expectation value of $\hat{H}$, evaluated with a trial wave function Ψ_T, provides an upper bound on the exact ground state energy E_0

$$E_V = \frac{\int \Psi_T^*(\mathbf{R})\hat{H}\Psi_T(\mathbf{R})d\mathbf{R}}{\int \Psi_T^*(\mathbf{R})\Psi_T(\mathbf{R})d\mathbf{R}} \geqslant E_0, \tag{7.16}$$

where $\mathbf{R}=(\mathbf{r}_1, \mathbf{r}_2, \ldots, \mathbf{r}_N)$ is a $3N$-dimensional vector with the coordinates of the N particles. This property can be easily verified, it is enough to consider the expansion

$$\Psi_T = \sum_i \alpha_i \Psi_i, \tag{7.17}$$

where $\{\Psi_i\}$ are the eigenstates of $\hat{H}$ with eigenvalues $\{E_i\}$. The substitution of the last expression in Eq. (7.16) shows that E_V is an upper bound of the exact ground state energy.

The application of the Monte Carlo method in the evaluation of Eq. (7.16) is accomplished by rewriting this equation in the form

$$E_V = \frac{\int |\Psi_T(\mathbf{R})|^2 \left[\Psi_T(\mathbf{R})^{-1}\hat{H}\Psi_T(\mathbf{R})\right] d\mathbf{R}}{\int |\Psi_T(\mathbf{R})|^2 d\mathbf{R}}. \tag{7.18}$$

The Metropolis algorithm then can be used to sample a set of points $\{\mathbf{R}_m : m = 1, M\}$ from the configuration-space, with probability density $\mathcal{P}(\mathbf{R}) = |\Psi_T(\mathbf{R})|^2 / \int |\Psi_T(\mathbf{R})|^2 d\mathbf{R}$. We define a "local energy" $E_L(\mathbf{R}) = \Psi_T(\mathbf{R})^{-1}\hat{H}\Psi_T(\mathbf{R})$ and at each of the points it is evaluated and average energy accumulated

$$E_V \approx \frac{1}{M}\sum_{m=1}^{M} E_L(\mathbf{R}_m). \tag{7.19}$$

The trial moves can be sampled from a Gaussian centered on the current position of the walker and the variance is chosen such that the average acceptance probability is ≈ 50%. Expectation values of operators other than the Hamiltonian can be computed in analogous ways.

7.4 Diffusion Monte Carlo

Diffusion Monte Carlo (DMC) is a method for solving the imaginary-time many-body Schrödinger equation [131]

$$-\partial_t \Phi(\mathbf{R}, t) = (\hat{H} - E_T)\Phi(\mathbf{R}, t), \tag{7.20}$$

where t is real and measures the progress in imaginary time and E_T is an energy offset. In the integral form Eq. (7.20) is rewritten as

$$\Phi(\mathbf{R}, t+\tau) = \int G(\mathbf{R} \leftarrow \mathbf{R}', \tau)\Phi(\mathbf{R}', t)d\mathbf{R}' \tag{7.21}$$

where

$$G(\mathbf{R} \leftarrow \mathbf{R}', \tau) = \langle \mathbf{R}| \exp\left[-\tau(\hat{H} - E_T)\right]|\mathbf{R}'\rangle \tag{7.22}$$

is the Green's function. It obeys the same equation as $\Phi(\mathbf{R}, t)$

$$-\partial_t G(\mathbf{R} \leftarrow \mathbf{R}', \tau) = (\hat{H} - E_T)G(\mathbf{R} \leftarrow \mathbf{R}', \tau), \tag{7.23}$$

with the initial condition $G(\mathbf{R} \leftarrow \mathbf{R}', 0) = \delta(\mathbf{R} - \mathbf{R}')$. The Green's function can be expressed as

$$G(\mathbf{R} \leftarrow \mathbf{R}', \tau) = \sum_i \Psi_i(\mathbf{R}) \exp\left\{-\tau(E_i - E_T)\right\}\Psi_i^*(\mathbf{R}'), \tag{7.24}$$

where $\{\Psi_i\}$ and $\{E_i\}$ are the complete set of eigenstates and eigenenergies of $\hat{H}$, respectively. As $\tau \to \infty$, the operator $\exp\{-\tau(E_i - E_T)\}$ projects out the lowest eigenstate $|\Psi_0\rangle$ that has non-zero overlap with an initial state $|\Phi_{\text{init}}\rangle$

$$\begin{aligned}\lim_{\tau\to\infty} \langle \mathbf{R}| \exp\left[-\tau(\hat{H} - E_T)\right]|\Phi_{\text{init}}\rangle &= \lim_{\tau\to\infty} \int G(\mathbf{R} \leftarrow \mathbf{R}', \tau)\Phi_{\text{init}}(\mathbf{R}')d\mathbf{R}' \\ &= \lim_{\tau\to\infty} \sum_i \Psi_i(\mathbf{R}) \exp\left[-\tau(E_i - E_T)\right]\langle \Psi_i|\Phi_{\text{init}}\rangle \end{aligned} \tag{7.25}$$

By adjusting $E_T = E_0$ and taking the limit $\tau \to \infty$ only the $|\Psi_0\rangle$ state is projected, since the higher states are all exponentially damped because their energies are higher than E_0.

If we neglect potential terms in Eq. (7.20) it simplifies to

$$\partial_t \Phi_0(\mathbf{R}, t) = \frac{\hbar^2}{2m} \sum_{i=1}^{N} \nabla_i^2 \Phi_0(\mathbf{R}, t). \tag{7.26}$$

The Green's function for this problem is

$$G_0(\mathbf{R} \leftarrow \mathbf{R}', \tau) = \left[\frac{m}{2\pi\hbar^2\tau}\right]^{3N/2} \exp\left[-\frac{m(\mathbf{R} - \mathbf{R}')^2}{2\hbar^2\tau}\right]. \tag{7.27}$$

If we consider the Hamiltonian with both kinetic and potential terms, the exact Green's function is known only for a few special cases. The Trotter-Suzuki formula can be used to obtain an approximation of the Green's function. For two operators $\hat{A}$ and $\hat{B}$

$$e^{-\tau(\hat{A}+\hat{B})} = e^{-\tau\hat{B}/2}e^{-\tau\hat{A}}e^{-\tau\hat{B}/2} + \mathcal{O}(\tau^3). \tag{7.28}$$

If $\hat{A} = \hat{T}$, where $\hat{T}$ is the kinetic energy operator, and $\hat{B} = \hat{V} - E_T$, $\hat{V}$ being the potential energy operator, we have

$$G(\mathbf{R} \leftarrow \mathbf{R}', \tau) = \langle \mathbf{R}|e^{-\tau(\hat{T}+\hat{V}-E_T)}|\mathbf{R}'\rangle \approx e^{-\tau[V(\mathbf{R})-E_T]/2}\langle \mathbf{R}|e^{-\tau\hat{T}}|\mathbf{R}'\rangle e^{-\tau[V(\mathbf{R}')-E_T]/2}. \tag{7.29}$$

The approximate Green's function for small τ is therefore

$$G(\mathbf{R} \leftarrow \mathbf{R}', \tau) = G_0(\mathbf{R} \leftarrow \mathbf{R}', \tau)\exp\left[-\tau[V(\mathbf{R}) + V(\mathbf{R}') - 2E_T]/2\right], \tag{7.30}$$

and the error is proportional to τ^3. The exponential

$$P = \exp\left[-\tau[V(\mathbf{R}) + V(\mathbf{R}') - 2E_T]/2\right] \tag{7.31}$$

is a time-depending reweighting of the Green's function. This change of normalization is incorporated in the calculations by using the *branching* algorithm, in which P determines the number of surviving walkers in each step. The procedure is:

`(1) If` $P < 1$ `the walker continues its evolution with probability` P.

`(2) If` $P \geqslant 1$ `the walker continues and, in addition, a new walker is created in the same position with probability` $P - 1$.

The number M_{new} of walkers evolving to the next step at a given position can be coded as

$$M_{\text{new}} = \text{INT}(P + \xi), \tag{7.32}$$

where INT is the integer part of a real number and ξ is a random number drawn from a uniform distribution in the interval [0,1]. The energy offset E_T is used to control the population of walkers. By adjusting E_T the total number of walkers fluctuates around a desirable value.

The ground state energy can be calculated by the mixed estimate

$$\langle H\rangle_{\text{mix}} = \frac{\langle \Psi_T|\hat{H}|\Phi(t\to\infty)\rangle}{\langle \Psi_T|\Phi(t\to\infty)\rangle} = E_0\frac{\langle \Psi_T|\Phi(t\to\infty)\rangle}{\langle \Psi_T|\Phi(t\to\infty)\rangle} = E_0 \tag{7.33}$$

7.4.1 Importance sampling

The simple DMC algorithm described so far is spectacularly inefficient. The main reason is that P from Eq. (7.31) may fluctuate wildly between steps. This difficulty is overcome by carrying out an *importance-sampling transformation* using a trial wavefunction $\Psi_T(\mathbf{R})$. Let us multiply Eq. (7.20) by $\Psi_T(\mathbf{R})$ and introduce $f(\mathbf{R}, t) = \Phi(\mathbf{R}, t)\Psi_T(\mathbf{R})$. After some manipulations,

$$-\partial f(\mathbf{R}, t) = -\frac{1}{2}\nabla^2 f(\mathbf{R}, t) + \nabla \cdot [\mathbf{v}_D(\mathbf{R}) f(\mathbf{R}, t)] + [E_L(\mathbf{R}) - E_T] f(\mathbf{R}, t), \qquad (7.34)$$

where $\nabla = (\nabla_1, \ldots, \nabla_N)$, $\mathbf{v}_D(\mathbf{R})$ is the $3N$-dimensional drift velocity,

$$\mathbf{v}_D(\mathbf{R}) = \nabla \ln |\Psi_T(\mathbf{R})| = \Psi_T(\mathbf{R})^{-1} \nabla \Psi_T(\mathbf{R}). \qquad (7.35)$$

The integral equation becomes

$$f(\mathbf{R}, t + \tau) = \int \tilde{G}(\mathbf{R} \leftarrow \mathbf{R}', \tau) f(\mathbf{R}', t) d\mathbf{R}', \qquad (7.36)$$

where

$$\tilde{G}(\mathbf{R} \leftarrow \mathbf{R}', \tau) \equiv \Psi_T(\mathbf{R}) G(\mathbf{R} \leftarrow \mathbf{R}', \tau) \Psi_T(\mathbf{R}')^{-1}. \qquad (7.37)$$

The short-time approximation to $\tilde{G}(\mathbf{R} \leftarrow \mathbf{R}', \tau)$ is

$$\tilde{G}(\mathbf{R} \leftarrow \mathbf{R}', \tau) \approx G_d(\mathbf{R} \leftarrow \mathbf{R}', \tau) G_b(\mathbf{R} \leftarrow \mathbf{R}', \tau), \qquad (7.38)$$

where

$$\begin{aligned} G_d(\mathbf{R} \leftarrow \mathbf{R}', \tau) &= (2\pi\tau)^{-3N/2} \exp\left[-\frac{[\mathbf{R} - \mathbf{R}' - \tau \mathbf{v}_D(\mathbf{R}')]^2}{2\tau}\right], \\ G_b(\mathbf{R} \leftarrow \mathbf{R}', \tau) &= \exp\left\{-\tau[E_L(\mathbf{R}) + E_L(\mathbf{R}') - 2E_T]/2\right\}. \qquad (7.39) \end{aligned}$$

Importance sampling has several consequences. The density of walkers is increased (decreased) where Ψ_T is large (small), because $\mathbf{v}_D(\mathbf{R})$ carries the walkers along in the direction of increasing $|\Psi_T|$. Moreover, the exponent in the reweighting term contains the local energy, instead of the potential. This is crucial because, for a good trial wavefunction, the local energy is close to the ground-state energy and approximately constant, thus diminishing population fluctuations.

Importance sampling is also extremely helpful in fulfilling the fixed-node constraint. Whenever a walker approaches the nodal surface, the drift velocity grows and pushes it away. Despite that, in the event of a walker crossing the nodal surface, the walker is eliminated.

Note that the trial wave function $\Psi_T(\mathbf{R})$ is used in three different ways: approximation of the ground state in the VMC calculation, importance function and for avoiding the sign problem as we will see in the next section.

7.4.2 The fixed-node approximation

So far we have assumed that the wavefunction is positive everywhere, which is not true for fermions due to the antisymmetry requirement. Unfortunately, DMC can only handle positive distributions. For example, the denominator of a matrix element such as the mixed energy contains the sum $\sum_{i=1}^{N_s} P_i \Psi_T(\mathbf{R}_i)$. If the path of sample i has crossed nodes of Ψ_T an odd number of times, the contribution to the sum will be negative. For large times, the contributions of the negative paths cancel almost completely the contributions of the paths that have not crossed the nodes (or crossed an even number of times). The signal dies out exponentially compared to the noise.

Fixed-node DMC [133] is an alternative method to overcome the sign problem. A trial many-body wavefunction is chosen and used to define a trial many-body nodal surface. In a tridimensional system with N fermions, the wavefunction depends on $3N$ variables and the trial nodal surface is a $(3N-1)$-dimensional surface. If a walker in a proposed move crosses the nodal surface, it is deleted.

The fixed-node DMC algorithm then produces the lowest-energy state given the nodal surface. Therefore, fixed-node DMC may be regarded as a variational method that gives exact results provided that the nodal surface is exact.

7.4.3 Extrapolated estimators

Expectations of quantities that do not commute with the Hamiltonian can be calculated using a combination of mixed and variational estimators [131],

$$\langle\Phi|\hat{S}|\Phi\rangle \approx 2\langle\Phi|\hat{S}|\Psi_T\rangle - \langle\Psi_T|\hat{S}|\Psi_T\rangle + \mathcal{O}\left[(\Phi-\Psi_T)^2\right], \tag{7.40}$$

where $\hat{S}$ is the operator related to some physical quantity of interest. For nonnegative quantities, for example the density, another possibility is

$$\langle\Phi|\hat{S}|\Phi\rangle \approx \frac{\langle\Phi|\hat{S}|\Psi_T\rangle^2}{\langle\Psi_T|\hat{S}|\Psi_T\rangle} + \mathcal{O}\left[(\Phi-\Psi_T)^2\right]. \tag{7.41}$$

Such combinations of VMC and DMC estimators are called extrapolated estimators.

7.4.4 QMC on parallel computers

Monte Carlo calculations are intrinsically parallel. The calculations performed on each walker are independent, and may be carried on in parallel. QMC calculations are very suitable for parallel architecture machines, which offer orders of magnitude more computational power.

The most common paradigm used in QMC on massively parallel processors is the "master-slave", with one processor orchestrating the whole simulation. In VMC simulations, the argument for using parallel computers is even more compelling. Each process independently runs a simulation and accumulates its own set of observables; at the end of the run the master processor gathers and averages the results. The situation is similar in DMC simulations, however some inter-process communication is required during the simulation to control the population of walkers and perform the load balance between processes.

7.5 Vortex line

7.5.1 Introduction

Since the first observations of quantized vortices in superfluid ^{4}He a large body of experimental and theoretical work has been carried out concerning bosonic systems [134, 135]. On the other hand, the discovery of vortex lattices in a strongly interacting rotating Fermi gas of ^{6}Li [28] was a milestone in the study of superfluidity in cold Fermi gases. Many aspects of the core region of the quantum vortex remain to be studied.

A vortex line consists of an extended irrotational flow field, with a core region where the vorticity is concentrated, Eq. (D.6); in appendix D we introduce some useful concepts in classical hydrodynamics concerning vortices. The quantization of the flow manifests itself in the quantized units $h/(2M)$ of circulation, Eq. (D.19), where h is Planck's constant and M is the mass of the fermion. Astonishingly, there is no evidence for stable quantized vortices with more than one unit of circulation. Many questions remain to be answered concerning the structure of the vortex core for fermions. The purpose of our study is to present results of quantities that may help to shed light to these unsolved questions. First, we wish to study the properties of the ground state of cold dilute spin-1/2 unitary Fermi gases in a cylindrical container. Then we proceed to the investigation of the excited state with the presence of a vortex line.

The potential of interaction between fermions of the unlike spins is presented in 7.5.2. Sec. 7.5.3 contains the information on the wavefunctions we constructed to simulate the systems of interest. We begin by solving Schrodinger's equation in cylindrical coordinates in Sec. 7.5.3; we particle-project the BCS wavefunction in Sec. 7.5.3; the wavefunctions for the ground state and vortex line excitation are presented in Secs. 7.5.3 and 7.5.3, respectively; finally we comment on parameter optimization in Sec. 7.5.3.

7.5.2 Potential

The model we considered consists of A fermions in a cylinder of radius $\mathcal{R}$ and height $\mathcal{L}$. We considered periodic boundary conditions in the axis direction (z direction) and rigid walls. Fermions of the same spin do not feel the effects of interaction because it is short range and Pauli exclusion principle dominates. We must use a potential with the following characteristics:

(i) It is attractive with very short range, as we assume the dilute limit;

(ii) the details of the potential do not matter, in principle we can think of it as an attractive δ-function potential;

(iii) the potential needs to be adjusted such that we can reproduce the regime of $ak_F \to \infty$.

For different spins we have assumed a central potential $V(r)$ that has those desirable features

$$V(r) = -v_0 \frac{2\hbar^2}{M} \frac{\mu^2}{\cosh^2(\mu r)}, \tag{7.42}$$

where v_0 is adjusted to obtain the desired value of ak_F and μ controls the effective range R_{eff} of the potential. We chose $v_0 = 1$ which implies $a = \pm\infty$ and $R_{eff} = 2/\mu$. The calculations were performed with $\mu r_0 = 24$.

7.5.3 Wavefunctions

The trial wave function for this problem must have several characteristics. It must reflect the fact that fermions with attractive interaction can form bound Cooper pairs in the ground state. We also desire to have the possibility to vary the nodal surface, in order to minimize the energy. Finally, the wave function must obey the boundary conditions of the cylindrical container.

Schrödinger's equation in cylindrical coordinates

We begin by looking at the solution of Schrodinger's equation for a free particle in a cylinder of radius $\mathcal{R}$ and height $\mathcal{L}$. We wish to solve

$$-\frac{\hbar^2}{2M}\left(\frac{\partial^2\Psi_{nmp}}{\partial\rho^2} + \frac{1}{\rho}\frac{\partial\Psi_{nmp}}{\partial\rho} + \frac{1}{\rho^2}\frac{\partial^2\Psi_{nmp}}{\partial\varphi^2} + \frac{\partial^2\Psi_{nmp}}{\partial z^2}\right) = E_{nmp}\Psi_{nmp}, \tag{7.43}$$

where (ρ, φ, z) are the usual cylindrical coordinates. We suppose a separable solution of the form $\Psi_{nmp}(\rho, \varphi, z) = P(\rho)\Phi(\varphi)Z(z)$, subject to the boundary conditions

$$\begin{gathered}\Psi_{nmp}(\rho = \mathcal{R}, \varphi, z) = 0, \\ \Psi_{nmp}(\rho, \varphi, z) = \Psi_{nmp}(\rho, \varphi + 2\pi, z), \\ \Psi_{nmp}(\rho, \varphi, z) = \Psi_{nmp}(\rho, \varphi, z + \mathcal{L}),\end{gathered} \tag{7.44}$$

and that it is finite at $\rho = 0$. The functions $\Phi(\varphi)$ and $Z(z)$ are elementary complex exponential functions. The equation for $P(\rho)$ is

$$\rho^2 P''(\rho) + \rho P'(\rho) + (k_{mp}\rho^2 - m^2)P(\rho) = 0, \tag{7.45}$$

where k_{mp} is a constant dependent on the labels m and p. The solutions of this equation, with the imposed boundary conditions, are the Bessel functions of first-kind $J_m(k_{mp}\rho)$ such that $k_{mp}\mathcal{R} = j_{mp}$, j_{mp} being the p-th zero of J_m.

The total solution is

$$\Psi_{nmp}(\rho, \varphi, z) = \mathcal{N}_{mp} J_m\left(j_{mp}\rho/\mathcal{R}\right) \exp\left[i(k_z z + m\varphi)\right], \tag{7.46}$$

where $\mathcal{N}_{mp}$ is a normalization constant dependent of m, p, $\mathcal{R}$ and $\mathcal{L}$; and $k_z = 2\pi n/\mathcal{L}$. The quantum numbers can take the values $n = 0, \pm1, \pm2, \ldots$; $m = 0, \pm1, \pm2, \ldots$; and $p = 1, 2, 3, \ldots$. The eigenenergies are

$$E_{nmp} = \frac{\hbar^2}{2M}\left[\left(\frac{j_{mp}}{\mathcal{R}}\right)^2 + \left(\frac{2\pi n}{\mathcal{L}}\right)^2\right]. \tag{7.47}$$

The set of states $\{\Psi_{nmp}\}$ with corresponding energies $\{E_{nmp}\}$ is a complete set, therefore we can use it to expand our trial wave function.

BCS wavefunction projected to a fixed number of particles

The BCS wave function is used to describe the bound Cooper pairs in the ground state. We write

$$\begin{aligned} |BCS\rangle_\theta &= \prod_{\mathbf{k}}(u_{\mathbf{k}} + e^{i\theta} v_{\mathbf{k}} \hat{a}^\dagger_{\mathbf{k}\uparrow} \hat{a}^\dagger_{\mathcal{T}\mathbf{k}\downarrow})|0\rangle, \\ u^2_{\mathbf{k}} + v^2_{\mathbf{k}} &= 1, \end{aligned} \tag{7.48}$$

where $u_{\mathbf{k}}$ and $v_{\mathbf{k}}$ are real numbers, $\mathbf{k}$ is the wavenumber vector, $\mathcal{T}$ is the time reversal operator[1] and $|0\rangle$ represents the vacuum. However this function has broken particle number symmetry, i.e., it is not an eigenstate of the particle number operator. In fact, expanding the wave function we can write

$$|BCS\rangle_\theta = |0\rangle + e^{i\theta}\hat{\mathcal{P}}^\dagger|0\rangle + e^{i2\theta}(\hat{\mathcal{P}}^\dagger)^2|0\rangle + e^{i3\theta}(\hat{\mathcal{P}}^\dagger)^3|0\rangle + \ldots, \tag{7.49}$$

where $\hat{\mathcal{P}}^\dagger = \sum_{\mathbf{k}}(v_{\mathbf{k}}/u_{\mathbf{k}})\hat{a}^\dagger_{\mathbf{k}\uparrow}\hat{a}^\dagger_{\mathcal{T}\mathbf{k}\downarrow}$ is the pair creation operator. The component which corresponds to A particles, $\mathcal{M} = A/2$ pairs, is

$$|BCS\rangle_A = \frac{1}{2\pi}\int_0^{2\pi} e^{-i\theta\mathcal{M}}|BCS\rangle_\theta d\theta = (\hat{\mathcal{P}}^\dagger)^{\mathcal{M}}|0\rangle. \tag{7.50}$$

---

[1] If we consider plane waves in a cube, $\mathcal{T}\mathbf{k} = -\mathbf{k}$. In general, $\mathcal{T}\mathbf{k}$ is not $-\mathbf{k}$ in the cylindrical geometry.

We wish to write the BCS function for a fixed number of particles as a function of pair wavefunctions. We proceed analogously to [136], considering our cylindrical geometry. We begin by considering the antisymmetric position- and spin-projected states

$$\begin{aligned} \mathcal{A}|\mathbf{r}_1, s_1, \ldots, \mathbf{r}_A, s_A\rangle &= \frac{1}{A!} \sum_{\text{permutations P}} (-1)^P |P(\mathbf{r}_1, s_1, \ldots, \mathbf{r}_A, s_A)\rangle \\ &= \frac{1}{\sqrt{A!}} \hat{\psi}^\dagger_{s_1}(\mathbf{r}_1) \ldots \hat{\psi}^\dagger_{s_A}(\mathbf{r}_A)|0\rangle, \end{aligned} \tag{7.51}$$

where P represents the permutation of particle labels, $(-1)^P$ is 1 (-1) for even (odd) permutations and $\hat{\psi}^\dagger_{s_i}(\mathbf{r}_i)$ is the fermionic creation operator for the i-th particle of spin s_i at $\mathbf{r}_i$. The position and momentum creation operators are related by

$$\hat{a}^\dagger_{\mathbf{k}s} = \int_{-\mathcal{L}/2}^{\mathcal{L}/2} dz \int_0^{\mathcal{R}} d\rho\, \rho \int_0^{2\pi} d\varphi\, \mathcal{N}_{mp} J_m\left(j_{mp}\rho/\mathcal{R}\right) \exp\left[i(k_z z + m\varphi)\right] \hat{\psi}^\dagger_s(\mathbf{r}), \tag{7.52}$$

where we should note that specifying one $\mathbf{k}$ is equivalent to specifying the quantum numbers (n, m, p) of Eq. (7.46), $k_z = 2\pi n/\mathcal{L}$.

The standard BCS state is normalized according to Eq. (7.48). Since we will project the part with A particles, even if we begin with a normalized state, the projected part will no longer be normalized. Thus, there is no advantage to begin with a normalized state and we divide each term by the corresponding $u_{\mathbf{k}}$. If one or more are zero, it means that we should drop the 1 term for that $\mathbf{k}$ since it is always filled. Hence

$$|BCS\rangle_\theta = \prod_{\mathbf{k}} \left[1 + \frac{v_{\mathbf{k}}}{u_{\mathbf{k}}} \hat{a}^\dagger_{\mathbf{k}\uparrow} \hat{a}^\dagger_{\mathcal{T}\mathbf{k}\downarrow}\right] |0\rangle. \tag{7.53}$$

The particle-projected BCS wavefunction can be cast in the form

$$\Psi_{BCS}(\mathbf{R}, S) = \langle \mathbf{R}, S|BCS\rangle = \frac{1}{\sqrt{A!}} \left[\langle 0|\hat{\psi}_{s_A}(\mathbf{r}_A) \ldots \hat{\psi}_{s_1}(\mathbf{r}_1)\right] \prod_{\mathbf{k}} \left[1 + \frac{v_{\mathbf{k}}}{u_{\mathbf{k}}} \hat{a}^\dagger_{\mathbf{k}\uparrow} \hat{a}^\dagger_{\mathcal{T}\mathbf{k}\downarrow}\right] |0\rangle. \tag{7.54}$$

We use Wick's theorem [137] to change from the given order to the normal order. Contracting $\psi_s(\mathbf{r})$ and $\hat{a}^\dagger_{\mathbf{k}s'}$ yields

$$\overbracket{\psi_s(\mathbf{r}) \hat{a}^\dagger_{\mathbf{k}s'}} = \mathcal{N}_{mp} J_m\left(j_{mp}\rho/\mathcal{R}\right) \exp\left[i(k_z z + m\varphi)\right] \delta_{ss'}. \tag{7.55}$$

A careful analysis of Eq. (7.54) shows that one particular contraction occurs when $\psi_{s_1}(\mathbf{r}_1)$ and $\psi_{s_2}(\mathbf{r}_2)$ contract with a pair in $\mathbf{k}_1$; $\psi_{s_3}(\mathbf{r}_3)$ and $\psi_{s_4}(\mathbf{r}_4)$ contract with another pair in

$\mathbf{k}_2$; and so forth:

$$
\begin{aligned}
\overbracket{\psi_{s_2}(\mathbf{r}_2)\psi_{s_1}(\mathbf{r}_1)\hat{a}^{\dagger}_{\mathbf{k}_1\uparrow}\hat{a}^{\dagger}_{\mathcal{T}\mathbf{k}_1\downarrow}} &= (-1)^{m_1}\mathcal{N}^2_{m_1p_1}J_{m_1}\left(\frac{j_{m_1p_1}\rho_1}{\mathcal{R}}\right)J_{m_1}\left(\frac{j_{m_1p_1}\rho_2}{\mathcal{R}}\right)\times \\
&\exp\left\{i\left[k_{z_1}(z_1-z_2)+m_1(\varphi_1-\varphi_2)\right]\right\}\langle s_1s_2|\uparrow\downarrow\rangle; \\
\overbracket{\psi_{s_4}(\mathbf{r}_4)\psi_{s_3}(\mathbf{r}_3)\hat{a}^{\dagger}_{\mathbf{k}_2\uparrow}\hat{a}^{\dagger}_{\mathcal{T}\mathbf{k}_2\downarrow}} &= (-1)^{m_2}\mathcal{N}^2_{m_2p_2}J_{m_2}\left(\frac{j_{m_2p_2}\rho_3}{\mathcal{R}}\right)J_{m_2}\left(\frac{j_{m_2p_2}\rho_4}{\mathcal{R}}\right)\times \\
&\exp\left\{i\left[k_{z_2}(z_3-z_4)+m_2(\varphi_3-\varphi_4)\right]\right\}\langle s_3s_4|\uparrow\downarrow\rangle; \\
&\vdots \\
\overbracket{\psi_{s_A}(\mathbf{r}_A)\psi_{s_{A-1}}(\mathbf{r}_{A-1})\hat{a}^{\dagger}_{\mathbf{k}_{A/2}\uparrow}\hat{a}^{\dagger}_{\mathcal{T}\mathbf{k}_{A/2}\downarrow}} &= (-1)^{m_{A/2}}\mathcal{N}^2_{m_{A/2}p_{A/2}}J_{m_{A/2}}\left(\frac{j_{m_{A/2}p_{A/2}}\rho_{A-1}}{\mathcal{R}}\right)\times \\
&J_{m_{A/2}}\left(\frac{j_{m_{A/2}p_{A/2}}\rho_A}{\mathcal{R}}\right)\times \\
&\exp\left\{i\left[k_{z_{A/2}}(z_{A-1}-z_A)+m_{A/2}(\varphi_{A-1}-\varphi_A)\right]\right\}\times \\
&\langle s_{A-1}s_A|\uparrow\downarrow\rangle. \qquad (7.56)
\end{aligned}
$$

This gives a term

$$
\begin{aligned}
&\frac{v_{\mathbf{k}_1}}{u_{\mathbf{k}_1}}(-1)^{m_1}\mathcal{N}^2_{m_1p_1}J_{m_1}\left(\frac{j_{m_1p_1}\rho_1}{\mathcal{R}}\right)J_{m_1}\left(\frac{j_{m_1p_1}\rho_2}{\mathcal{R}}\right)\times \\
&\exp\left\{i\left[k_{z_1}(z_1-z_2)+m_1(\varphi_1-\varphi_2)\right]\right\}\langle s_1s_2|\uparrow\downarrow\rangle\times \\
&\frac{v_{\mathbf{k}_2}}{u_{\mathbf{k}_2}}(-1)^{m_2}\mathcal{N}^2_{m_2p_2}J_{m_2}\left(\frac{j_{m_2p_2}\rho_3}{\mathcal{R}}\right)J_{m_2}\left(\frac{j_{m_2p_2}\rho_4}{\mathcal{R}}\right)\times \\
&\exp\left\{i\left[k_{z_2}(z_3-z_4)+m_2(\varphi_3-\varphi_4)\right]\right\}\langle s_3s_4|\uparrow\downarrow\rangle\times \\
&\ldots\frac{v_{\mathbf{k}_{A/2}}}{u_{\mathbf{k}_{A/2}}}(-1)^{m_{A/2}}\mathcal{N}^2_{m_{A/2}p_{A/2}}J_{m_{A/2}}\left(\frac{j_{m_{A/2}p_{A/2}}\rho_{A-1}}{\mathcal{R}}\right)J_{m_{A/2}}\left(\frac{j_{m_{A/2}p_{A/2}}\rho_A}{\mathcal{R}}\right)\times \\
&\exp\left\{i\left[k_{z_{A/2}}(z_{A-1}-z_A)+m_{A/2}(\varphi_{A-1}-\varphi_A)\right]\right\}\langle s_{A-1}s_A|\uparrow\downarrow\rangle, \qquad (7.57)
\end{aligned}
$$

where we have dropped the overall normalization. Choosing different $\mathbf{k}$ terms to contract with corresponds to summing over all values of $\mathbf{k}_1$, $\mathbf{k}_2$, etc., with the constraint that no two of the $\mathbf{k}_i$ should be equal,

$$
\begin{aligned}
&\left[\sum_{\mathbf{k}}\frac{v_{\mathbf{k}}}{u_{\mathbf{k}}}(-1)^m\mathcal{N}^2_{mp}J_m\left(\frac{j_{mp}\rho_1}{\mathcal{R}}\right)J_m\left(\frac{j_{mp}\rho_2}{\mathcal{R}}\right)\exp\left\{i\left[k_z(z_1-z_2)+m(\varphi_1-\varphi_2)\right]\right\}\left[\langle s_1s_2|\uparrow\downarrow\rangle\right]\right]\times \\
&\left[\sum_{\mathbf{k}}\frac{v_{\mathbf{k}}}{u_{\mathbf{k}}}(-1)^m\mathcal{N}^2_{mp}J_m\left(\frac{j_{mp}\rho_3}{\mathcal{R}}\right)J_m\left(\frac{j_{mp}\rho_4}{\mathcal{R}}\right)\exp\left\{i\left[k_z(z_3-z_4)+m(\varphi_3-\varphi_4)\right]\right\}\left[\langle s_3s_4|\uparrow\downarrow\rangle\right]\right]\times \\
&\ldots\ \text{(subject to the constraint that no two of the } \mathbf{k}_i \text{ should be equal).} \qquad (7.58)
\end{aligned}
$$

Choosing other contractions completely antisymmetrizes this form, and we can include all terms in the $\mathbf{k}$ sums since these cancel when antisymmetrized. The result is

$$\psi_{BCS}(\mathbf{R},S)=\mathcal{A}[\phi(\mathbf{r}_1,s_1,\mathbf{r}_2,s_2)\phi(\mathbf{r}_3,s_3,\mathbf{r}_4,s_4)\ldots\phi(\mathbf{r}_{\mathcal{A}-1},s_{A-1},\mathbf{r}_{\mathcal{A}},s_A)], \tag{7.59}$$

where, for example,

$$\begin{aligned}\phi(\mathbf{r}_1,s_1,\mathbf{r}_2,s_2)=\sum_{\mathbf{k}}\frac{v_{\mathbf{k}}}{u_{\mathbf{k}}}(-1)^m\mathcal{N}^2_{mp}J_m\left(j_{mp}\rho_1/\mathcal{R}\right)J_m\left(j_{mp}\rho_2/\mathcal{R}\right)\times\\ \exp\left\{i\left[k_z(z_1-z_2)+m(\varphi_1-\varphi_2)\right]\right\}\left[\langle s_1s_2|\uparrow\downarrow\rangle\right].\end{aligned} \tag{7.60}$$

Since the many-body antisymmetrizer will interchange the particles in ϕ, we usually explicitly antisymmetrize ϕ. Up to an unimportant normalization we get

$$\begin{aligned}\phi(\mathbf{r}_1,s_1,\mathbf{r}_2,s_2)=\sum_{\mathbf{k}}\frac{v_{\mathbf{k}}}{u_{\mathbf{k}}}(-1)^m\mathcal{N}^2_{mp}J_m\left(j_{mp}\rho_1/\mathcal{R}\right)J_m\left(j_{mp}\rho_2/\mathcal{R}\right)\times\\ \exp\left\{i\left[k_z(z_1-z_2)+m(\varphi_1-\varphi_2)\right]\right\}\left[\langle s_1s_2|\uparrow\downarrow\rangle-\langle s_1s_2|\downarrow\uparrow\rangle\right],\end{aligned} \tag{7.61}$$

demonstrating singlet pairing.

Often we want to simulate systems that are not fully paired. We include unpaired particles in specific states (n,m,p) by multiplying the $|BCS\rangle$ state by a product (or linear combinations) of creation operators for those states. The change in the previously described procedure is that these creation operators must be contracted with one of the $\psi_s(\mathbf{r})$, or the result is zero. For q pairs and o occupied single-particle states, thus $A=2q+o$, we have

$$\psi_{BCS}(\mathbf{R},S)=\mathcal{A}[\phi_{12}\phi_{34}\ldots\phi_{2q-1,2q}\;\psi_1\ldots\psi_o]. \tag{7.62}$$

Ground state

For the ground state of fermions in a cylindrical container, we use Eq. (7.59), or Eq. (7.62) if we have unpaired particles. We define $\alpha_{\mathbf{k}}\equiv v_{\mathbf{k}}/u_{\mathbf{k}}$ as our real variational parameters. The momentum vectors in the cylinder are quantized and the system has a shell structure with closures which depend on $\mathcal{R}$ and $\mathcal{L}$, see Eq. (7.47).

In the present calculations, we assume the pair wave function $\phi(\mathbf{r},\mathbf{r}')$ to be

$$\begin{aligned}\phi(\mathbf{r},\mathbf{r}')=\tilde{\beta}(\mathbf{r},\mathbf{r}')+\sum_{I\leqslant I_C}\alpha_I\mathcal{N}^2_{mp}(-1)^mJ_m\left(j_{mp}\rho/\mathcal{R}\right)J_m\left(j_{mp}\rho'/\mathcal{R}\right)\times\\ \exp\left\{i\left[k_z(z-z')+m(\varphi-\varphi')\right]\right\},\end{aligned} \tag{7.63}$$

where we adopted hereafter primed indexes to denote spin-down particles and unprimed ones to refer to spin-up particles and we omit the spin part. Here I_C is a cutoff shell number and we assume that contributions of shells with $I > I_C$ are present in the $\tilde{\beta}(\mathbf{r}, \mathbf{r}')$ function, given by

$$\tilde{\beta}(\mathbf{r}, \mathbf{r}') = \begin{cases} \mathcal{N}_{01}^2 J_0\left(j_{01}\rho/\mathcal{R}\right) J_0\left(j_{01}\rho'/\mathcal{R}\right) \times & \\ \quad (\beta(r) + \beta(\mathcal{L} - r) - 2\beta(\mathcal{L}/2)) & \text{for} \quad r \leqslant \mathcal{L}/2 \\ \qquad 0 & \text{for} \quad r > \mathcal{L}/2 \end{cases}$$

and

$$\beta(r) = [1 + \gamma br][1 - e^{-cbr}]\frac{e^{-br}}{cbr}, \tag{7.64}$$

where $r = |\mathbf{r} - \mathbf{r}'|$ and b, c and γ are variational parameters. It is convenient to require $\partial\tilde{\beta}/\partial r = 0$ at $r = 0$ because the local energy has terms like $(1/r)(\tilde{\beta}/\partial r)$ which would have large fluctuations at $r = 0$ otherwise. The factor $[1 - e^{-cbr}]$ cuts off $1/cbr$ dependence of β at $br < 1/c$. The set of parameters which yielded the lowest energy was $c = 10$, $\gamma = 5$ and b =0.5.

We also included an one-body Jastrow factor of the form

$$\chi(\rho_i) = \left(\frac{a}{\sqrt{2\pi\sigma^2}} \exp\left\{\frac{(\rho_i - \bar{\rho})^2}{2\sigma^2}\right\} + \nu\right)^{\lambda}, \tag{7.65}$$

where a, σ, $\bar{\rho}$, ν and λ are variational parameters. The correlation between antiparallel spins is included in the two-body Jastrow factor $f(r_{ij'})$. It is obtained from solutions of the two-body Schrodinger equation

$$\left[-\frac{1}{M}\nabla^2 + V(r)\right] f(r < d) = \lambda f(r < d), \tag{7.66}$$

where d is a variational parameter. The boundary conditions are $f(r > d) = 1$ and $f'(r = d) = 0$ [138].

The total wave function for the ground state of fermions in a cylindrical container is

$$\psi_0(\mathbf{R}) = \prod_k \chi(\rho_k) \prod_{i,j'} f(r_{ij'})\psi_{BCS}(\mathbf{R}), \tag{7.67}$$

with $\psi_{BCS}(\mathbf{R})$ given by Eq. (7.59) (or Eq. (7.62) if we have unpaired particles) and the pairing function given by Eq. (7.63).

Vortex line

In order to introduce the vortex line in the system we need to have Cooper pairs which are eigenstates of L_z with eigenvalues $\pm\hbar$. This can be accomplished by coupling single particle states that have the quantum number m with $(-m+1)$. The proposed pair wave function is

$$\begin{aligned}
&\phi_V(\mathbf{r},\mathbf{r}') = \tilde{\beta}(\mathbf{r},\mathbf{r}') + \sum_{i=1}^{K} \tilde{\alpha}_i \mathcal{N}_{m;p}\mathcal{N}_{-m+1;p}\, \{ \\
&J_m\left(\frac{j_{mp}\rho}{\mathcal{R}}\right) J_{-m+1}\left(\frac{j_{-m+1;p}\rho'}{\mathcal{R}}\right) \exp\{i\left[k_z(z-z') + m\varphi + (-m+1)\varphi'\right)]\} + \\
&J_m\left(\frac{j_{mp}\rho'}{\mathcal{R}}\right) J_{-m+1}\left(\frac{j_{-m+1;p}\rho}{\mathcal{R}}\right) \exp\{i\left[k_z(z'-z) + m\varphi' + (-m+1)\varphi\right)]\}\}\,, \quad (7.68)
\end{aligned}$$

where K is the number of single particle states with quantum numbers (n, m, p) being paired with $(-n, -m+1, p)$. A few words are in order regarding this choice of coupling. We do not wish to have a winding number in the z direction, that is why we have the quantum number n for a particle and the time-reversed $-n$ for the other. Also, the largest contribution was assume to be from states with the same quantum number p for the radial part. Another important property of the pair function is being symmetric under exchange of two particles, because we are considering the spin part as singlet. The total wave function is

$$\begin{aligned}
\psi_1(\mathbf{R}) &= \mathcal{A}[\phi_V(\mathbf{r}_1,\mathbf{r}_{1'})\phi_V(\mathbf{r}_2,\mathbf{r}_{2'})\ldots\phi_V(\mathbf{r}_{\mathcal{M}},\mathbf{r}_{\mathcal{M}'})], \\
\psi_V(\mathbf{R}) &= \prod_k \chi(\rho_k) \prod_{i,j'} f(r_{ij'})\psi_1(\mathbf{R}). \quad (7.69)
\end{aligned}$$

The wave function ψ_V describes a quantized vortex line with circulation $\kappa = h/(2M)$, with localized vorticity on the vortex axis.

Variational Parameters Optimization

The variational parameters for the pairing functions and two-body Jastrow factor were optimized using the Stochastic Reconfiguration method [139], described in detail in Appendix E. The parameters for the one-body term were chosen to maximize the overlap of the density profile along the radial coordinate between the DMC and VMC calculations.

Chapter 8

Results

8.1 Introduction

In this chapter we present the results obtained with the BCS wave function ψ_0 for fermions in a cylinder, Eq. (7.67); and the results for the system with a vortex line along the z-axis, ψ_V from Eq. (7.69). Energy related quantities are calculated using the DMC method, as described in Sec. 7.4. The density profile calculations involve results of both DMC and VMC simulations, as it was discussed in Sec. 7.3.

We have fixed the number density at $k_F^3/(3\pi^2)$, which is the density of the free Fermi gas. Thus, we have freedom to choose the radius $\mathcal{R}$ and the height $\mathcal{L}$ of the cylinder. In all simulations we set $\mathcal{L} = 2\mathcal{R}$, so that the diameter is equal to the height of the cylinder.

The ground state of spin-1/2 fermions in a cylinder presents a shell structure, with closures given by the free state energy levels. Interestingly, the shell structure must be determined for each value of A, because the energy levels depend on $\mathcal{R}$ and $\mathcal{L}$.

In Sec. 8.2 we present the spatial distribution of the particles in the cylinder for both the ground state and the system with a vortex line. Energy related quantities, such as the ground state energy, the superfluid pairing gap and the vortex excitation energy are shown in Sec. 8.3.

8.2 Density profile

In order to study the spatial distribution of the particles in the cylinder we calculated the density profile along the radial direction ρ, $\mathcal{D}(\rho)$. Because the density operator does not commute with the Hamiltonian, we extrapolate the values using the procedure described in Sec. 7.4.3, see Eq. 7.40. The normalization is chosen so that

$$\int_V \mathcal{D}(\rho) dv = 1, \tag{8.1}$$

where the integral is over the volume $V = \pi\mathcal{R}^2\mathcal{L} = 2\pi\mathcal{R}^3$ of the cylinder.

Figs. 8.1 and 8.2 show the ground state density profile for open and closed shells, respectively. Due to unfilled states, the density profiles of Fig. 8.1 present more oscillations, whereas the profiles of Fig. 8.2 tend to be more flat. This behavior is expected because closed shells correspond to isotropic (in the sense of the cylindrical geometry) wavefunctions, while an open shell privileges certain directions, in this case they are related to the angular direction.

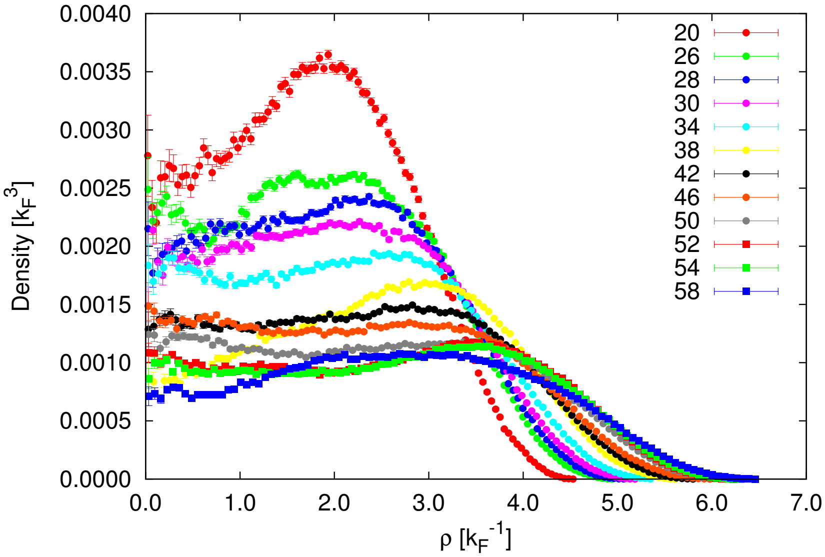

Figure 8.1: Ground state density as a function of the cylindrical coordinate ρ at the given values of A, all corresponding to systems with open shells.

Considering both the open and closed shell systems we notice that, for $A \gtrsim 34$, the behavior is qualitatively the same. The density is approximately flat near the center of the cylinder and it smoothly decreases until it vanishes at the wall. A constant density for small ρ is consistent with the ground state, since it corresponds to the bulk of the system. We note as well that, as the number of particles increases, size effects decrease. This can be observed by a more uniform density up to a region near the border of the cylinder. For the largest number of particles we have considered size effects to be negligible.

In Figs. 8.3 and 8.4 we present the density profile for systems with a vortex line excitation with open and closed shells, respectively. For $A \gtrsim 30$ the form of the curve is qualitatively the same. The most interesting feature of this quantity is a non-zero density at the core, near $\rho = 0$. The densities of the ground state and the vortex line system are very close, however they do differ for small ρ. Fig. 8.5 shows a comparison between the ground state and the vortex for $A = 50$, for other values of A the behavior is qualitatively

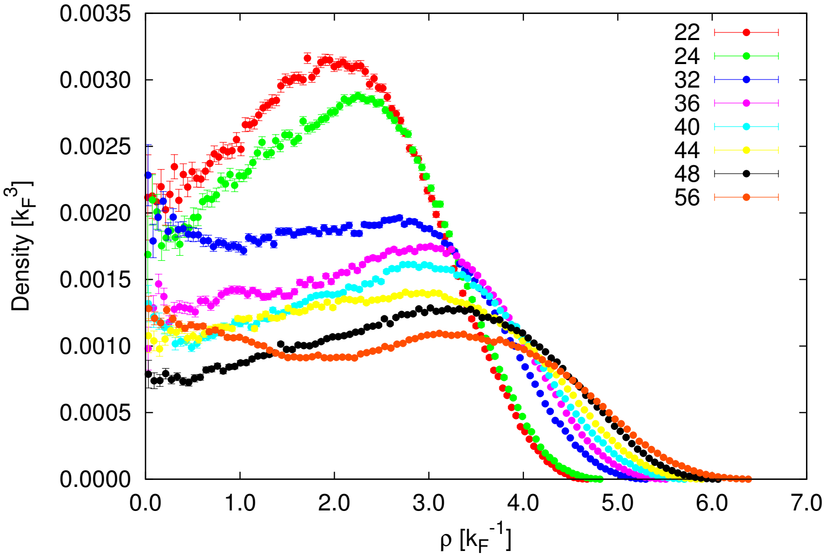

Figure 8.2: Ground state density as a function of the cylindrical coordinate ρ at the given values of A, all corresponding to systems with closed shells.

the same. The density of the vortex, although not zero at the core, is considerably lower than the ground state.

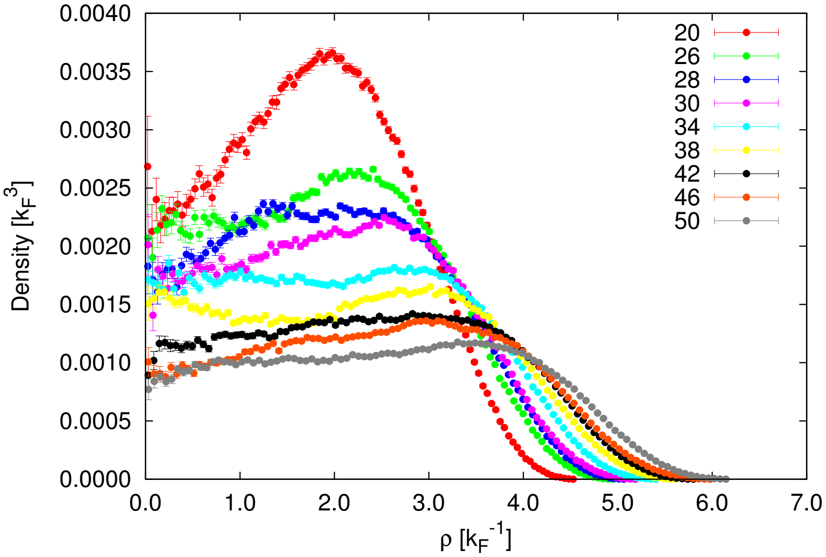

Figure 8.3: Density of the system with a vortex line as a function of the cylindrical coordinate ρ at the given values of A, all corresponding to systems with open shells.

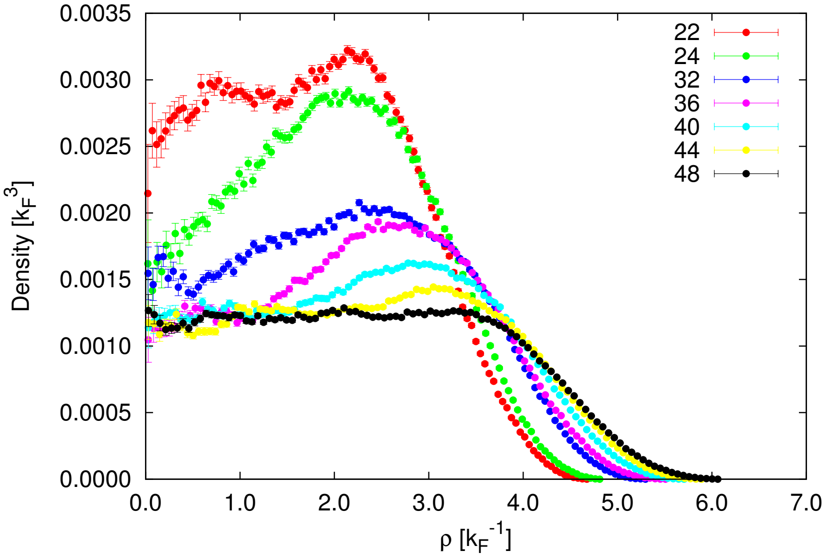

Figure 8.4: Density of the system with a vortex line as a function of the cylindrical coordinate ρ for various values of A, all corresponding to systems with closed shells.

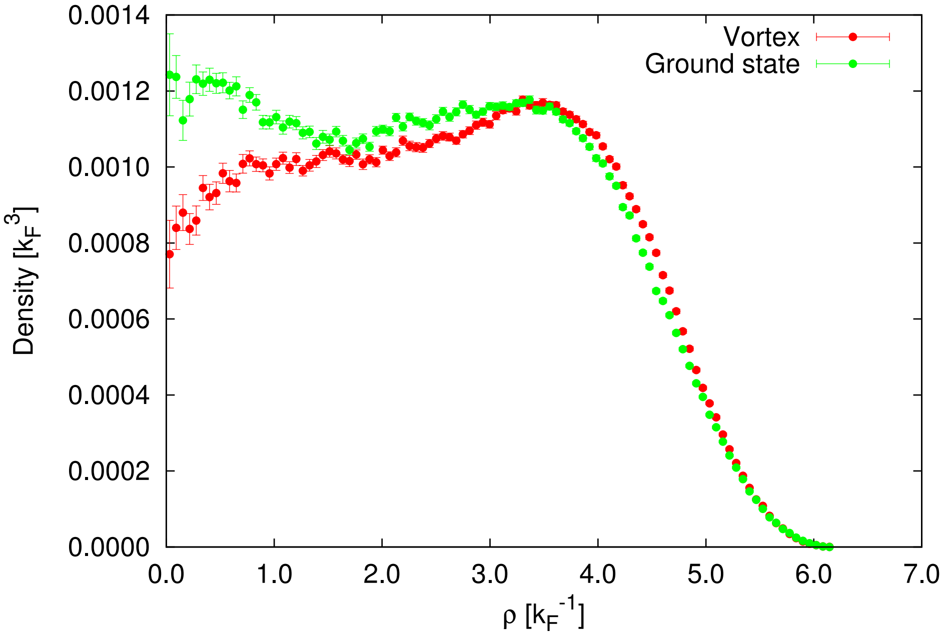

Figure 8.5: Comparison between the density profile for the ground state and the system with a vortex line, both for $A = 50$.

8.3 Energy

Some words about the chosen energy units are in order. The usual energy unity for superfluid Fermi gases is the energy of the noninteracting Fermi gas, see Eq. (C.10). However, it is not possible to calculate analytically this energy for a cylindrical geometry. Instead, we sum the energy levels of the free gas, Eq. (7.47), and use this sum as energy unit. For each value of A, $\mathcal{R}$ and $\mathcal{L}$ this energy unity must be computed

$$E_{FG} = \sum_{i=1}^{A} E^{(i)}_{nmp}, \tag{8.2}$$

where the sum is over the A-lowest level energies $E^{(i)}_{nmp}$.

8.3.1 Ground state

Fig. 8.6 presents the ground state energy per particle for $20 \leqslant A \leqslant 58$, where we have indicated whether the shell is opened or closed.

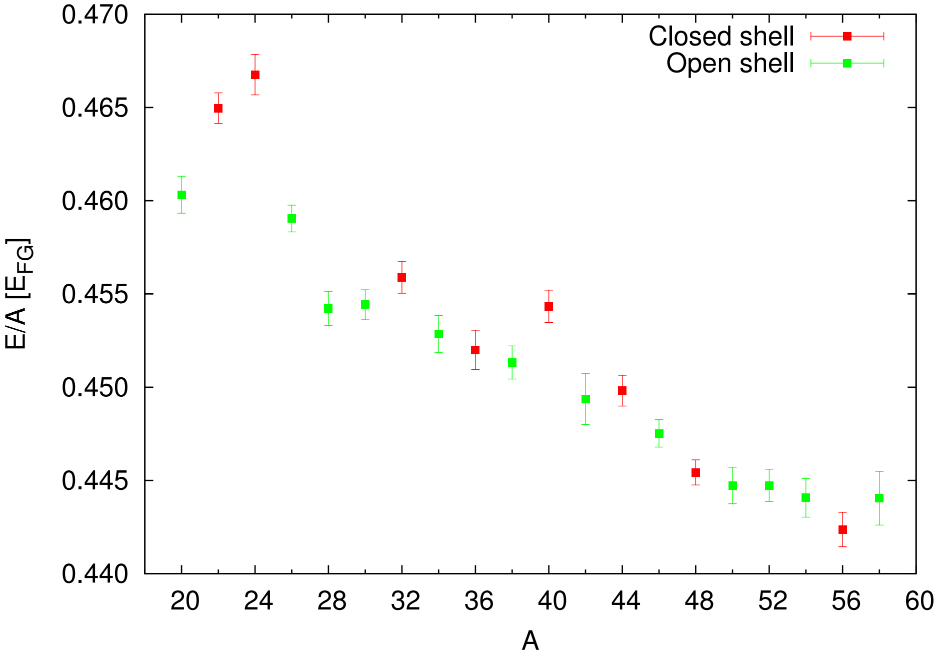

Figure 8.6: Ground state energy per particle as a function of the number of particles for open and closed shells.

In the limit of $\mathcal{R}, \mathcal{L} \to \infty$ the energy per particle in the cylindrical geometry should be equal to the energy per particle of the same system in a cubic box with periodic boundary conditions. Because the chosen wavefunction vanishes at the cylinder walls, we expect that the energy should be related to the surface area of the wall, $S = 2\pi\mathcal{R}\mathcal{L} = 4\pi\mathcal{R}^2$. We propose a functional form to the energy per particle as a function of the radius,

$$\epsilon(\mathcal{R}) = \frac{E(\mathcal{R})}{A} = \epsilon_0 + \frac{\epsilon_s}{4\pi\mathcal{R}^2}, \tag{8.3}$$

where ϵ_0 and ϵ_s are constants. For $A < 26$, the energy per particle seems to be suffering from size effects, due to the small number of particles. Thus, we fitted the energy per particle as a function of the radius for $A \geqslant 26$ using Eq. (8.3). The resulting parameters were $\epsilon_0 = (0.42 \pm 0.01)E_{FG}$ and $\epsilon_s = (11.4 \pm 1.0)E_{FG}k_F^{-2}$, and $\epsilon(\mathcal{R})$ is shown in Fig. 8.7.

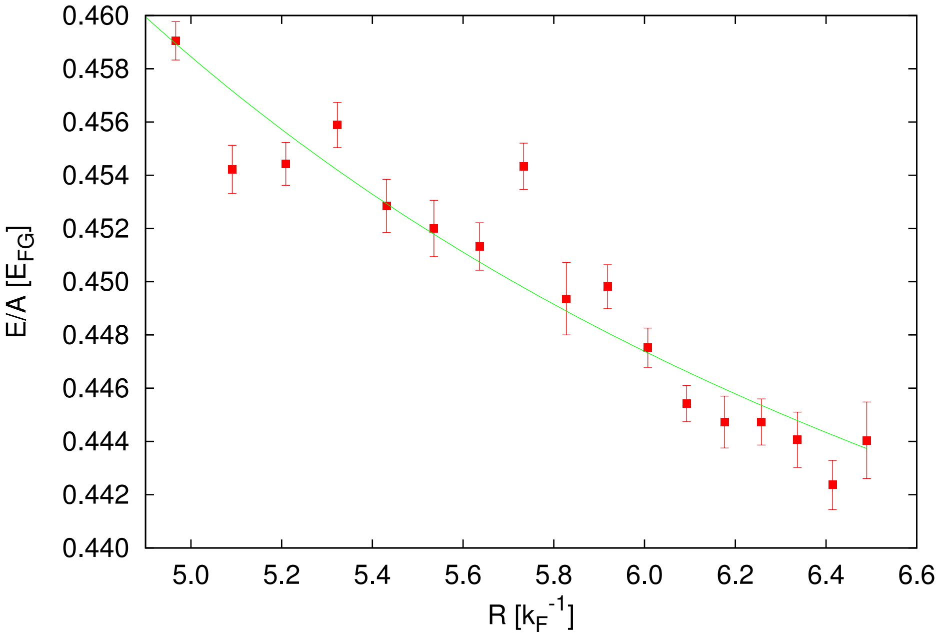

Figure 8.7: Ground state energy per particle as a function of the cylinder radius $\mathcal{R}$. The solid line corresponds to the fitted energy per particle (Eq. (8.3)).

8.3.2 Superfluid pairing gap

Ultracold atomic gases and low-density neutron matter are unique in the sense that they exhibit pairing gaps comparable to the Fermi energy [140]. Although the energy and momentum scales of cold atomic gases and atomic nuclei differ by many orders of magnitude, dilute neutron matter and ultracold unitary Fermi gases present similar pairing gaps. The possibility to tune particle-particle interactions experimentally in cold atomic gases systems provides an emulation of low-density neutron matter, which is beyond direct experimental reach.

Experiments with cold atom gases determined the pairing gap to be approximately half of the Fermi energy [128]. The pairing gap at $T = 0$ is calculated using the odd-even staggering formula [140]

$$\Delta(2A+1) = E(2A+1) - \frac{1}{2}\left[E(2A) + E(2A+2)\right], \tag{8.4}$$

where A is the number of fermions.

We consider that, for an even number of particles, all of them are paired; and for an odd number, one must be unpaired. The unpaired particle may be in any of the free particle states of Eq. (7.46) (or in a linear combination of them), however we must find the one which yields the lowest total energy for the system. We suppose that n and m are good quantum numbers for the unpaired particle, because we employ periodic boundary conditions in the z-direction and the wavefunction must be an eigenstate of L_z. Thus, we chose the wavefunction of the unpaired particle to be a linear combination of free particle states,

$$\psi_{nm}(\rho, \phi, z) = \sum_p \nu_p \Psi_{nmp}(\rho, \phi, z), \tag{8.5}$$

where the ν_p are variational coefficients and Ψ_{nmp} is given by Eq. (7.46). For different values of n and m we determine the ν_p which minimize the total energy of the system. Then, we perform DMC simulations using the resulting wavefunctions as guiding functions and we choose the lowest energy result.

Fig. 8.8 shows the total energy of the system for $20 \leqslant A \leqslant 40$. Using Eq. (8.4) we estimate the pairing gap to be $\Delta = (0.76 \pm 0.01)E_{FG}$. Another estimate is provided by using Eq. (8.3) to correct Eq. (8.4) for different cylinder radii. Denoting the parameters of $\epsilon(\mathcal{R})$ by $\epsilon_0^{(even)}$ and $\epsilon_s^{(even)}$ for an even number of particles, as in Sec. 8.3.1, and $\epsilon_0^{(odd)}$ and $\epsilon_s^{(odd)}$ for the systems with an odd number of particles, we have

$$\begin{aligned}\Delta_{\mathcal{R}} &= (2A+1)\left\{\epsilon_0^{(odd)} + \left.\frac{\epsilon_s^{(odd)}}{4\pi\mathcal{R}^2}\right|_{2A+1}\right\} - \frac{1}{2}\left[2A\left\{\epsilon_0^{(even)} + \left.\frac{\epsilon_s^{(even)}}{4\pi\mathcal{R}^2}\right|_{2A}\right\} + \right. \\ &\qquad \left.(2A+2)\left\{\epsilon_0^{(even)} + \left.\frac{\epsilon_s^{(even)}}{4\pi\mathcal{R}^2}\right|_{2A+2}\right\}\right] = \\ &= (2A+1)\left\{\epsilon_0^{(odd)} - \epsilon_0^{(even)} + \left.\frac{\epsilon_s^{(odd)}}{4\pi\mathcal{R}^2}\right|_{2A+1}\right\} - \frac{\epsilon_s^{(even)}}{4\pi}\left[\left.\frac{A}{\mathcal{R}}\right|_{2A} + \left.\frac{A+1}{\mathcal{R}}\right|_{2A+2}\right]\end{aligned} \tag{8.6}$$

Thus we fit the data, for $25 \leqslant A \leqslant 39$, for an odd number of particles using Eq. (8.3), which yields $\epsilon_0^{(odd)} = (0.42 \pm 0.01)E_{FG}$ and $\epsilon_s^{(odd)} = (21.1 \pm 3.2)E_{FG}k_F^{-2}$. Finally, (8.6) provides the estimate $\Delta_{\mathcal{R}} = (0.77 \pm 0.11)E_{FG}$.

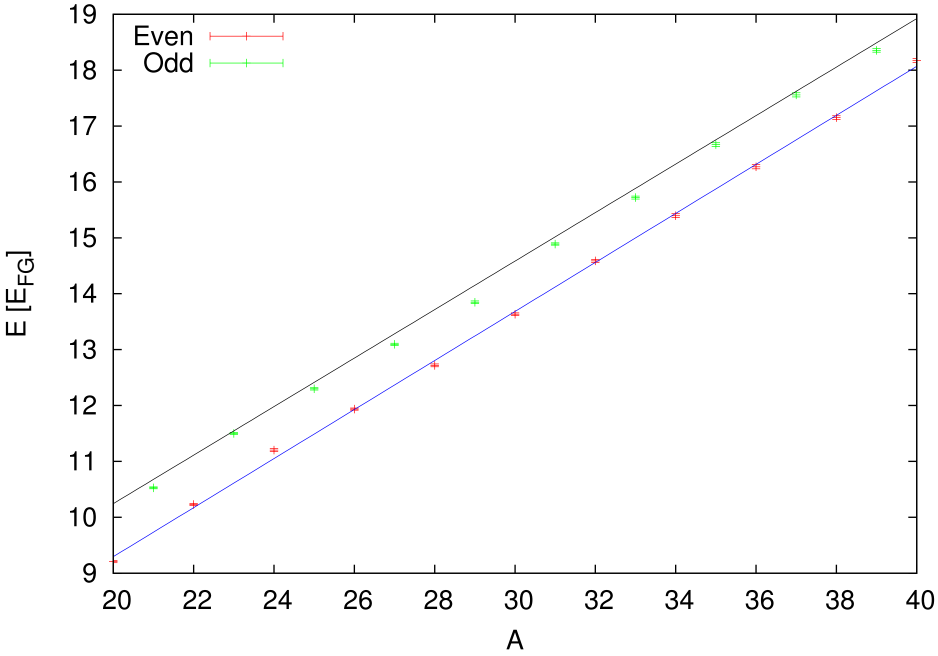

Figure 8.8: Ground state energy for even and odd number of particles. The solid lines correspond to linear fits of the even and odd system energies.

8.3.3 Excitation energy

A vortex line in the unitary Fermi gas is an excited state, and the excitation energy is given by the difference between the energy of the system with a vortex and the ground state energy. In Fig. 8.9 we present both energies for $22 \leqslant A \leqslant 48$. For $A < 26$, the systems suffer from size effects, so we chose to calculate the excitation energy only for $A \geqslant 26$. The corresponding excitation energy per particle is $\epsilon_{ex} = (0.0058 \pm 0.0003)E_{FG}$.

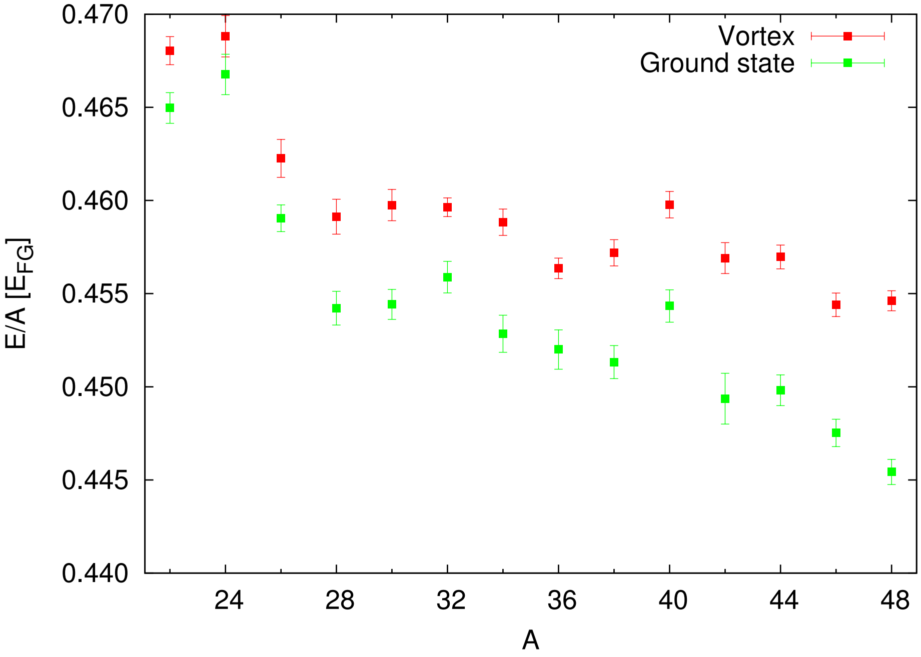

Figure 8.9: Ground state and vortex line energy per particle.

Chapter 9

Conclusions

Ultracold Fermi gases are remarkable fermionic systems due to the possibility to tune their interparticle interactions from weak to very strongly interacting regimes. Through Feshbach resonances in the BCS-BEC crossover we have the unitary Fermi gas, a strongly interacting system with short-range interactions.

A large body of experimental and theoretical work has been carried out concerning bosonic systems that led us to an improved knowledge of them. However, many questions remain to be answered regarding quantized vortices in fermionic systems. A vortex line consists of an irrotational flow field with a core region, where the vorticity is concentrated. The quanta of circulation is $h/(2M)$ and, amazingly, there is no evidence for quantized vortices with more than one quanta of circulation.

Our premise was to study properties of a single vortex line in the unitary Fermi gas. We developed wavefunctions, inspired by the BCS wavefunction, to describe the ground state of the superfluid unitary Fermi gas in a cylindrical container and the excited state of a vortex line in this system.

We consider that our results elucidate many aspects of the ground state in this non-trivial[1] geometry. In addition, our calculations for the system with a single vortex line shed light on some properties of this excited state.

We obtained the density profile of the ground state, which is flat near the center of the cylinder and it smoothly decreases until the density vanishes at the wall. The density profile of the ground state was compared to the vortex line system. The most interesting feature of the later is a non-vanishing density at the core, $\rho = 0$, however considerably lower than the ground state density for small ρ.

For this geometry, we calculated the energy of the ground state for an even number of particles (all paired). Because the wavefunction vanishes at the walls of the cylinder, we would need very large values of $\mathcal{R}$ and $\mathcal{L}$ to neglect the effects introduced by this condition. We proposed a functional form for the energy per particle as a function of the radius of the cylinder which takes into account the energy term due to the walls. The value found for the constant term $\epsilon_0 = (0.42 \pm 0.01)E_{FG}$ does not differ much, considering these effects, from the value of $(0.383 \pm 0.001)E_{FG}$ found for much larger systems in a box with periodic boundary conditions [127].

---

[1] For example, the ordering of the free particle energy levels depends on the radius and height of the cylinder.

The superfluid pairing gap of these ultra cold atomic gases is of interest because it is comparable to the Fermi energy of the system. We found two estimates for the pairing gap; the usual odd-even staggering formula [140] yields a gap of $\Delta = (0.76 \pm 0.01)E_{FG}$, and we propose a correction, due to different radii of the cylinders, which provides a gap of $\Delta_{\mathcal{R}} = (0.77 \pm 0.11)E_{FG}$. Previous quantum Monte Carlo simulations of fermions in a box, using periodic boundary conditions, predicted $\Delta = (0.84 \pm 0.05)E_{FG}$ [130]; while an experiment at finite temperature produced the value $\Delta = (0.45 \pm 0.05)E_{FG}$ [128].

The excitation energy is readily calculated from the energies of the ground state and the vortex line system. The calculated excitation energy per particle is $\epsilon_{ex} = (0.0058 \pm 0.0003)E_{FG}$. Associating a frequency ω with this energy we may write

$$\epsilon_{ex} = \hbar\omega = (0.0058 \pm 0.0003)E_{FG}. \tag{9.1}$$

We now compare our results to one of the milestones in the study of vortices in Fermi gases [28], which used ^{6}Li atoms to study the BCS-BEC crossover. The experiment focused on obtaining vortex lattices for different interaction strengths, ranging from the BCS limit to the BEC scheme. In the experiment, they found the characteristic microscopic length to be $1/k_F = 0.3$ μm, which yields a Fermi energy

$$E_F = \frac{\hbar^2 k_F^2}{2m} \approx 3.30 \times 10^{-11} \text{ eV}, \tag{9.2}$$

where $m = 1.17 \times 10^{26}$ kg. Using this Fermi energy in Eq. 9.1 we obtain $\varepsilon_{ex} = \hbar\omega = (1.9 \pm 0.1) \times 10^{-13}$ eV. They found the rotational frequency of the lattice to be close to the stirring frequency, which is $f_{stirr} \simeq 45$ Hz near unitarity. Hence, $\hbar\omega_{stirr} = \hbar\, 2\pi f_{stirr} \simeq 1.86 \times 10^{-13}$ eV. Although we compare these two quantities, the systems are quite different: we studied a single vortex line, and the experiment is comprised of a vortex lattice. However, if we neglect the vortices interactions in the experiment, the agreement between experiment and theory is a good one.

Chapter 10

Final remarks

The two parts of this dissertation deal with very distinct systems. We chose a classical approach to the first one, and the second is intrinsically in the realm of quantum mechanics. The common aspect between parts I and II is that we employed simulations to tackle both problems. Simulations fill a gap between theory and experiments: we may resort to numerical solutions of equations, that would be otherwise unsolvable; and we can simulate systems at extreme conditions, which could require ingenious experiments to be observed. The possibilities are innumerable, from single particle simulations up to large proteins chains.

The earliest work of Metropolis *et al.* [132] in 1953 laid the foundations to modern Monte Carlo simulations, so-called because of the role that random numbers play in the algorithm. The origin of molecular dynamics, in the sense of numerical solutions of Newton's equation for a many-body system, can be traced to the study of hard spheres by Alder and Wainwright [141] in 1957. These techniques evolved, efficient algorithms were devised and decades later we were able to investigate two intricate problems using these methods.

There are many other simulation methods available, such as Density Functional Theory (DFT) and Path Integral Monte Carlo (PIMC). Nevertheless, we feel that the triplet employed in this dissertation, Molecular Dynamics, Variational Monte Carlo and Diffusion Monte Carlo, gives us a solid basis for simulations of other systems in the future, to uncover fascinating properties of many-body systems.

Bibliography

[1] L.W. Bruch, M.W. Cole, and E. Zaremba. *Physical Adsorption: Forces and Phenomena*. International series of monographs on chemistry. Clarendon Press, 1997.

[2] Ronald A. Aziz and M.J. Slaman. The ne-ne interatomic potential revisited. *Chemical Physics*, 130(1–3):187 – 194, 1989.

[3] Ronald A. Aziz and M.J. Slaman. The argon and krypton interatomic potentials revisited. *Molecular Physics*, 58(4):679–697, 1986.

[4] Ronald A. Aziz and M.J. Slaman. On the xe-xe potential energy curve and related properties. *Molecular Physics*, 57(4):825–840, 1986.

[5] Ronald A. Aziz. A highly accurate interatomic potential for argon. *The Journal of Chemical Physics*, 99(6):4518–4525, 1993.

[6] K. T. Tang and J. P. Toennies. The van der waals potentials between all the rare gas atoms from he to rn. *The Journal of Chemical Physics*, 118(11):4976–4983, 2003.

[7] J. Tersoff. Modeling solid-state chemistry: Interatomic potentials for multicomponent systems. *Phys. Rev. B*, 39:5566–5568, Mar 1989.

[8] J. Tersoff. Erratum: Modeling solid-state chemistry: Interatomic potentials for multicomponent systems. *Phys. Rev. B*, 41:3248–3248, Feb 1990.

[9] S. Calisti, J. Suzanne, and J.A. Venables. A {LEED} study of adsorbed neon on graphite. *Surface Science*, 115(3):455 – 468, 1982.

[10] A. A. Antoniou. The adsorption of neon on graphitized carbon in the submonolayer and multilayer region between 1.5 and 30k. *The Journal of Chemical Physics*, 64(12):4901–4911, 1976.

[11] E. Lerner and F. Hanono. Vapor pressure measurements of adsorbed neon on exfoliated graphite between 15 and 30 k. *Journal of Low Temperature Physics*, 35(3-4):363–370, 1979.

[12] E Lerner, S.G Hedge, and J.G Daunt. Transitions in neon submonolayers adsorbed on argon-coated grafoil. *Physics Letters A*, 41(3):239 – 240, 1972.

[13] G.B. Huff and J.G. Dash. Phases of neon monolayers adsorbed on basal plane graphite. *Journal of Low Temperature Physics*, 24(1-2):155–174, 1976.

[14] J.L.M. Demétrio de Souza, R.E. Rapp, E.P. de Souza, and E. Lerner. Two-dimensional pressure-temperature phase diagram and latent heats of neon adsorbed on exfoliated graphite. *Journal of Low Temperature Physics*, 55(3-4):273–281, 1984.

[15] Christopher G. Shaw and Samuel C. Fain Jr. Condensation and compression of argon monolayers on graphite. *Surface Science*, 83(1):1 – 10, 1979.

[16] Gerald L. Pollack. The solid state of rare gases. *Rev. Mod. Phys.*, 36:748–791, Jul 1964.

[17] Jean Rouquerol, Stanislas Partyka, and Francoise Rouquerol. Calorimetric evidence for a bidimensional phase change in the monolayer of nitrogen or argon adsorbed on graphite at 77 k. *J. Chem. Soc., Faraday Trans. 1*, 73:306–314, 1977.

[18] Y. Larher. ”phase transitions” between dense monolayers of atoms and simple molecules on the cleavage face of graphite, with particular emphasis on the transition of nitrogen from a fluid to a registered monolayer. *The Journal of Chemical Physics*, 68(5):2257–2263, 1978.

[19] C. F. Prenzlow and G. D. Halsey. Argon-xenon layer formation on graphitized carbon black from 65 to 80k. *The Journal of Physical Chemistry*, 61(9):1158–1165, 1957.

[20] D. M. Butler, J. A. Litzinger, and G. A. Stewart. Completion of the phase diagram for the monolayer regime of the krypton-graphite adsorption system. *Phys. Rev. Lett.*, 44:466–468, Feb 1980.

[21] E.D. Specht, A. Mak, C. Peters, M. Sutton, R.J. Birgeneau, K.L. D’Amico, D.E. Moncton, S.E. Nagler, and P.M. Horn. Phase diagram and phase transitions of krypton on graphite in the extended monolayer regime. *Zeitschrift für Physik B Condensed Matter*, 69(2-3):347–377, 1987.

[22] Ju Li. Atomeye: an efficient atomistic configuration viewer. *Modelling and Simulation in Materials Science and Engineering*, 11(2):173, 2003.

[23] Mohit Randeria and Edward Taylor. Crossover from bardeen-cooper-schrieffer to bose-einstein condensation and the unitary fermi gas. *Annual Review of Condensed Matter Physics*, 5(1):209–232, 2014.

[24] J. J. Sakurai. *Modern Quantum Mechanics (Revised Edition)*. Addison Wesley, 1 edition, 1993.

[25] L. W. Bruch, R. D. Diehl, and J. A. Venables. Progress in the measurement and modeling of physisorbed layers. *Rev. Mod. Phys.*, 79:1381–1454, Nov 2007.

[26] E. Flenner and R. D. Etters. Properties of argon adlayers deposited on graphite from monte carlo calculations. *Phys. Rev. B*, 73:125419, Mar 2006.

[27] C. A. Regal, M. Greiner, and D. S. Jin. Observation of resonance condensation of fermionic atom pairs. *Phys. Rev. Lett.*, 92:040403, Jan 2004.

[28] M. W. Zwierlein, J. R. Abo-Shaeer, A. Schirotzek, C. H. Schunck, and W. Ketterle. Vortices and superfluidity in a strongly interacting fermi gas. *Nature*, 435(7045):1047–1051, Jun 2005.

[29] K. T. Tang and J. Peter Toennies. An improved simple model for the van der waals potential based on universal damping functions for the dispersion coefficients. *The Journal of Chemical Physics*, 80(8):3726–3741, 1984.

[30] K.T. Tang and J.Peter Toennies. New combining rules for well parameters and shapes of the van der waals potential of mixed rare gas systems. *Zeitschrift für Physik D Atoms, Molecules and Clusters*, 1(1):91–101, 1986.

[31] J M Kosterlitz and D J Thouless. Ordering, metastability and phase transitions in two-dimensional systems. *Journal of Physics C: Solid State Physics*, 6(7):1181, 1973.

[32] B. I. Halperin and David R. Nelson. Theory of two-dimensional melting. *Phys. Rev. Lett.*, 41:121–124, Jul 1978.

[33] B. I. Halperin and David R. Nelson. Theory of two-dimensional melting. *Phys. Rev. Lett.*, 41:519–519, Aug 1978.

[34] David R. Nelson and B. I. Halperin. Dislocation-mediated melting in two dimensions. *Phys. Rev. B*, 19:2457–2484, Mar 1979.

[35] A. P. Young. Melting and the vector coulomb gas in two dimensions. *Phys. Rev. B*, 19:1855–1866, Feb 1979.

[36] JeffreyM. Greif and DavidL. Goodstein. Orientational ordering in incommensurate solid helium monolayers on graphite. *Journal of Low Temperature Physics*, 44(3-4):347–366, 1981.

[37] C. Tiby, H. Wiechert, and H.J. Lauter. A neutron diffraction and vapor pressure study of neon physisorbed on grafoil near monolayer completion. *Surface Science*, 119(1):21 – 34, 1982.

[38] L.W. Bruch. On the orientational alignment of neon adsorbed on basal plane graphite. *Surface Science*, 115(1):L67 – L70, 1982.

[39] L. W. Bruch. Zone-center gap in the frequency spectrum of a commensurate monolayer. *Phys. Rev. B*, 37:6658–6662, Apr 1988.

[40] S. Calisti and J. Suzanne. Orientational epitaxy of an incommensurate neon monolayer adsorbed on graphite. *Surface Science*, 105(1):L255 – L259, 1981.

[41] R. E. Rapp, E. P. de Souza, and E. Lerner. Two-dimensional phase diagram of neon adsorbed on exfoliated graphite. heat-capacity measurements. *Phys. Rev. B*, 24:2196–2204, Aug 1981.

[42] L.W. Bruch, J.M. Phillips, and X.-Z. Ni. Model calculations of adsorbed solids of neon on graphite. *Surface Science*, 136(2–3):361 – 380, 1984.

[43] Ludwig W. Bruch and Xuan-Zhong Ni. Three-layer inert gas films. *Faraday Discuss. Chem. Soc.*, 80:217–226, 1985.

[44] T. M. Hakim and H. R. Glyde. Dynamics of solid neon monolayers. *Phys. Rev. B*, 37:984–992, Jan 1988.

[45] K. L. D'Amico, J. Bohr, D. E. Moncton, and Doon Gibbs. Melting and orientational epitaxy in argon and xenon monolayers on graphite. *Phys. Rev. B*, 41:4368–4376, Mar 1990.

[46] A. D. Migone, Z. R. Li, and M. H. W. Chan. Melting transition of submonolayer ar adsorbed on graphite. *Phys. Rev. Lett.*, 53:810–813, Aug 1984.

[47] Yves Larher and Bernard Gilquin. Critical temperatures of two-dimensional condensation in the first adlayer of noble gases on the cleavage face of graphite. *Phys. Rev. A*, 20:1599–1602, Oct 1979.

[48] H. Taub, K. Carneiro, J. K. Kjems, L. Passell, and J. P. McTague. Neutron scattering study of ^{36}Ar monolayer films adsorbed on graphite. *Phys. Rev. B*, 16:4551–4568, Nov 1977.

[49] J. L. Seguin, J. Suzanne, M. Bienfait, J. G. Dash, and J. A. Venables. Complete and incomplete wetting in multilayer adsorption: High-energy electron-diffraction studies of xe, ar, n_2, and ne films on graphite. *Phys. Rev. Lett.*, 51:122–125, Jul 1983.

[50] Thomas T. Chung. Heat capacity of ar monolayer adsorbed on basal plane graphite. *Surface Science*, 87(2):348 – 356, 1979.

[51] Jian Ma, Eleanor D. Carter, and Hillary B. Kleinberg. Effects of impurity on two-dimensional melting transitions. *Phys. Rev. B*, 57:9270–9273, Apr 1998.

[52] J. P. McTague, J. Als-Nielsen, J. Bohr, and M. Nielsen. Synchrotron x-ray study of melting in submonolayer ar and other rare-gas films on graphite. *Phys. Rev. B*, 25:7765–7772, Jun 1982.

[53] M. Nielsen, J. Als-Nielsen, J. Bohr, J. P. McTague, D. E. Moncton, and P. W. Stephens. Melting studies of argon on *ZYX* graphite. *Phys. Rev. B*, 35:1419–1425, Jan 1987.

[54] Christopher G. Shaw, S. C. Fain, and M. D. Chinn. Observation of orientational ordering of incommensurate argon monolayers on graphite. *Phys. Rev. Lett.*, 41:955–957, Oct 1978.

[55] J.A. Litzinger and G.A. Stewart. *in Ordering in two dimensions.* Elsevier North Holland, 1980. pp. 267-9.

[56] A. J. Jin, M. R. Bjurstrom, and M. H. W. Chan. Thermodynamic evidence of first-order melting of xe on graphite. *Phys. Rev. Lett.*, 62:1372–1375, Mar 1989.

[57] T. F. Rosenbaum, S. E. Nagler, P. M. Horn, and Roy Clarke. Experimental observation of continuous melting into a hexatic phase. *Phys. Rev. Lett.*, 50:1791–1794, May 1983.

[58] Farid F. Abraham. Melting transition of submonolayer xenon, krypton, and argon films on graphite: A computer simulation study. *Phys. Rev. B*, 28:7338–7341, Dec 1983.

[59] Richard Etters, Elijah Flenner, Bogdan Kuchta, Lucyna Firlej, and Witold Przydrozny. On the character of atomic adlayers physiadsorbed on an incommensurate substrate. *Journal of Low Temperature Physics*, 122(3-4):121–128, 2001.

[60] Elijah Flenner and Richard D. Etters. Behavior of partial monolayers of argon adlayers deposited on graphite. *Phys. Rev. Lett.*, 88:106101, Feb 2002.

[61] D. M. Butler, J. A. Litzinger, G. A. Stewart, and R. B. Griffiths. Heat capacity of krypton physisorbed on graphite. *Phys. Rev. Lett.*, 42:1289–1292, May 1979.

[62] A D Migone, M H W Chan, K J Niskanen, and R B Griffiths. Incipient triple point for n 2 adsorbed on graphite. *Journal of Physics C: Solid State Physics*, 16(31):L1115, 1983.

[63] Y. Larher and A. Terlain. Transition from fluid to registered solid of the krypton monolayer adsorbed on the basal face of graphite. *The Journal of Chemical Physics*, 72(2):1052–1054, 1980.

[64] R. M. Suter, N. J. Colella, and R. Gangwar. Location of the tricritical point for the melting of commensurate solid krypton on *ZYX* graphite. *Phys. Rev. B*, 31:627–630, Jan 1985.

[65] P. Bak, D. Mukamel, J. Villain, and K. Wentowska. Commensurate-incommensurate transitions in rare-gas monolayers adsorbed on graphite and in layered charge-density-wave systems. *Phys. Rev. B*, 19:1610–1613, Feb 1979.

[66] S. N. Coppersmith, Daniel S. Fisher, B. I. Halperin, P. A. Lee, and W. F. Brinkman. Dislocations and the commensurate-incommensurate transition in two dimensions. *Phys. Rev. B*, 25:349–363, Jan 1982.

[67] Tatsuya Shirakami, Akira Inaba, and Hideaki Chihara. Vibrational states and phase diagram of the submonolayer krypton adsorbed on graphite by the low temperature heat capacity. *Thermochimica Acta*, 163(0):233 – 240, 1990.

[68] R. J. Gooding, B. Joos, and B. Bergersen. Krypton on graphite: Microstructure at zero temperature. *Phys. Rev. B*, 27:7669–7675, Jun 1983.

[69] Frank Hanson and John P. McTague. Molecular dynamics simulation of submonolayer krypton films on graphite. *The Journal of Chemical Physics*, 72(12):6363–6367, 1980.

[70] S. W. Koch and Farid F. Abraham. Temperature-induced commensurate-incommensurate transition of submonolayer krypton on graphite. *Phys. Rev. B*, 33:5884–5885, Apr 1986.

[71] M B Gordon and F Lancon. The commensurate-incommensurate transition of kr monolayers on graphite. ii. wall and wall crossing energies. *Journal of Physics C: Solid State Physics*, 18(20):3929, 1985.

[72] Farid F. Abraham, William E. Rudge, Daniel J. Auerbach, and S. W. Koch. Molecular-dynamics simulations of the incommensurate phase of krypton on graphite using more than 100 000 atoms. *Phys. Rev. Lett.*, 52:445–448, Feb 1984.

[73] S.W Koch, W.E Rudge, and F.F Abraham. The commensurate-incommensurate transition of krypton on graphite: A study via computer simulation. *Surface Science*, 145(2–3):329 – 344, 1984.

[74] Venkat Bhethanabotla and William Steele. Simulations of the thermodynamic properties of krypton adsorbed on graphite at 100 k. *The Journal of Physical Chemistry*, 92(11):3285–3291, 1988.

[75] Hawoong Hong and R.J. Birgeneau. X-ray diffraction study of the structure of xenon multilayers on single crystal graphite. *Zeitschrift für Physik B Condensed Matter*, 77(3):413–419, 1989.

[76] E M Hammonds, P Heiney, P W Stephens, R J Birgeneau, and P Horn. Structure of liquid and solid monolayer xenon on graphite. *Journal of Physics C: Solid State Physics*, 13(12):L301, 1980.

[77] P.S. Schabes-Retchkiman and J.A. Venables. Structural studies of xenon and krypton solid monolayers on graphite using transmission electron diffraction. *Surface Science*, 105(2–3):536 – 564, 1981.

[78] W J Nuttall, K P Fahey, M J Young, B Keimer, R J Birgeneau, and H Suematsu. A synchrotron x-ray diffraction study of the structural phase behaviour of multilayer xenon on single-crystal graphite. *Journal of Physics: Condensed Matter*, 5(44):8159, 1993.

[79] A. Q. D. Faisal, M. Hamichi, G. Raynerd, and J. A. Venables. Low-temperature structures of xenon monolayers adsorbed on graphite. *Phys. Rev. B*, 34:7440–7443, Nov 1986.

[80] P. A. Heiney, P. W. Stephens, R. J. Birgeneau, P. M. Horn, and D. E. Moncton. X-ray scattering study of the structure and freezing transition of monolayer xenon on graphite. *Phys. Rev. B*, 28:6416–6434, Dec 1983.

[81] P. Dimon, P. M. Horn, M. Sutton, R. J. Birgeneau, and D. E. Moncton. First-order and continuous melting in a two-dimensional system: Monolayer xenon on graphite. *Phys. Rev. B*, 31:437–447, Jan 1985.

[82] Hawoong Hong, C. J. Peters, A. Mak, R. J. Birgeneau, P. M. Horn, and H. Suematsu. Synchrotron x-ray study of the structures and phase transitions of monolayer xenon on single-crystal graphite. *Phys. Rev. B*, 40:4797–4807, Sep 1989.

[83] N. J. Colella and R. M. Suter. Thermodynamics of first-order and continuous melting of xenon on graphite. *Phys. Rev. B*, 34:2052–2055, Aug 1986.

[84] R. Gangwar, N. J. Colella, and R. M. Suter. Thermodynamics of freezing in two dimensions: The compressibility of monolayer xenon on graphite. *Phys. Rev. B*, 39:2459–2471, Feb 1989.

[85] W J Nuttall, D Y Noh, B O Wells, and R J Birgeneau. Isothermal melting of near-monolayer xenon on single-crystal graphite. *Journal of Physics: Condensed Matter*, 7(23):4337, 1995.

[86] T. E. A. Zerrouk, M. Hamichi, J. D. H. Pilkington, and J. A. Venables. Observation of solid-hexatic-liquid phase transitions of submonolayer xenon on graphite by transmission-electron diffraction. *Phys. Rev. B*, 50:8946–8949, Sep 1994.

[87] Hawoong Hong, C. J. Peters, A. Mak, R. J. Birgeneau, P. M. Horn, and H. Suematsu. Commensurate-incommensurate and rotational transitions of monolayer xenon on single-crystal graphite. *Phys. Rev. B*, 36:7311–7314, Nov 1987.

[88] M. Hamichi, A. Q. D. Faisal, J. A. Venables, and R. Kariotis. Lattice parameter and orientation of xenon on graphite at low pressures. *Phys. Rev. B*, 39:415–425, Jan 1989.

[89] E. de Rouffignac, G. P. Alldredge, and F. W. de Wette. Dynamics of xenon-covered graphite slabs. *Phys. Rev. B*, 24:6050–6059, Nov 1981.

[90] Farid F. Abraham. Melting transition of near-monolayer xenon films on graphite: A computer simulation study. *Phys. Rev. Lett.*, 50:978–981, Mar 1983.

[91] S. W. Koch and Farid F. Abraham. Freezing transition of xenon on graphite: A computer-simulation study. *Phys. Rev. B*, 27:2964–2979, Mar 1983.

[92] Farid F. Abraham. Melting transition of near-monolayer xenon films on graphite: A computer simulation study. ii. *Phys. Rev. B*, 29:2606–2610, Mar 1984.

[93] Soong-Hyuck Suh, Noah Lermer, and Seamus F. O'Shea. Simulation of finite patches of xenon on graphite. *Chemical Physics*, 129(2):273 – 284, 1989.

[94] B. Joos, B. Bergersen, and M. L. Klein. Ground-state properties of xenon on graphite. *Phys. Rev. B*, 28:7219–7224, Dec 1983.

[95] J. P. Hobson. Calculated physical adsorption isotherms of neon and radon on a heterogeneous surface. *Journal of Vacuum Science & Technology A*, 15(3):728–730, 1997.

[96] B. Eichler, H. P. Zimmermann, and H. W. Gäggeler. Adsorption of radon on ice surfaces. *The Journal of Physical Chemistry A*, 104(14):3126–3131, 2000.

[97] V. Pershina, A. Borschevsky, E. Eliav, and U. Kaldor. Adsorption of inert gases including element 118 on noble metal and inert surfaces from ab initio dirac–coulomb atomic calculations. *The Journal of Chemical Physics*, 129(14):–, 2008.

[98] L W Bruch, Milton W Cole, and Hye-Young Kim. Transitions of gases physisorbed on graphene. *Journal of Physics: Condensed Matter*, 22(30):304001, 2010.

[99] Li Sheng, Yuriko Ono, and Tetsuya Taketsugu. Ab initio study of xe adsorption on graphene. *The Journal of Physical Chemistry C*, 114(8):3544–3548, 2010.

[100] R. Majidi and K. Ghafoori Tabrizi. Study of neon adsorption on carbon nanocones using molecular dynamics simulation. *Physica B: Condensed Matter*, 405(8):2144 – 2148, 2010.

[101] S. Rols, M. R. Johnson, P. Zeppenfeld, M. Bienfait, O. E. Vilches, and J. Schneble. Argon adsorption in open-ended single-wall carbon nanotubes. *Phys. Rev. B*, 71:155411, Apr 2005.

[102] M.R. Babaa, I. Stepanek, K. Masenelli-Varlot, N. Dupont-Pavlovsky, E. McRae, and P. Bernier. Opening of single-walled carbon nanotubes: evidence given by krypton and xenon adsorption. *Surface Science*, 531(1):86 – 92, 2003.

[103] Vahan V. Simonyan, J. Karl Johnson, Anya Kuznetsova, and John T. Yates. Molecular simulation of xenon adsorption on single-walled carbon nanotubes. *The Journal of Chemical Physics*, 114(9):4180–4185, 2001.

[104] M. Mercedes Calbi, Silvina M. Gatica, Mary J. Bojan, and Milton W. Cole. Phases of neon, xenon, and methane adsorbed on nanotube bundles. *The Journal of Chemical Physics*, 115(21):9975–9981, 2001.

[105] M. Tuckerman, B. J. Berne, and G. J. Martyna. Reversible multiple time scale molecular dynamics. *The Journal of Chemical Physics*, 97(3):1990–2001, 1992.

[106] D. Frenkel and B. Smit. *Understanding Molecular Simulation: From Algorithms to Applications*. Academic Press, 1996.

[107] P. Allen and D.J. Tildesley. *Computer simulation of liquids*. Oxford science publications. Clarendon Press, 1987.

[108] Steve Plimpton. Fast parallel algorithms for short-range molecular dynamics. *Journal of Computational Physics*, 117(1):1 – 19, 1995.

[109] Norio Inui, Kozo Mochiji, and Kousuke Moritani. Actuation of a suspended nanographene sheet by impact with an argon cluster. *Nanotechnology*, 19(50):505501, 2008.

[110] J. Tersoff. New empirical approach for the structure and energy of covalent systems. *Phys. Rev. B*, 37:6991–7000, Apr 1988.

[111] S.R. Salinas. *Introdução a Física Estatística Vol. 09*. EDUSP, 1997.

[112] Tetsuya Morishita. Fluctuation formulas in molecular-dynamics simulations with the weak coupling heat bath. *The Journal of Chemical Physics*, 113(8):2976–2982, 2000.

[113] C.J. Pethick and H. Smith. *Bose-Einstein Condensation in Dilute Gases*. Cambridge University Press, 2002.

[114] B. DeMarco and D. S. Jin. Onset of fermi degeneracy in a trapped atomic gas. *Science*, 285(5434):1703–1706, 1999.

[115] B. DeMarco, S. B. Papp, and D. S. Jin. Pauli blocking of collisions in a quantum degenerate atomic fermi gas. *Phys. Rev. Lett.*, 86:5409–5412, Jun 2001.

[116] Andrew G. Truscott, Kevin E. Strecker, William I. McAlexander, Guthrie B. Partridge, and Randall G. Hulet. Observation of fermi pressure in a gas of trapped atoms. *Science*, 291(5513):2570–2572, 2001.

[117] F. Schreck, G. Ferrari, K. L. Corwin, J. Cubizolles, L. Khaykovich, M.-O. Mewes, and C. Salomon. Sympathetic cooling of bosonic and fermionic lithium gases towards quantum degeneracy. *Phys. Rev. A*, 64:011402, Jun 2001.

[118] Takeshi Fukuhara, Yosuke Takasu, Mitsutaka Kumakura, and Yoshiro Takahashi. Degenerate fermi gases of ytterbium. *Phys. Rev. Lett.*, 98:030401, Jan 2007.

[119] W. Ketterle and M. Zwierlein. Making, probing and understanding ultracold fermi gases. *arXiv pre-print*, 2008. arXiv:0801.2500v1 [cond-mat.other].

[120] G. B. Partridge, K. E. Strecker, R. I. Kamar, M. W. Jack, and R. G. Hulet. Molecular probe of pairing in the bec-bcs crossover. *Phys. Rev. Lett.*, 95:020404, Jul 2005.

[121] C. A. R. Sá de Melo, Mohit Randeria, and Jan R. Engelbrecht. Crossover from bcs to bose superconductivity: Transition temperature and time-dependent ginzburg-landau theory. *Phys. Rev. Lett.*, 71:3202–3205, Nov 1993.

[122] P. Nozières and S. Schmitt-Rink. Bose condensation in an attractive fermion gas: From weak to strong coupling superconductivity. *Journal of Low Temperature Physics*, 59(3-4):195–211, 1985.

[123] George A. Baker. Neutron matter model. *Phys. Rev. C*, 60:054311, Oct 1999.

[124] Henning Heiselberg. Fermi systems with long scattering lengths. *Phys. Rev. A*, 63:043606, Mar 2001.

[125] J. Carlson, S.-Y. Chang, V. R. Pandharipande, and K. E. Schmidt. Superfluid fermi gases with large scattering length. *Phys. Rev. Lett.*, 91:050401, Jul 2003.

[126] G. E. Astrakharchik, J. Boronat, J. Casulleras, and S. Giorgini. Equation of state of a fermi gas in the bec-bcs crossover: A quantum monte carlo study. *Phys. Rev. Lett.*, 93:200404, Nov 2004.

[127] Michael McNeil Forbes, Stefano Gandolfi, and Alexandros Gezerlis. Resonantly interacting fermions in a box. *Phys. Rev. Lett.*, 106:235303, Jun 2011.

[128] J. Carlson and Sanjay Reddy. Superfluid pairing gap in strong coupling. *Phys. Rev. Lett.*, 100:150403, Apr 2008.

[129] Aurel Bulgac, Joaquín E. Drut, and Piotr Magierski. Quantum monte carlo simulations of the bcs-bec crossover at finite temperature. *Phys. Rev. A*, 78:023625, Aug 2008.

[130] J. Carlson and Sanjay Reddy. Asymmetric two-component fermion systems in strong coupling. *Phys. Rev. Lett.*, 95:060401, Aug 2005.

[131] W. M. C. Foulkes, L. Mitas, R. J. Needs, and G. Rajagopal. Quantum monte carlo simulations of solids. *Rev. Mod. Phys.*, 73:33–83, Jan 2001.

[132] Nicholas Metropolis, Arianna W. Rosenbluth, Marshall N. Rosenbluth, Augusta H. Teller, and Edward Teller. Equation of state calculations by fast computing machines. *The Journal of Chemical Physics*, 21(6):1087–1092, 1953.

[133] James B. Anderson. A random-walk simulation of the schrodinger equation: H+3. *The Journal of Chemical Physics*, 63(4):1499–1503, 1975.

[134] R.J. Donnelly. *Quantized Vortices in Helium II.* Number v. 2 in Cambridge Studies in American Literature and Culture. Cambridge University Press, 1991.

[135] S. A. Vitiello, L. Reatto, G. V. Chester, and M. H. Kalos. Vortex line in superfluid ^{4}He: A variational monte carlo calculation. *Phys. Rev. B*, 54:1205–1212, Jul 1996.

[136] S. Gandolfi, A. Yu. Illarionov, F. Pederiva, K. E. Schmidt, and S. Fantoni. Equation of state of low-density neutron matter, and the $^1S_0$ pairing gap. *Phys. Rev. C*, 80:045802, Oct 2009.

[137] G. C. Wick. The evaluation of the collision matrix. *Phys. Rev.*, 80:268–272, Oct 1950.

[138] S. Cowell, H. Heiselberg, I. E. Mazets, J. Morales, V. R. Pandharipande, and C. J. Pethick. Cold bose gases with large scattering lengths. *Phys. Rev. Lett.*, 88:210403, May 2002.

[139] Michele Casula, Claudio Attaccalite, and Sandro Sorella. Correlated geminal wave function for molecules: An efficient resonating valence bond approach. *The Journal of Chemical Physics*, 121(15):7110–7126, 2004.

[140] J. Carlson, S. Gandolfi, and A. Gezerlis. Superfluid pairing in neutrons and cold atoms. *arXiv pre-print*, 2012. arXiv:1204.2596 [nucl-th].

[141] B. J. Alder and T. E. Wainwright. Phase transition for a hard sphere system. *The Journal of Chemical Physics*, 27(5):1208–1209, 1957.

[142] Shuichi Nosé. An extension of the canonical ensemble molecular dynamics method. *Molecular Physics*, 57(1):187–191, 1986.

[143] Glenn J. Martyna, Michael L. Klein, and Mark Tuckerman. Nosé–hoover chains: The canonical ensemble via continuous dynamics. *The Journal of Chemical Physics*, 97(4):2635–2643, 1992.

[144] J. Bardeen, L. N. Cooper, and J. R. Schrieffer. Theory of superconductivity. *Phys. Rev.*, 108:1175–1204, Dec 1957.

[145] David J Thouless. Perturbation theory in statistical mechanics and the theory of superconductivity. *Annals of Physics*, 10(4):553 – 588, 1960.

[146] L.P. Gorkov and T.K. Melik-Barkhudarov. Contribution to the theory of superfluidity in an imperfect fermi gas. *Journal of Experimental and Theoretical Physics*, 13(5):1018, 1961.

[147] H. Heiselberg, C. J. Pethick, H. Smith, and L. Viverit. Influence of induced interactions on the superfluid transition in dilute fermi gases. *Phys. Rev. Lett.*, 85:2418–2421, Sep 2000.

Appendix A

Implementation of the Nosé-Hoover thermostat

We showed that the Nosé equations of motion can be written in terms of virtual or real variables. Because it is convenient to work with fixed time steps we favor the real-variable formulation. Hoover showed that the equations derived by Nosé could be simplified [142]. In the Eq. set (3.39) the variables s', p'_s and Q occur only as the combination $s'p'_s/Q$. Thus, we introduce a thermodynamic friction coefficient $\xi = s'p'_s/Q$ to simplify these equations. Dropping the primes, we have

$$\dot{\mathbf{r}}_i = \frac{\mathbf{p}_i}{m_i}, \tag{A.1}$$

$$\dot{\mathbf{p}}_i = -\frac{\partial \mathcal{U}(\mathbf{r}^N)}{\partial \mathbf{r}_i} - \xi \mathbf{p}_i, \tag{A.2}$$

$$\dot{\xi} = \frac{1}{Q}\left(\sum_i \frac{p_i^2}{m_i} - \frac{L}{\beta}\right), \tag{A.3}$$

$$\frac{\dot{s}}{s} = \frac{d\ln s}{dt} = \xi. \tag{A.4}$$

The last equation is redundant, since the other three form a closed set. However, if we solve the equation for s as well, we can use the conserved quantity of Eq. (3.40) as a diagnostic tool during the simulation. In terms of real-variables and thermodynamic friction coefficient formulation, $H_{\text{Nosé}}$ is

$$H_{\text{Nosé}} = \sum_{i=1}^{N} \frac{\mathbf{p}_i^2}{2m_i} + \mathcal{U}(\mathbf{r}^N) + \frac{\xi^2 Q}{2} + \frac{L}{\beta}\ln s, \tag{A.5}$$

where we take $L = 3N$.

The equations of motion of the Nosé-Hoover scheme cannot be derived from a Hamiltonian. The consequence of this non-Hamiltonian dynamics is that the Nosé-Hoover algorithm only generates the correct distribution if there is a *single* constant of motion, which is $H_{\text{Nosé}}$ for most systems. If we want to simulate systems with more than one conservation law, we have to use Nosé-Hoover chains to obtain the correct canonical distribution.

A.1 Nosé-Hoover chains

In order to alleviate the restriction of only one conserved quantity for the Nosé-Hoover thermostat, Martyna *et al.* [143] proposed a scheme in which the Nosé-Hoover thermostat is coupled to another one or, if necessary, to a chain of thermostats. In [143] it is shown that this construction still generates a canonical distribution.

The equations of motion for N particles coupled with M Nosé-Hoover chains are given, in real variables ($L = 3N$), by

$$\begin{aligned}
\dot{\mathbf{r}}_i &= \frac{\mathbf{p}_i}{m_i}; \\
\dot{\mathbf{p}}_i &= \mathbf{F}_i - \frac{p_{\xi_1}}{Q_1}\mathbf{p}_i; \\
\dot{\xi}_k &= \frac{p_{\xi_k}}{Q_k} \quad k = 1, \ldots, M; \\
\dot{p}_{\xi_1} &= \left(\sum_i \frac{p_i^2}{m_i} - Lk_BT\right) - \frac{p_{\xi_2}}{Q_2}p_{\xi_1}; \\
\dot{p_{\xi_k}} &= \left[\frac{p^2_{\xi_{k-1}}}{Q_{k-1}} - k_BT\right] - \frac{p_{\xi_{k+1}}}{Q_{k+1}}p_{\xi_k}; \\
\dot{p}_{\xi_M} &= \left[\frac{p^2_{\xi_{M-1}}}{Q_{M-1}} - k_BT\right].
\end{aligned} \tag{A.6}$$

For these equations of motion, the conserved energy is

$$H_{NHC} = \mathcal{H}(\mathbf{r}, \mathbf{p}) + \sum_{k=1}^{M} \frac{p^2_{\xi_k}}{2Q_k} + Lk_BT\xi_1 + \sum_{k=2}^{M} k_BT\xi_k, \tag{A.7}$$

thus we use this quantity to check the integration scheme. The additional $M-1$ equations of motion are relatively easy to implement because they form an one-dimensional chain.

We now use the Liouville approach of Sec. 3.2.1 to derive a set of time-reversible, area preserving integrators for the Nosé-Hoover chains. The Liouville operator is defined as

$$iL \equiv \dot{\boldsymbol{\eta}}\frac{\partial}{\partial \boldsymbol{\eta}}, \tag{A.8}$$

where $\boldsymbol{\eta} = (\mathbf{r}^N, \mathbf{p}^N, \xi^M, p_\xi^M)$. Using the equations of motion

$$\begin{aligned}
\mathbf{p}_i &= m_i\mathbf{v}_i, \\
p_{\xi_k} &= Q_k v_{\xi_k},
\end{aligned} \tag{A.9}$$

we obtain the Liouville operator

$$iL_{NHC} = \sum_{i=1}^{N} \mathbf{v}_i \cdot \nabla_{\mathbf{r}_i} + \sum_{i=1}^{N} \left[\frac{\mathbf{F}_i(\mathbf{r}_i)}{m_i}\right] \cdot \nabla_{\mathbf{v}_i} - \sum_{i=1}^{N} v_{\xi_1} \mathbf{v}_i \cdot \nabla_{\mathbf{v}_i} + \sum_{k=1}^{M} v_{\xi_k} \frac{\partial}{\partial \xi_k} + \sum_{k=1}^{M-1} (G_k - v_{\xi_k} v_{\xi_{k+1}}) \frac{\partial}{\partial v_{\xi_k}} + G_M \frac{\partial}{\partial v_{\xi_M}}, \tag{A.10}$$

with

$$\begin{aligned} G_1 &= \frac{1}{Q_1}\left(\sum_{i=1}^{N} m_i \mathbf{v}_i^2 - L k_B T\right) \\ G_k &= \frac{1}{Q_k}(Q_{k-1} v_{\xi_{k-1}}^2 - k_B T). \end{aligned} \tag{A.11}$$

We break the Liouville operator into iL_r, only position dependent, iL_v, which depends only on velocities, and iL_C, which contains the chain of thermostats

$$iL_{NHC} = iL_r + iL_v + iL_C, \tag{A.12}$$

with

$$\begin{aligned} iL_r &= \sum_{i=1}^{N} \mathbf{v}_i \cdot \nabla_{\mathbf{r}_i}, \\ iL_v &= \sum_{i=1}^{N} \left[\frac{\mathbf{F}_i(\mathbf{r}_i)}{m_i}\right] \cdot \nabla_{\mathbf{v}_i}, \\ iL_C &= -\sum_{i=1}^{N} v_{\xi_1} \mathbf{v}_i \cdot \nabla_{\mathbf{v}_i} + \sum_{k=1}^{M} v_{\xi_k} \frac{\partial}{\partial \xi_k} + \sum_{k=1}^{M-1} (G_k - v_{\xi_k} v_{\xi_{k+1}}) \frac{\partial}{\partial v_{\xi_k}} + G_M \frac{\partial}{\partial v_{\xi_M}}. \end{aligned} \tag{A.13}$$

One way to use the Trotter formula (Eq. (3.14)), out of the several possibilities, is

$$e^{(iL\Delta t)} = e^{(iL_C \Delta t/2)} e^{(iL_v \Delta t/2)} e^{(iL_r \Delta t)} e^{(iL_v \Delta t/2)} e^{(iL_C \Delta t/2)} + \mathcal{O}((\Delta t)^3). \tag{A.14}$$

The Nosé-Hoover chain part needs to be broken into smaller pieces. We will consider the case $M = 2$, but more general cases are possible. We separate iL_C into

$$iL_C = iL_\xi + iL_{C_v} + iL_{G_1} + iL_{v_{\xi_1}} + iL_{G_2}, \tag{A.15}$$

with

$$\begin{aligned} iL_\xi &\equiv \sum_{k=1}^{2} v_{\xi_k}\frac{\partial}{\partial \xi_k}, \\ iL_{C_v} &\equiv -\sum_{i=1}^{N} v_{\xi_1}\mathbf{v}_i\cdot\nabla_{\mathbf{v}_i}, \\ iL_{G_1} &\equiv G_1\frac{\partial}{\partial v_{\xi_1}}, \\ iL_{v_{\xi_1}} &\equiv -(v_{\xi_1}v_{\xi_2})\frac{\partial}{\partial v_{\xi_1}}, \\ iL_{G_2} &\equiv G_2\frac{\partial}{\partial v_{\xi_2}}. \end{aligned} \tag{A.16}$$

The factorization for the Trotter equation that we employ is

$$\begin{aligned} e^{(iL_C\Delta t/2)} &= e^{(iL_{G_2}\Delta t/4)}e^{(iL_{v_{\xi_1}}\Delta t/4+iL_{G_1}\Delta t/4)}e^{(iL_\xi\Delta t/2)}\times \\ &\quad e^{(iL_{C_v}\Delta t/2)}e^{(iL_{G_1}\Delta t/4+iL_{v_{\xi_1}}\Delta t/4)}e^{(iL_{G_2}\Delta t/4)} \\ &= e^{(iL_{G_2}\Delta t/4)}\left[e^{(iL_{v_{\xi_1}}\Delta t/8)}e^{(iL_{G_1}\Delta t/4)}e^{(iL_{v_{\xi_1}}\Delta t/8)}\right] \\ &\times\; e^{(iL_\xi\Delta t/2)}e^{(iL_{C_v}\Delta t/2)} \\ &\times\; \left[e^{(iL_{v_{\xi_1}}\Delta t/8)}e^{(iL_{G_1}\Delta t/4)}e^{(iL_{v_{\xi_1}}\Delta t/8)}\right]e^{(iL_{G_2}\Delta t/4)}. \end{aligned} \tag{A.17}$$

This seemingly complicated Liouville operator is relatively easy to implement in a computer program. We need to know how the operators act on the coordinates $\boldsymbol{\eta} = (\mathbf{r}^N, \mathbf{v}^N, \xi_1, v_{\xi_1}, \xi_2, v_{\xi_2})$. If we start at $t = 0$, at $t = \Delta t$ we have

$$e^{iL_{NHC}\Delta t} f[\mathbf{r}^N, \mathbf{v}^N, \xi_1, v_{\xi_1}, \xi_2, v_{\xi_2}]. \tag{A.18}$$

We can apply each term of iL_{NHC} sequentially. We begin with iL_{G_2},

$$\begin{aligned} e^{(iL_{G_2}\Delta t/4)} f[\mathbf{r}^N, \mathbf{v}^N, \xi_1, v_{\xi_1}, \xi_2, v_{\xi_2}] &= \sum_{n=0}^{\infty}\frac{(G_2\Delta t/4)^n}{n!}\frac{\partial^n}{\partial v_{\xi_2}^n} f[\mathbf{r}^N, \mathbf{v}^N, \xi_1, v_{\xi_1}, \xi_2, v_{\xi_2}] \\ &= f[\mathbf{r}^N, \mathbf{v}^N, \xi_1, v_{\xi_1}, \xi_2, v_{\xi_2} + G_2\Delta t/4]. \end{aligned} \tag{A.19}$$

Hence, iL_{G_2} affects only v_{ξ_2}, giving a simple transformation rule for this operator

$$e^{(iL_{G_2}\Delta t/4)} : v_{\xi_2} \to v_{\xi_2} + G_2\Delta t/4. \tag{A.20}$$

The action of the operator $iL_{v_{\xi_1}}$ can be evaluated using the identity

$$\exp\left(a\frac{\partial}{\partial g(x)}\right) f(x) = f\{g^{-1}[g(x) + a]\}. \tag{A.21}$$

Thus,

$$\exp\left(-\frac{\Delta t}{8}v_{\xi_2}v_{\xi_1}\frac{\partial}{\partial v_{\xi_1}}\right)f[\mathbf{r}^N,\mathbf{v}^N,\xi_1,v_{\xi_1},\xi_2,v_{\xi_2}] =$$

$$f[\mathbf{r}^N,\mathbf{v}^N,\xi_1,\exp\left(-\frac{\Delta t}{8}v_{\xi_2}\right)v_{\xi_1},\xi_2,v_{\xi_2}], \tag{A.22}$$

giving the transformation rule

$$e^{(iL_{v_{\xi_1}}\Delta t/8)}\,:\,v_{\xi_1}\rightarrow\exp\left(-\frac{\Delta t}{8}v_{\xi_2}\right)v_{\xi_1}. \tag{A.23}$$

Similarly, we can derive the action of the other operators

$$\begin{aligned} e^{(iL_{G_1}\Delta t/4)} \quad &: \quad v_{\xi_1}\rightarrow v_{\xi_1}+G_1\Delta t/4, \\ e^{(iL_{\xi}\Delta t/8)} \quad &: \quad \xi_1\rightarrow\xi_1-v_{\xi_1}\Delta t/2, \\ & \quad\quad \xi_2\rightarrow\xi_2-v_{\xi_2}\Delta t/2, \\ e^{(iL_{C_v}\Delta t/2)} \quad &: \quad v_i\rightarrow\exp\left(-\frac{\Delta t}{2}v_{\xi_1}\right)v_i. \end{aligned} \tag{A.24}$$

Finally, the transformations associated with iL_v and iL_r are similar to the velocity Verlet

$$\begin{aligned} e^{iL_v\Delta t/2} \quad &: \quad \mathbf{v}_i\rightarrow\mathbf{v}_i+\mathbf{F}_i\Delta t/(2m), \\ e^{iL_r\Delta t} \quad &: \quad \mathbf{r}_i\rightarrow\mathbf{r}_i+\mathbf{v}_i\Delta t. \end{aligned} \tag{A.25}$$

With the set of rules of Eqs. (A.20), (A.23)-(A.25) we can write our numerical algorithm and apply the transformations according to the order defined by Eqs. (A.14) and (A.17).

Appendix B

Scattering theory

B.1 The Lippmann-Schwinger equation

We begin with the time-independent scattering process [24]. We assume the Hamiltonian to be

$$H = H_0 + V \ , \tag{B.1}$$

where $H_0 = \mathbf{p}^2/2m$. In the absence of a scatterer, $V = 0$ and an energy eigenstate would be $|\mathbf{p}\rangle$, the same as a free-particle state. If we consider an elastic scattering we are interested in the full Hamiltonian with the same energy eigenvalue. Let $|\phi\rangle$ be the energy eigenket of H_0, then

$$H_0|\phi\rangle = E|\phi\rangle. \tag{B.2}$$

The equation we want to solve is

$$(H_0 + V)|\psi\rangle = E|\psi\rangle. \tag{B.3}$$

The energy spectrum is continuous for both H_0 and $(H_0 + V)$. We want a solution of Eq. (B.3) such that $|\psi\rangle \to |\phi\rangle$ as $V \to 0$, where ϕ is a solution of Eq. (B.2) with the **same** energy. The desired solution is

$$|\psi\rangle = \frac{1}{E - H_0} V|\psi\rangle + |\phi\rangle, \tag{B.4}$$

which reduces to $|\phi\rangle$ as $V \to 0$. However, we still need to deal with the singular operator $1/(E - H_0)$. We make E sightly complex

$$|\psi^{(\pm)}\rangle = |\phi\rangle + \frac{1}{E - H_0 \pm i\varepsilon} V|\psi^{(\pm)}\rangle. \tag{B.5}$$

This is the Lippmann-Schwinger equation. The physical meaning of ± will be discussed in a moment. This equation is independent of the representation, let us look at it in the position basis

$$\langle \mathbf{x}|\psi^{(\pm)}\rangle = \langle \mathbf{x}|\phi\rangle + \int d^3x' \langle \mathbf{x}|\frac{1}{E - H_0 \pm i\varepsilon}|\mathbf{x}'\rangle\langle \mathbf{x}'|V|\psi^{(\pm)}\rangle. \tag{B.6}$$

If $|\phi\rangle$ stands for a plane-wave state with momentum $\mathbf{p}$ then

$$\langle \mathbf{x}|\phi\rangle = \frac{e^{i\mathbf{p}\cdot\mathbf{x}/\hbar}}{(2\pi\hbar)^{3/2}}. \tag{B.7}$$

We must evaluate the kernel of the integral equation Eq. (B.6), defined by

$$G_\pm(\mathbf{x},\mathbf{x}') = \frac{\hbar^2}{2m}\langle \mathbf{x}|\frac{1}{E - H_0 \pm i\varepsilon}|\mathbf{x}'\rangle. \tag{B.8}$$

Alternatively, $G_\pm(\mathbf{x},\mathbf{x}')$ is given by

$$G_\pm(\mathbf{x},\mathbf{x}') = -\frac{1}{4\pi}\frac{e^{\pm ik|\mathbf{x}-\mathbf{x}'|}}{|\mathbf{x}-\mathbf{x}'|}, \tag{B.9}$$

where $E = \hbar^2k^2/(2m)$. For the proof we evaluate:

$$\begin{aligned} G_\pm(\mathbf{x},\mathbf{x}') &= \frac{\hbar^2}{2m}\langle \mathbf{x}|\frac{1}{E - H_0 \pm i\varepsilon}|\mathbf{x}'\rangle \\ &= \frac{\hbar^2}{2m}\int d^3p' \int d^3p'' \langle \mathbf{x}|\mathbf{p}'\rangle\langle \mathbf{p}'|\frac{1}{E - (\mathbf{p}'^2/2m) \pm i\varepsilon}|\mathbf{p}''\rangle\langle \mathbf{p}''|\mathbf{x}'\rangle. \end{aligned} \tag{B.10}$$

We can use

$$\begin{aligned} &\langle \mathbf{p}'|\frac{1}{E - (\mathbf{p}'^2/2m) \pm i\varepsilon}|\mathbf{p}''\rangle = \frac{\delta^{(3)}(\mathbf{p}' - \mathbf{p}'')}{E - (\mathbf{p}'^2/2m) \pm i\varepsilon} \\ &\langle \mathbf{x}|\mathbf{p}'\rangle = \frac{e^{i\mathbf{p}'\cdot\mathbf{x}/\hbar}}{(2\pi\hbar)^{3/2}} \\ &\langle \mathbf{p}''|\mathbf{x}'\rangle = \frac{e^{-i\mathbf{p}''\cdot\mathbf{x}'/\hbar}}{(2\pi\hbar)^{3/2}}. \end{aligned} \tag{B.11}$$

Therefore

$$G_\pm(\mathbf{x},\mathbf{x}') = \frac{\hbar^2}{2m}\int \frac{d^3p'}{(2\pi\hbar)^3}\frac{e^{i\mathbf{p}'\cdot(\mathbf{x}-\mathbf{x}')/\hbar}}{[E - (\mathbf{p}'^2/2m) \pm i\varepsilon]}. \tag{B.12}$$

We set $\mathbf{p}' = \hbar\mathbf{q}$ and $E = \hbar^2k^2/(2m)$

$$\begin{aligned} &G_\pm(\mathbf{x},\mathbf{x}') = \frac{1}{(2\pi)^3}\int_0^\infty q^2dq \int_0^{2\pi} d\phi \int_0^\pi \sin\theta d\theta \frac{e^{i|\mathbf{q}||\mathbf{x}-\mathbf{x}'|\cos\theta}}{k^2 - q^2 \pm i\varepsilon} = \\ &-\frac{1}{8\pi^2}\frac{1}{i|\mathbf{x}-\mathbf{x}'|}\int_{-\infty}^{\infty} dqq \frac{(e^{iq|\mathbf{x}-\mathbf{x}'|} - e^{-iq|\mathbf{x}-\mathbf{x}'|})}{q^2 - k^2 \mp i\varepsilon}. \end{aligned} \tag{B.13}$$

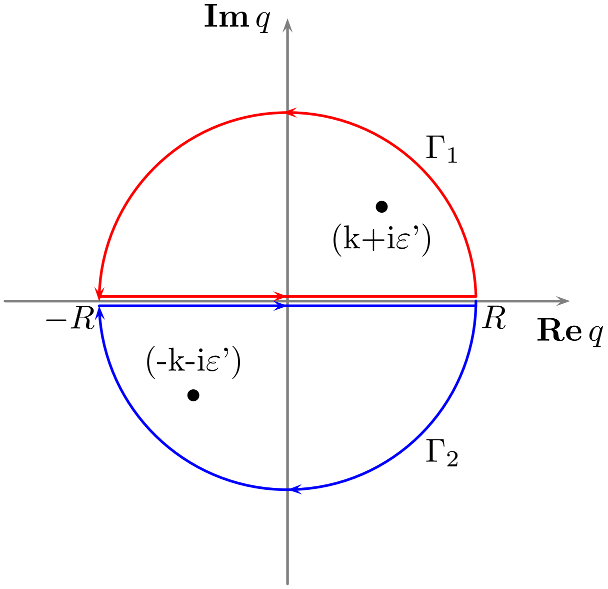

Figure B.1: Integration in the complex plane using the residues method.

The integrand has poles in the complex plane at $q^2 - k^2 \mp i\varepsilon$, or, $q = \pm(k \pm i\varepsilon')$, with $\varepsilon' = \varepsilon/k^2$. The original $+i\varepsilon$ corresponds to $+k + i\varepsilon'$ and $-k - i\varepsilon'$; and $-i\varepsilon$ corresponds to $+k - i\varepsilon'$ and $-k + i\varepsilon'$. The $+i\varepsilon$ case is represented in Figure (B.1).

Let us begin with $G_+(\mathbf{x}, \mathbf{x}')$

$$G_+(\mathbf{x}, \mathbf{x}') = -\frac{1}{8\pi^2} \frac{1}{i|\mathbf{x} - \mathbf{x}'|} \int_{-\infty}^{\infty} dq q \frac{(e^{iq|\mathbf{x}-\mathbf{x}'|} - e^{-iq|\mathbf{x}-\mathbf{x}'|})}{q^2 - k^2 \mp i\varepsilon} = \frac{-1}{8\pi^2 i|\mathbf{x} - \mathbf{x}'|} \left(\oint_{\Gamma_1} dq \frac{q(e^{iq|\mathbf{x}-\mathbf{x}'|})}{q^2 - k^2 - i\varepsilon} - \oint_{\Gamma_2} dq \frac{q(e^{-iq|\mathbf{x}-\mathbf{x}'|})}{q^2 - k^2 - i\varepsilon} \right), \tag{B.14}$$

where Γ_1 and Γ_2 are the paths shown in Figure (B.1). If we take the limit $\varepsilon \to 0$ and use

$$\frac{1}{q^2 - k^2} = \frac{1}{2q} \left(\frac{1}{q - k} + \frac{1}{q + k} \right), \tag{B.15}$$

the expression for $G_+(\mathbf{x}, \mathbf{x}')$ is

$$G_+(\mathbf{x}, \mathbf{x}') = \frac{-1}{16\pi^2 i|\mathbf{x} - \mathbf{x}'|} \left(\oint_{\Gamma_1} dq \frac{q(e^{iq|\mathbf{x}-\mathbf{x}'|})}{q - k} + \oint_{\Gamma_1} dq \frac{q(e^{iq|\mathbf{x}-\mathbf{x}'|})}{q + k} - \oint_{\Gamma_2} dq \frac{q(e^{-iq|\mathbf{x}-\mathbf{x}'|})}{q - k} - \oint_{\Gamma_2} dq \frac{q(e^{-iq|\mathbf{x}-\mathbf{x}'|})}{q + k} \right). \tag{B.16}$$

Only the integrals along paths that enclose a pole contribute. Using Cauchy's Theorem

$$\oint \frac{f(z)}{z - z_i} dz = 2\pi i f(z_i), \tag{B.17}$$

where z_i is a pole and the integral is taken in a counterclockwise path that encloses z_i, we evaluate $G_+(\mathbf{x},\mathbf{x}')$

$$G_+(\mathbf{x},\mathbf{x}') = -\frac{1}{4\pi}\frac{e^{ik|\mathbf{x}-\mathbf{x}'|}}{|\mathbf{x}-\mathbf{x}'|}. \tag{B.18}$$

The whole calculation can be repeated for $G_-(\mathbf{x},\mathbf{x}')$. Finally

$$G_\pm(\mathbf{x},\mathbf{x}') = -\frac{1}{4\pi}\frac{e^{\pm ik|\mathbf{x}-\mathbf{x}'|}}{|\mathbf{x}-\mathbf{x}'|}. \tag{B.19}$$

Using this result we may rewrite Eq. (B.6) as

$$\langle\mathbf{x}|\psi^{(\pm)}\rangle = \langle\mathbf{x}|\phi\rangle - \frac{2m}{\hbar^2}\int d^3x'\frac{1}{4\pi}\frac{e^{\pm ik|\mathbf{x}-\mathbf{x}'|}}{|\mathbf{x}-\mathbf{x}'|}\langle\mathbf{x}'|V|\psi^{(\pm)}\rangle. \tag{B.20}$$

Let us look at a local potential

$$\langle\mathbf{x}'|V|\mathbf{x}''\rangle = V(\mathbf{x}')\delta(\mathbf{x}'-\mathbf{x}''). \tag{B.21}$$

Then, Eq. (B.20) becomes

$$\langle\mathbf{x}|\psi^{(\pm)}\rangle = \langle\mathbf{x}|\phi\rangle - \frac{2m}{\hbar^2}\int d^3x'\frac{1}{4\pi}\frac{e^{\pm ik|\mathbf{x}-\mathbf{x}'|}}{|\mathbf{x}-\mathbf{x}'|}V(\mathbf{x}')\langle\mathbf{x}'|\psi^{(\pm)}\rangle. \tag{B.22}$$

As depicted in Figure B.2, the vector $\mathbf{x}$ is directed towards the observation point, at which the wavefunction is going to be evaluated. The potential is limited in space and we are interested in the study of a scatterer very far from the range of the potential, thus $|\mathbf{x}| \gg |\mathbf{x}'|$. We introduce the variables $r = |\mathbf{x}|$, $r' = |\mathbf{x}'|$ and α (the angle between $\mathbf{x}$ and $\mathbf{x}'$).

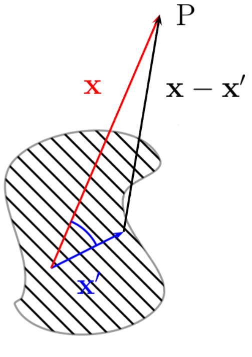

Figure B.2: The dashed region corresponds to the finite-range scattering potential. The point P denotes where the wavefunction $\langle\mathbf{x}|\psi^{(\pm)}\rangle$ is going to be evaluated.

For $r \gg r'$

$$|\mathbf{x}-\mathbf{x}'| = \sqrt{r^2 - 2rr'\cos\alpha + r'^2} = r\left(1 - \frac{2r'}{r}\cos\alpha + \frac{r'^2}{r^2}\right)^{1/2} \approx r - \hat{\mathbf{r}}\cdot\mathbf{x}', \tag{B.23}$$

with $\hat{\mathbf{r}} = \mathbf{x}/|\mathbf{x}|$. We also define $\mathbf{k}' = k\hat{\mathbf{r}}$ so that $\mathbf{k}'$ represents the propagation vector for waves reaching the observation point ($\mathbf{x}$). Thus

$$e^{\pm ik|\mathbf{x}-\mathbf{x}'|} \approx e^{\pm ikr \mp i\mathbf{k}'\cdot\mathbf{x}'} \text{ (large } r\text{)}. \tag{B.24}$$

Using $|\mathbf{k}\rangle$ instead of $|\mathbf{p}\rangle$, we have an expression for large r

$$\langle\mathbf{x}|\psi^{(+)}\rangle = \langle\mathbf{x}|\mathbf{k}\rangle - \frac{1}{4\pi}\frac{2m}{\hbar^2}\frac{e^{ikr}}{r}\int d^3x' \frac{e^{-i\mathbf{k}'\cdot\mathbf{x}'}}{|\mathbf{x}-\mathbf{x}'|}V(\mathbf{x}')\langle\mathbf{x}'|\psi^{(+)}\rangle = \frac{1}{(2\pi)^{3/2}}\left[e^{i\mathbf{k}\cdot\mathbf{x}} + \frac{e^{ikr}}{r}f(\mathbf{k}',\mathbf{k})\right] \quad \text{(large } r\text{)}. \tag{B.25}$$

Therefore, for large r, we have the original plane wave in the propagation direction $\mathbf{k}$ plus an outgoing spherical wave with amplitude $f(\mathbf{k}',\mathbf{k})$

$$f(\mathbf{k}',\mathbf{k}) = -\frac{1}{4\pi}\frac{2m}{\hbar^2}(2\pi)^3\int d^3x' \frac{e^{-i\mathbf{k}'\cdot\mathbf{x}'}}{(2\pi)^{3/2}}V(\mathbf{x}')\langle\mathbf{x}'|\psi^{(+)}\rangle = -\frac{1}{4\pi}\frac{2m}{\hbar^2}(2\pi)^3\langle\mathbf{k}'|V|\psi^{(+)}\rangle. \tag{B.26}$$

Similarly for $\langle\mathbf{x}|\psi^{(-)}\rangle$ we have the original plane wave plus an *incoming* spherical wave.

$$\langle\mathbf{x}|\psi^{(-)}\rangle = \frac{1}{(2\pi)^{3/2}}\left[e^{i\mathbf{k}\cdot\mathbf{x}} + \frac{e^{-ikr}}{r}f(\mathbf{k}',\mathbf{k})\right], \tag{B.27}$$

$$f(\mathbf{k}',\mathbf{k}) = -\frac{1}{4\pi}\frac{2m}{\hbar^2}(2\pi)^3\langle-\mathbf{k}'|V|\psi^{(-)}\rangle. \tag{B.28}$$

The differential cross section $d\sigma/d\Omega$ is related to the amplitude $f(\mathbf{k}',\mathbf{k})$

$$\frac{d\sigma}{d\Omega} = |f(\mathbf{k}',\mathbf{k})|^2. \tag{B.29}$$

B.2 Transition operator

Eq. (B.26) contains the unknown $|\psi^{(+)}\rangle$. The transition operator T is defined such that

$$V|\psi^{(+)}\rangle = T|\phi\rangle. \tag{B.30}$$

Multiplying the Lippmann-Schwinger equation, Eq. (B.5) , by V yields

$$T|\phi\rangle = V|\phi\rangle + V\frac{1}{E-H_0+i\varepsilon}T|\phi\rangle. \tag{B.31}$$

The $|\phi\rangle$ are plane-wave states, which are a complete set. Therefore, the following equation must be satisfied

$$T = V + V\frac{1}{E-H_0+i\varepsilon}T. \tag{B.32}$$

We rewrite Eq. (B.26) as

$$f(\mathbf{k}', \mathbf{k}) = -\frac{1}{4\pi}\frac{2m}{\hbar^2}(2\pi)^3\langle \mathbf{k}'|T|\mathbf{k}\rangle. \tag{B.33}$$

Hence, to determine $f(\mathbf{k}', \mathbf{k})$ it is sufficient to know the transition operator T. We can obtain an iterative solution

$$T = V + V\frac{1}{E - H_0 + i\varepsilon}V + V\frac{1}{E - H_0 + i\varepsilon}V\frac{1}{E - H_0 + i\varepsilon}V + \cdots \tag{B.34}$$

We expand $f(\mathbf{k}', \mathbf{k})$ as

$$f(\mathbf{k}', \mathbf{k}) = \sum_{n=1}^{\infty} f^{(n)}(\mathbf{k}', \mathbf{k}), \tag{B.35}$$

where n is the number of times the V operator appears

$$\begin{aligned} f^{(1)}(\mathbf{k}', \mathbf{k}) &= -\frac{1}{4\pi}\frac{2m}{\hbar^2}(2\pi)^3\langle \mathbf{k}'|V|\mathbf{k}\rangle, \\ f^{(2)}(\mathbf{k}', \mathbf{k}) &= -\frac{1}{4\pi}\frac{2m}{\hbar^2}(2\pi)^3\langle \mathbf{k}'|V\frac{1}{E - H_0 + i\varepsilon}V|\mathbf{k}\rangle, \\ &\vdots \end{aligned} \tag{B.36}$$

A physical interpretation is that $f^{(2)}$ is viewed as a two-step process, $f^{(3)}$ is a three-step process, and so on.

B.3 Partial waves method

In the previous discussions we have considered the free-particle states as plane-waves, however the free-particle Hamiltonian H_0 also commutes with $\mathbf{L}^2$ and L_z. It is useful to introduce the spherical-wave states $|E, l, m\rangle$, such that

$$\begin{aligned} H_0|E, l, m\rangle &= E|E, l, m\rangle, \\ \mathbf{L}^2|E, l, m\rangle &= \hbar^2 l(l+1)|E, l, m\rangle, \\ L_z|E, l, m\rangle &= \hbar m|E, l, m\rangle. \end{aligned} \tag{B.37}$$

These states are

$$\begin{aligned} \langle \mathbf{k}|E, l, m\rangle &= \frac{\hbar}{\sqrt{mk}}\delta\left(E - \frac{\hbar^2 k^2}{2m}\right)Y_l^m(\hat{\mathbf{k}}), \\ \langle \mathbf{x}|E, l, m\rangle &= \frac{i^l}{\hbar}\sqrt{\frac{2mk}{\pi}}j_l(kr)Y_l^m(\hat{\mathbf{r}}), \end{aligned} \tag{B.38}$$

in the momentum and position basis, respectively. The Y_l^m are the spherical harmonics and j_l is the spherical Bessel function of order l.

Let us assume that the potential is spherically symmetric, that is, invariant under rotations in three dimensions. Then the T operator, Eq. (B.34), commutes with $\mathbf{L}^2$ and $\mathbf{L}$. In other words, T is a scalar operator. It is now useful to use the spherical-wave basis, because the Wigner-Eckart theorem applied to a scalar operator yields

$$\langle E', l', m'|T|E, l, m\rangle = T_l(E)\delta_{ll'}\delta_{mm'}. \tag{B.39}$$

Thus, T is diagonal both in l and m. Furthermore, the diagonal non-vanishing element depends on E and l, but not m.

Let us look again at the scattering amplitude, Eq. (B.33),

$$\begin{aligned} f(\mathbf{k}', \mathbf{k}) &= -\frac{1}{4\pi}\frac{2m}{\hbar^2}(2\pi)^3\langle\mathbf{k}'|T|\mathbf{k}\rangle \\ &= -\frac{1}{4\pi}\frac{2m}{\hbar^2}(2\pi)^3\sum_{l,m,l',m'}\int dE\int dE'\langle\mathbf{k}'|E'l'm'\rangle\langle E'l'm'|T|Elm\rangle\langle Elm|\mathbf{k}\rangle \\ &= -\frac{4\pi^2}{k}\sum_{l,m}T_l(E)\Big|_{E=\hbar^2k^2/(2m)} Y_l^m(\hat{\mathbf{k}'})Y_l^{m*}(\hat{\mathbf{k}}). \end{aligned} \tag{B.40}$$

We define the partial-wave amplitude

$$f_l(k) \equiv -\frac{\pi T_l(E)}{k}, \tag{B.41}$$

choose $\mathbf{k}$ in the positive z-direction, and θ the angle between $\mathbf{k}'$ and $\mathbf{k}$. The result is

$$f(\mathbf{k}', \mathbf{k}) = f(\theta) = \sum_{l=0}^{\infty}(2l+1)f_l(k)P_l(\cos\theta), \tag{B.42}$$

where the P_l are Legendre polynomials. For large r we have

$$\langle\mathbf{x}|\psi^{(+)}\rangle \xrightarrow{\text{large } r} \frac{1}{(2\pi)^{3/2}}\sum_l(2l+1)\frac{P_l}{2ik}\left[[1+2ikf_l(k)]\frac{e^{ikr}}{r} - \frac{e^{-i(kr-l\pi)}}{r}\right]. \tag{B.43}$$

The physics behind scattering is now clear: in the absence of a scatterer, the plane-wave behaves as a sum of a spherically outgoing wave plus a spherically incoming wave (for each l). The presence of the scatterer changes the coefficient of the outgoing wave

$$1 \to 1 + 2ikf_l(k). \tag{B.44}$$

As for the incoming wave, it is completely unaffected.

B.3.1 Unitarity and phase shifts

We now examine the consequences of unitarity. The current density $\mathbf{j}$ must satisfy

$$\nabla \cdot \mathbf{j} = -\frac{\partial |\psi|^2}{\partial t} = 0. \tag{B.45}$$

Let us consider a spherical surface of very large radius; by Gauss's theorem we have

$$\int_{\text{spherical surface}} \mathbf{j} \cdot d\mathbf{S} = 0. \tag{B.46}$$

Physically this means that there is no source or sink of particles. Because of angular momentum conservation, this must hold for each partial wave separately. We define

$$S_l(k) \equiv 1 + 2ikf_l(k), \tag{B.47}$$

with

$$|S_l(k)| = 1, \tag{B.48}$$

consequence of Eq. (B.44). Thus, the most that can happen is a change in the phase of the outgoing wave. Eq. (B.48) is know as the **unitary relation** for the l-th partial wave. Calling this phase $2\delta_l$ [1], we write

$$S_l = e^{2i\delta_l}, \tag{B.49}$$

with real δ_l, which is a function of k. From Eq. (B.47),

$$f_l = \frac{(S_l - 1)}{2ik} = \frac{(e^{2i\delta_l} - 1)}{2ik} = \frac{e^{i\delta_l}\sin\delta_l}{k} = \frac{1}{k\cot\delta_l - ik}. \tag{B.50}$$

The full scattering amplitude is

$$f(\theta) = \frac{1}{k}\sum_{l=0}(2l+1)e^{i\delta_l}\sin\delta_l P_l(\cos\theta). \tag{B.51}$$

B.3.2 Determination of phase shifts

Let us consider how we may actually determine the phase shifts given a potential V. We assume that the potential vanishes for $r > R$, R being the range of the potential. Outside, the wavefunction must be a free spherical wave, a linear combination of $j_l(kr)P_l(\cos\theta)$ and $n_l(kr)P_l(\cos\theta)$, where n_l is the spherical Bessel function of second kind of order l. Alternatively, we may use the spherical Hankel functions

$$\begin{aligned} h_l^{(1)} &= j_l + in_l, \\ h_l^{(2)} &= j_l - in_l, \end{aligned} \tag{B.52}$$

---

[1] The factor of 2 is conventional.

with asymptotic behavior

$$\begin{aligned} h_l^{(1)} &\xrightarrow{\text{large } r} \frac{e^{i(kr-(l\pi/2))}}{ikr}, \\ h_l^{(2)} &\xrightarrow{\text{large } r} -\frac{e^{-i(kr-(l\pi/2))}}{ikr}. \end{aligned} \tag{B.53}$$

The full wavefunction may be written as

$$\langle \mathbf{x}|\psi^{(+)}\rangle = \frac{1}{(2\pi)^{3/2}}\sum_l i^l(2l+1)A_l(r)P_l(\cos\theta) \quad (r > R), \tag{B.54}$$

with the radial wavefunction

$$A_l = c_l^{(1)}h_l^{(1)}(kr) + c_l^{(2)}h_l^{(2)}(kr). \tag{B.55}$$

The coefficients are chosen such that, for $V = 0$, A_l coincides with $j_l(kr)$ everywhere; furthermore, the coefficients must reproduce the expected behavior for large r. The coefficients are $c_l^{(1)} = e^{2i\delta_l}/2$ and $c_l^{(2)} = 1/2$, so that

$$A_l(r) = e^{i\delta_l}[\cos\delta_l j_l(kr) - \sin\delta_l n_l(kr)]. \tag{B.56}$$

Now we can evaluate the logarithmic derivative at $r = R$,

$$\beta_l \equiv \left(\frac{r}{A_l}\frac{dA_l}{dr}\right)_{r=R} = kR\left[\frac{j_l'(kR)\cos\delta_l - n_l'(kR)\sin\delta_l}{j_l(kR)\cos\delta_l - n_l(kR)\sin\delta_l}\right]. \tag{B.57}$$

Conversely,

$$\tan\delta_l = \frac{kRj_l'(kR) - \beta_l j_l(kR)}{kRn_l'(kR) - \beta_l n_l(kR)}, \tag{B.58}$$

and the problem of obtaining the phase shift is reduced to obtaining β_l.

Now we look at the solution of Schrodinger's equation for $r < R$. For a spherically symmetric potential, it is equivalent to the unidimensional equation

$$\frac{d^2u_l}{dr^2} + \left(k^2 - \frac{2m}{\hbar^2}V - \frac{l(l+1)}{r^2}\right)u_l = 0, \tag{B.59}$$

with $u_l = rA_l(r)$. The boundary condition is $u_l|_{r=0} = 0$. We obtain the logarithmic derivative and match the inside and outside solutions at $r = R$,

$$\beta_l|_{\text{inside}} = \beta_l|_{\text{outside}}. \tag{B.60}$$

B.4 Low-energy scattering and bound states

At low energies, precisely when $\lambdabar = 1/k$ is comparable to or larger than R, partial waves for large l are unimportant. The effective potential for the l-th partial wave is given by

$$V_{eff} = V(r) + \frac{\hbar^2}{2m}\frac{l(l+1)}{r^2}. \tag{B.61}$$

Unless the potential is strong enough to accommodate $l \neq 0$ bound states, the behavior of the wavefunction is largely determined by the centrifugal barrier term, so it should resemble $j_l(kr)$. Qualitatively, the integral equation for the partial wave is

$$\frac{e^{i\delta_l \sin\delta_l}}{k} = -\frac{2m}{\hbar^2}\int_0^\infty j_l(kr)V(r)A_l(r)r^2 dr. \tag{B.62}$$

If $A_l(r) \sim j_l(kr)$ and $1/k$ is much larger than R, the right-hand side varies as $\sim k^{2l}$, and for small δ_l the left-hand side goes with δ_l/k. Hence, the phase shift goes to zero as $\delta_l \sim k^{2l+1}$ (for small k). It is clear that at low energies and finite range potential, s-wave scattering is very important.

B.4.1 Rectangular well or barrier

Let us consider the s-wave scattering by the potential

$$V = \begin{cases} V_0 = \text{ constant} & \text{if } \quad r < R \\ 0 & \text{otherwise.} \end{cases} \tag{B.63}$$

For $V_0 > 0$ it is repulsive and for $V_0 < 0$ it is attractive. Many of the features obtained in this simple model are common to more complicate finite range potentials.

The outside wavefunction must behave like

$$e^{i\delta_0}[j_0(kr)\cos\delta_0 - n_0(kr)\sin\delta_0] \simeq \frac{e^{i\delta_0}\sin(kr+\delta_0)}{kr}. \tag{B.64}$$

The inside solution is

$$u_{l=0}(r) \propto \sin(k'r), \tag{B.65}$$

with k' satisfying

$$E - V_0 = \frac{\hbar^2 k'^2}{2m}. \tag{B.66}$$

We used the boundary condition $u(r=0)=0$, so that the inside wavefunction is sinusoidal as long $E > V_0$ holds. The curvature of the sinusoidal wave changes from the $V = 0$ case; it can be pushed in for $\delta_0 > 0$, or pulled out for $\delta_0 < 0$, depending if $V_0 < 0$ or $V_0 > 0$, Fig. B.3. For $V_0 > E$ we have to change the inside solution to

$$u(r) \propto \sinh[\kappa r], \tag{B.67}$$

with

$$V_0 - E = \frac{\hbar^2 \kappa^2}{2m}. \tag{B.68}$$

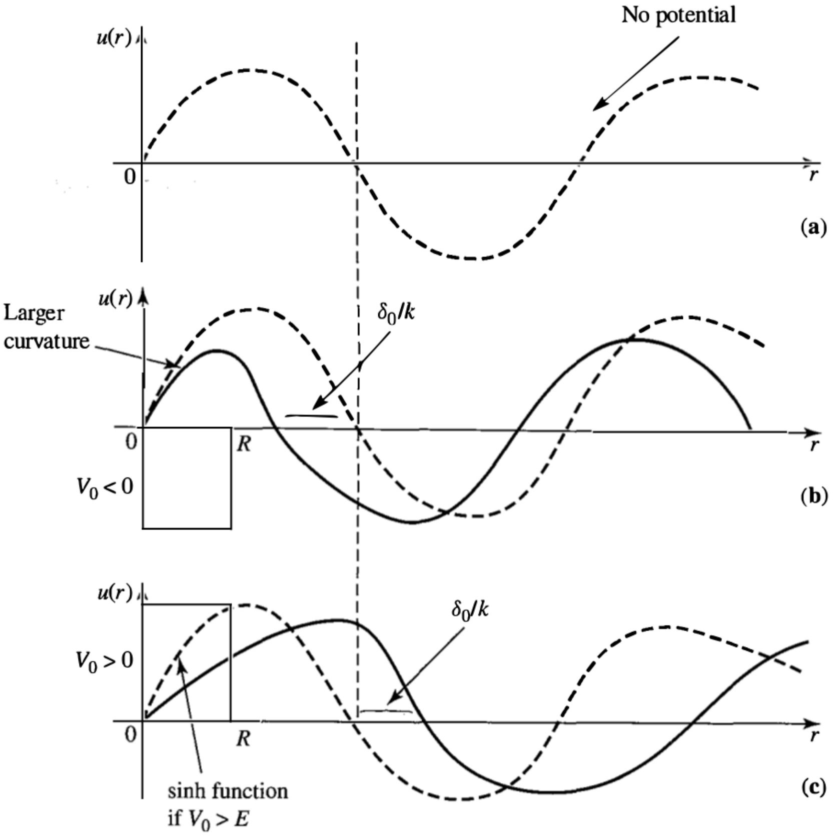

Figure B.3: Figures from [24] showing $u(r) \times r$ for $V = 0$ (a); $V_0 < 0$ and $\delta_0 > 0$ (b); $V_0 > 0$ and $\delta_0 < 0$ (c).

B.4.2 Zero-energy scattering and bound states

Let us consider scattering at extremely low energies, $k \simeq 0$. The outside wavefunction, $r > R$, for $l = 0$ satisfies

$$\frac{d^2u}{dr^2} = 0. \tag{B.69}$$

The solution is

$$u(r) = \text{constant}(r - a). \tag{B.70}$$

The physical meaning of the solution is an infinitely long wavelength limit of the outside wavefunction. We have

$$\lim_{k\to 0} \sin(kr + \delta_0) = \lim_{k\to 0} \sin\left[k\left(r + \frac{\delta_0}{k}\right)\right], \tag{B.71}$$

hence

$$\frac{u'}{u} = k\cot\left[k\left(r + \frac{\delta_0}{k}\right)\right] \xrightarrow{k\to 0} \frac{1}{r-a}. \tag{B.72}$$

Setting $r = 0$,

$$\lim_{k\to 0} k\cot\delta_0 \xrightarrow{k\to 0} -\frac{1}{a}. \tag{B.73}$$

The quantity a is known as the **scattering length**.

Both a and R have the same dimensions, but they can differ by orders of magnitude. To see the physical meaning of a, we note that a is the intercept of the outside wavefunction. For an attractive potential, the intercept is on the negative side, Fig. B.4 (a). If we increase the attraction, the outside wavefunction can again cross the r-axis on the positive side, Fig. B.4 (b).

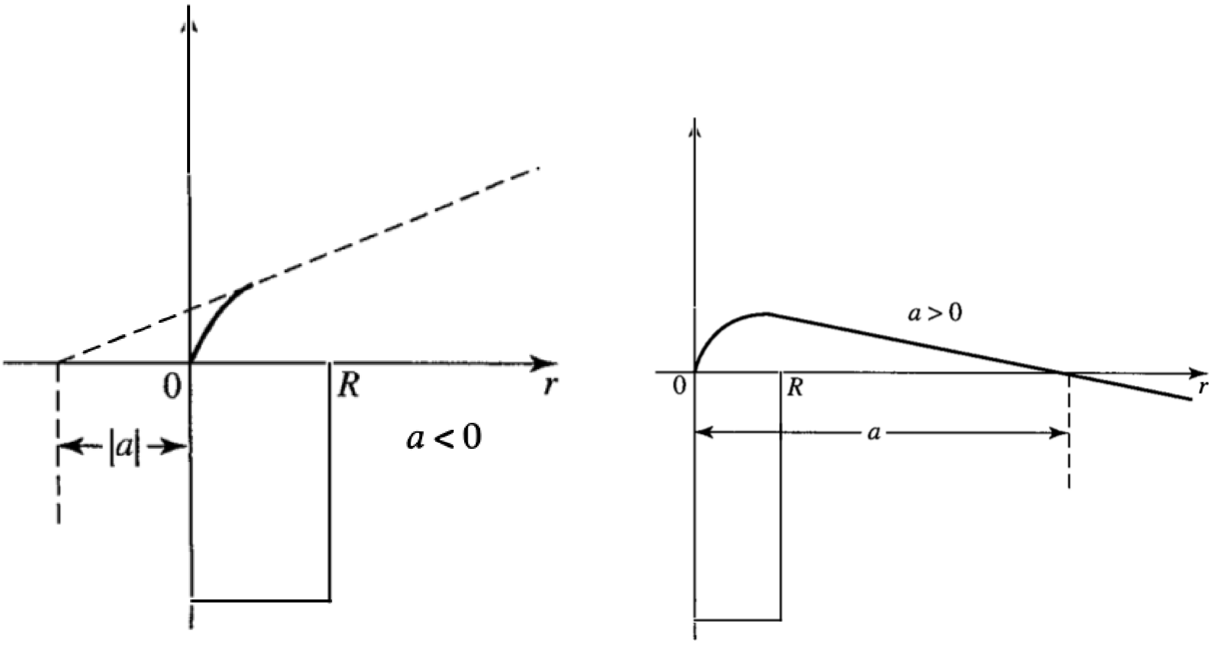

(a) (b)

Figure B.4: Figures from [24] showing $u(r) \times r$ for an attractive potential (a) and deeper attraction (b). For each case the intercept a of the zero-energy outside wavefunction with the r-axis is shown.

The sign change with increasing attraction is result of the appearance of a bound state. If a is very large and positive, the wavefunction is flat for $r > R$, Fig. B.4 (b). However, from Eq. (B.70), a very large is not too different from $e^{-\kappa r}$ with $\kappa \simeq 0$. Now $e^{-\kappa r}$ with κ essentially zero is a bound-state for $r > R$ with energy infinitesimally negative. The inside wavefunction, $r < R$, for the $E = 0+$ case, and the $E = 0-$ case are essentially the same; in both cases k' is given by

$$\frac{\hbar^2 k'^2}{2m} = E - V_0 \simeq |V_0|, \tag{B.74}$$

with infinitesimal E (positive or negative).

The inside wavefunctions are the same for $E = 0+$ and $E = 0-$, so we calculate the logarithmic derivative of the bound-state wavefunction and equate it with the logarithmic derivative of the zero kinetic energy scattering,

$$-\frac{\kappa e^{-\kappa r}}{e^{-\kappa r}}\bigg|_{r=R} = \left(\frac{1}{r-a}\right)\bigg|_{r=R}. \tag{B.75}$$

If $R \ll a$, then

$$\kappa \simeq \frac{1}{a}. \tag{B.76}$$

The binding energy is

$$E_{BE} = -E_{\text{bound state}} = \frac{\hbar^2\kappa^2}{2m} \simeq \frac{\hbar^2}{2ma^2}. \tag{B.77}$$

We have a relation between the scattering length and the bound-state energy!

B.5 Identical particles and scattering

Let us consider the scattering of identical particles. The wavefunction must be symmetric under interchange of the coordinates of two particles if they are bosons, and antisymmetric if they are fermions. Interchanging two particles corresponds to changing the sign of the relative coordinate, that is $\mathbf{r} \to -\mathbf{r}$. In terms of the spherical coordinates

$$\begin{aligned} r &\to r, \\ \theta &\to \pi - \theta, \\ \varphi &\to \pi + \varphi. \end{aligned} \tag{B.78}$$

The symmetrized wavefunction corresponding to Eq. (B.25) is

$$\langle \mathbf{x}|\psi^{(+)}\rangle = \frac{1}{(2\pi)^{3/2}}\left[\left\{e^{i\mathbf{k}\cdot\mathbf{x}} \pm e^{-i\mathbf{k}\cdot\mathbf{x}}\right\} + \frac{e^{ikr}}{r}\left\{f(\theta) \pm f(\pi-\theta)\right\}\right]. \tag{B.79}$$

Thus, the differential cross section is

$$\frac{d\sigma}{d\Omega} = |f(\theta) \pm f(\pi-\theta)|^2, \tag{B.80}$$

with the plus sign for bosons and the minus sign for fermions. Considering the problem of zero-energy scattering, Sec. B.4.2, the total cross section is

$$\sigma = \begin{cases} 8\pi a^2 & \text{for bosons} \\ 0 & \text{for fermions.} \end{cases} \tag{B.81}$$

Appendix C

Superfluid Fermi gases

In this Appendix we review some aspects of superfluidity in Fermi gases. In the next section, Sec. C.1, we review some equilibrium properties of Fermi gases; we study the effects of interactions between the components of the gas in Sec. C.2; and we briefly introduce properties of the condensed phase, Sec. C.3.

C.1 Equilibrium properties of Fermi gases

Let us consider N fermions of mass m in the same internal state. The density of states of particles in a box of volume V is

$$g(\epsilon) = \frac{V(2m)^{3/2}}{4\pi^2\hbar^3}\epsilon^{1/2}. \tag{C.1}$$

We define a function $G(\epsilon)$ which is the number of states with energy less than ϵ. Thus, $g(\epsilon) = \frac{dG(\epsilon)}{d\epsilon}$ and we find

$$G(\epsilon) = \frac{V(2m\epsilon)^{3/2}}{6\pi^2\hbar^3}. \tag{C.2}$$

In the ground state, all states with energy less than the zero-temperature chemical potential μ are occupied, hence $G(\mu) = N$. Also, the Fermi energy is equal to the chemical potential at $T = 0$, thus

$$G(\mu = \epsilon_F) = \frac{V(2m\epsilon_F)^{3/2}}{6\pi^2\hbar^3} = N. \tag{C.3}$$

Accordingly,

$$g(\mu) = \frac{3N}{2\mu}. \tag{C.4}$$

The Fermi temperature is defined as $T_F = \epsilon_F/k_B$, hence

$$kT_F = \frac{(6\pi^2)^{2/3}}{2}\frac{\hbar^2}{m}n^{2/3} \approx 7.596\frac{\hbar^2}{m}n^{2/3}. \tag{C.5}$$

We also introduce the density of states per unit of volume

$$N(\epsilon) = \frac{g(\epsilon)}{V} = \frac{m^{3/2}}{2^{1/2}\pi^2\hbar^3}\epsilon^{1/2}. \tag{C.6}$$

This function evaluated at the Fermi energy is

$$N(\epsilon_F) = \frac{3n}{2\epsilon_F}, \tag{C.7}$$

in accordance with Eq. (C.4).

In order to study the thermodynamical properties, we consider the Fermi function

$$f = \frac{1}{e^{(\epsilon-\mu)/k_BT}+1}, \tag{C.8}$$

where $\mu = \mu(T)$. The total energy is given by

$$E(T) = \int_0^\infty d\epsilon\ \epsilon\ g(\epsilon)f(\epsilon). \tag{C.9}$$

At $T = 0$ the distribution function reduces to a step function, hence

$$E(T=0) = \frac{3}{5}N\mu. \tag{C.10}$$

For temperatures lower than T_F, a low-temperature expansion may be carried out. The expansion for the energy is [113]

$$E \simeq E(T=0) + \frac{\pi^2}{6}g(\mu)(k_BT)^2, \tag{C.11}$$

with the chemical potential given by Eq. (C.4). High-temperatures expansions are also possible. The energy E tends toward its classical value $(3/2)Nk_BT$.

C.2 Effects of interactions

Interactions can play a very important role in mixtures of two kinds of fermions. For example, let us consider a uniform gas of equal densities of two kinds of fermions, with same mass. The kinetic energy per particle is $\sim \epsilon_F = (\hbar k_F)^2/2m$, and the interaction energy per particle is $\sim nU_0$, where $U_0 = 4\pi\hbar^2 a/m$ is the effective interaction between two unlike fermions [113], a being the scattering length. The ratio of the interaction energy to the Fermi energy is

$$\frac{nU_0}{\epsilon_F} = \frac{4}{3\pi}k_F a, \tag{C.12}$$

which is of the order of the scattering length divided by the interparticle spacing; a typical value for this quantity is 10^{-2}. Therefore, we expect particle interactions to have little influence of thermodynamical quantities of the gas, except when the magnitude of the scattering length is comparable to, or larger than, the interparticle separation.

C.2.1 Superfluidity

As we have seen, the effects of interactions can be quite small, but they can be significant if the effective interaction is attractive. The gas undergoes a transition to a superfluid state in which atoms are paired analogously to electrons in superconductors as predicted by Bardeen, Cooper and Schrieffer (BCS) [144].

The properties of mixtures of dilute Fermi gases with attractive interactions are of interest in a wide number of contexts other than cold atoms. One of these is nuclear physics and astrophysics, where dilute mixtures of neutrons and protons (with two spin states each) are encountered in the outer parts of atomic nuclei and in the crust of neutron stars. Another example is the BCS-BEC crossover, as discussed in Chapter 6, which is related to the change in the regime when the interaction strength is varied.

A rough estimate of the transition temperature may be obtained by considering a simplified model, where the interaction between fermions is a constant $-|U|$ for states with energies within E_c of the Fermi energy, and zero otherwise. The prediction of this model is [113]

$$kT_c \sim E_c e^{-\frac{1}{N(\epsilon_F)|U|}}. \tag{C.13}$$

For electrons in metals, the attractive interaction arises from the exchange of phonons, and the cutoff energy E_c is comparable with the maximum energy of an acoustic phonon $\hbar\omega_D$, where ω_D is the Debye frequency. In dilute gases, the dominant part of the interaction is the direct interaction between atoms. We take $U = U_0$, the usual low-energy result, and the cutoff energy to be an energy scale over which the density of states varies, namely ϵ_F. This leads to [113]

$$kT_c \sim \epsilon_c e^{-\frac{1}{N(\epsilon_F)|U_0|}}. \tag{C.14}$$

In the following sections we describe the quantitative theory of the condensed state. We follow closely the approach of [113]. First, we calculate the transition temperature. We show the existence of a bound state considering two-body scattering *in vacuo*, which causes a divergence in the T matrix at the energy of the state. Similarly, for two-particles in a medium, the pairing is signalled by a divergence in the two-body scattering, as shown in [145]. The transition temperature is determined by analyzing when the scattering of two fermions becomes singular.

C.2.2 Transition temperature

Let us begin with the scattering of two fermions in a uniform Fermi gas, which differs from two-particle scattering *in vacuo* due to the effects of other fermions. Since there is no scattering at low energies for fermions in the same internal state, we consider a mixture of two kinds of fermions ‘a’ and ‘b’, which can be different internal states of the same isotope with same mass and equal densities. The common Fermi wave number will be denoted by k_F.

The fact that two-body scattering takes place in a medium has a number of effects on the scattering process. For example, the energies of the particles are shifted by the mean field of the other particles and, in a dilute gas, this effect is independent of the momentum of a particle. Thus, the equation for the T matrix will be unaltered, provided that we consider the constant energy shift. A second effect is that some states are occupied, hence they are unavailable as intermediate scattering states. In the Lippmann-Schwinger equation, Eq. (B.5), the intermediate state is an a-particle with momentum $\mathbf{p}''$ and a b-particle with momentum $-\mathbf{p}''$, represented in Fig. C.1 (a). The probabilities that these states are unoccupied are $1 - f_{\mathbf{p}''}$ and $1 - f_{-\mathbf{p}''}$, therefore the contributions from these intermediate states must be accounted for in the blocking factors. We omit the hyperfine state labels 'a' and 'b' because the distribution functions, in this case, are the same. Modifying the Lippmann-Schwinger equation with the previous arguments yields

$$T(\mathbf{p}', \mathbf{p}; E) = U(\mathbf{p}', \mathbf{p}) + \frac{1}{V}\sum_{\mathbf{p}''} U(\mathbf{p}', \mathbf{p}'')\frac{(1 - f_{\mathbf{p}''})(1 - f_{-\mathbf{p}''})}{E - 2\epsilon^0_{\mathbf{p}''} + i\delta} T(\mathbf{p}'', \mathbf{p}; E), \tag{C.15}$$

where $\epsilon^0_{\mathbf{p}} = p^2/(2m)$ is the free-particle energy.

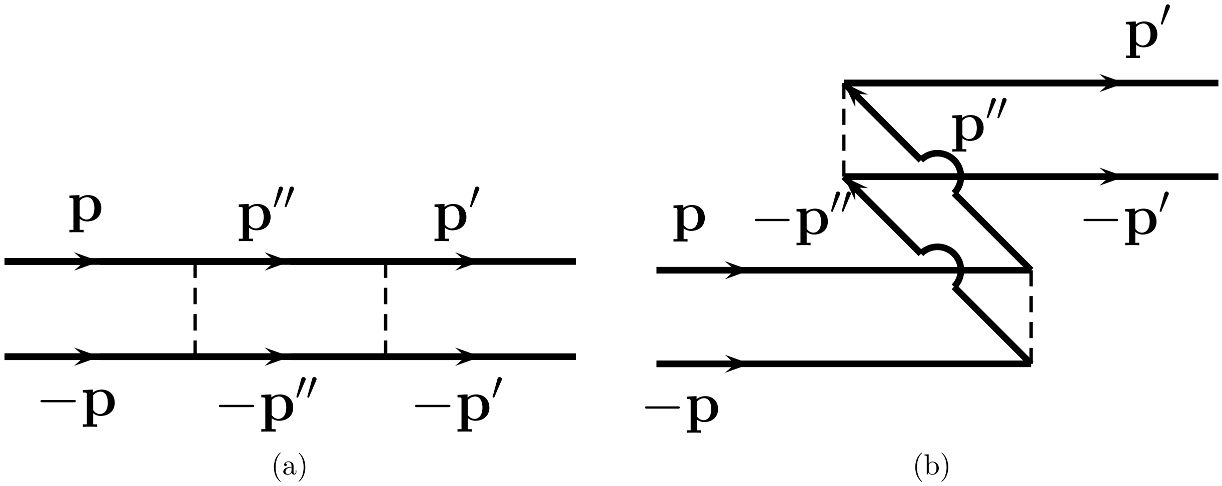

Figure C.1: Diagrams representing two-particle (a) and two-hole (b) intermediate states in two-particle scattering. Solid lines represent the two kinds of fermions, and dashed lines correspond to the bare interactions. Time advances from left to right, thus arrows to the right stand for particles and arrows to the left are holes.

A third effect of the medium is that interactions can excite two fermions from the Fermi sea to states outside, that is, two particles and two holes are created. The two holes then annihilate with the two incoming particles, Fig. C.1 (b). The contribution to the Lippmann-Schwinger equation from this process differs much from that of two-particles. First, holes can only be created in occupied states, with probability $f_{\pm\mathbf{p}''}$ for the two states. Hence, the thermal factors are $f_{\pm\mathbf{p}''}$ (opposed to $1 - f_{\pm\mathbf{p}''}$). Second, the energy to create a hole is the negative of the energy for a particle. Also, the intermediate state contains the pairs of particles in the initial and final states, each of energy E, thus the energy of the intermediate state is $2E - 2\epsilon_{\mathbf{p}''}$. The difference between E and the energy of the intermediate state is, in the hole-hole case, the negative of that for particle-particle one. The equation including both types of intermediate states is

$$\begin{aligned} T(\mathbf{p}', \mathbf{p}; E) &= U(\mathbf{p}', \mathbf{p}) + \frac{1}{V}\sum_{\mathbf{p}''} U(\mathbf{p}', \mathbf{p}'') \frac{(1 - f_{\mathbf{p}''})(1 - f_{-\mathbf{p}''}) - f_{\mathbf{p}''} f_{-\mathbf{p}''}}{E - 2\epsilon^0_{\mathbf{p}''} + i\delta} T(\mathbf{p}'', \mathbf{p}; E) \\ &= U(\mathbf{p}', \mathbf{p}) + \frac{1}{V}\sum_{\mathbf{p}''} U(\mathbf{p}', \mathbf{p}'') \frac{1 - f_{\mathbf{p}''} - f_{-\mathbf{p}''}}{E - 2\epsilon^0_{\mathbf{p}''} + i\delta} T(\mathbf{p}'', \mathbf{p}; E). \end{aligned} \tag{C.16}$$

The greatest effect of intermediate states is achieved when $E = 2\mu = p_F^2/m$, since the sign of $1 - f_{\mathbf{p}''} - f_{-\mathbf{p}''}$ is the opposite of the sign of the energy denominator, thus all terms of the sum have the same sign.

When the T matrix diverges, the first term on the right-hand side of Eq. (C.16) may be neglected, and the resulting expression is

$$T(\mathbf{p}', \mathbf{p}; 2\mu) = -\frac{1}{V}\sum_{\mathbf{p}''} U(\mathbf{p}', \mathbf{p}'') \frac{1 - 2f_{\mathbf{p}''}}{2\xi_{\mathbf{p}''}} T(\mathbf{p}'', \mathbf{p}; 2\mu), \tag{C.17}$$

with $\xi_{\mathbf{p}} = p^2/(2m) - \mu$. We did not include the infinitesimal imaginary part since the numerator vanishes at the Fermi surface. The temperature is present in the right-hand side of the equation through the Fermi function, and this equation determines the temperature at which the scattering diverges.

C.2.3 Eliminating the bare interaction

Replacing the bare interaction by a constant, the sum on the right-hand side of Eq. (C.17) for momenta less than some cutoff p_c, diverges as $p_c \to \infty$. To remove the high-momenta dependence, we eliminate the bare potential in favor of U_0. We write Eq. (C.17) as

$$T = UG_M T, \tag{C.18}$$

where G_M is the propagator for two particles and the subscript M refers to the presence of the medium. We denote by T_0 the T matrix in free space and for $E = 0$,

$$T(\mathbf{p}', \mathbf{p}; 0) = U(\mathbf{p}', \mathbf{p}) - \frac{1}{V}\sum_{\mathbf{p}''} U(\mathbf{p}', \mathbf{p}'') \frac{1}{2\epsilon^0_{\mathbf{p}''} - i\delta} T_0(\mathbf{p}'', \mathbf{p}; 0), \tag{C.19}$$

formally written as

$$T_0 = U + UG_0T_0, \tag{C.20}$$

where G_0 is the propagator of two free particles *in vacuo*. The infinitesimal imaginary part accounts for intermediate states having the same energy as the initial state. Its contributions are proportional to the density of states, which varies as $\sim p_F$. These are small at low densities, thus we neglect them and use the principal-value of the integrals. Solving for U,

$$U = T_0(1 + G_0T_0)^{-1} = (1 + G_0T_0)^{-1}T_0. \tag{C.21}$$

Eq. (C.18) can be rewritten as

$$T = (1 + T_0G_0)^{-1}T_0G_MT. \tag{C.22}$$

Multiplying on the left by $(1 + T_0G_0)$ yields

$$T = T_0(G_M - G_0)T, \tag{C.23}$$

or

$$T(\mathbf{p}', \mathbf{p}; 2\mu) = \frac{1}{V}\sum_{\mathbf{p}''} T_0(\mathbf{p}', \mathbf{p}''; 0)\left[\frac{2f_{\mathbf{p}''} - 1}{2\xi_{\mathbf{p}''}} + \frac{1}{2\epsilon^0_{\mathbf{p}''}}\right] T(\mathbf{p}'', \mathbf{p}; 2\mu). \tag{C.24}$$

The quantity inside the square bracket is appreciable only for momenta less than or approximately p_F, because high-momenta contributions are now incorporated in the effective interaction. Hence, we may replace T_0 by its zero-energy and zero-momentum, $U_0 = 4\pi\hbar^2 a/m$. T also depends weakly on momentum for momenta of order of p_F, Eq. (C.24) is then

$$\frac{U_0}{V}\sum_{\mathbf{p}''}\left[\frac{2f_{\mathbf{p}''} - 1}{2\xi_{\mathbf{p}''}} + \frac{1}{2\epsilon^0_{\mathbf{p}''}}\right] = U_0\int_0^\infty d\epsilon N(\epsilon)\left(\frac{f(\epsilon)}{\epsilon - \mu} - \frac{1}{2(\epsilon - \mu)} + \frac{1}{2\epsilon}\right) = 1, \tag{C.25}$$

where $f(\epsilon) = \{\exp[(\epsilon - \mu)/(k_BT)] + 1\}^{-1}$ and $N(\epsilon)$ is the single hyperfine state density of states per unit volume, Eq. (C.6). We take μ to be positive[1] so the integration over ϵ should be understood as the principal value. For positive μ

$$\int_0^\infty d\epsilon\ \epsilon^{1/2}\left(-\frac{1}{\epsilon - \mu} + \frac{1}{\epsilon}\right) = 0, \tag{C.26}$$

then Eq. (C.25) reduces to

$$U_0\int_0^\infty d\epsilon N(\epsilon)\frac{f(\epsilon)}{\epsilon - \mu} = 1. \tag{C.27}$$

In the following we solve this equation for an attractive interaction $U_0 < 0$ in the weak-coupling limit, $N(\epsilon_F)|U_0| \ll 1$.

---

[1] For strong interactions the chemical potential can be negative.

C.2.4 Analytical results

At $T = 0$ the integral in Eq. (C.27) diverges as $\epsilon \to \mu$, whereas at non-zero temperatures it is cutoff by the Fermi function at $|\xi_{\mathbf{p}}| \sim k_B T$. Hence, there is always a temperature T_c satisfying Eq. (C.27). We set $T = T_c$ and introduce dimensionless quantities $x = \epsilon/\mu$ and $y = \mu/(k_B T_c)$, thus we may write Eq. (C.27) as

$$\frac{1}{N(\epsilon_F)|U_0|} = -\int_0^\infty dx\, \frac{x^{1/2}}{x-1}\frac{1}{e^{(x-1)y}+1}. \tag{C.28}$$

In the weak-coupling limit, $T_c \ll T_F$, so we evaluate Eq. (C.28) at low-temperatures, $k_B T_c \ll \mu$, which implies $\mu \simeq \epsilon_F$. We also use the identity

$$\frac{x^{1/2}}{x-1} = \frac{1}{x^{1/2}+1} + \frac{1}{x-1}. \tag{C.29}$$

The first term on the right-hand side of Eq. (C.29) does not diverge at the Fermi surface in the zero-temperature limit. Hence, we replace the integral by its value at $T = 0$ ($y \to \infty$), which is

$$\int_0^1 \frac{dx}{x^{1/2}+1} = 2(1 - \ln 2). \tag{C.30}$$

The second term on the right-hand side of Eq. (C.29) has a singularity at the Fermi surface, thus the integral must be interpreted as a principal value one. We split the range of integration from 0 to $1-\delta$, and from $1+\delta$ to ∞, where δ is a small quantity and we will take the limit $\delta \to 0$ afterwards. Integrating by parts, and changing the lower limit of integration to $-\infty$ (because $T_c \ll T_F$), yields

$$\int_0^\infty \frac{dx}{x-1}\frac{1}{e^{(x-1)y}+1} = \int_0^\infty dz \ln\left(\frac{z}{y}\right)\frac{1}{2\cosh^2\left(\frac{z}{2}\right)} = -\ln\left(\frac{2\gamma y}{\pi}\right), \tag{C.31}$$

where $\gamma = e^C \approx 1.781$ and C is the Euler-Mascheroni constant [2]. The transition temperature is found by adding the contributions from Eqs. (C.30) and (C.31), which is [146]

$$kT_c = \frac{8\gamma}{\pi e^2}\epsilon_F e^{-\frac{1}{N(\epsilon_F)|U_0|}} \approx 0.61\epsilon_F e^{-\frac{1}{N(\epsilon_F)|U_0|}}. \tag{C.32}$$

This result confirms the qualitative estimate of Eq. (C.14), although it is not a final answer because it neglects the influence of the medium on the interactions between atoms. We now analyze the effects of induced interactions in mixtures of fermions and show that they significantly reduce the transition temperature.

---

[2] The Euler-Mascheroni constant arises in many integrals, one of them is

$$C = -\int_0^\infty e^{-u} \ln u \, du \approx 0.577.$$

C.2.5 Induced interactions

The interaction between two fermions in a medium differs from the interaction between two fermions *in vacuo*, as we have already mentioned. Surprisingly, the net effect of the influence of the medium is changing the prefactor of Eq. (C.32), as shown in [147].

Consider an a-fermion with momentum $\mathbf{p}$ and a b-fermion with momentum $-\mathbf{p}$ that scatter to states with momenta $\mathbf{p}'$ and $-\mathbf{p}'$, respectively. The previous assumption was that only the bare two-body interaction could accomplish this momentum transfer. However, in the presence of a medium, it is possible that the incoming a-fermion interacts with a b-fermion in the medium with momentum $\mathbf{p}''$ and scatters to a state with an a-fermion with momentum $\mathbf{p}+\mathbf{p}'+\mathbf{p}''$ and a b-fermion with momentum $-\mathbf{p}'$. Then, the a-fermion interacts with the other incoming b-fermion with momentum $-\mathbf{p}$ to give an a-fermion with momentum $-\mathbf{p}'$ and a b-fermion with momentum $\mathbf{p}''$. The overall result is the same as the original process, since the particle from the medium that participated in the process returned to its original state. An illustration of this process is shown in Fig. C.2 (a); a related process is shown in Fig. C.2 (b), where the b-fermion interacts first with an a-particle in the Fermi sea.

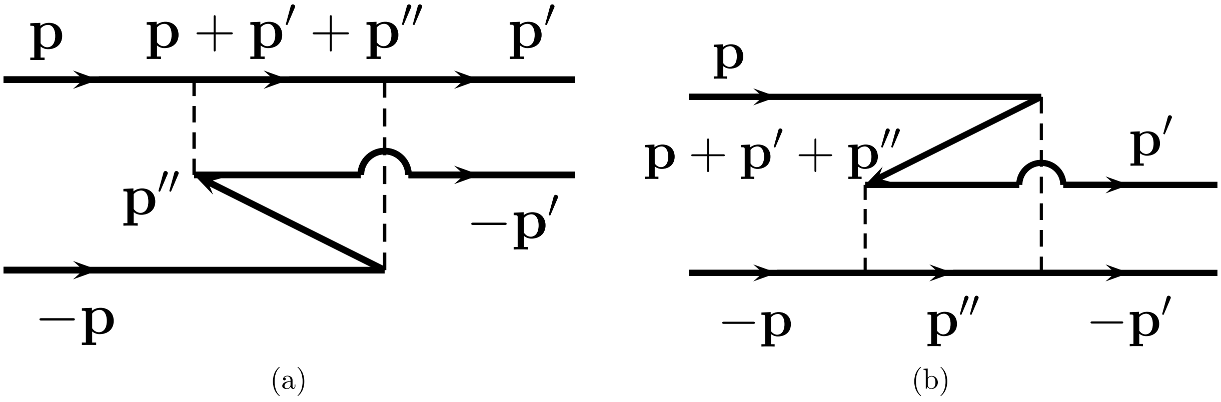

Figure C.2: Diagrams representing two-particle interactions in the presence of a medium. The notation is the same of Fig. C.1.

To calculate the change in the effective interaction due to the medium we consider only interactions between particles close to the Fermi surface, because of the factor $1/(\epsilon-\mu)$ in Eq. (C.25). Thus we set the momentum equal to the Fermi momentum and the energy equal to the chemical potential. We use second-order perturbation theory alongside with the appropriate thermal factors, so that the induced interaction is given by

$$
\begin{aligned}
U_{ind}(\mathbf{p},\mathbf{p}') &= -\frac{1}{V}\sum_{\mathbf{p}''} U_0^2 \left[\frac{f_{\mathbf{p}''}(1-f_{\mathbf{p}+\mathbf{p}'+\mathbf{p}''})}{\epsilon_{\mathbf{p}''}-\epsilon_{\mathbf{p}+\mathbf{p}'+\mathbf{p}''}} + \frac{f_{\mathbf{p}+\mathbf{p}'+\mathbf{p}''}(1-f_{\mathbf{p}''})}{\epsilon_{\mathbf{p}+\mathbf{p}'+\mathbf{p}''}-\epsilon_{\mathbf{p}''}}\right] \\
&= \int \frac{d\mathbf{p}''}{(2\pi\hbar)^3} U_0^2 \frac{f_{\mathbf{p}''}-f_{\mathbf{p}+\mathbf{p}'+\mathbf{p}''}}{\epsilon_{\mathbf{p}+\mathbf{p}'+\mathbf{p}''}-\epsilon_{\mathbf{p}''}} \\
&= U_0^2 L(|\mathbf{p}'+\mathbf{p}|). \qquad \text{(C.33)}
\end{aligned}
$$

The minus sign in the first equation arises from the anticommutation relations of fermionic creation and annihilation operators. If we consider the creation and annihilation operators $\hat{a}^\dagger$, $\hat{a}$, $\hat{b}^\dagger$ and $\hat{b}$ for the two states, the combination $\hat{a}^\dagger_{\mathbf{p}'}\hat{b}_{-\mathbf{p}}\hat{b}^\dagger_{-\mathbf{p}'}\hat{a}_{\mathbf{p}}$ corresponds to Fig. C.2 (a) and the operators $\hat{b}^\dagger_{-\mathbf{p}'}\hat{a}_{\mathbf{p}}\hat{a}^\dagger_{\mathbf{p}'}\hat{b}_{-\mathbf{p}}$ to Fig. C.2 (b). If we arrange the operators in the standard order $\hat{a}^\dagger_{\mathbf{p}'}\hat{b}^\dagger_{-\mathbf{p}'}\hat{b}_{-\mathbf{p}}\hat{a}_{\mathbf{p}}$, we get a minus sign in both cases. The quantity $L(q)$ is the static Lindhard screening function,

$$
L(q) = \int \frac{d\mathbf{p}}{(2\pi\hbar)^3}\frac{f_{\mathbf{p}}-f_{\mathbf{p}+\mathbf{q}}}{\epsilon_{\mathbf{p}+\mathbf{q}}-\epsilon_{\mathbf{p}}} \simeq N(\epsilon_F)\left[\frac{1}{2}+\frac{(1-w^2)}{4w}\ln\left|\frac{1+w}{1-w}\right|\right], \qquad \text{(C.34)}
$$

with $w = q/(2p_F)$. The temperatures of interest are much less than the Fermi temperature, and the second expression is at $T = 0$. The Lindhard function is the negative of the density-density response function $\chi(q)$ for an one-component Fermi gas, $L(q) = -\chi(q)$. The sign of U_{ind} is positive, corresponding to a repulsive interaction, thus pairing is not favored.

Solving Eq. (C.17) with U_{ind} as a perturbation yields T_c of Eq. (C.32) with U_0 replaced by $U_0 + \langle U_{ind}\rangle$, where

$$
\langle U_{ind}\rangle = \frac{1}{2}\int_{-1}^{1} U_{ind}\, d(\cos\theta), \qquad \text{(C.35)}
$$

denoting an average over the Fermi surface. The angle θ is measured between $\mathbf{p}$ and $\mathbf{p}'$. From Eq. (C.33) we have

$$
U_0 + \langle U_{ind}\rangle \simeq U_0 - U_0^2\langle\chi(q)\rangle. \qquad \text{(C.36)}
$$

Therefore,

$$
\frac{1}{U_0+\langle U_{ind}\rangle} \simeq \frac{1}{U_0} + \langle\chi(q)\rangle. \qquad \text{(C.37)}
$$

Since $p = p' = p_F$, $q^2 = 2p_F^2(1+\cos\theta)$. The integral of the Lindhard function over the Fermi surface is proportional to

$$
\int_0^1 dw\; 2w\left[\frac{1}{2}+\frac{1}{4w}(1-w^2)\ln\left(\frac{1+w}{1-w}\right)\right] = \frac{2}{3}\ln 2 + \frac{1}{3} = \ln(4e)^{1/3}. \qquad \text{(C.38)}
$$

Hence, the induced interaction lowers the transition temperature by a factor of $(4e)^{1/3} \approx 2.22$,

$$k_B T_c = \left(\frac{2}{e}\right)^{7/3} \frac{\gamma}{\pi} \epsilon_F e^{-\frac{1}{N(\epsilon_F)|U_0|}} \approx 0.28 \epsilon_F e^{-\frac{1}{N(\epsilon_F)|U_0|}}. \tag{C.39}$$

C.3 The condensed phase

At T_c the fermionic system is unstable with respect to pair formation, and below the critical temperature there is a condensate of pairs in a zero-momentum state. This is intrinsically a many-body process, not simply the formation of two-fermions molecules. We introduce a quantitative theory of the condensated state supposing a uniform gas with equal densities of the two different internal states of the fermionic species. Because of the Pauli exclusion principle, interactions between particles in the same state are suppressed and we neglect them. The Hamiltonian we consider is

$$\hat{H} = \sum_{\mathbf{p}} \epsilon^0_{\mathbf{p}} (\hat{a}^\dagger_{\mathbf{p}} \hat{a}_{\mathbf{p}} + \hat{b}^\dagger_{\mathbf{p}} \hat{b}_{\mathbf{p}}) + \frac{1}{V} \sum_{\mathbf{p}\mathbf{p}'\mathbf{q}} U(\mathbf{p}, \mathbf{p}', \mathbf{q}) \hat{a}^\dagger_{\mathbf{p}+\mathbf{q}} \hat{b}^\dagger_{\mathbf{p}'-\mathbf{q}} \hat{b}^\dagger_{\mathbf{p}'} \hat{a}^\dagger_{\mathbf{p}}, \tag{C.40}$$

where the operators $\hat{a}^\dagger$, $\hat{a}$, $\hat{b}^\dagger$ and $\hat{b}$ are creation and annihilation for the two kinds of fermions. There is no 1/2 factor in the interaction term because the two particles belong to different internal states. The operators obey the Fermi anticommutation rules

$$\begin{aligned} \{\hat{a}_{\mathbf{p}}, \hat{a}^\dagger_{\mathbf{p}'}\} &= \{\hat{b}_{\mathbf{p}}, \hat{b}^\dagger_{\mathbf{p}'}\} = \delta_{\mathbf{p},\mathbf{p}'}; \\ \{\hat{a}_{\mathbf{p}}, \hat{b}_{\mathbf{p}'}\} &= \{\hat{a}^\dagger_{\mathbf{p}}, \hat{b}_{\mathbf{p}'}\} = \{\hat{a}_{\mathbf{p}}, \hat{b}^\dagger_{\mathbf{p}'}\} = \{\hat{a}^\dagger_{\mathbf{p}}, \hat{b}^\dagger_{\mathbf{p}'}\} = 0. \end{aligned} \tag{C.41}$$

It is convenient to work with the operator $\hat{K} = \hat{H} - \mu \hat{N}$, where μ is the chemical potential chosen to keep the average number of particles fixed. It is given by

$$\hat{K} = \sum_{\mathbf{p}} (\epsilon^0_{\mathbf{p}} - \mu)(\hat{a}^\dagger_{\mathbf{p}} \hat{a}_{\mathbf{p}} + \hat{b}^\dagger_{\mathbf{p}} \hat{b}_{\mathbf{p}}) + \frac{1}{V} \sum_{\mathbf{p}\mathbf{p}'\mathbf{q}} U(\mathbf{p}, \mathbf{p}', \mathbf{q}) \hat{a}^\dagger_{\mathbf{p}+\mathbf{q}} \hat{b}^\dagger_{\mathbf{p}'-\mathbf{q}} \hat{b}^\dagger_{\mathbf{p}'} \hat{a}^\dagger_{\mathbf{p}}. \tag{C.42}$$

Elementary excitations

We use the Bogoliubov approach to calculate properties of the Fermi gas. For a Bose gas, it amounts to assuming that the creation and annihilation operators may be written as a classical part, a c number, plus a fluctuation term. For the fermionic case, the condensate consists of pairs of fermions, so that we substitute the c number for pair creation and pair annihilation operators. For a condensate with total momentum zero, the two paired fermions must have equal and opposite momenta. They also must be in different internal states, as discussed previously. We write

$$\hat{b}_{-\mathbf{p}} \hat{a}_{\mathbf{p}} = C_{\mathbf{p}} + (\hat{b}_{-\mathbf{p}} \hat{a}_{\mathbf{p}} - C_{\mathbf{p}}), \tag{C.43}$$

where $C_{\mathbf{p}}$ is a c number. The relative phases of states with particle number differing by two can be chosen so that $C_{\mathbf{p}}$ is real. We substitute this expression into Eq. (C.42) and retain terms with two or fewer creation or annihilation operators, leading to

$$\hat{K} = \sum_{\mathbf{p}}(\epsilon^0_{\mathbf{p}} - \mu)(\hat{a}^\dagger_{\mathbf{p}}\hat{a}_{\mathbf{p}} + \hat{b}^\dagger_{-\mathbf{p}}\hat{b}_{-\mathbf{p}}) + \sum_{\mathbf{p}}\Delta_{\mathbf{p}}(\hat{a}^\dagger_{\mathbf{p}}\hat{b}^\dagger_{-\mathbf{p}} + \hat{b}_{-\mathbf{p}}\hat{a}_{\mathbf{p}}) - \frac{1}{V}\sum_{\mathbf{pp}'}U(\mathbf{p},\mathbf{p}')C_{\mathbf{p}}C_{\mathbf{p}'} \tag{C.44}$$

Here,

$$\Delta_{\mathbf{p}} = \frac{1}{V}\sum_{\mathbf{p}'}U(\mathbf{p},\mathbf{p}')C_{\mathbf{p}'}. \tag{C.45}$$

For simplicity, we have omitted the final argument in the interaction $U(\mathbf{p}, -\mathbf{p}, \mathbf{p}' - \mathbf{p}) \to U(\mathbf{p}, \mathbf{p}')$. The $C_{\mathbf{p}}$ must be determined self-consistently, hence

$$C_{\mathbf{p}} = \langle \hat{b}_{-\mathbf{p}}\hat{a}_{\mathbf{p}}\rangle = \langle \hat{a}^\dagger_{\mathbf{p}}\hat{b}^\dagger_{-\mathbf{p}}\rangle, \tag{C.46}$$

where $\langle\cdot\rangle$ denotes an expectation value.

The Hamiltonian is now a sum of independent terms of the type

$$\hat{h} = \epsilon_0(\hat{a}^\dagger\hat{a} + \hat{b}^\dagger\hat{b}) + \epsilon_1(\hat{a}^\dagger\hat{b}^\dagger + \hat{b}\hat{a}), \tag{C.47}$$

where $\hat{a} = \hat{a}_{\mathbf{p}}$ and $\hat{b} = \hat{b}_{-\mathbf{p}}$. We introduce new operators $\hat{\alpha}$ and $\hat{\beta}$ defined by the transformation

$$\begin{aligned} \hat{\alpha} &= u\hat{a} + v\hat{b}^\dagger, \\ \hat{\beta} &= u\hat{b} - v\hat{a}^\dagger, \end{aligned} \tag{C.48}$$

with u and v real, and we impose that they satisfy the Fermi commutation rules,

$$\begin{aligned} \{\hat{\alpha}, \hat{\alpha}^\dagger\} &= \{\hat{\beta}, \hat{\beta}^\dagger\} = 1 \\ \{\hat{\alpha}, \hat{\beta}^\dagger\} &= \{\hat{\beta}, \hat{\alpha}^\dagger\} = \{\hat{\alpha}, \hat{\beta}\} = \{\hat{\alpha}^\dagger, \hat{\beta}^\dagger\} = 0. \end{aligned} \tag{C.49}$$

These restrictions are satisfied if

$$u^2 + v^2 = 1. \tag{C.50}$$

Inverting the Eqs. (C.48) we find

$$\begin{aligned} \hat{a} &= u\hat{\alpha} - v\hat{\beta}^\dagger, \\ \hat{b} &= u\hat{\beta} + v\hat{\alpha}^\dagger. \end{aligned} \tag{C.51}$$

Inserting Eqs. (C.51) into Eq. (C.47) yields

$$\begin{aligned} \hat{h} = 2v^2\epsilon_0 - 2uv\epsilon_1 &+ [\epsilon_0(u^2 - v^2) + 2uv\epsilon_1](\hat{\alpha}^\dagger\hat{\alpha} + \hat{\beta}^\dagger\hat{\beta}) \\ &- [\epsilon_1(u^2 - v^2) - 2uv\epsilon_0](\hat{\alpha}\hat{\beta} + \hat{\beta}^\dagger\hat{\alpha}^\dagger). \end{aligned} \tag{C.52}$$

We choose u and v so that

$$\epsilon_1(u^2 - v^2) - 2uv\epsilon_0 = 0, \tag{C.53}$$

thus eliminating the term proportional to $\hat{\alpha}\hat{\beta}+\hat{\beta}^\dagger\hat{\alpha}^\dagger$. We write, in accordance to Eq. (C.50),

$$\begin{aligned} u &= \cos t, \\ v &= \sin t, \end{aligned} \tag{C.54}$$

where t is a parameter to be determined. This amounts to

$$\epsilon_1(\cos^2 t - \sin^2 t) - 2\epsilon_0 \sin t \cos t = 0, \tag{C.55}$$

or alternatively,

$$\tan(2t) = \frac{\epsilon_1}{\epsilon_0}. \tag{C.56}$$

Hence,

$$\begin{aligned} u^2 - v^2 &= \frac{\epsilon_0}{\sqrt{\epsilon_0^2 + \epsilon_1^2}}, \\ 2uv &= \frac{\epsilon_1}{\sqrt{\epsilon_0^2 + \epsilon_1^2}}. \end{aligned} \tag{C.57}$$

Substituting this result into Eq. (C.52),

$$\hat{h} = \epsilon(\hat{\alpha}^\dagger\hat{\alpha} + \hat{\beta}^\dagger\hat{\beta}) + \epsilon_0 - \epsilon, \tag{C.58}$$

where $\epsilon \equiv \sqrt{\epsilon_0^2 + \epsilon_1^2}$. We chose the positive sign for the square root in order to guarantee that the excitations have positive energy.

In order to diagonalize $\hat{K}$ from Eq. (C.42) we introduce the operators

$$\begin{aligned} \hat{\alpha}_{\mathbf{p}} &= u_{\mathbf{p}}\hat{a}_{\mathbf{p}} + v_{\mathbf{p}}\hat{b}^\dagger_{-\mathbf{p}}, \\ \hat{\beta}_{-\mathbf{p}} &= u_{\mathbf{p}}\hat{b}_{-\mathbf{p}} - v_{\mathbf{p}}\hat{a}^\dagger_{\mathbf{p}}. \end{aligned} \tag{C.59}$$

The normalization requires

$$u_{\mathbf{p}}^2 + v_{\mathbf{p}}^2 = 1, \tag{C.60}$$

and if we choose

$$u_{\mathbf{p}}v_{\mathbf{p}} = \frac{\Delta_{\mathbf{p}}}{2\epsilon_{\mathbf{p}}}, \tag{C.61}$$

the terms in Hamiltonian proportional to $\hat{\alpha}\hat{\beta}$ or $\hat{\beta}^\dagger\hat{\alpha}^\dagger$ vanish. The excitation energy $\epsilon_{\mathbf{p}}$ is given by

$$\epsilon_{\mathbf{p}}^2 = \Delta_{\mathbf{p}}^2 + \xi_{\mathbf{p}}^2, \tag{C.62}$$

with

$$\xi_{\mathbf{p}} = \epsilon^0_{\mathbf{p}} - \mu. \tag{C.63}$$

Near the Fermi surface, $\xi_{\mathbf{p}} \approx (p - p_F)v_F$, where $v_F = p_F/m$ is the Fermi velocity, and the spectrum exhibits a gap $\Delta_{\mathbf{p}}$ for $p = p_F$. Excitations exhibit free particle behavior for $p - p_F \gg \Delta/v_F$. The characteristic length, which is the healing distance for disturbances in the Fermi gas, is given by

$$\xi_{BCS} \equiv \frac{\hbar v_F}{\Delta}. \tag{C.64}$$

In the BCS theory, its zero-temperature value is $\xi_0 = \hbar v_F/(\pi\Delta(0))$, where $\Delta(0)$ is the gap at $T = 0$.

The coefficients u and v are

$$\begin{aligned} u^2_{\mathbf{p}} &= \frac{1}{2}\left(1 + \frac{\xi_{\mathbf{p}}}{\epsilon_{\mathbf{p}}}\right), \\ v^2_{\mathbf{p}} &= \frac{1}{2}\left(1 - \frac{\xi_{\mathbf{p}}}{\epsilon_{\mathbf{p}}}\right). \end{aligned} \tag{C.65}$$

Substituting in the Hamiltonian Eq. (C.44) yields

$$\hat{K} = \sum_{\mathbf{p}} \epsilon_{\mathbf{p}}(\hat{\alpha}^\dagger_{\mathbf{p}}\hat{\alpha}_{\mathbf{p}} + \hat{\beta}^\dagger_{\mathbf{p}}\hat{\beta}_{\mathbf{p}}) - \sum_{\mathbf{p}}(\epsilon_{\mathbf{p}} - \epsilon^0_{\mathbf{p}} + \mu) - \frac{1}{V}\sum_{\mathbf{p}\mathbf{p}'} U(\mathbf{p}, \mathbf{p}')C_{\mathbf{p}}C_{\mathbf{p}'}, \tag{C.66}$$

thus describing non-interacting excitations with energy $\epsilon_{\mathbf{p}}$.

The gap equation

The gap $\Delta_{\mathbf{p}}$ is determined by Eq. (C.45) when we know $C_{\mathbf{p}}$, Eq. (C.46), given by

$$C_{\mathbf{p}} = \langle(u_{\mathbf{p}}\hat{\beta}_{-\mathbf{p}} + v_{\mathbf{p}}\hat{\alpha}^\dagger_{\mathbf{p}})(u_{\mathbf{p}}\hat{\alpha}_{\mathbf{p}} - v_{\mathbf{p}}\hat{\beta}^\dagger_{-\mathbf{p}})\rangle = -[1 - 2f(\epsilon_{\mathbf{p}})]\frac{\Delta_{\mathbf{p}}}{2\epsilon_{\mathbf{p}}}. \tag{C.67}$$

The thermal averages of the operators for the numbers of excitations are

$$\langle\hat{\alpha}^\dagger_{\mathbf{p}}\hat{\alpha}_{\mathbf{p}}\rangle = \langle\hat{\beta}^\dagger_{\mathbf{p}}\hat{\beta}_{\mathbf{p}}\rangle = f(\epsilon_{\mathbf{p}}) = \frac{1}{\exp[\epsilon_{\mathbf{p}}/(k_BT)] + 1}, \tag{C.68}$$

hence the gap is given by

$$\Delta_{\mathbf{p}} = -\frac{1}{V}\sum_{\mathbf{p}'} U(\mathbf{p}, \mathbf{p}')\frac{1 - 2f(\epsilon'_{\mathbf{p}})}{2\epsilon_{\mathbf{p}'}}\Delta_{\mathbf{p}'}. \tag{C.69}$$

At the transition temperature the gap vanishes $\Delta_{\mathbf{p}} = 0$, thus the excitation energy may be replaced by $\epsilon_{\mathbf{p}} = |\epsilon^0_{\mathbf{p}} - \mu|$. The gap equation becomes

$$\begin{aligned}\Delta_{\mathbf{p}} &= -\frac{1}{V}\sum_{\mathbf{p}'} U(\mathbf{p},\mathbf{p}')\frac{1-2f(|\epsilon^0_{\mathbf{p}'}-\mu|)}{2|\epsilon^0_{\mathbf{p}'}-\mu|}\Delta_{\mathbf{p}'} \\ &= -\frac{1}{V}\sum_{\mathbf{p}'} U(\mathbf{p},\mathbf{p}')\frac{1-2f(\epsilon^0_{\mathbf{p}'}-\mu)}{2(\epsilon^0_{\mathbf{p}'}-\mu)}\Delta_{\mathbf{p}'}. \qquad \text{(C.70)}\end{aligned}$$

The last equation follows from the even parity of $[1-2f(\epsilon)]/\epsilon$. This equation contains the same information as Eq. (C.17), which gives the temperature at which two-body scattering becomes singular.

In order to solve the gap equation, we eliminate the bare interaction U in favor of T_0, the T matrix in free space. We formally write $\Delta = UG_M\Delta$ and repeat the steps described in Sec. C.2.3. The result is

$$\Delta_{\mathbf{p}} = -\frac{U_0}{V}\sum_{\mathbf{p}'}\left[\frac{1-2f(\epsilon_{\mathbf{p}'})}{2\epsilon_{\mathbf{p}'}} - \frac{1}{2\epsilon^0_{\mathbf{p}'}}\right]\Delta_{\mathbf{p}'}. \qquad \text{(C.71)}$$

An equivalent form for $\mu > 0$, using the identity from Eq. (C.26), is

$$\Delta_{\mathbf{p}} = -\frac{U_0}{V}\sum_{\mathbf{p}'}\left[\frac{1-2f(\epsilon_{\mathbf{p}'})}{2\epsilon_{\mathbf{p}'}} - \frac{1}{2(\epsilon^0_{\mathbf{p}'}-\mu)}\right]\Delta_{\mathbf{p}'}. \qquad \text{(C.72)}$$

The gap at T=0

We now determine the gap at $T = 0$. Neglecting the induced interactions, Eq. (C.72) reduces to

$$\Delta_{\mathbf{p}} = -\frac{U_0}{V}\sum_{\mathbf{p}'}\left[\frac{1}{2\epsilon_{\mathbf{p}'}} - \frac{1}{2(\epsilon^0_{\mathbf{p}'}-\mu)}\right]\Delta_{\mathbf{p}'}. \qquad \text{(C.73)}$$

We notice that the gap corresponds to an s-wave pairing, because $\Delta_{\mathbf{p}}$ is independent of the direction of $\mathbf{p}$. Since the main contributions to the integral come from momenta of order p_F, we replace the gap by its value at the Fermi surface, Δ. The result is

$$\begin{aligned}1 &= -\frac{U_0}{2V}\sum_{\mathbf{p}}\left[\frac{1}{(\xi^2_{\mathbf{p}}+\Delta^2)^{1/2}} - \frac{1}{\xi_{\mathbf{p}}}\right] \\ &= -\frac{U_0 N(\epsilon_F)}{2}\int_0^\infty dx\, x^{1/2}\left[\frac{1}{[(x-1)^2+(\Delta/\epsilon_F)^2]^{1/2}} - \frac{1}{x-1}\right]. \qquad \text{(C.74)}\end{aligned}$$

Similar to what we did when evaluating the integrals for T_c, we split this integral into two, using $x^{1/2} = (x^{1/2}-1)+1$. The integral with the first term may be evaluated with $\Delta = 0$, and the second may be evaluated directly, since $\Delta/\epsilon_F \ll 1$. The result is

$$\Delta = \frac{8}{e^2}\epsilon_F e^{-1/(N(\epsilon_F)|U_0|)}. \qquad \text{(C.75)}$$

Including induced interactions reduces the gap by a factor of $(4e)^{-1/3}$, as it was for the transition temperature, hence

$$\Delta = \left(\frac{2}{e}\right)^{7/3} \epsilon_F e^{-1/(N(\epsilon_F)|U_0|)}. \tag{C.76}$$

The ratio between the gap at $T = 0$ and the transition temperature is given by

$$\frac{\Delta(T=0)}{kT_c} = \frac{\pi}{\gamma} \approx 1.76. \tag{C.77}$$

Pairing in dilute gases differs much from phonon-exchange interaction in metals. The former presents interactions of importance in excess of the Fermi energy, whereas in metals they are significant only over an interval of $\hbar\omega_D$ about the Fermi surface.

Appendix D

Classical hydrodynamics

The main reason that vortices have been an important branch of fluid dynamics is the belief that turbulence may be represented as a superposition of interacting vortices. We begin by reviewing some concepts of fluid dynamics, which will be useful when dealing with quantized vortices [134].

The equation of conservation of mass for a fluid of density ρ and velocity $\mathbf{v}$ is

$$\frac{\partial \rho}{\partial t} + \nabla \cdot (\rho \mathbf{v}) = 0. \tag{D.1}$$

If the fluid is incompressible then

$$\nabla \cdot \mathbf{v} = 0. \tag{D.2}$$

The equation of motion for an incompressible viscous fluid, known as the Navier-Stokes equation, is

$$\frac{d\mathbf{v}}{dt} = \frac{\partial \mathbf{v}}{\partial t} + (\mathbf{v} \cdot \nabla)\mathbf{v} = -\frac{1}{\rho}\nabla p + \nu \nabla^2 \mathbf{v}, \tag{D.3}$$

where $\mathbf{v}$ is the velocity, p is the pressure and $\nu = \eta/\rho$ is the ratio of the dynamic viscosity η to density ρ. The Navier-Stokes equation is usually very difficult to solve, even numerically. For the flow of an incompressible, adiabatic and inviscid (without viscosity) fluid, we have

$$\frac{d\mathbf{v}}{dt} = \frac{\partial \mathbf{v}}{\partial t} + (\mathbf{v} \cdot \nabla)\mathbf{v} = -\frac{1}{\rho}\nabla p, \tag{D.4}$$

which is known as Euler's equation. Defining $w \equiv p/\rho$ and using the vector identity $\frac{1}{2}\nabla v^2 = \mathbf{v} \times (\nabla \times \mathbf{v}) + (\mathbf{v} \cdot \nabla)\mathbf{v}$, Euler's equation takes the form

$$\frac{\partial \mathbf{v}}{\partial t} - \mathbf{v} \times (\nabla \times \mathbf{v}) = -\nabla \left(w + \frac{1}{2} v^2 \right). \tag{D.5}$$

Realistic approaches can be obtained by considering a boundary layer. At high Reynolds numbers, the flow near a boundary is described by Eq. (D.3); and the remainder of the flow can be described by Eq. (D.5), with appropriate joining of solutions.

We proceed to include in the flow of the inviscid fluid such features as circulation and vortices, whose generation depends on viscosity. The curl of the velocity field,

$$\boldsymbol{\omega} = \nabla \times \mathbf{v}, \tag{D.6}$$

is known as vorticity and may be thought of as the circulation per unit area. A curve drawn from point to point in the fluid, so that its direction is always the instantaneous direction of $\boldsymbol{\omega}$, is called *vortex line*. The differential equation describing the line is $\boldsymbol{\omega} \times d\mathbf{l} = 0$. Because of Eq. (D.6), we have

$$\nabla \cdot \boldsymbol{\omega} = 0. \tag{D.7}$$

If we draw a closed curve C in the fluid and include every vortex line passing through this curve, we have a *vortex tube*. It follows from Gauss' theorem that the integral of the normal component of $\boldsymbol{\omega}$ over any closed surface vanishes,

$$\int_S \boldsymbol{\omega} \cdot d\mathbf{S} = 0. \tag{D.8}$$

If we apply this result to two cross-sections $d\mathbf{S}_1$ and $d\mathbf{S}_2$ of the tube, the sides do not contribute, and we have

$$\int_{S_1} \boldsymbol{\omega} \cdot d\mathbf{S}_1 = \int_{S_2} \boldsymbol{\omega} \cdot d\mathbf{S}_2. \tag{D.9}$$

Thus the flux of vorticity across any section of the tube is conserved and it is a characteristic of the tube. Vortex tubes cannot terminate in the fluid; they must be closed or terminate on the boundaries.

The Navier-Stokes equation, Eq. (D.3), can be written as

$$\frac{\partial \boldsymbol{\omega}}{\partial t} = \nabla \times (\mathbf{v} \times \boldsymbol{\omega}) + \nu \nabla^2 \boldsymbol{\omega} = (\boldsymbol{\omega} \cdot \nabla)\mathbf{v} - (\mathbf{v} \cdot \nabla)\boldsymbol{\omega} + \boldsymbol{\omega} \nabla^2 \boldsymbol{\omega}. \tag{D.10}$$

We introduce a characteristic length L and velocity V, and we make Eq. (D.10) dimensionless with the following transformations:

$$\begin{aligned} \boldsymbol{\omega} &\rightarrow \frac{\boldsymbol{\omega} V}{L}, \\ t &\rightarrow \frac{tL}{V}, \\ v &\rightarrow vV, \end{aligned} \tag{D.11}$$

which yield

$$\frac{\partial \boldsymbol{\omega}}{\partial t} = (\boldsymbol{\omega} \cdot \nabla)\mathbf{v} - (\mathbf{v} \cdot \nabla)\boldsymbol{\omega} + \frac{1}{Re} \nabla^2 \boldsymbol{\omega}, \tag{D.12}$$

with the Reynolds number $Re = VL/\nu$. For an ideal fluid, Eq. (D.12) is reduced to

$$\frac{\partial \boldsymbol{\omega}}{\partial t} - \nabla \times (\mathbf{v} \times \boldsymbol{\omega}) = 0. \tag{D.13}$$

Consider a surface S enclosed by a contour C. Let $d\mathbf{S}$ be an infinitesimal element of this surface. Multiplying scalarly by $d\mathbf{S}$ and integrating over the surface yields

$$\int_S \frac{\partial \boldsymbol{\omega}}{\partial t} \cdot d\mathbf{S} - \int_S \nabla \times (\mathbf{v} \times \boldsymbol{\omega}) \cdot d\mathbf{S} = 0. \tag{D.14}$$

Using Stokes' theorem for the second integral, we have

$$\int_S \frac{\partial \boldsymbol{\omega}}{\partial t} \cdot d\mathbf{S} + \int_C \boldsymbol{\omega} \cdot (\mathbf{v} \times d\mathbf{l}) = 0, \tag{D.15}$$

where $d\mathbf{l}$ is an element along the contour C defining the vortex tube at a particular cross-section. A careful argument in [134] shows that

$$\frac{d}{dt} \int_S \boldsymbol{\omega} \cdot d\mathbf{S} = 0. \tag{D.16}$$

Thus, the integral of the normal component of $\boldsymbol{\omega}$ over any surface bound by a closed curve remains constant as we follow the surface S,

$$\int_S \boldsymbol{\omega} \cdot d\mathbf{S} = \text{constant}. \tag{D.17}$$

We can use Eq. (D.17) together with Stokes' theorem to write

$$\Gamma = \int_S \boldsymbol{\omega} \cdot d\mathbf{S} = \int_C \mathbf{v} \cdot d\mathbf{l} = \text{constant}, \tag{D.18}$$

where Γ is the circulation. This definition shows why the vorticity is the circulation per unit area. Furthermore, Eq. (D.18) can be rewritten as

$$\begin{aligned} \frac{d\Gamma}{dt} = \frac{d}{dt} \int_C \mathbf{v} \cdot d\mathbf{l} &= 0 \quad \text{or} \\ \int_C \mathbf{v} \cdot d\mathbf{l} &= \text{constant}, \end{aligned} \tag{D.19}$$

which is known as the law of conservation of circulation.

Appendix E

Stochastic reconfiguration method

The Stochastic Reconfiguration (SR) method [139] allows us to minimize the energy expectation value of a variational wavefunction containing many variational parameters in an arbitrary functional form. We assume that the wavefunction Ψ has p variational parameters $\{\alpha_k^0\}_{k=1,\cdots,p}$ and we seek the solution of the linear system

$$\sum_{k=0}^{p} s_{j,k} \Delta\alpha_k = \langle\Psi|O_k(\Lambda I - H)|\Psi\rangle, \tag{E.1}$$

where the operators O_k are defined on each N particle configuration $x = \{\mathbf{r}_1, \cdots, \mathbf{r}_N\}$ as the logarithmic derivatives with respect to the parameters α_k

$$O_k(x) = \frac{\partial}{\partial\alpha_k} \ln\Psi(x) \text{ for } k > 0. \tag{E.2}$$

The operator $O_{k=0}$ is the identity, equal to one independent on the configuration. The $(p+1) \times (p+1)$ matrix $s_{k,j}$ is given by

$$s_{j,k} = \frac{\langle\Psi|O_j O_k|\Psi\rangle}{\langle\Psi|\Psi\rangle}, \tag{E.3}$$

and is calculated at each iteration through standard variational Monte Carlo sampling; the single iteration constitutes a small simulation referred hereafter as bin. After each bin, the wavefunction parameters are iteratively updated

$$\alpha_k \to \alpha_k + \frac{\Delta\alpha_k}{\Delta\alpha_0}. \tag{E.4}$$

The method is convergent to an energy minimum for large enough Λ.

SR is similar to a standard steepest descent (SD) calculation, where the expectation value of the energy

$$E(\alpha_k) = \frac{\langle\Psi|H|\Psi\rangle}{\langle\Psi|\Psi\rangle} \tag{E.5}$$

is optimized by iteratively changing α_i according to the derivatives of the energy (generalized forces f_k)

$$\begin{gathered} f_k = -\tfrac{\partial E}{\partial \alpha_k} = -\tfrac{\langle\Psi|O_k H + H O_k + (\partial_{\alpha_k} H)|\Psi\rangle}{\langle\Psi|\Psi\rangle} + 2\tfrac{\langle\Psi|O_k|\Psi\rangle\langle\Psi|H|\Psi\rangle}{\langle\Psi|\Psi\rangle^2} \\ \alpha_k \to \alpha_k + \Delta t f_k. \end{gathered} \tag{E.6}$$

The small time step Δt can be taken as a suitable fixed value or determined at each iteration by minimizing the energy expectation value. Notice that we have assumed that the variational parameters may also appear in the Hamiltonian. The variation of the total energy ΔE at each step is negative for small enough Δt

$$\Delta E = -\Delta t \sum_i f_i^2 + \mathcal{O}(\Delta t^2), \tag{E.7}$$

thus the method certainly converges at the minimum when all the forces vanish.

In the following we will show that similar considerations hold for the SR method. Indeed, by eliminating the equation with $k = 0$ from the linear system (Eq. E.1), the SR iteration can be written in a form similar to SD

$$\alpha_i \to \alpha_i + \Delta t \sum_k \bar{s}_{i,k}^{-1} f_k, \tag{E.8}$$

where $\bar{s}$ is the reduced $p \times p$ matrix

$$\bar{s}_{j,k} = s_{j,k} - s_{j,0} s_{0,k} \tag{E.9}$$

and Δt is given by

$$\Delta t = \frac{1}{2\left(\Lambda - \frac{\langle\Psi|H|\Psi\rangle}{\langle\Psi|\Psi\rangle} - \sum\limits_{k>0} \Delta\alpha_k s_{k,0}\right)}. \tag{E.10}$$

Thus the value of Δt changes during the simulation and remains small for large enough energy shift Λ. However, analogy with the SD shows that an energy minimum is reached when Δt is sufficiently small and constant between iterations. The energy variation for a small change of the parameters is

$$\Delta E = -\Delta t \sum_{i,j} \bar{s}_{i,j}^{-1} f_i f_j. \tag{E.11}$$

The above term is always negative because $\overline{s}$ and $\overline{s}^{-1}$ are positive definite; s being an overlap matrix with all positive eigenvalues.

A condition for the stability of the SR, or SD, is that at each iteration the new parameters α' are close to the old α according to a distance. The most important difference between SR and SD is the definition of this distance. For SD we use the Cartesian metric

$$\Delta_\alpha = \sum_k |\alpha'_k - \alpha_k|^2. \tag{E.12}$$

Instead the SR uses the physical Hilbert space metric of the wavefunction Ψ

$$\Delta_\alpha = \sum_{i,j} \overline{s}_{i,j}(\alpha'_i - \alpha_i)(\alpha'_j - \alpha_j), \tag{E.13}$$

namely the square distance between the two normalized wavefunctions corresponding to two different sets of parameters $\{\alpha'_k\}$ and $\{\alpha_k\}$. The most convenient change of the variational parameters minimizes the functional $\Delta E + \overline{\Lambda}\Delta_\alpha$, where ΔE is the linear change in the energy $\Delta E = -\sum_i f_i(\alpha'_i - \alpha_i)$; and $\overline{\Lambda}$ is a Lagrange multiplier that allows a stable minimization of Ψ (with small change Δ_α). Finally, the iteration is obtained from Eq. (E.8).

The advantage of SR over SD is that sometimes a small change of the variational parameters correspond to a large change of the wavefunction, and SD takes into account this effect by using the Hilbert space metric of the wavefunction Ψ. A weak tolerance criterion $\epsilon \simeq 10^{-3}$ provides a very stable algorithm even when the dimension of the variational space is large.

Instead of setting the constant Λ, we choose to determine Δt by verifying the stability and convergence of the algorithm at fixed Δt. The simulation is stable whenever $1/\Delta t > \Lambda_{cut}$, where Λ_{cut} is strongly dependent on the wavefunction. A rough estimate of the number of iterations P is $P\Delta t \gg 1/G$, where G is the typical energy gap of the system.

Our aim is to conduct simulations with small bins, so many iterations can be performed. However, in the Monte Carlo framework the forces f_k are determined with some statistical noise, and there is an optimal value for the bin length which guarantees fast convergence and unbiased forces.